Numerical and experimental study of laser absorption in a plasma by inverse bremsstrahlung

Ronan Devriendt

INSTITUT POLYTECHNIQUE DE PARIS

NNT : 2022IPPAX078

Thèse de doctorat

Étude numérique et expérimentale de l'absorption laser dans un plasma par bremsstrahlung inverse

Thèse de doctorat de l'Institut Polytechnique de Paris
préparée à l'École polytechnique

École doctorale n°626 École doctorale de l'Institut Polytechnique de Paris (EDIPP)
Spécialité de doctorat : Physique

Thèse présentée et soutenue à Palaiseau, le 9 septembre 2022, par

RONAN DEVRIENDT

Composition du Jury :

Patrick Mora Directeur de recherche CNRS, École Polytechnique (CPHT)	Président
Scott Baalrud Associate Professor, University of Michigan	Rapporteur
Laurent Berthe Directeur de recherche CNRS, Université Paris XI (PIMM)	Rapporteur
Alexis Casner Directeur de recherche CEA, CEA CELIA	Examinateur
Sophie Baton Directrice de recherche CNRS, École Polytechnique (LULI)	Directrice de thèse
Olivier Poujade Ingénieur-chercheur, CEA/Bruyères-le-Châtel	Co-directeur de thèse
Stefan Hüller Directeur de recherche CNRS, École Polytechnique (CPHT)	Invité

Contents

Acknowledgments

Une thèse, c'est d'abord une formation. Effectivement, si le premier jour il est difficile d'imaginer un jour écrire un manuscrit, j'ai bien fini par y arriver. Cette évolution a d'abord été possible grâce à toutes les personnes qui m'ont aidé de près ou de loin, de l'encadrement jusqu'aux autres thésards qui partagent l'expérience de la thèse. Je remercie ici tous ceux qui ont contribué à cette thèse.

En premier lieu, je tiens à remercier Olivier Poujade qui a été mon encadrant pendant ces plus de trois ans et demi de thèse. De ses explications sur la relativité jusqu'aux conseils de rédaction, il m'a énormément apporté au quotidien tout au long de la thèse. Il a su me faire voir les bons côtés de la recherche : ça ne se passe pas toujours comme on voudrait, mais on fait tout de même avancer le problème. Ces quelques lignes sont largement insuffisantes pour exprimer ma gratitude, alors je terminerai simplement par dire que je n'aurais pas pu imaginer avoir un meilleur encadrant. Je souhaite remercier ma directrice de thèse Sophie Baton, en particulier pour nos nombreuses discussions sur la partie expérimentale de la thèse, dont l'importance a malheureusement été limitée par la pandémie.

Je tiens également à remercier l'ensemble de mon jury de thèse, spécifiquement Scott Baalrud ainsi que Laurent Berthe, qui ont accepté de relire mon manuscrit de thèse. Leurs commentaires notamment sur l'aspect expérimental de la thèse ont permis d'ouvrir un grand nombre de pistes à explorer dans une campagne future. *Thanks to Pr. Scott Baalrud, who accepted to review my thesis manuscript and provided many insightful comments.* Je remercie également le président du jury Patrick Mora pour l'intérêt qu'il a porté à mon travail, ainsi que Alexis Casner et Stefan Hüller. Leurs questions pendant la soutenance concernant la confrontation des résultats de la thèse avec les résultats de la littérature ont été particulièrement enrichissantes dans ma réflexion.

Je remercie Emilien Lescoute et Arnaud Sollier qui ont non seulement opéré le laser pendant la campagne expérimentale, mais qui ont continué à répondre à mes nombreuses questions de longs mois après la campagne. Merci également à Laurent Masse pour ses commentaires sur la première partie de la thèse.

Que serait une thèse sans cotoyer d'autres doctorants ? Je remercie tous les doctorants, post-docs et stagiaires du couloir au CEA qui ont peuplé mon quotidien et grâce à qui ces trois ans et demi sont passés si rapidement. Merci à mes aînés : Marie, Grégoire, Cécile, Antoine, Christina, Corentin et bien sûr Mathieu alias *Père*, qui m'a tout appris, à commencer par le fait que le temps est une construction sociale. Merci à Éric, qui a su me dynamiser avec ses piques, mais surtout grâce aux petits-dejs de ses paris perdus. Merci à tous les post-sas : Jisse, m'avoir guidé

pendant mes deux premières années ; Charles pour nos conversations toujours enrichissantes ; Adrien pour les discussions scientifiques et m'avoir appris à apprécier pgfplots, mais aussi pour les meilleurs cookies du couloir ; Olivier, expert LaTeXet emacs aux réflexes impressionants ; Étienne, co-bureau qui sait apprécier mon humour. Merci à Victor pour son enthousiasme infatigable ; à Victor (facteur 2 !) pour le soutien inestimable pendant qu'on rédigeait tous les deux ; Albertine, avec qui j'ai fait toutes mes confs ; Mathilde, gardienne des pots et des mots fléchés ; Baptiste, qui m'a appris à faire mes lacets ; Bastien, la commère du couloir ; Louise, qui a fini sa thèse en un temps record ; Sébastien, scribe officiel des mots fléchés ; Jean-Gabriel (j'ai beaucoup de choses à dire, mais rien que je puisse écrire ici) ; Corentin, qui sait donner du sens à ses graphes ; Kévin, et sa patience légendaire ; Matthéo, et sa bonne humeur rayonnante ; Paul, coureur solitaire ; Joël, qui fait du deltaplane au dessus des blagues. Enfin, aux jeunes qui prennent la relève maintenant que je profite de ma retraite bien méritée : Marin, Ulrich et Léa, bon courage à vous !

Enfin, j'ai une pensée pour mes amis et ma famille qui m'ont soutenu tout au long de la thèse (mais aussi bien avant), qui ont pris de mes nouvelles, en un mot qui m'ont permis de tenir le coup (mention spéciale à mes compagnons de musée Winnie et Kevin). Ma reconnaissance pour vous dépasse ce que je pourrais écrire ici.

> L'algèbre s'applique aux nuages ; l'irradiation de l'astre profite à la rose ; aucun penseur n'oserait dire que le parfum de l'aubépine est inutile aux constellations. Qui donc peut calculer le trajet d'une molécule ? que savons-nous si des créations de mondes ne sont point déterminées par des chutes de grains de sable ? qui donc connaît les flux et les reflux réciproques de l'infiniment grand et de l'infiniment petit,le retentissement des causes dans les précipices de l'être, et les avalanches de la création ?
>
> Victor Hugo, *Les Misérables*

Introduction

This thesis falls within the context of Inertial Confinement Fusion (ICF). The principle behind ICF is to rapidly compress a small capsule containing fusible materials so as to reach conditions suitable to thermonuclear fusion. To achieve this compression, intense laser beams can either be focused directly onto the capsule or can be used indirectly to produce X-rays, in a cavity, that will irradiate and compress the capsule. In both cases, absorption of laser beams is a critical part and its understanding paramount to ICF.

ICF experiments have been carried out at the National Ignition Facility in the USA for more than 10 years and yet many problems related to absorption have eluded our understanding. Numerical simulations using radiation hydrodynamics codes such as TROLL at CEA or HYDRA at LLNL have beeen carried out to design and reproduce those experiments. In the literature, comparisons of experimental results with simulations have shown that the description of laser absorption in the codes is not completely faithful to experiments.

This is why, in this thesis, we investigate one of the main absorption mechanism of laser beams by a plasma: inverse bremsstrahlung (IB) absorption. It occurs when radiation propagates through a plasma and the associated electric field induces a coherent oscillating motion of the electrons of the plasma. Meanwhile, the ions of the plasma are almost motionless as compared to the electrons, due to their mass difference. Collisions between ions and oscillating electrons tend to transfer some of the radiation energy to the plasma.

It follows that the frequency at which electrons and ions interact with each other, which is called the electron-ion collision frequency is a very important parameter for the description of IB heating, and it has been extensively studied in the literature since the 1950s. Still, a consensus on the modelling of the electron-ion collision frequency has not yet been reached. While multiple models exist that take into account different effects (strong laser field, quantum effects, *etc.*), the inclusion of collective effects, has proven to be difficult.

One possible way to account for these collective effects is to resort to Classical Molecular Dynamics Simulations (CMDS). Indeed, in these simulations, trajectories of all particles of the plasma are calculated using Newton's law of motion with the interaction of each particle with every other along with the laser electric field. On the one hand, because of the multitude of interactions that are taken into account (and of finite computational means), domains of simulation are limited to very small volumes. But on the other hand, for the very same reason, CMDS take into account collective effects and are perfectly suited to the measurement of local quantities such as the IB heating rate.

In this work, multiple series of CMDS have been carried out to measure the IB heating rate for a vast range of plasmas and laser conditions. Two sets of simulations can be distinguished. In the first set, plasmas with degree of ionization $Z = 1$ were simulated in conditions where electron velocity distributions are Maxwellian. This is a common assumption of IB heating models in the literature and these simulations were used to discriminate these models. The second set of CMDS used plasmas with a higher degree of ionization ($Z = 10$), which is a known condition to get distorted electron velocity distributions. This non-Maxwellian effect, known as the Langdon effect, has been predicted to affect the IB heating rate.

These series of CMDS allowed us to elaborate a new IB heating model that was implemented in the radiation hydrodynamics code TROLL. Since this new model was devised from theoretical considerations and numerical simulations, it needed to be confronted to experiments. This was one of the objective of a campaign that took place at the GCLT installation at CEA/DAM in october 2021 as part of this tesis. In this campaign, an intense laser beam (1.053 µm wavelength, 40 J total energy with duration of the pulse ranging from 4 ns to 10 ns and intensity comprised between 1 $\mathrm{TW/cm^2}$ and 80 $\mathrm{TW/cm^2}$) was focused onto slabs of pure elements of the periodic table at a 45° angle. The time-resolved incident and reflected power profiles were measured. Since absorption and reflection are complementary (in these conditions, backscattered energy was evaluated as negligible), this provided data about the absorption rate of lasers at multiple intensities for a wide class of plasmas. Additionnally, a streak and a CCD camera monitored the induced plasma, in order to better calibrate radiation hydrodynamics simulations. Preliminary comparisons of TROLL simulations, using the IB heating model devised from CMDS, with these experimental measurements are discussed.

As a practical guide to this manuscript, chapter 1 explains why ICF is a promising technique to achieve a controlled self-sustained fusion reaction, and presents the modelling of laser propagation and IB absorption, of interest to this thesis, which are implemented in radiation hydrodynamics codes. Chapter 2 expands upon the theoretical modelling of the electron-ion collision frequency, and in particular why collective effects, through the Coulomb logarithm, are difficult to take into account. Chapter 3 presents the first set of CMDS, and the development of our IB heating model. In chapter 4, the second set of CMDS is detailed. They improve the characterization of the Langdon effect and how it impacts the IB heating rate. Chapter 5 first reviews experiments from the literature similar to our campaign before explaining the details of our experimental setup. Finally, the experimental results of the campaign are shown in chapter 6, and preliminary comparisons of these results with simulations carried out with TROLL, configured with our new IB model, are laid out.

Part I

On the importance of laser absorption in inertial confinement fusion

Chapter 1

Inertial confinement fusion and its numerical modelling

Contents

This chapter describes the context of this thesis. In its first part, section 1.1.1, we will expand on what nuclear fusion is, and why it is so difficult to control and sustain. Despite the arduous conditions required, the first laboratory fusion reactions were observed by Cockroft and Walton in 1932 [Atzeni & Meyer-ter Vehn, 2004]. Nowadays, the objective of laboratory fusion experiments is for the experiment to release more energy than what was provided to reach fusion conditions. One of the promising methods to do so, inertial confinement fusion (ICF) will be presented in section 1.1.2. Indeed, a 2021 ICF experiment released 70 % as much energy as the laser energy used to initiate it [LLNL, 2021]. A short literature review on past ICF experiments in section 1.1.3 will then expand upon the progress that has been made in the understanding of the physics involved in ICF, and upon the progress that remains to be made, particularly in the description of laser absorption.

In this thesis, we will shed some new light on laser absorption by plasmas. This is why, in the second part of this chapter, we will first describe the viewpoint from the literature. After a succint presentation of radiation hydrodynamics codes, we will explain how laser propagation and

inverse bremsstrahlung absorption are typically modelled in radiation hydrodynamics codes, in order to show the underlying approximations (especially within the so called Coulomb logarithm).

Finally, in the last part of this first chapter, we will present a simple way to get insight on the variability of radiation hydrodynamics simulations outcomes due to an uncertainty of the Coulomb logarithm.

1.1 From nuclear fusion to inertial confinement fusion

1.1.1 Nuclear Fusion

Nuclear fusion happens when multiple nuclei combine together to form a heavier nucleus. Nuclei, the central core of atoms, are positively charged, so Coulomb interaction tends to keep them apart. At very close distances however, the strong nuclear force, which is attractive, becomes dominant. The strong nuclear force is responsible for keeping the protons and neutrons of a nucleus together. Nuclear fusion occurs when two nuclei are close enough for the strong nuclear force to overcome the repulsive Coulomb interaction. This happens when the nuclei collide together while going very fast. It translates into being very hot, to go fast enough to overcome Coulomb repulsion, as well as very dense, in order to actually collide with each other [Blatt & Weisskopf, 1991].

When fusion does occur, it releases large quantities of energy. This is because the products of fusion are lighter than the parent nuclei (see [Wang *et al.*, 2021] for a list of atomic masses). The mass difference Δm corresponds to an increase in the binding energy of the system following Einstein's formula $E = \Delta m\, c^2$. In Fig. 1.1, the average binding energy is plotted versus the number of nucleons. When this binding energy increases during a nuclear reaction, the reaction releases energy. Thus, Fig. 1.1 shows that to produce energy, heavy nuclei such as uranium can undergo nuclear fission, or light nuclei such as deuterium (D) and tritium (T) can fuse together. The fusion reaction of Deuterium and Tritium is

$$\mathrm{D} + \mathrm{T} \longrightarrow {}^4\mathrm{He}\ (3.5\,\mathrm{MeV}) + \mathrm{n}\ (14.1\,\mathrm{MeV}). \tag{1.1}$$

The volumetric reaction rate for the fusion of two nuclei is proportionnal to the number density of the two nuclei [Clayton, 1983]. In the case of Deuterium-Tritium fusion, both nuclei are needed in the same proportions. Assuming n is the total number density of the plasma, Deuterium and Tritium would ideally each have a number density of $n/2$. The volumetric rate of fusion processes is thus $\langle \sigma\, v \rangle\, n^2/4$, where the coefficient $\langle \sigma\, v \rangle$ is the reactivity. σ is the fusion cross-section and v is the relative velocity of the nuclei. Since all of the particles in a plasma do not have the same velocity, the cross-section is averaged on all the relative velocities that are present in the plasma [Atzeni & Meyer-ter Vehn, 2004]. This process is denoted by the brackets $\langle\ \rangle$.

The volumic power produced by fusion reactions can thus be expressed as

$$p_{\mathrm{fusion}} = \frac{n^2}{4}\ \langle \sigma\, v \rangle\ Q, \tag{1.2}$$

where Q is the energy released by each fusion reaction. As mentioned in the introduction, laboratory fusion experiments seek to produce more energy than the energy expanded to reach fusion conditions. A first step on the way to achieve this is for the reaction to be self-sustained, *i.e.* fusion reactions release enough energy to maintain fusion conditions inside the fuel. Reaching

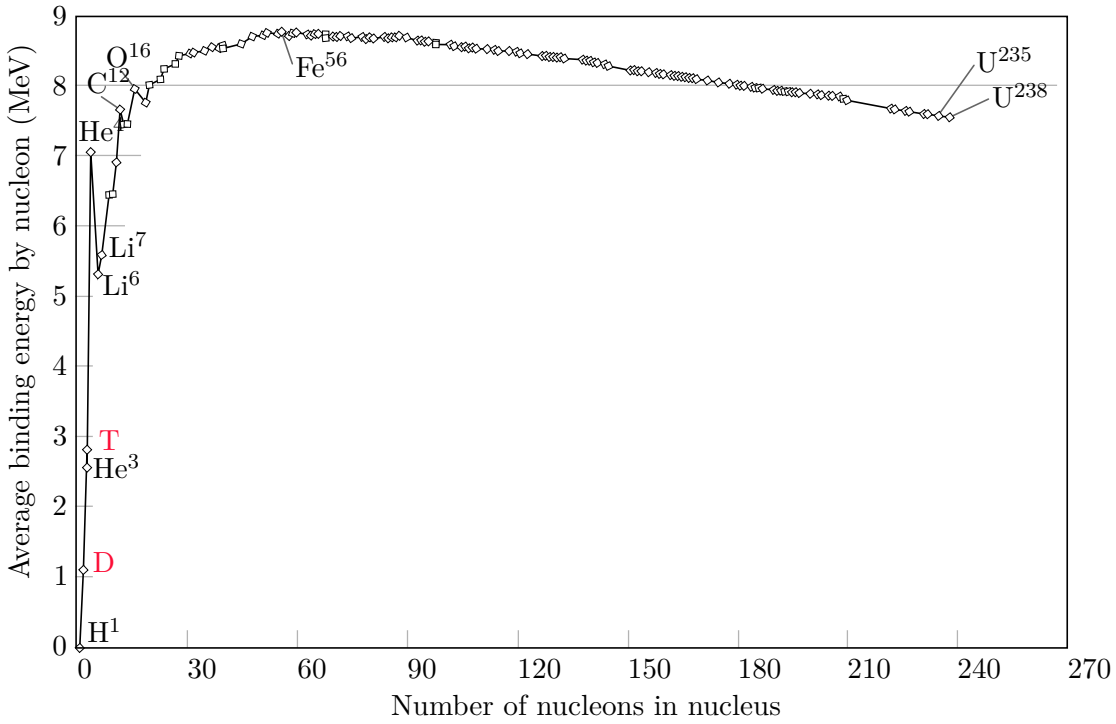

Figure 1.1: Average binding energy by nucleons as a function of the number of nucleon in the nucleus. This shows that heavy nucleus, such as uranium can undergo fission and release energy, whereas lighter nuclei such as deuterium and tritium can fuse together to release energy.

this state is necessary in order to trigger more fusion reactions, and if it is maintained long enough, fusion reactions will eventually release more energy than the energy provided to initiate the experiment. For the reaction to be self-sustaining, p_{fusion} must thus be higher than the power lost to the environment [Atzeni & Meyer-ter Vehn, 2004]. The power loss is usually expressed from the energy density of the plasma W as

$$p_{\text{loss}} = \frac{W}{\tau_E}, \tag{1.3}$$

where τ_E is the energy confinement time, which corresponds to the time it would take for the system to lose all its internal energy if the energy loss rate was constant. The energy density of the nuclei at a certain temperature T is $(3/2)\, n\, k_B T$, with k_B the Boltzmann constant. In practice, the electrons also have to be at this temperature, so the internal energy associated with the temperature T of a Deuterium-Tritium plasma is $W = 3\, n\, k_B T$, since there are as much electrons as nuclei in this case.

For the fusion reaction to be self-sustaining, the power produced by fusion reactions p_{fusion} must be greater than p_{loss}. In practice, not all the energy released by fusion reactions can be used to heat the plasma and counteract losses. In particular, neutrons goes through the plasma almost unaffected, so in the case of Deuterium-Tritium, at most the 3.5 MeV of the ^{4}He can be absorbed by the plasma. With f the fraction of the energy released by fusion reactions that is used to heat the plasma, the condition for a self sustaining fusion reaction is $f\, p_{\text{fusion}} \geq p_{\text{loss}}$,

which can be recast using eqs. (1.2) and (1.3) as

$$n\,\tau_E \geq \frac{12\,k_B T}{\langle\sigma\,v\rangle\;f\,Q} = (n\,\tau_E)_{thr}(T). \tag{1.4}$$

This is known as the Lawson criterion [Lawson, 1957]. The part of fusion energy that heats the plasma, $f\,Q$ depends on the reaction considered. Only $\langle\sigma\,v\rangle$ depends both on the reaction considered and on the plasma temperature. Because of this, the threshold $(n\,\tau_E)_{thr}$ depends on the temperature and reaction. In Fig. 1.2, σ is plotted as a function of the temperature for multiple reactions. It can be seen on the graph that the reaction with the highest cross section σ is Deuterium-Tritium, at least at temperatures under 100 keV [Angulo *et al.*, 1999, Bosch & Hale, 1992].

Even for this particular reaction, reaching a significant reactivity requires reaching temperatures of tens of millions of Kelvin[1]. At these temperatures, the plasma tends to expand, which reduces the number density n and makes producing energy more difficult, per eq. (1.4). To keep the plasma from expanding, the plasma has to be confined. In stars for instance, the gravitational force fullfill this role because they are so massive. For laboratory experiments, other confinements methods have been considered, such as magnetic confinement, Z-pinch, stellerator, and inertial confinement, which is the one of interest in this work.

1.1.2 Inertial Confinement Fusion

In Inertial Confinement Fusion (ICF), a mix of Deuterium and Tritium (DT) called the fuel is contained in a small spherical capsule. Part of the fuel can be cryogenic, in order to increase its density, and have more DT in a given volume. The outer part of the capsule is a spherical shell called the ablator, made out of plastic (CH), beryllium (Be), high-density carbon (HDC) or another low-Z material. The principle of ICF is to quickly heat up the ablator, which causes it to expand rapidly. This causes the fuel in the interior of the capsule to implode by reaction, as shown in the bottom of Fig. 1.3. When the pressure in the center of the capsule balances out the pressure induced by the implosion, the kinetic energy stored in the shell is converted into internal energy, leading to high densities and temperatures at the center of the capsule. This region, called the hot-spot, is where the fusion reactions starts.

Ideally, the fusion reactions in the hot-spot release enough energy to heat the rest of the fuel to fusion conditions, and so all of the fuel undergo nuclear fusion, leading to a large quantity of energy released. However, anisotropies in the implosion can result in mixing of ablator material and cold fuel inside the hot-spot [Pfalzner, 2006], which cools it down.

There are two main ways to implode a capsule using lasers, shown in Fig. 1.3.

- Direct-drive, where the lasers directly hit the capsule.
- Indirect-drive, where the capsule is placed inside a cavity that is irradiated by the lasers. This cavity, also known as hohlraum is made out of high-Z materials that turns into a hot X-ray emitting plasma when irradiated by the lasers. The capsule implosion is driven by this X-ray radiation. See Fig. 1.4 for pictures of a typical hohlraum, and Fig. 1.5 for the configuration of laser beams.

Both of these methods have their advantages [Atzeni & Meyer-ter Vehn, 2004, Lindl *et al.*, 2014].

[1] multiples keV (1 keV ≈ 11.6 millions of Kelvin)

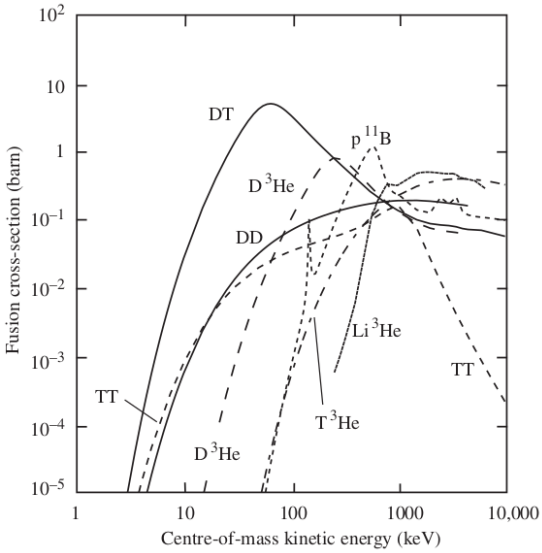

Figure 1.2: Fusion cross-section σ for multiple fusion reactions. The deuterium-tritium (D-T) reaction has the highest reactivity at temperatures below 100 keV. Image credit: Atzeni & Meyer-ter Vehn [2004].

For example, direct-drive is more efficient at coupling laser energy to the capsule. However, it can be difficult to distribute the laser energy homogeneously over the surface of the ablator. Indeed, when the lasers drive the capsule implosion, a small disturbance in the uniformity of the laser irradiation is directly imprinted on the capsule. This is at variance with indirect drive, where the X-ray emission of the hohlraum plasma is much less dependant on the uniformity of the laser irradiation. However, the conversion with X-ray is not lossless, and thus indirect drive is less efficient than direct drive at coupling laser energy to the capsule. In both techniques, there are also engineering limitations that make it more difficult to have an isotropic implosion: the capsule has a fill tube, required to put the fuel inside, and it has to somehow be held in place during the experiment in both cases. In direct drive, the capsule is usually held at the end of a thin stalk [Igumenshchev *et al.*, 2009]. In indirect drive, a very thin membrane called the tent is placed inside the hohlraum and holds the capsule at the desired position inside the hohlraum [Betti & Hurricane, 2016, Haan *et al.*, 2011], as shown in Fig. 1.4.

Two facilities have been constructed with the explicit goal of reaching ignition: the Laser Méga Joule (LMJ) in France, which is not yet fully completed, and the National Ignition Facility (NIF) in the USA. Ignition is meant here to refer to experiments where fusion reactions yield more energy than lasers supplied to the experiment *i.e.* the gain is greater than one. Since its completion in 2009, numerous ICF experiments have been carried out at the NIF. Although ignition has not yet been reached, understanding of the physics involved as well as experimental designs have been substantially improved.

Fig. 1.6 shows an overview of the NIF. A representation of the target bay of the LMJ is given in Fig. 1.7 to show the paths that the lasers have to take to reach the experimental chamber. These two images hint at the scale and complexity of the NIF and LMJ facility, which participate to explain why only two facilities have been built with the goal to reach ignition.

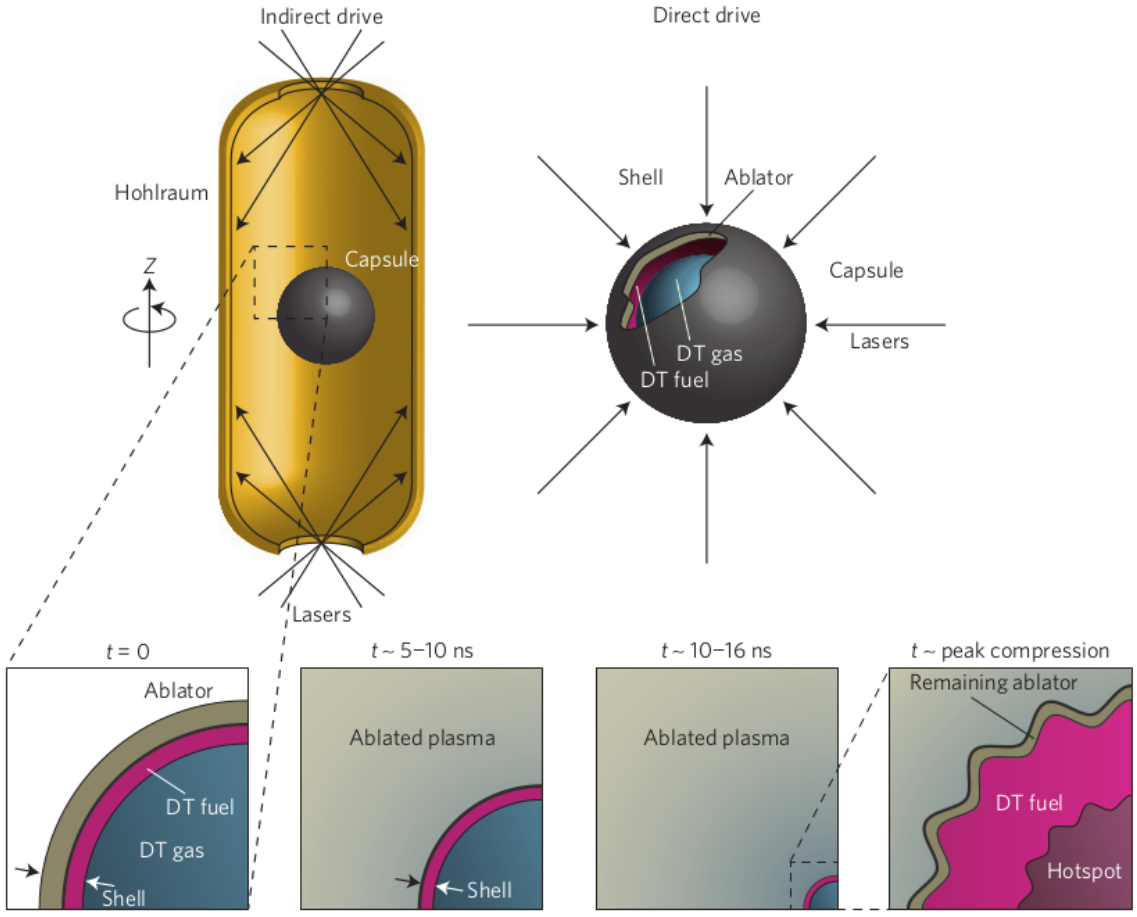

Figure 1.3: Schematics of direct (top right) and indirect (top left) drive ICF. In indirect drive, lasers are targeted on the hohlraum wall be converted into X-rays that irradiate the capsule. In direct-drive, lasers directly impact the capsule. On the bottom is a representation of the capsule during an implosion. The ablator expands and compresses the DT. Around peak compression, asymmetries in the implosions can lead to mixing of ablator with fuel and degrade the implosion performance. Image credit: Betti & Hurricane [2016]

1.1.3 Past experiments at the National Ignition Facility

The first campaign of ignition experiments on the NIF between 2009 and 2012 was called the National Ignition Campaign (NIC) [Edwards *et al.*, 2013, Lindl *et al.*, 2014]. The NIC demonstrated control over the velocity, entropy and shape of the implosion. This was achieved by adjusting the target geometry as well as the shape of the laser pulse. The top performing implosion of the NIC reached[2] a $(P\,\tau_E)$ about 30% of that predicted to reach ignition [Lindl *et al.*, 2014].

However, increasing the implosion velocity in the top-performing NIC experiment did not result in an increase in yield because of ablator-fuel mixing, which resulted in pollution of the hot spot [Meezan *et al.*, 2017]. The mixing of ablator material into the hot spot was found to be correlated with a decrease in the yield [Ma *et al.*, 2013]. The leading candidate to explain the mixing is the ablative Rayleigh-Taylor instability seeded by the tent [Kilkenny *et al.*, 1994, Tommasini *et al.*, 2015]. To mitigate this, the use of a different laser pulse shape, called 'high-foot'

[2]The Lawson criterion eq. (1.4) can be expressed with $(P\,\tau_E)$ using the pressure of the plasma $P = n\,k_B T$

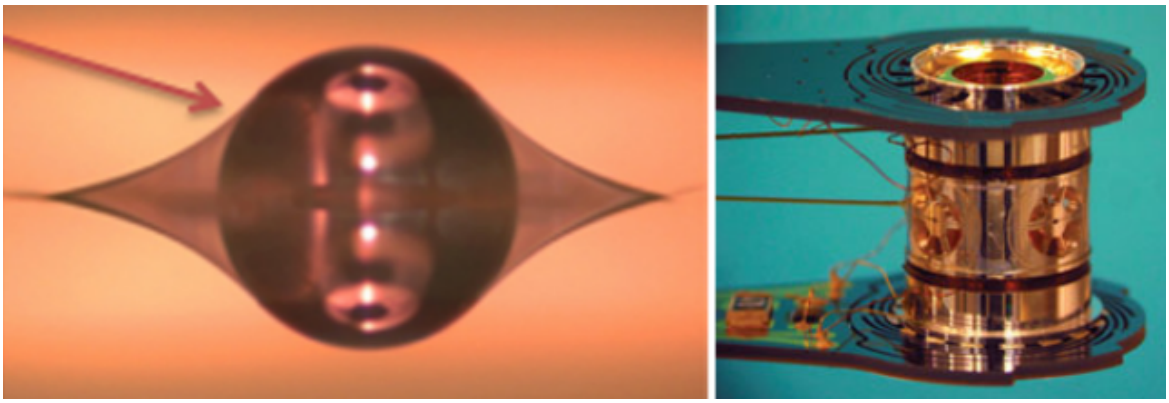

Figure 1.4: Pictures of an hohlraum, the metallic cavity inside which is placed the capsule of Deuterium-Tritium in ICF experiments. The left picture shows the the capsule inside the hohlraum. It is held by the tent. The right picture show the outside of a hohlraum. Images credit: Callahan *et al.* [2015] (left), Lawrence Livermore National Laboratory (right).

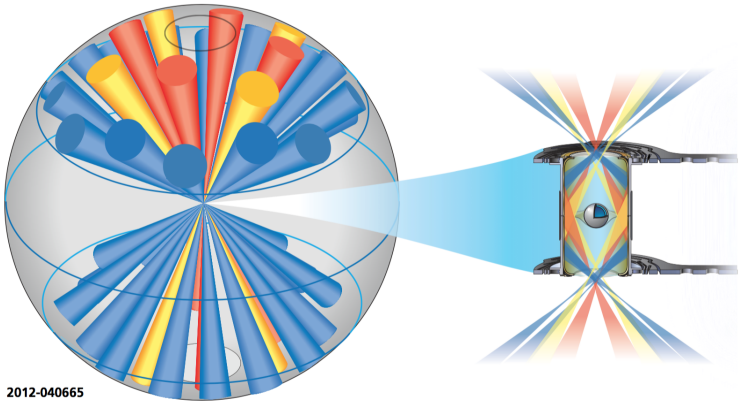

Figure 1.5: Configuration of the laser beams inside the experimental chamber at the NIF. There are four possible angles of incidence: 23.5° (in red), 30° (in yellow), 44.5° and 50° (in blue), which are pointed at different places inside the hohlraum. The inner beams (red and yellow) irradiate the waist of the hohlraum, where it is closest to the capsule, and the outer beams (blue) irradiate the hohlraum closer to the entrance hole. Image credit: Lawrence Livermore National Laboratory.

was proposed [Dittrich *et al.*, 2014, Park *et al.*, 2014]. It delivers more power in the beginning of the laser pulse, compared with the 'low-foot' pulse shape used for most of the NIC, as shown in Fig. 1.8. The 'high-foot' design has proved to be less sensitive to instabilities [Peterson *et al.*, 2015], and showed little ablator-fuel mixing [Callahan *et al.*, 2015]. This design made it possible to reach conditions closer to ignition. However, only 60% of the $(P\,\tau_E)$ predicted to reach ignition was achieved.

2D and 3D numerical simulations [Clark *et al.*, 2016, Kritcher *et al.*, 2016] of 'high-foot' experiments compared to 1D simulations of ideal, perfectly symetrical implosions identified two important sources of yield degradation, shown in Fig. 1.9. The first corresponds to the instabilites seeded by the tent, the fill-tube, and the surface defects of the capsule, although the threshold for these instabilities is reached at a much higher implosion velocity than in 'low-foot' designs. The second source of yield degradation is from asymmetry of the X-ray flux coming from the

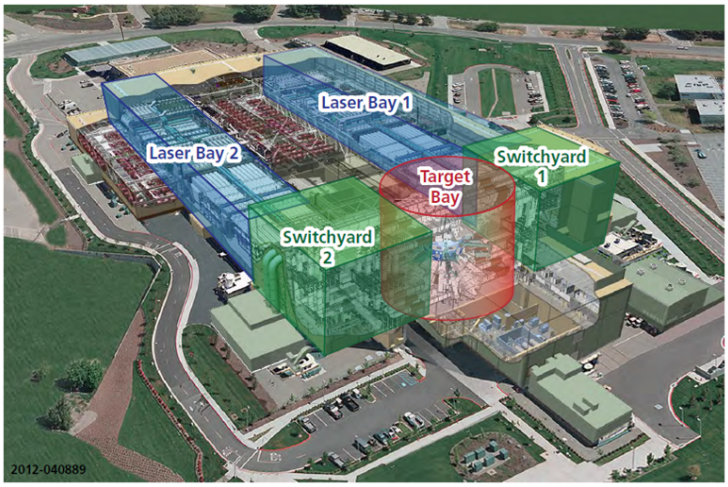

Figure 1.6: Overview of the National Ignition Facility. This image shows the scale of the lasers amplification systems, which take up whole buildings. After the amplification in the laser bays, the lasers are directed into the target bay by the switchyards. Image credit: Lawrence Livermore National Laboratory.

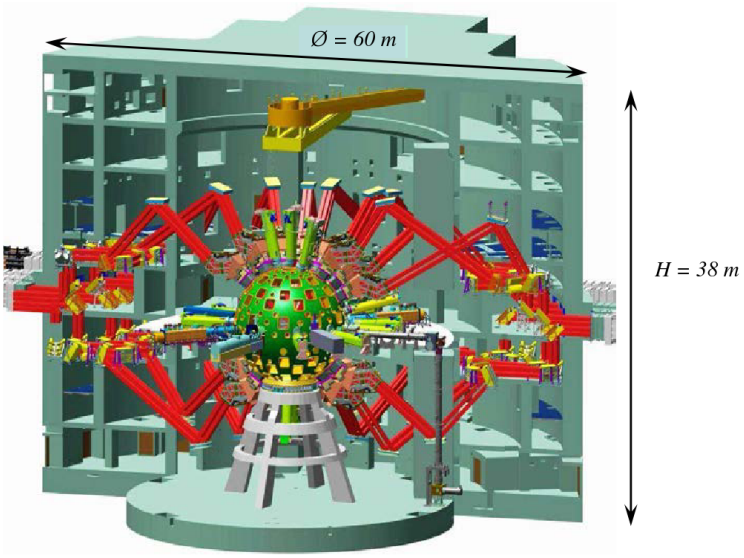

Figure 1.7: Overview of the target bay of the LMJ, which is roughly the same size as that of the NIF. The paths of the laser beams are represented in red. The experimental chamber is in green. It is inside this chamber that the capsule and hohlraum are placed during experiments. The lasers amplification systems, though not shown here, are on the same scale as those at the NIF, which are shown in Fig. 1.6. Image credit: CEA-DAM.

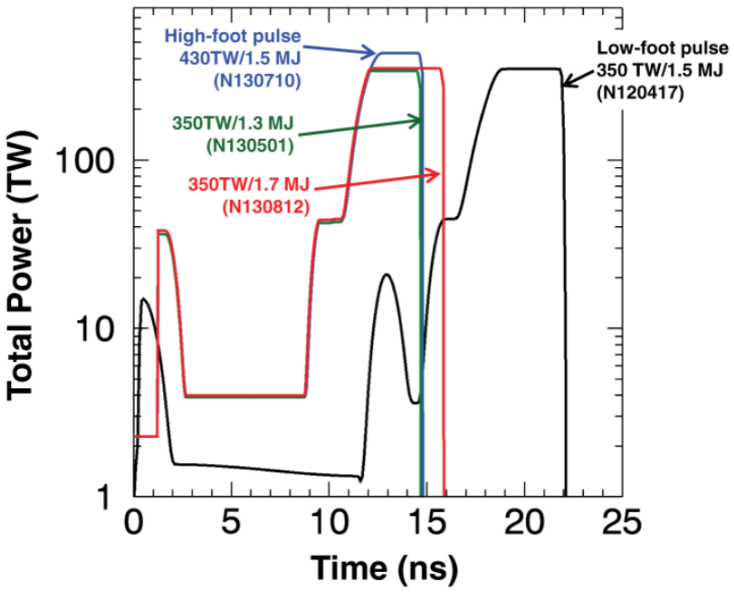

Figure 1.8: Profile of laser power delivered in the hohlraum during a low-foot pulse (black) and three high-foot pulses (red, green and blue). The high-foot pulses are shorter, and deliver more power at the beginning of the pulse (before 10 ns in the graph). Image credit: Park *et al.* [2014]

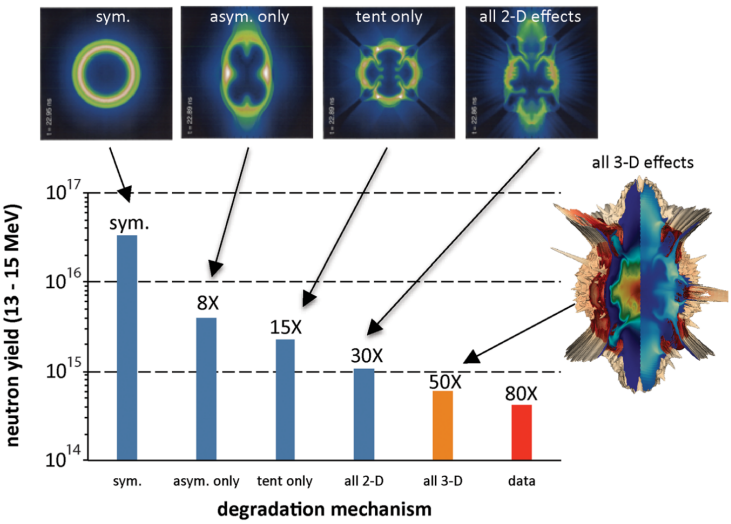

Figure 1.9: Effect of multiple degradation mechanisms on the yield of the experiment. This graph shows which mechanisms have the most impact on the neutron yield, and thus, which aspects of the experiments can be improved on the most. Image credit: Clark *et al.* [2016]

hohlraum.

Flux symetry in the hohlraum is usually controlled by adjusting the shape of the laser pulse, the pointing of the beams, their wavelengths, and the power balance between the inner and outer beams (see Fig. 1.5). At later times during the laser pulse, the hohlraum plasma expansion becomes significant. This is detrimental to the X-ray flux symetry control, and so the hohlraum can be filled with a gas in order to reduce the plasma expansion.

The presence of this gas slows down the expansion of the hohlraum plasma, which makes it easier to control the flux symetry inside the hohlraum. However, the gas fill does absorb a portion of the laser energy, which means less energy is available to the capsule, and thus to reach fusion. The gas also makes it possible for Laser Plasma Interactions (LPI) to occur inside the hohlraum, which can further drain energy away from the capsule. In particular, one LPI, Cross Beam Energy Transfer (CBET) can transfer energy from one laser beam to another [Dewald *et al.*, 2013]. This mechanism is used to help control flux symetry inside the hohlraum, but it remains a source of uncertainty.

The gas fill also reduces the coupling of laser energy to the capsule through phenomena such as Stimulated Brillouin Scattering (SBS), Stimulated Raman Scattering (SRS) or other LPI, which can cause the laser energy to backscatter out of the hohlraum. It has been shown [Berzak Hopkins *et al.*, 2015] that in high density gas fill experiments (density higher than $0.96\,\mathrm{mg/cm^3}$), $\sim 15\%$ of the laser energy is backscattered, and thus is not available for X-ray conversion. In Near-Vacuum Hohlraums (NVHs) less than 5% of the laser energy is backscattered.

However, as stated before, X-ray flux symetry is difficult to control in NVHs towards the end of the pulse, because of the expanding hohlraum plasma. A compromise was adopted by using low-density gas filled hohlraums [Hall *et al.*, 2017, Loomis *et al.*, 2018]. High Density Carbon (HDC) has also become a promising ablator material, since its high density allows for shorter laser pulses [MacKinnon *et al.*, 2014], and thus a shorter implosion.

All in all, three major points are currently being worked on in order to reach ignition in indirect-drive experiments [Kline *et al.*, 2019].

- The first is a better control of the hydrodynamic instabilities occuring in the capsule, which is achieved by improving the target quality [Hamza *et al.*, 2016, Ross *et al.*, 2021]. Indeed, non-uniformity of the ablator shell thickness, as well as imperfections in the material itself (such as small voids) can all lead to hydrodynamic instabilities [Casey *et al.*, 2021, Zylstra *et al.*, 2020, 2021]. Additionally, engineering features such as the fill tube as well as ways to mount the capsule inside the hohlraum are also investigated [MacPhee *et al.*, 2018, Nagel *et al.*, 2015] in order to reduce their impact on the experiment.

- The second is work on laser technology, in order to increase the energy available to the hohlraum [Suter *et al.*, 2004].

- The last is flux symmetry inside the hohlraum, for example with novel hohlraum designs such as rugby shapes; I-raum or frustraum [Bhandarkar *et al.*, 2018, Masson-Laborde *et al.*, 2016, Vandenboomgaerde *et al.*, 2007, Xu *et al.*, 2011].

Progresses in these three areas as well as others have already been evidenced by the fact that a burning plasma regime has been reached at the NIF [Zylstra *et al.*, 2022]. This means that fusion reactions themselves provided most of the energy necessary to initiate more fusion reactions.

Additionnally, in August 2021, a shot at the NIF reached a yield of 1.3 MJ, to be compared with the 1.9 MJ that was provided to the experiments by lasers [LLNL, 2021]. The 1.3 MJ yield of this shot can also be compared with the 170 kJ yield reached in previous experiments [Zylstra *et al.*, 2022]. Though this shot proved difficult to be reproduced, it showed that conditions currently reached during experiments are very close to those required for ignition.

A good description of the laser to capsule coupling is critical in order to gain a better understanding of the conditions required to reach ignition. As can be seen in Fig. 1.10, laser to capsule coupling can roughly be split into two steps. The first is the laser to X-rays conversion, and the second is the X-ray to capsule coupling.

The X-ray energy is involved in the heating of the hohraum wall, the heating of the outer surface of the capsule and preheating of the capsule interior, and part of it escapes the hohlraum through the LEHs. The direction of emitted X-rays is highly dependant on the geometry of the hohlraum. The X-ray to capsule coupling is thus primarily described by the hohlraum geometry, and the radiation temperature inside the hohlraum [Lindl *et al.*, 2004]. These parameters cannot be easily adjusted without impacting the whole experiment. For example, increasing the capsule size will increase the coupling (since a bigger capsule has more area to absorb X-rays), but bigger capsules require more energy to reach ignition.

The laser energy entering the hohlraum can either exit the hohlraum or stay inside. The energy that stays inside the hohlraum is absorbed, mainly by the hohlraum wall, but also by the gas fill, if any. The hot hohlraum wall then converts part of this energy into X-ray radiation. Energy exiting the hohlraum can be caused by LPIs such as SRS or SBS, which can backscatter laser energy out of the hohlraum. Part of the laser energy can also be reflected specularly on the hohlraum wall, which is a phenomenon known as glint [Honda *et al.*, 1998]. Depending on the laser beam it comes from, glinted light can directly irradiate the capsule, which disturbs the flux symmetry, or it can exit the hohlraum. Additionally, glint light can also seed LPIs [Turnbull *et al.*, 2015], which can further increase the lost energy.

A good description of absorption, glint and LPIs is thus critical to predict the correct energy balance inside of a hohlraum. However, in radiation hydrodynamics codes used to simulate experiments, such as HYDRA at LLNL [Marinak *et al.*, 1998] or TROLL at CEA [Lefebvre *et al.*, 2018], SRS and SBS are too costly to simulate fully, since these codes already have to solve radiation hydrodynamics equations in the hohlraum and capsule. Thus, the SRS and SBS energy is often accounted for by simply reducing the laser energy [Jones *et al.*, 2012], though recent works have attempted to improve this modelling [Colaïtis *et al.*, 2021, Debayle *et al.*, 2019].

In gas-filled hohlraum, this means that around 85% of the experimental laser energy is put into simulations [Moody *et al.*, 2014]. Even so, there is a drive-deficit, *i.e.* the simulated drive is stronger than the experimental one, in terms of implosion velocity for example. In fact, only 60-70% of the experimental laser energy has to be simulated in order to reproduce experimental measurements.

This means that the numerical description of the laser to capsule coupling is not entirely faithful to experiments. This work aims to improve this description by enhancing the modelling of laser absorption in radiation hydrodynamics codes used to design ICF experiments. Multiple laser absorption mechanisms are relevant to ICF conditions [Pfalzner, 2006], notably inverse bremsstrahlung, resonance absorption, and parametric absorption.

Parametric absorption consists in three waves interactions, which include the LPIs that were

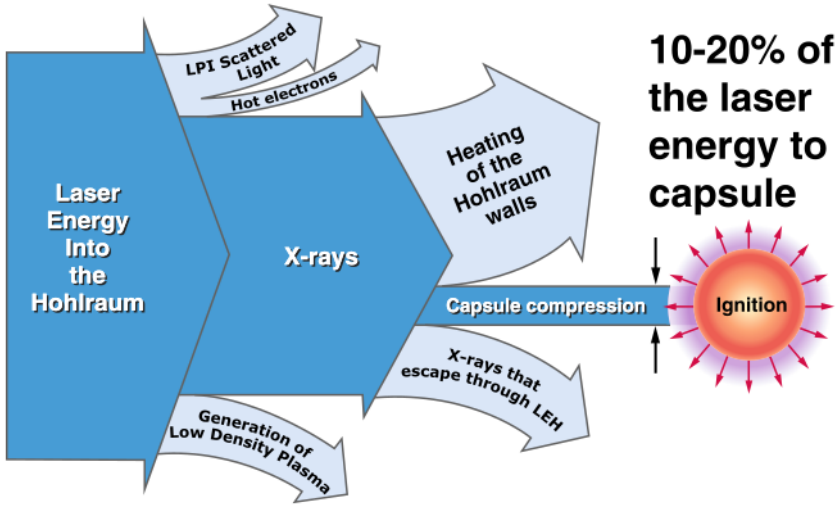

Figure 1.10: Repartition of energy during a typical NIF experiment. Only part of the laser energy will actually heat up the capsule. A very accurate description of all the energy losses is thus paramount to be able to predict this small fraction. Image credit: presentation given by J. Lindl at the Plasma Science Committee at Beckman Center of the National Academies on September 24, 2005.

mentioned previously. Resonance absorption can be responsible for up to 50% of laser absorption in ICF conditions [Eliezer, 2002, Igumenshchev *et al.*, 2007, Kull, 1983], depending on the laser polarization and angle of incidence. Parametric and resonance absorption tend to produce hot electrons, which have a much higher temperature than their surroundings. These hot electrons tend to carry their energy away rather than heat up the ions of the plasma locally. This is why experimental configurations tend to minimize laser absorption due to these mechanisms. The rest of laser absorption (which is actually most of the absorption except in specific situations favourable to resonance absorption) is due to inverse bremsstrahlung, which is the mechanism this work will be focusing on. Before attempting to improve the description of inverse bremsstrahlung absorption in radiation hydrodynamics codes, it is important to explain how it is currently modelled, which we will do in the next section.

1.2 The modelling of lasers in codes used to design ICF experiments

We will now briefly present radiation hydrodynamics codes in section 1.2.1. Then, we will focus on the modelling of laser in section 1.2.2, in order to show what approximations are made in the modelling process. Finally, the modelling of the propagation and inverse bremsstrahlung absorption will be detailed in section 1.2.3.

1.2.1 Presentation of radiation hydrodynamics codes

Physical modelling

Ignition experiments have time scales on the order of few tens of nanoseconds and length scales on the order of millimeters, as evidenced by the size of a hohlraum shown in Fig. 1.4, and the

length of typical laser pulses shown in Fig. 1.8. To assess the validity of the fluid approximation, these scales are to be compared to the particles mean free path in ICF experiments. In Fig. 1.11 are shown the ion-ion λ_{ii}, electron-ion λ_{ei} and electron-electron λ_{ee} mean free paths at an early stage of a typical ICF experiment. These mean free paths are given by

$$\lambda_{ee} = \frac{v_{\text{th}}^{e}}{\nu_{ee}}, \quad \lambda_{ei} = \frac{v_{\text{th}}^{e}}{\nu_{ei}}, \quad \lambda_{ii} = \frac{v_{\text{th}}^{i}}{\nu_{ii}}, \tag{1.5}$$

where the collision frequencies ν_{ee}, ν_{ei} and ν_{ii} are given by

$$\nu_{ee} = C_\nu \frac{e^4\, n_e}{\sqrt{m_e}\,(k_B T_e)^{3/2}}, \quad ,\nu_{ei} = C_\nu \frac{\bar{Z}\, e^4\, n_e}{\sqrt{m_e}\,(k_B T_e)^{3/2}}, \quad \nu_{ii} = C_\nu \frac{\bar{Z}^3\, e^4\, n_e}{\sqrt{m_i}\,(k_B T_i)^{3/2}}, \tag{1.6}$$

where $v_{\text{th}}^{e,i} = \sqrt{k_B T_{e,i}/m_{e,i}}$ is the electron (resp. ion) thermal velocity, $k_B T_{e,i}$ is the electron (resp. ion) temperature, $m_{e,i}$ the electron (resp. ion) mass, $n_{e,i}$ is the electron (resp. ion) number density, $\bar{Z}$ is the average degree of ionization and $C_\nu = 4\sqrt{2\pi}/3\,(4\pi\,\varepsilon_0)^2$ is a constant. The fluid approximation is most correct for ions, since the ion-ion mean free path is always less than a micron, which is much less than any gradient length in the hohlraum. The electron-ion mean free path can be comparable to gradient lengths in the hohlraum, especially in the low density gas fill that is initially in the cavity, but it is much smaller everwhere else. The electron-electron mean free path is on the order of 100 µm in the low density gas fill and in the hohlraum plasma.

The hydrodynamic equations are therefore used to simulate ICF experiments, keeping in mind that kinetic effects can be at play in a few locations. Indeed, though the hydrodynamic approximation is not valid everywhere at every time during the simulation, it is valid in areas of interest (such as the capsule and the hohlraum plasma). Furthermore, a kinetic description of the whole hohlraum for the duration of an ICF experiment is beyond current computational means. This explain why hydrodynamics code such as TROLL or HYDRA are used for the simulations of ICF experiments.

These codes use a three-temperature one fluid model for the plasma. Indeed, the laser energy is primarily deposited on the electrons, before being transmitted to ions via collisions, so a two-temperature model is needed to capture the dynamics of both components of the plasma. However, the timescale of momentum transfer between electrons and ions is very small compared to the typical simulation timestep. This is why electrons and ions can be considered as comoving at the plasma velocity $\boldsymbol{u}$. Additionnally, radiation is not always at equilibrium with matter, and so it is described by its own temperature T_r, which may not be equal to the temperatures of electrons T_e and ions T_i. The main hydrodynamic equations are then [Eliezer, 2002]

$$\begin{cases} \partial_t \rho + \boldsymbol{\nabla}\cdot\rho\boldsymbol{u} = 0 & \text{Mass conservation,} \quad (1.7a) \\ \rho\,\partial_t \boldsymbol{u} + \rho\,\boldsymbol{u}\cdot\boldsymbol{\nabla}\boldsymbol{u} = -\boldsymbol{\nabla}P & \text{Momentum conservation,} \quad (1.7b) \\ \partial_t e_e + \boldsymbol{u}\cdot\boldsymbol{\nabla}e_e + (e_e + P_e)\,\boldsymbol{\nabla}\cdot\boldsymbol{u} = \boldsymbol{\nabla}\cdot\boldsymbol{Q}_e + \mathcal{S}_{\text{e}} & \text{Energy conservation (electrons),} \quad (1.7c) \\ \partial_t e_i + \boldsymbol{u}\cdot\boldsymbol{\nabla}e_i + (e_i + P_i)\,\boldsymbol{\nabla}\cdot\boldsymbol{u} = \boldsymbol{\nabla}\cdot\boldsymbol{Q}_i + \mathcal{S}_{\text{i}} & \text{Energy conservation (ions),} \quad (1.7d) \end{cases}$$

where ρ is the plasma density, $P = P_e + P_i$ the total, electron and ion pressures respectively, $e_{e,i}$ the electron (resp. ion) volumetric internal energy, $\boldsymbol{Q}_{e,i}$ the electron (resp. ion) heat flux, and

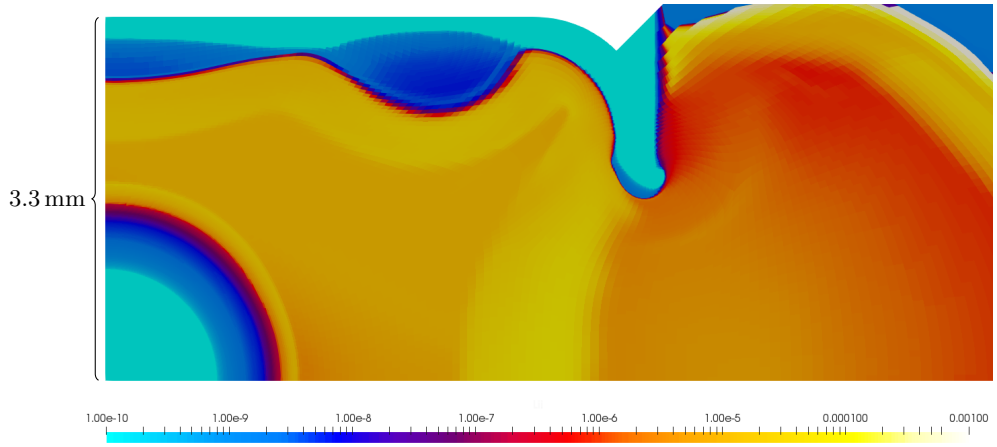

a) Ion-ion mean free path (m)

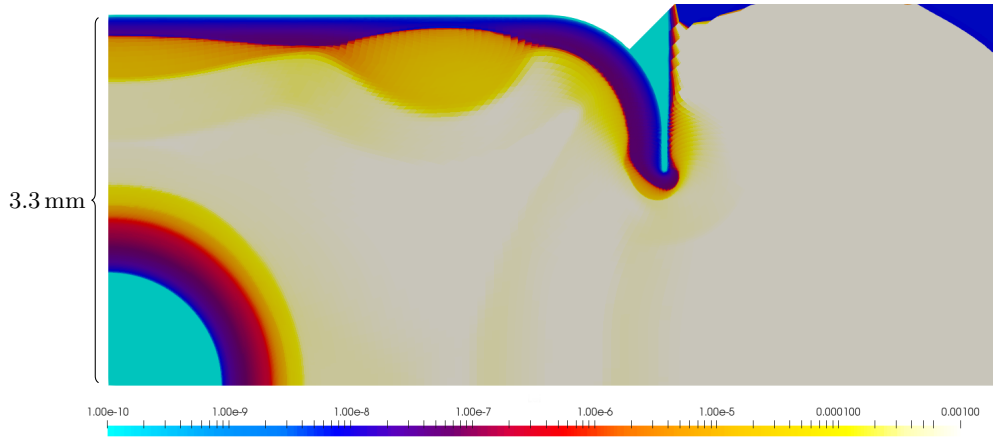

b) Electron-ion mean free path (m)

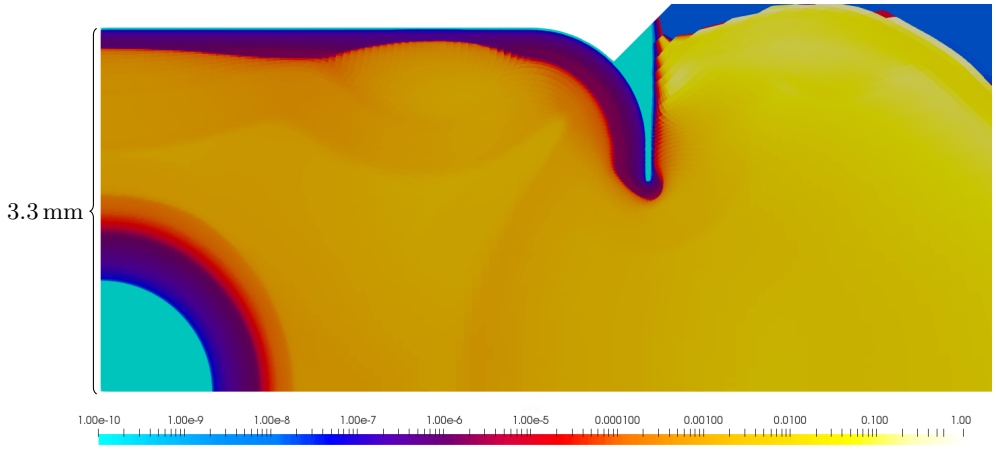

c) Electron-electron mean free path (m)

Figure 1.11: Images from a typical TROLL simulation using a high-foot laser pulse at $t = 3\,\mathrm{ns}$. The color scale shows either the ion-ion mean free path (top), the electron-ion mean free path (middle) or the electron-electron mean free path (bottom). At this stage of the experiments, most of the cavity (except for the capsule) is occupied by the low density gas fill. Notice the different color scale for the electron-electron mean free path. The ion-ion mean free path is much smaller than the diameter of the hohlraum everywhere.

$\mathcal{S}_{e,i}$ the exchange term for electrons (resp. ions), which include laser heating for the electrons, exchange between electrons and ions, exchange with the radiative field.

Other relations are necessary to close the system. Equations of State (EOS) for both the electrons and ions give $e_{e,i}(\rho, T_{e,i})$ and $P_{e,i}(\rho, T_{e,i})$. A heat flux model, typically a flux-limited Spitzer-Härm [Spitzer & Härm, 1953] or Braginskii [Braginskii, 1965] model yields $\boldsymbol{Q}_e$, which may be non-local [Schurtz *et al.*, 2000]. The ion heat flux $\boldsymbol{Q}_i$ is generally much smaller than its electron counterpart, and so is often treated as linear diffusion, $\boldsymbol{Q}_i = -\kappa_i \boldsymbol{\nabla} T_i$, where κ_i is the thermal conductivity of the ions. Equations for nuclear reactions and neutron transport are also included for the simulations of experiments with fusible material.

Radiation is of paramount importance in indirect-drive ICF experiments: laser beams irradiate the hohlraum, and X-ray radiation drive the implosion of the capsule. Thus, codes used to simulate ICF experiments such as TROLL and HYDRA must describe both hydrodynamics and radiation transport. They are called radiation hydrodynamics codes.

The two main types of radiation encountered in ICF simulations, X-ray and laser are simulated differently. On the one hand, X-ray photons propagate almost in a straight line through the plasma, because of their high energy. Furthermore, they are emitted by a nearly black-body hohlraum plasma, so a wide spectrum of energy, from $\sim 50\,\text{eV}$ to $\sim 4000\,\text{eV}$, has to be taken into account. On the other hand, laser beams are made up of monoenergetic low energy ($\sim 3\,\text{eV}$) photons, so they may have curved trajectories. In practice, a multi-group Monte Carlo method using tabulated opacities and emissivities is used to transport X-rays, and a ray-tracing algorithm is used for the propagation of the laser beams.

Numerical aspects

Fully 3D simulations would be necessary to describe all the phenomena occuring during an ICF experiments [Clark *et al.*, 2016], but they are very computationally costly. Therefore, the dimensionality of the simulations is reduced when possible thanks to symmetries of the experimental configuration. Indeed, hohlraums typically have multiple symmetry axis which can be used to reduce the simulation domain. In particular, ICF hohlraums with a capsule have an axis of revolution, and a symmetry plane that bissects the hohlraum (though not directly outlined, the symmetry is apparent in the top left of Fig. 1.3). Only the configuration of laser beams, shown in Fig. 1.5, does not have this symmetry, but this may be neglected in first approximation to use 2D axisymmetric simulations. As a result, the simulated domain is typically only what is shown in Fig. 1.12. In this image, the left side is an axis of symmetry, so that only one side of the hohlraum is simulated. Additionnally, the bottom of the image is an axis of cylindrical symmetry.

In 2D simulations, and even more so in 3D simulations, the number of cells in the mesh has to be limited as much as possible, in order to reduce the computational cost of the simulation. However, there are multiple areas where the mesh has to be well resolved in order to accurately describe the experiment. For example, two of these areas are the hohlraum plasma and the capsule. The hohlraum plasma must be well described because it produces the X-ray radiation that drives the implosion of the capsule. The mesh also has to be well resolved in the capsule in order to capture the physics of the hot spot. These areas move during the experiment: the hohlraum wall is ablated, the center of the capsule is compressed, and the ablator expands. Thus, it can be convenient to use a Lagrangian numerical scheme, in which the mesh is made to move

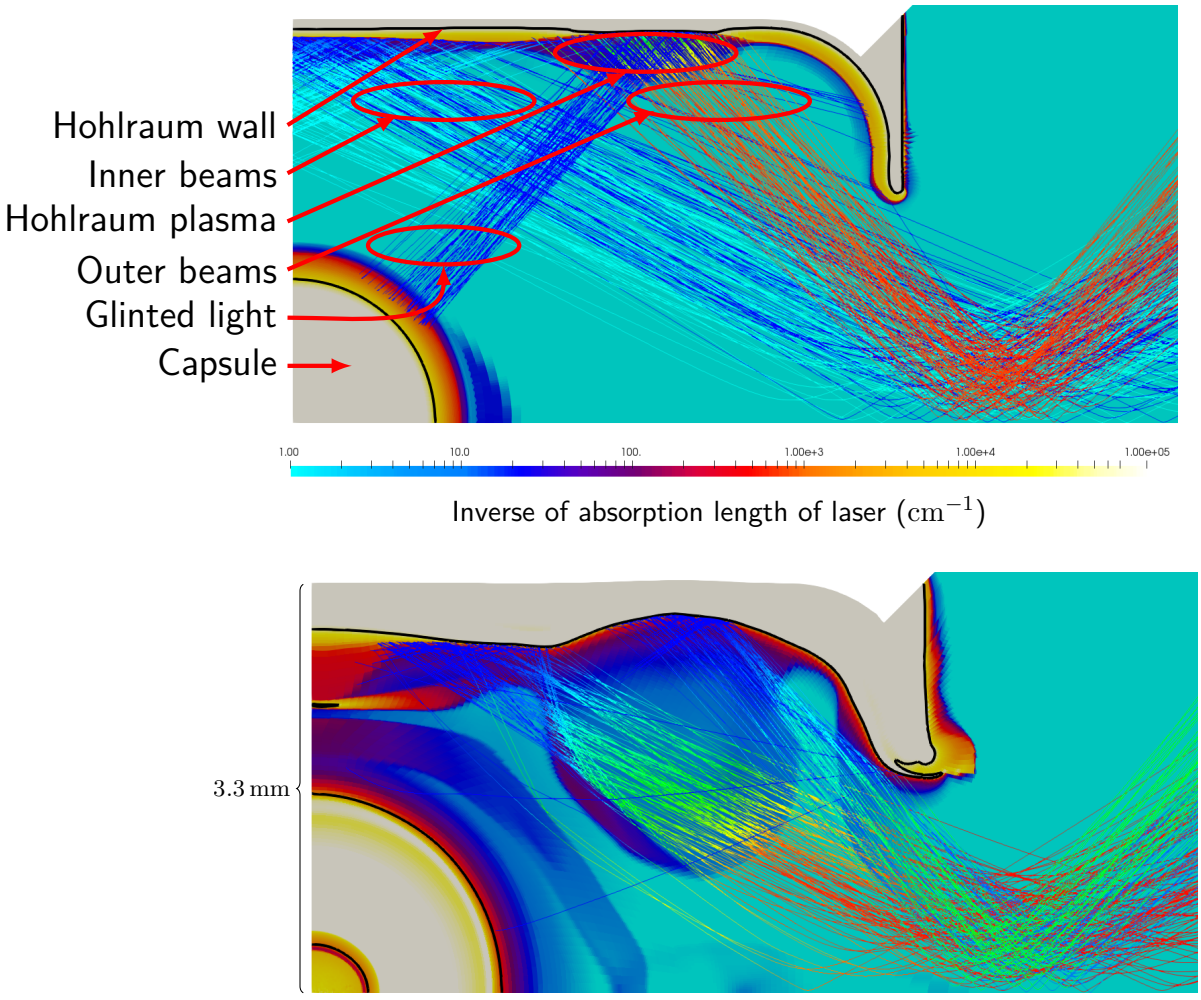

Figure 1.12: Images from a typical TROLL simulation at $t = 2\,\text{ns}$ (top) and $t = 6.7\,\text{ns}$ (bottom). The trajectory of some laser beams, computed with a ray-tracing algorithm is represented. The color of each ray is related to the power it carries, with the outer beams carrying the most power before interacting wih the hohlraum wall. These images are from the same simulation as Fig. 1.11, so the space scale is the same. The color scale, which is the same for both images, shows the inverse of the characteristic absorption length of the laser. The cyan part corresponds to the outside vacuum and the cavity gas, which do not absorb much laser energy. Energy is mainly absorbed in the hohlraum plasma, in dark blue. In the bottom image, the compression of the hot spot has started, and the hohlraum wall has significantly expanded.

with the matter it describes. However, having the mesh completely bound to matter can have unwanted effects, for example in vortices and shear flows, where the mesh can be distorted to such a degree that the simulation can fail. The strategy used in TROLL to deal with this is to use an Arbitrary Lagrange Eulerian description, in which the Lagrangian mesh is periodically transformed into a more regular mesh. In addition to maintaining mesh quality, this method also allows for dynamic resolution. This means that areas of interest may be dynamically remeshed more finely, for a better description.

1.2.2 Laser modelling

As mentioned before, radiation hydrodynamic codes used to design ICF experiments use a ray-tracing algorithm to compute laser energy deposition in matter. This section shows the derivation of the ray-tracing propagation equation, to bring out the limits of this modelling.

The dispersion relation

Laser beams are electromagnetic waves that propagate according to Maxwell equations [Born & Wolf, 1959, Jackson, 1999]

$$\begin{cases} \boldsymbol{\nabla}\times\boldsymbol{E} = -\partial_t \boldsymbol{B} & \text{Faraday's law of induction,} \quad (1.8a) \\ \boldsymbol{\nabla}\cdot\boldsymbol{B} = 0 & \text{Gauss's law for magnetism,} \quad (1.8b) \\ \boldsymbol{\nabla}\times\boldsymbol{B} = \dfrac{1}{c^2}\,\partial_t \boldsymbol{E} + \mu_0\,\boldsymbol{J} & \text{Ampère's circuital law,} \quad (1.8c) \\ \varepsilon_0\,\boldsymbol{\nabla}\cdot\boldsymbol{E} = \rho_e & \text{Gauss's law,} \quad (1.8d) \end{cases}$$

where $\boldsymbol{E}$ is the electric field, $\boldsymbol{B}$ the magnetic induction, ρ_e the electric charge density, and $\boldsymbol{J}$ the current density. We use Ohm's law to write $\boldsymbol{J} = \sigma\,\boldsymbol{E}$, with σ the electric conductivity. Since the electrons and ions are co-moving, the average charge density ρ_e is zero. This system of equation can be further simplified using the fact that the electromagnetic field described here is due to laser beams. Laser beams can be readily approximated by a wave with a pulsation ω, which varies slowly on the trajectory of the beam, compared with the wavelength $\lambda = 2\pi\,c/\omega$. This is a very good approximation in practice. The frequency of a laser beam in ICF can evolve, for example because of Doppler effect due to propagating through moving material [Dewandre, 1981]. However, these materials move very slowly compared to c, and so the frequency shift is very small compared to the laser frequency.

As a result, we consider the pulsation as a constant in first approximation, and write in the usual complex notation $\boldsymbol{E} = \mathfrak{Re}[\boldsymbol{E}_0(\boldsymbol{r})\,\exp(-i\,\omega\,t)]$, and $\boldsymbol{B} = \mathfrak{Re}[\boldsymbol{B}_0\,(\boldsymbol{r})\exp(-i\,\omega\,t)]$ where $\boldsymbol{E}_0$ and $\boldsymbol{B}_0$ contain the spatial variation of the field. Inserting these expressions into Maxwell's equations yields

$$\begin{cases} \boldsymbol{\nabla}\times\boldsymbol{E}_0 = i\,\omega\,\boldsymbol{B}_0, & (1.9a) \\ \boldsymbol{\nabla}\cdot\boldsymbol{B}_0 = 0, & (1.9b) \\ \boldsymbol{\nabla}\times\boldsymbol{B}_0 = \left(-\dfrac{i\,\omega}{c^2} + \mu_0\,\sigma\right)\boldsymbol{E}_0, & (1.9c) \\ \boldsymbol{\nabla}\cdot\boldsymbol{E}_0 = 0. & (1.9d) \end{cases}$$

We now introduce the medium complex permittivity as

$$\varepsilon = 1 + i\frac{\sigma}{\varepsilon_0\,\omega}. \quad (1.10)$$

Taking the curl of eq. (1.9c) and inserting eq. (1.9c) in the result then yields the Helmholtz equation

$$\nabla^2\boldsymbol{E}_0 + \frac{\omega^2}{c^2}\,\varepsilon\,\boldsymbol{E}_0 = \boldsymbol{0}. \quad (1.11)$$

Similarly, it is also possible to obtain this equation on $\boldsymbol{B}_0$ instead of $\boldsymbol{E}_0$. This equation can be solved numerically in order to model the propagation of laser beams. In 3D codes used to design ICF experiments such as TROLL or HYDRA however, this is prohibitively costly from a numerical point of view. This is the reason why further approximations that leads to geometrical optics are carried out.

In order to show where these approximations come from, we write, without loss of generality, $\boldsymbol{E}_0 = \boldsymbol{A}(\boldsymbol{r}) \exp(i\, k_0\, \psi(\boldsymbol{r}))$ where $k_0 = \omega/c$ is the vacuum wavenumber, $\psi(\boldsymbol{r})$ is a real coefficient that takes into account the variation of the wavenumber, and $\boldsymbol{A}$ is the real amplitude of the field. Inserting this into the Helmholtz equation eq. (1.11) yields

$$\nabla^2 \boldsymbol{A} + 2\, i\, k_0\, (\boldsymbol{\nabla}\psi \cdot \boldsymbol{\nabla})\boldsymbol{A} + i\, k_0\, \nabla^2\psi\, \boldsymbol{A} - k_0^2\, (\boldsymbol{\nabla}\psi)^2\, \boldsymbol{A} + k_0^2\, \varepsilon\, \boldsymbol{A} = \boldsymbol{0}. \tag{1.12}$$

With $\varepsilon_r = \mathfrak{Re}(\varepsilon)$, $\varepsilon_i = \mathfrak{Im}(\varepsilon)$, the real and imaginary parts of this equation can be separated into

$$\begin{cases} \nabla^2 \boldsymbol{A} - k_0^2\, (\boldsymbol{\nabla}\psi)^2\, \boldsymbol{A} + k_0^2\, \varepsilon_r\, \boldsymbol{A} = \boldsymbol{0}, & \text{(1.13a)} \\ 2\, k_0\, (\boldsymbol{\nabla}\psi \cdot \boldsymbol{\nabla})\boldsymbol{A} + k_0\, \nabla^2\psi\, \boldsymbol{A} + k_0^2\, \varepsilon_i\, \boldsymbol{A} = \boldsymbol{0}. & \text{(1.13b)} \end{cases}$$

The main approximation of geometric optics is that the amplitude vary very slowly compared to the scale of the propagation of the wave, which is roughly $1/k_0$. This means $k_0^2\, \boldsymbol{A} \gg \nabla^2 \boldsymbol{A}$, so the first term of eq. (1.13a) can be neglected. Assuming ε_r is of order unity, this yields

$$\varepsilon_r = (\boldsymbol{\nabla}\psi)^2, \tag{1.14}$$

which is called the eikonal relation. With $\boldsymbol{k} = k_0\, \boldsymbol{\nabla}\psi$, the eikonal relation becomes the dispersion relation

$$k^2 = \frac{\omega^2}{c^2}\, \varepsilon_r. \tag{1.15}$$

The light rays in geometrical optics are defined as orthogonal trajectories to the wavefronts $k_0\, \psi(\boldsymbol{r}) =$ constant. This means that the direction of propagation of a ray is given by a unit vector in the direction of $\boldsymbol{\nabla}\psi$. Using eq. (1.14),

$$\frac{\mathrm{d}\boldsymbol{r}}{\mathrm{d}s} = \frac{\boldsymbol{\nabla}\psi}{\sqrt{\varepsilon_r}}, \tag{1.16}$$

where $\boldsymbol{r}$ is the position of a ray and s is the curvilinear abscissa along its trajectory. The propagation is characterized by

$$\begin{aligned} \frac{\mathrm{d}}{\mathrm{d}s}\left[\sqrt{\varepsilon_r}\, \frac{\mathrm{d}\boldsymbol{r}}{\mathrm{d}s}\right] &= \frac{\mathrm{d}}{\mathrm{d}s}\boldsymbol{\nabla}\psi & \text{(1.17)} \\ &= \left(\frac{\mathrm{d}\boldsymbol{r}}{\mathrm{d}s} \cdot \boldsymbol{\nabla}\right) \boldsymbol{\nabla}\psi & \text{(1.18)} \\ &= \frac{1}{\sqrt{\varepsilon_r}}\, (\boldsymbol{\nabla}\psi \cdot \boldsymbol{\nabla})\, \boldsymbol{\nabla}\psi & \text{(1.19)} \\ &= \frac{1}{2\sqrt{\varepsilon_r}}\, \boldsymbol{\nabla}\left((\boldsymbol{\nabla}\psi)^2\right) & \text{(1.20)} \\ &= \frac{1}{2\sqrt{\varepsilon_r}}\, \boldsymbol{\nabla}\varepsilon_r, & \text{(1.21)} \end{aligned}$$

where we used $\mathrm{d}/\mathrm{d}s = (\mathrm{d}\boldsymbol{r}/\mathrm{d}s)\ \mathrm{d}/\mathrm{d}\boldsymbol{r}$, and the eikonal equation, eq. (1.14). This equation is more conveniently written using the optical coordinate τ which is defined such that $\mathrm{d}\tau = \mathrm{d}s/\sqrt{\varepsilon_r}$. Eq. (1.21) can be recast as

$$\frac{\mathrm{d}^2\boldsymbol{r}}{\mathrm{d}\tau^2} = \frac{1}{2}\,\boldsymbol{\nabla}\varepsilon_r. \tag{1.22}$$

This is the equation used for the propagation of rays. We can now go back to eq. (1.13b) to see how the amplitude vary along the propagation of the ray. At highest order in k_0, this equation simply yields $\varepsilon_i = 0$. This means that in geometrical optics, ε_i must be very small, so that it is not of order unity like we assumed ε_r to be, but of order $1/k_0$. Since eq. (1.22) shows that ε_r controls the ray propagation, and we will show that ε_i controls the absorption of the ray, this essentially means that the propagation length of the ray must be much smaller than its absorption length for geometrical optics to be usable. With this assumption on ε_i, eq. (1.13b) yields

$$(\boldsymbol{\nabla}\psi\cdot\boldsymbol{\nabla})\boldsymbol{A} = -\frac{1}{2}\left(\nabla^2\psi + k_0\,\varepsilon_i\right)\boldsymbol{A}. \tag{1.23}$$

This can be simplified by using $\mathrm{d}/\mathrm{d}\tau = \sqrt{\varepsilon_r}\ \mathrm{d}/\mathrm{d}s = \sqrt{\varepsilon_r}\ \mathrm{d}\boldsymbol{r}/\mathrm{d}s\cdot\boldsymbol{\nabla} = \boldsymbol{\nabla}\psi\cdot\boldsymbol{\nabla}$, in which we used eq. (1.16). This yields

$$\frac{\mathrm{d}\boldsymbol{A}}{\mathrm{d}\tau} = -\underbrace{\frac{1}{2}\nabla^2\psi\,\boldsymbol{A}}_{\text{reversible term}} - \underbrace{\frac{1}{2}\,k_0\,\varepsilon_i\,\boldsymbol{A}}_{\text{absorption term}}, \tag{1.24}$$

which is the equation that describes the propagation of the amplitude of the ray along its trajectory. The origin of the variation of amplitude along the trajectory of a ray is twofold. The first term, outlined by the first brace in eq. (1.24) is purely reversible. Indeed, the trajectory of the wave or variation of the wavelength can lead to a growing surface of the wavefront $\psi =$ constant, so even without any absorption, the same energy is spread out over a larger surface. In geometrical optics, this corresponds to a decrease of the amplitude carried by the rays. The second term corresponds to energy that is irreversibly absorbed by the medium.

The condition for the absorption length to be much greater than the propagation length can now be formally expressed. The propagation length is given by eq. (1.15) as $(k_0\,\varepsilon_r)^{-1}$. The absorption length is given by the absorption term in eq. (1.24) as $(k_0\,\varepsilon_i)^{-1}$. Thus, the condition of validity of geometrical optics reduces to $\varepsilon_i \ll \varepsilon_r$. To use the amplitude equation eq. (1.24), and the propagation equation eq. (1.22) in radiation hydrodynamics codes, an expression of the plasma permittivity ε is needed.

The Drude Optical Index

The Drude model [Drude, 1900] is a model for the transport properties, and in particular the conductivity, of free electrons in a material where ions are motionless. Indeed, we recall that the conductivity σ appeared in the definition of the permittivity eq. (1.10), which we recall is given by

$$\varepsilon = 1 + \frac{i\,\sigma}{\varepsilon_0\,\omega}. \tag{1.25}$$

The derivation of the conductivity in the Drude model is based upon Ohm's law, $\boldsymbol{J} = \sigma\,\boldsymbol{E}$ and upon the definition of the current density

$$\boldsymbol{J} = \sum_{\alpha} n_\alpha\, q_\alpha\, \bar{\boldsymbol{v}}_\alpha, \tag{1.26}$$

where α runs over the species of the plasma (tyically electrons and ions), n_α, q_α and $\bar{\boldsymbol{v}}_\alpha$ being respectively the number density, average charge and average velocity of species alpha. The Drude model first takes advantage of the fact that ions are so massive compared to electrons. The velocity of ions can be neglected if the ration of temperature is much smaller than the ratio of masses, $T_i/T_e \ll m_i/m_e$, which is always verified in ICF plasmas. Therefore, the only non-zero term in the current density eq. (1.26) is the one related to the electrons, which leaves

$$\boldsymbol{J} = -e\, n_e\, \bar{\boldsymbol{v}}_e. \tag{1.27}$$

The evolution of the average electron velocity is due to the effect of the electric field, and to collisions on ions. We will show in chapter 2 that collisions on ions can be modelled by a damping term at a rate corresponding to the electron-ion collision frequency ν_{ei}. This means that

$$m_e\, \frac{\mathrm{d}\bar{\boldsymbol{v}}_e}{\mathrm{d}t} = -e\,\boldsymbol{E} - m_e\,\nu_{ei}\,\bar{\boldsymbol{v}}_e. \tag{1.28}$$

Since we are looking for solutions oscillating at the pulsation of the laser ω, we use the complex notation $\boldsymbol{v} = \mathrm{Re}[\boldsymbol{v}_0(\boldsymbol{r})\,\exp(-i\,\omega\,t)]$, $\boldsymbol{E} = \mathrm{Re}[\boldsymbol{E}_0(\boldsymbol{r})\,\exp(-i\,\omega\,t)]$ and $\boldsymbol{J} = \mathrm{Re}[\boldsymbol{J}_0(\boldsymbol{r})\,\exp(-i\,\omega\,t)]$, which yields

$$\bar{\boldsymbol{v}}_0 = \frac{-e}{m_e\,(\nu_{ei} - i\,\omega)}\boldsymbol{E}_0, \tag{1.29}$$

which can be inserted into eq. (1.27) to yield

$$\boldsymbol{J}_0 = \frac{e^2\, n_e}{m_e\,(\nu_{ei} - i\,\omega)}\,\boldsymbol{E}_0 = \frac{\varepsilon_0\,\omega_p^2}{\nu_{ei} - i\,\omega}\,\boldsymbol{E}_0, \tag{1.30}$$

where the plasma pulsation $\omega_p^2 = n_e\, e^2/(\varepsilon_0\, m_e)$ was introduced. It is straightforward to identify $\sigma = \varepsilon_0\,\omega_p^2/(\nu_{ei} - i\,\omega)$ by comparison with Ohm's law. Inserting this into the expression of the optical index eq. (1.10) yields

$$\epsilon = 1 - \frac{\omega_p^2}{\omega\,(\omega + i\,\nu_{ei})}. \tag{1.31}$$

The real and imaginary parts of the permittivity $\varepsilon_r = \mathfrak{Re}(\varepsilon)$ and $\varepsilon_i = \mathfrak{Im}(\varepsilon)$ can both be extracted from eq. (1.31) as

$$\varepsilon_r = 1 - \frac{1}{\dfrac{\omega^2}{\omega_p^2} + \dfrac{\nu_{ei}^2}{\omega_p^2}}, \tag{1.32}$$

$$\varepsilon_i = \frac{\nu_{ei}/\omega_p}{\dfrac{\omega}{\omega_p}\left(\dfrac{\omega^2}{\omega_p^2} + \dfrac{\nu_{ei}^2}{\omega_p^2}\right)}. \tag{1.33}$$

Notice that when $\omega^2 < \omega_p^2 - \nu_{ei}^2$, ε_r becomes negative, which is problematic in the eikonal equation eq. (1.14). However, in this limit, the condition $\varepsilon_i \ll \varepsilon_r$ cannot be fullfilled, and so the equation of propagation eq. (1.22) and absorption eq. (1.24) are not valid anymore.

An additional simplification of eqs. (1.32) and (1.33) occurs when $\nu_{ei}/\omega_p \ll 1$. Fig. 1.13 shows the values taken by ν_{ei}/ω_p during a typical cavity simulation. The image shows that $\nu_{ei} \ll \omega_p$ almost everywhere inside the cavity, including in the hohlraum plasma. The real and imaginary parts of ε can then be expanded with respect to ν_{ei}/ω_p, which yields

$$\varepsilon_r = 1 - \frac{\omega_p^2}{\omega^2} + \mathcal{O}\left(\frac{\nu_{ei}^2}{\omega_p^2}\right), \tag{1.34}$$

$$\varepsilon_i = \frac{\nu_{ei}}{\omega_p}\frac{\omega_p^3}{\omega^3} + \mathcal{O}\left(\frac{\nu_{ei}^3}{\omega_p^3}\right). \tag{1.35}$$

Fig. 1.14 shows the optical index computed from eqs. (1.32) and (1.33) as a function of ω/ω_p for multiple values of ν_{ei}/ω_p. The approximated formulas eqs. (1.34) and (1.35) are also plotted in this graph. Clearly, eqs. (1.34) and (1.35) are good approximations in the vanishingly small limit of ν_{ei}/ω_p. The approximated formula of ε_r does not depend on ν_{ei}. This show that the trajectory of rays is almost independant of ν_{ei}, in the $\nu_{ei}/\omega_p \ll 1$ limit. The electron-ion collision frequency ν_{ei} is then solely associated with laser absorption.

Additionally, Fig. 1.14 explains why ray tracing is needed for lasers and not for X-ray radiation in ICF experiments. Laser beams in ICF usually have $\lambda = 351\,\text{nm}$, which corresponds to $\omega \approx 5 \times 10^{15}\,\text{rad/s}$. As a comparison, the plasma pulsation of gold at the solid density is roughly $\omega_p \approx 9 \times 10^{16}\,\text{rad/s}$. In the hohlraum plasma in which the laser propagates, the density is less than the solid density, and so ω_p has the same order of magnitude as ω. This means that ε_r is not always 1, and ε_i can be important, *i.e.* lasers do not propagate in a straight line, and they can be significantly absorbed by inverse bremsstrahlung. In contrast, the X-rays that drive the implosion of the capsule have a much higher energy, such that they have always have $\omega \gg \omega_p$, and so $\varepsilon_r \approx 1$, *i.e.* they propagate in a straight line. This explain why ray tracing in radiation hydrodynamics codes is only used for the laser beams and not for X-ray radiation.

A first look at the electron-ion collision frequency ν_{ei}

In this section, we present a back of the envelope derivation of the textbook formula of the electron-ion collision frequency ν_{ei}. A more detailed discussion on this frequency is deferred to chapter 2.

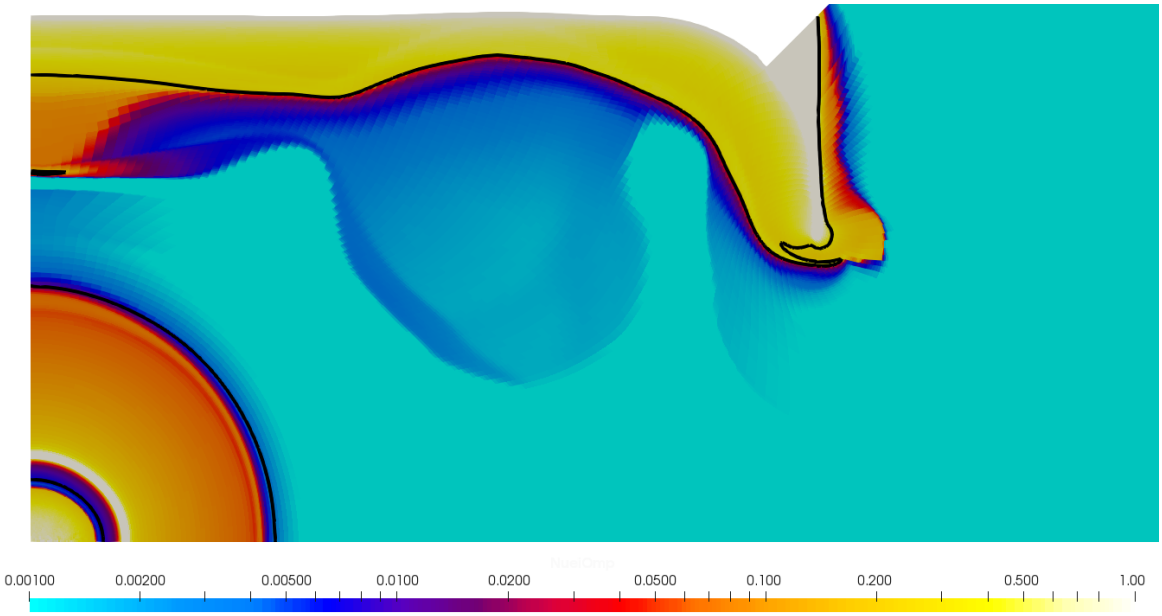

Figure 1.13: Ratio ν_{ei}/ω_p at $t = 6.7\,\text{ns}$ during a typical cavity simulation. The space scale is the same as in Fig. 1.11, so the radius of the hohlraum is 3.3 mm. The black line represent the isocontour $\omega = \omega_p$. We will show using eqs. (1.34) and (1.35) that the region in which the laser can propagate is where $\omega > \omega_p$, in which the image shows that ν_{ei}/ω_p takes values below 0.01, except very close to the critical surface, where ν_{ei}/ω_p can reach values as high as 0.05.

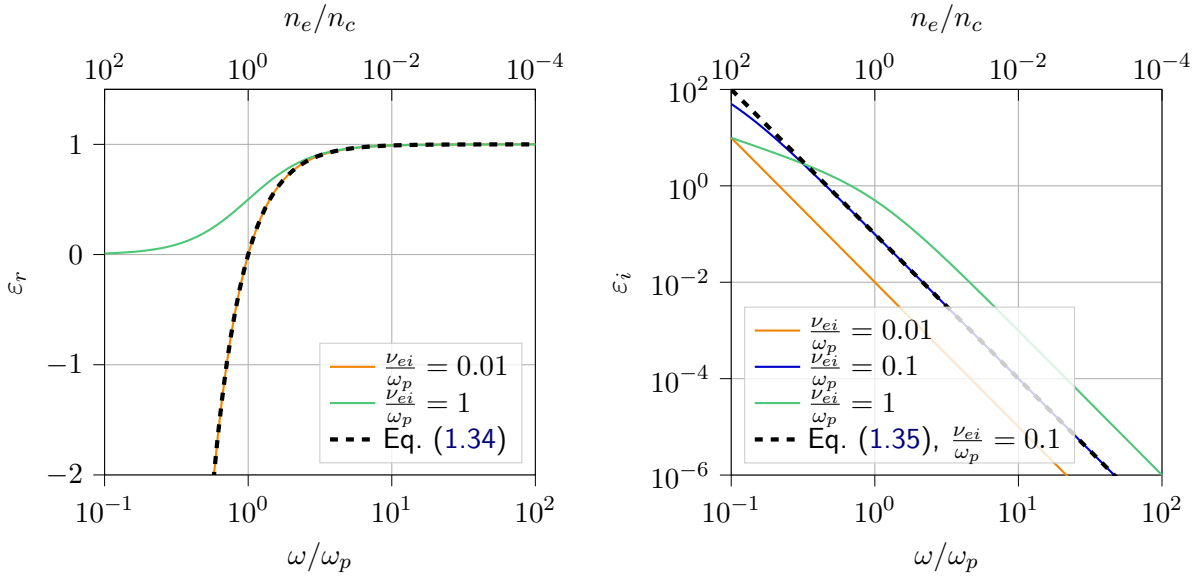

Figure 1.14: Real (left) and imaginary (right) parts of the permittivity computed using the Drude formulas eqs. (1.32) and (1.33) (solid lines) and from the approximated formulas eqs. (1.34) and (1.35) (dashed lines). Notice the linear scale in the left graph showing ε_r as opposed to the logarithmic scale in the right graph. The line $\nu_{ei}/\omega_p = 0.1$ for ε_r is not plotted for clarity because it is conflated with the orange line which is for $\nu_{ei}/\omega_p = 0.01$.

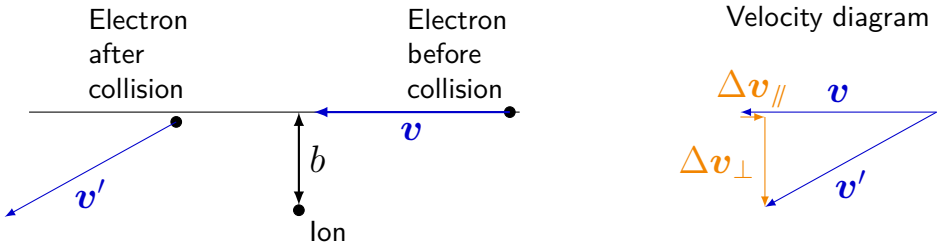

Figure 1.15: Schematic representation of the collision between an electron and an ion. The motion of the ion is neglected because it is so much heavier than the electron. The collision is elastic, so the magnitude of the velocity of the electron is conserved, only the direction changes. This is illustrated in the velocity diagram on the right, where $\Delta v_{/\!/}$ and $\Delta v_\perp$ are represented.

We first consider a classical collision between one electron and one ion, a representation of which is shown in Fig. 1.15. This collision is characterized by its impact parameter b, which would be the closest distance of approach had the particles not interacted and went in a straight line. The velocity of the ion can be neglected because it is so heavy compared to the electron. The velocity of the electron after the collision is

$$\boldsymbol{v}' = (v - \Delta v_{/\!/})\,\frac{\boldsymbol{v}}{v} + \Delta v_\perp\,\boldsymbol{n}, \tag{1.36}$$

where $\boldsymbol{v}$ is the velocity of the electron before the collision, and $\boldsymbol{n}$ is a unit vector normal to $\boldsymbol{v}$, see Fig. 1.15 for the notations. The collision is considered elastic, so the velocity of the electron after the collision has the same magnitude as before the collision, which means

$$\Delta v_{/\!/} = \frac{\Delta v_\perp^2}{2\,v}, \tag{1.37}$$

assuming $\Delta v_{/\!/} \ll v$. Additionally, the electron and ion are assumed to interact only by a Coulomb potential, so

$$m_e\,\frac{\mathrm{d}v}{\mathrm{d}t} = -\frac{Z\,e^2}{4\,\pi\,\varepsilon_0\,r^2}, \tag{1.38}$$

where r is the distance between the electron and the ion and Z is the charge of the ion. The velocity difference in the direction of $\boldsymbol{n}$, $\Delta v_\perp$ can be approximated by

$$m_e\,\frac{\Delta v_\perp}{\Delta t} \approx -\frac{Z\,e^2}{4\,\pi\,\varepsilon_0\,b^2}, \tag{1.39}$$

where $\Delta t \approx b/v$ is the characteristic time of the collision. Using eq. (1.37), the velocity difference can be expressed as

$$\Delta\boldsymbol{v} = \boldsymbol{v}' - \boldsymbol{v} = -\frac{Z^2\,e^4}{2\,(4\,\pi\,\varepsilon_0)^2\,m_e^2\,b^2\,v^3}\,\frac{\boldsymbol{v}}{v} - \frac{Z\,e^2}{4\,\pi\,\varepsilon_0\,m_e\,b\,v}\,\boldsymbol{n}. \tag{1.40}$$

The number of collisions with impact parameter between b and $b + \mathrm{d}b$ that occurs during Δt is $2\,\pi\,b\,\mathrm{d}b\,n_i\,v\,\Delta t$, where n_i is the number density of ions. When averaging over all collisions, the component of the velocity difference along $\boldsymbol{n}$ will cancel out because there are the same number of collisions with impact parameter b and "$-b$", *i.e.* with the same impact parameter, but opposite

relative position of the ion and electron. These collisions will produce the same $\Delta v_\perp$, but in opposite directions, so they cancel out on average. A more rigorous proof of this will be given in chapter 2. Finally, the average variation of velocity for an electron with velocity v is

$$\left\langle \frac{\Delta \boldsymbol{v}}{\Delta t} \right\rangle = -\int 2\,\pi\, b\ \mathrm{d}b\, n_i\, v\, \frac{Z^2\, e^4}{2\,(4\,\pi\,\varepsilon_0)^2\, m_e^2\, b^2\, v^3}\, \frac{\boldsymbol{v}}{v} \tag{1.41}$$

$$= \frac{\pi\, Z^2\, e^4\, \boldsymbol{v}}{(4\,\pi\,\varepsilon_0)^2\, m_e^2\, v^3}\ \ln\Lambda, \tag{1.42}$$

where $\ln\Lambda = \int \mathrm{d}b/b$ is the Coulomb logarithm. Obviously, the Coulomb logarithm is not defined if we consider all possible impact parameters, from 0 to ∞. Very large impact parameters have to be cut off because of collective effects that occur in a plasma. When an electron and an ion are sufficiently far from each other, they are shielded from each other by the other particles in the plasma, and so they do not interact. The characteristic length at which this occurs is the plasma Debye length

$$\lambda_{Dei} = \sqrt{\frac{\varepsilon_0}{e^2}\left(\frac{n_e}{k_B T_e} + \frac{\bar{Z}\, n_i}{k_B T_i}\right)^{-1}}, \tag{1.43}$$

so this is a common choice for the upper limit of the integral of the Coulomb logarithm. When the impact parameter is too small, eq. (1.39) is not a good approximation any more. Additionally, quantum-mechanical effects have to be taken into account when the electron and ion are too close to each other. These elements explain why a lower cut-off is needed for the integral of the Coulomb logarithm. A common choice for the classical cut-off is the Landau length

$$R_c = \frac{\bar{Z}\, e^2}{4\,\pi\,\varepsilon_0\, k_B T_e}, \tag{1.44}$$

which is the impact parameter for which the velocity is deviated by 90°. All in all, two cut-off impact parameters, which we will refer to as $b_{\min}$ and $b_{\max}$, have to be chosen to avoid divergence of the Coulomb logarithm $\ln\Lambda$. This yields

$$\left\langle \frac{\Delta \boldsymbol{v}}{\Delta t} \right\rangle = -\int 2\,\pi\, b\ \mathrm{d}b\, n_i\, v\, \frac{Z^2\, e^4}{2\,(4\,\pi\,\varepsilon_0)^2\, m_e^2\, b^2\, v^3}\, \frac{\boldsymbol{v}}{v} \tag{1.45}$$

$$= -\frac{\pi\, Z^2\, e^4\, n_i\, \boldsymbol{v}}{(4\,\pi\,\varepsilon_0)^2\, m_e^2\, v^3}\ \ln\Lambda, \tag{1.46}$$

where $\ln\Lambda = \ln b_{\max}/b_{\min}$. So far, we have only calculated the average change in velocity for one electrons. To get the effect on the average electron velocity $\bar{\boldsymbol{v}}$, this change has to be averaged with the electron velocity distribution f_e, so that

$$\frac{\mathrm{d}\bar{\boldsymbol{v}}}{\mathrm{d}t} = -\frac{\pi\, Z^2\, e^4\, n_i}{(4\,\pi\,\varepsilon_0)^2\, m_e^2}\ln\Lambda \int \frac{\boldsymbol{v}}{v^3}\, f_e(v)\ \mathrm{d}^3 v \tag{1.47}$$

In the case of a drifted Maxwellian distribution, $f_e(\boldsymbol{v}) = \exp(-(\boldsymbol{v}-\boldsymbol{v}_\mathrm{d})^2/2\,v_\mathrm{th}^2)/(2\,\pi\,v_\mathrm{th}^2)^{3/2}$, where

$v_{\text{th}} = \sqrt{k_B T_e / m_e}$ is the thermal velocity and $\boldsymbol{v}_d$ is the drift velocity,

$$\frac{\mathrm{d}\bar{\boldsymbol{v}}}{\mathrm{d}t} = -\frac{4\sqrt{2\,\pi}}{3}\frac{Z^2\,e^4\,n_i\,\ln\Lambda}{(4\,\pi\,\varepsilon_0)^2\,\sqrt{m_e}\,(k_B T_e)^{3/2}}\,\boldsymbol{v}\,\underbrace{\frac{3}{v_{\text{d}}^3}\int_0^{v_d} v^2\,\exp\left(-\frac{v^2}{2\,v_{\text{th}}^2}\right)\mathrm{d}v}_{\approx 1 \text{ when } v_{\text{d}} \ll v_{\text{th}}} \tag{1.48}$$

When the drift is small compared to the thermal velocity $v_{\text{d}} \ll v_{\text{th}}$, the last part of eq. (1.48), is approximately 1, as outlined in the equation. By comparison with eq. (1.28), the electron-ion collision frequency can then be expressed as

$$\nu_{ei} = \frac{4\sqrt{2\,\pi}}{3}\frac{Z\,e^4\,n_e}{\sqrt{m_e}(4\,\pi\,\varepsilon_0)^2\,(k_B T_e)^{3/2}}\,\ln\Lambda. \tag{1.49}$$

1.2.3 Ray-tracing and inverse bremsstrahlung absorption in codes

There are two aspects to ray-tracing algorithm in numerical codes: the propagation of the rays, and their absorption. After presenting how rays are propagated, we will take a look into the modelling of inverse bremsstrahlung. Other absorption phenomena do occur in ICF experiments, and they are modelled in the codes [Colaïtis *et al.*, 2021, Debayle *et al.*, 2019], but for the sake of conciseness, we only present inverse bremsstrahlung absorption, which is the focus of this thesis.

Propagation of rays in radiation hydrodynamics codes

In radiation hydrodynamics codes, the real part of the Drude optical index eq. (1.34) is used in conjunction with the propagation equation eq. (1.22) to compute the trajectory of each ray. Inserting eq. (1.34) into eq. (1.22) yields

$$\frac{\mathrm{d}^2\boldsymbol{r}}{\mathrm{d}\tau^2} = -\frac{1}{2\,n_c}\boldsymbol{\nabla} n_e \tag{1.50}$$

To be used in computational codes, this equation must first be discretized. One possible technique [Kaiser, 2000] is to mesh the simulation domain, for example using the hydrodynamic mesh. Cells should be small enough so that the electronic density can be considered to vary linearly with space inside each cell,

$$n_e(\boldsymbol{r}) = n_e(\boldsymbol{r}_c) + (\boldsymbol{r} - \boldsymbol{r}_c)\cdot\boldsymbol{\nabla} n_e(\boldsymbol{r}_c), \tag{1.51}$$

where $\boldsymbol{r}_c$ is the center of the cell. The electronic density and its gradient are usually reconstructed from hydrodynamic quantities such as the density and ionization state. Since the gradient of electronic density inside a cell is assumed constant, the ray-tracing equation eq. (1.50) can be solved analytically and yield

$$\frac{\mathrm{d}\boldsymbol{r}}{\mathrm{d}\tau}(\Delta\tau) = \frac{\mathrm{d}\boldsymbol{r}}{\mathrm{d}\tau}(0) - \frac{1}{2\,n_c}\boldsymbol{\nabla} n_e(\boldsymbol{r}_c)\Delta\tau, \tag{1.52}$$

$$\boldsymbol{r}(\Delta\tau) = \boldsymbol{r_0} + \frac{\mathrm{d}\boldsymbol{r}}{\mathrm{d}\tau}(0)\,\Delta\tau - \frac{1}{4\,n_c}\boldsymbol{\nabla} n_e(\boldsymbol{r}_c)\,\Delta\tau^2, \tag{1.53}$$

where $\boldsymbol{r}_0$ and $\frac{\mathrm{d}\boldsymbol{r}}{\mathrm{d}\tau}(0)$ refer to the initial position and $\frac{\mathrm{d}\boldsymbol{r}}{\mathrm{d}\tau}$, *i.e.* at the cell entry. Since $\mathrm{d}\tau = \mathrm{d}s/\sqrt{\varepsilon_r}$,

$$\frac{\mathrm{d}r}{\mathrm{d}\tau} = n_r \frac{\mathrm{d}r}{\mathrm{d}s} = n_r, \tag{1.54}$$

where we used the fact that $\mathrm{d}\boldsymbol{r}/\mathrm{d}s$ is a unit vector, as shown in eq. (1.16). Thus, the magnitude of $\frac{\mathrm{d}\boldsymbol{r}}{\mathrm{d}\tau}(0)$ is $n_r(\boldsymbol{r}_0)$ which can be computed from eqs. (1.34) and (1.51). All in all, eq. (1.53) can be solved with the initial position and direction of propagation of the ray. When passing from one cell to another, these informations come from eqs. (1.52) and (1.53) in the previous cell. At the beginning of the ray propagation, these informations have to be given as inputs to the ray-tracing algorithm.

Eq. (1.53) can be used to compute the optical abscissa at which the ray will exit the cell. This is done by inserting eq. (1.53) into the equation defining the surface of a face of the cell. As an example, for planar cell faces, eq. (1.53) is inserted into $\boldsymbol{u} \cdot \left(\boldsymbol{r} - \boldsymbol{f}_f\right)$, where $\boldsymbol{u}$ is a unit vector normal to the cell face, and $\boldsymbol{r}_f$ is the position of the center of the face. This allows the computation of the $\Delta\tau$ at which the trajectory of the ray will cross each face. The actual face by which the ray actually exits the cell is the one with the minimum exit $\Delta\tau$.

Because the electronic density is interpolated by eq. (1.51) inside each cell, the profile seen by the ray may not be continuous. To deal with this, Snell's laws can be used at the interfaces between cells.

The validity of the trajectory of a ray relies mainly on the linear interpolation of the electronic density eq. (1.51) that is done inside each cell. It is important to note that if there are not enough cells to properly describe the density profile, the trajectory may be significantly altered. Because the absorption is computed on the trajectory of the ray, the total energy deposited may also be altered.

The computation we have described here is only concerned with the ray trajectory. This is because the velocity of matter in ICF experiments is much less than the speed of light, therefore the time taken by a ray to propagate through the plasma is much less than the hydrodynamic timestep. This means that the ray can be considered to propagate instantly.

Inverse bremsstrahlung absorption in radiation hydrodynamics codes

The modelling of laser absorption in radiation hydrodynamics codes uses the same mesh that is used for propagation. The absorption is computed from eq. (1.24), however, it is the intensity carried by the ray I that is computed, rather than the amplitude $\boldsymbol{A}$ that appears in eq. (1.24). Since the intensity is proportional to the square of the amplitude of the field[3], this means

$$\frac{\mathrm{d}I}{\mathrm{d}\tau} = -\left(k_0\,\varepsilon_i + \boldsymbol{\nabla}\cdot\frac{\mathbf{k}}{k_0}\right) I. \tag{1.55}$$

The wave vector can be computed from eq. (1.52). To compute inverse bremsstrahlung absorption, the electron-ion collision frequency ν_{ei} has to be known. We recall the textbook expression [Atzeni

[3]In this work, intensity is defined as $I = \varepsilon_0 c E^2/2$. This definition, which does not take into account the refractive index was chosen to be consistent with the intensity in our molecular dynamics simulations presented in chapters 3 and 4, in which the refractive index is not captured.

& Meyer-ter Vehn, 2004, Eliezer, 2002] of ν_{ei}, which was given in eq. (1.49) by

$$\nu_{ei} = \frac{4\sqrt{2\pi}}{3} \frac{Z e^4 n_e}{\sqrt{m_e}(4\pi\varepsilon_0)^2 (k_B T_e)^{3/2}} \ln\Lambda, \tag{1.56}$$

where $\ln\Lambda$ is the Coulomb logarithm, which mainly depends upon n_e, T_e and Z, though it may also depends on I and ω. A thorough discussion on the Coulomb logarithm is deferred to chapter 2.

For now, we will only present the Skupsky [1987] model, which is one of the model of Coulomb logarithm that is available in TROLL

$$\ln\Lambda = \max\left(2.0,\ \frac{1}{2}\ln\left[1+\left(\frac{b_{\max}}{b_{\min}}\right)^2\right] - 1.25\right) \tag{1.57}$$

with

$$b_{\max} = \min\left(\lambda_D^c,\ \max(\lambda_D,\ a_i)\right), \qquad b_{\min} = \min\left(a_i,\ \max(\lambda_B,\ R_c)\right) \tag{1.58}$$

where

$$\lambda_D = \sqrt{\frac{\varepsilon_0}{e^2}\left(\frac{n_e}{k_B T_e} + \frac{\bar{Z}\, n_i}{k_B T_i}\right)^{-1}}, \tag{1.59}$$

is the plasma Debye length, in which $\bar{Z}$ is the average degree of ionization. When the distance between an electron and an ion exceeds λ_D, they are screened from each other and do not interact. This is the reason why $b_{\max}$ can be set to λ_D. For that to be true, λ_D must be larger than the average distance between ions

$$a_i = \left(\frac{3}{4\pi n_i}\right)^{1/3}. \tag{1.60}$$

When the Debye length λ_D is smaller than a_i, ions are strongly correlated to each other which modifies the screening and $b_{\max}$ should then be set to a_i, according to Skupsky [1987]. This is the reason why $\max(\lambda_D,\ a_i)$ appears in $b_{\max}$ in eq. (1.58). An additional condition on $b_{\max}$ in Skupsky [1987]'s model comes from the fact that the electron-ion collision time, which is b/v_{th} for an impact parameter b and a thermal velocity $v_{\text{th}} = \sqrt{k_B T_e/m_e}$, must be smaller than the laser period. If this were not the case, Skupsky [1987] argues that very little electron heating would occur. The conditions b/v_{th} smaller than the laser period correspond to an impact parameter smaller than the electron Debye length at the critical density,

$$\lambda_D^c = \sqrt{\frac{\varepsilon_0 k_B T_e}{n_c e^2}}, \tag{1.61}$$

where $n_c = \varepsilon_0 m_e \omega^2/e^2$ is the plasma critical density. These elements explain the expression of $b_{\max}$ in eq. (1.58).

In the expression of $b_{\min}$ in eq. (1.58), the presence of a_i is again a correction for situations where strong coupling occurs. The usual value of $b_{\min}$ is the impact parameter corresponding to

a collision with 90° scattering angle, which corresponds to the Landau length

$$R_c = \frac{\bar{Z}\, e^2}{4\,\pi\,\varepsilon_0\, k_B T_e}. \tag{1.62}$$

The presence of the De Broglie wavelength

$$\lambda_B = \frac{\hbar}{2\,\sqrt{3\, m_e\, k_B T_e}}, \tag{1.63}$$

is a correction to account for situations where electrons may approach ions closer than this distance, which is an indication that quantum-mechanical effects have to be taken into account.

A more explicit representation of which value is used for $b_{\min}$ and $b_{\max}$ according to plasma conditions is given in Fig. 1.16. In plasma conditions relevant to ray-tracing in ICF, $n_e < n_c$, and kT_e is between tens of eV and a few keV. Additionally, $\bar{Z}$ can be as high as 50 in the expanding gold bubble of a hohlraum plasma, and so $b_{\min}$ will almost always take the value of R_c. However, $b_{\max}$ can take any of the values of λ_D^c, a_i or λ_D. Since $n_c = \varepsilon_0 m_e \omega^2 / e^2$ is used to compute λ_D^c, the Coulomb logarithm depends on the laser frequency but not on its intensity. Therefore, in this model, the electron-ion collision frequency ν_{ei} depends upon the laser frequency even when the laser intensity is vanishingly small. While this does not appear problematic at first glance since the heating rate is proportional to laser intensity (therefore it tends to 0 in this limit), this is incoherent with the equation describing the evolution of the average velocity of the electrons eq. (1.28). Indeed, this equation stands even in the absence of a laser, in which case it should obviously not depend on any laser parameter. As will be explained in chapter 3, our Molecular Dynamics simulations have ruled out a dependancy of ν_{ei} on the laser frequency only.

Further investigation into the modelling of the electron-ion collision frequency will be carried out in chapters 2 and 3. The next section will explore the possible consequences of a modification in the modelling of laser absorption in a radiation hydrodynamics code. Indeed, even though inverse bremsstrahlung is the main focus of this thesis work, there are several other mechanisms of absorption and numerous ad-hoc techniques have been developed in the literature to take them into account. In the last section of this chapter, we describe one more of these ad-hoc technique that we have developed.

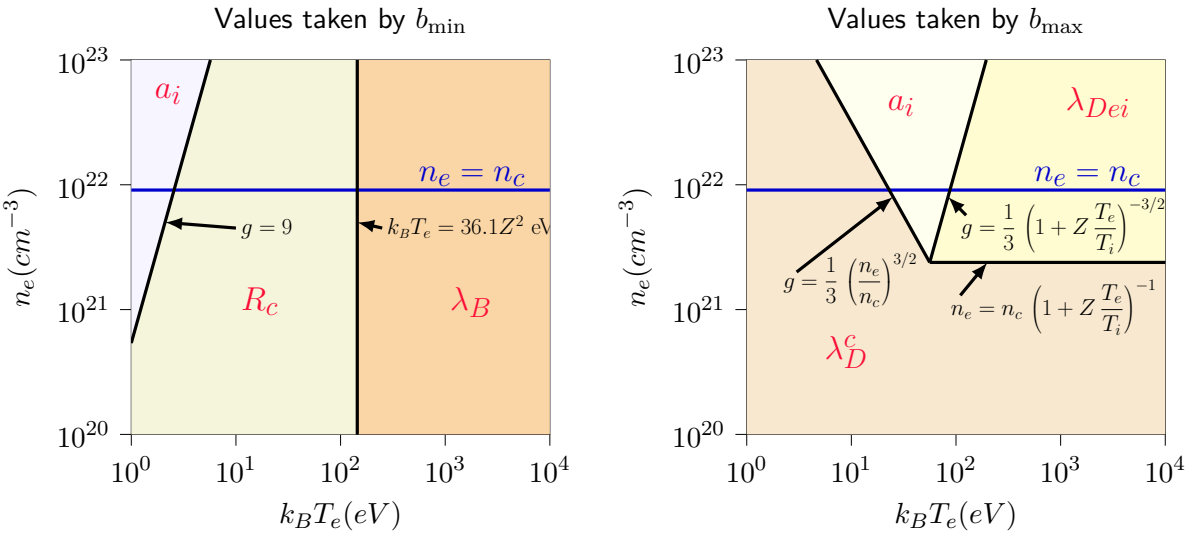

Figure 1.16: Values taken (in red) by the parameters $b_{\min}$ (left) and $b_{\max}$ (right) as a function of n_e and k_BT_e. In these graphs, $Z = 2$ and $T_e/T_i = 1.4$. The critical density corresponds to $\lambda = 351\,\text{nm}$. As an example, for $kT_e = 10\,\text{eV}$ and $n_e = 1 \times 10^{21}\,\text{cm}^{-}3$, $b_{\min}$ is equal to R_c and $b_{\max}$ is equal to λ_D^c. It should be noted that the value $Z = 2$ was chosen for clarity of representation. In actual ICF plasmas, Z can be as high as 50, and so, for example the limit between R_c and λ_B in the $b_{\min}$ graph is at a much higher temperature.

1.3 A simple ad hoc model to evaluate the importance of the Coulomb logarithm

We have shown how inverse bremsstrahlung is modelled in radiation hydrodynamics codes. However, as mentioned previously, there are other mechanisms contributing to laser absorption in a plasma [Eliezer, 2002], such as laser plasma instabilities, Raman scattering, Brillouin scattering, and cross beam energy transfer. Though recent models [Colaïtis *et al.*, 2021, Debayle *et al.*, 2019] have been developed in order to take these into account in ray-tracing algorithms, such models are not yet standard in radiation hydrodynamics codes such as TROLL [Lefebvre *et al.*, 2018], LASNEX or HYDRA [Marinak *et al.*, 2001].

However, these effects still have to be taken into account in order to reproduce experiments, even if they cannot be simulated accurately. Two main methods have been developed to overcome these issues: *power multipliers* (PM) and *enhanced propagation* (EP).

Power Multipliers consists in altering the incident laser intensity using so-called power multipliers [Jones *et al.*, 2012, Lindl *et al.*, 2014, 2018, Robey *et al.*, 2012]. These multipliers reduce the power delivered with the hohlraum. They are allowed to vary with respect to time, as well as with the laser beam they affect. Indeed, having different multipliers for different laser beams makes it possible to take cross-beam energy transfer into account. These multipliers can also be used to deduce energy that is backscattered out of the hohlraum, which cannot be computed with ray-tracing algorithms. Power multipliers have been used to reproduce VISAR shock velocity measurements and experimental symmetry of the hot-spot.

Enhanced propagation consists in modifying the laser frequency [Berzak Hopkins *et al.*, 2015, Turnbull *et al.*, 2016]. Indeed, eq. (1.55) shows that the laser absorption coefficient is $\propto \omega^{-2}$,

so a larger frequency means a smaller coefficient of absorption. This method also allows the modification of each laser beam's frequency separately from the others. It has been used to reproduce experimental hot-spot symmetry in ICF experiments [Berzak Hopkins *et al.*, 2015].

The main drawback of this method is that the laser frequency also appears in the real part of the optical index eq. (1.34), which itself appears in the equation used to compute the trajectory of rays eq. (1.50), so not only the power, but the trajectory of rays are affected by this method. Thus, we have proposed another technique, *absorption multipliers* (AM).

Absorption multipliers consists in an additional factor C_{abs} that is added to eq. (1.55), so that the absorption of laser intensity is now given by

$$\frac{\mathrm{d}I}{\mathrm{d}\tau} = -\frac{C_{\text{abs}}[\text{mat}]}{c\sqrt{1-\dfrac{\omega_p^2}{\omega^2}}}\,\frac{\omega_p^2}{\omega^2}\,\nu_{ei}\,I, \tag{1.64}$$

where the [mat] indicates that C_{abs} is allowed to depend on the material. The effect of C_{abs} is to multiply the laser absorption per unit length by a factor C_{abs} which can be used either to enhance propagation (when $C_{\text{abs}} < 1$) or to reduce propagation (when $C_{\text{abs}} > 1$).

Absorption Multipliers affect the modelling of absorption itself. This means that, contrary to Power Multipliers, the incident laser energy is the same in experiments and simulations. They also do not modify the trajectory of rays, in contrast with Enhanced Propagation.

All in all, absorption multipliers makes it possible to mimic poorly or not simulated absorption mechanisms (laser-plasma instabilities, cross-beam energy transfer, etc.) by using either a $C_{\text{abs}} > 1$ to enhance laser absorption in places where laser energy is known to be lost, or by using a $C_{\text{abs}} < 1$ to enhance laser propagation. Another benefit of the absorption multiplier, is that it can also be used to account for uncertainties in the electron-ion collision frequency which were introduced in the previous section.

These absorption multipliers have been developed as part of a contribution to [Poujade *et al.*, 2021]. In Fig. 1.17 are shown simulations of a cavity with different values of C_{abs}. A difference in the symmetry of the capsule can clearly be seen, with the top image ($C_{\text{abs}} = 1$) having a more symmetrical critical surface than the bottom image ($C_{\text{abs}} = 0.5$). This shows that the uncertainties on laser absorption, whether they come from approximations in the modelling of inverse bremsstrahlung or from laser plasma instabilities, can have a significant impact on ICF experiments.

In this chapter, we have presented the ray-tracing algorithm that is used to compute the propagation and absorption of the lasers in codes used to design ICF experiments. We have shown the assumptions made to go from Maxwell's equations to the ray-tracing equation eq. (1.50).

Additionally, we have shown how laser absorption is modelled in ray-tracing algorithms, and in particular the central role of the electron-ion collision frequency, ν_{ei}. In particular, ν_{ei} is proportional to the Coulomb logarithm $\ln\Lambda$. There is not a consensus in the literature for the modelling of the Coulomb logarithm. This term is thus a source of uncertainty in the modelling of inverse bremsstrahlung, which will be investigate in the following chapter.

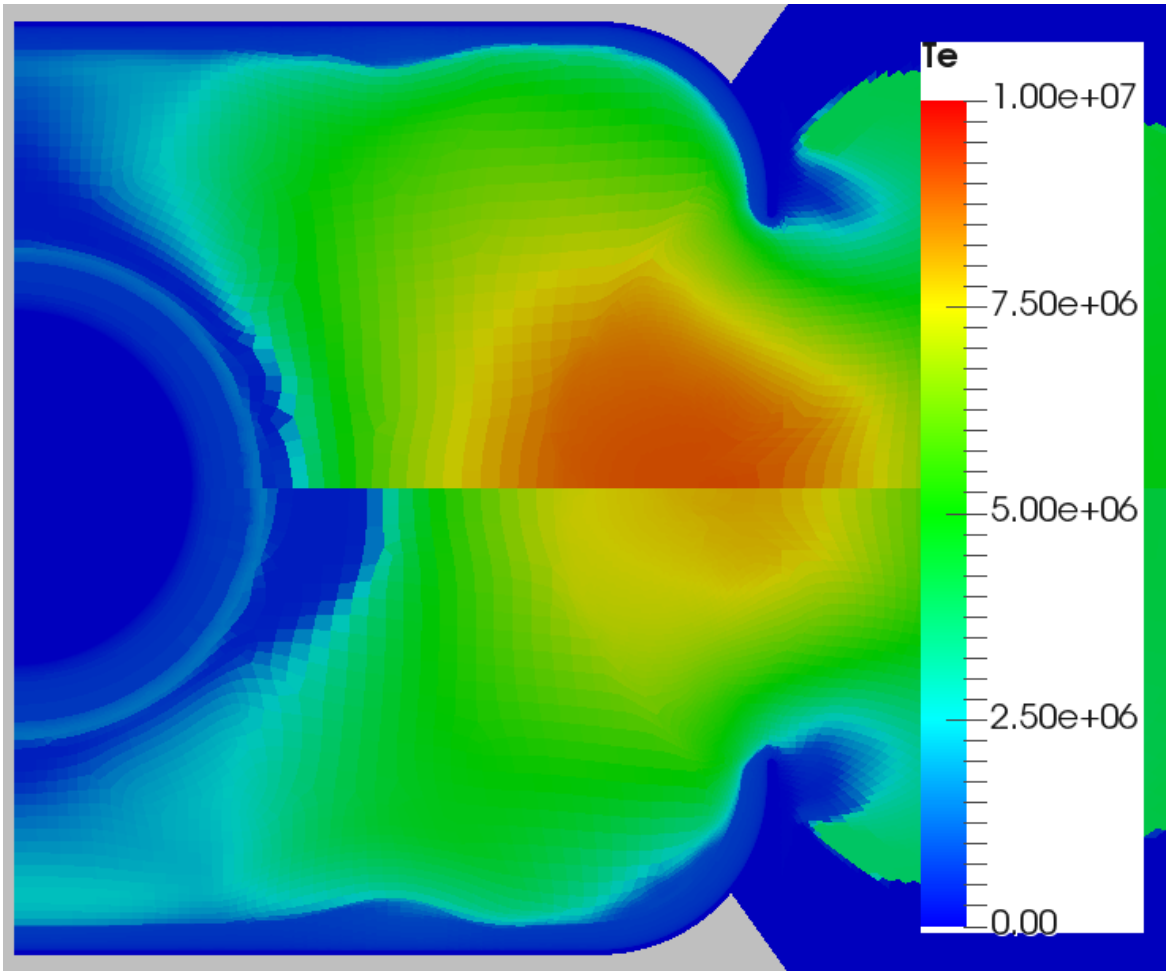

Figure 1.17: Electronic temperature in Kelvin during a typical TROLL simulation with $C_{\text{abs}} = 1$ (top) and $C_{\text{abs}} = 0.5$ (bottom). There are some differences near the laser entrance holes, and, most importantly, in the capsule. Indeed, these images show C_{abs} can modify the symmetry of the implosion, which can have a significant impact on the conditions inside the hot-spot, as explained in section 1.1.3.

Chapter 2

Theoretical basis for inverse bremsstrahlung heating

Contents

The principle of radiation absorption by inverse bremsstrahlung in a plasma involves its free electrons[Pfalzner, 2006]. When a laser propagates through a plasma, the free electrons of the plasma oscillates with the E-field of the laser. Electron-ion collisions converts a fraction of this oscillation energy into thermal energy. The same is true for ions, but because they are much more massive than electrons, they can be considered motionless. The decay rate of laser intensity as it goes through a plasma was derived in chapter 1, and was given in eq. (1.55). It can be related to the inverse bremsstrahlung heating rate by

$$\frac{3}{2} n_e \frac{\mathrm{d}k_B T_e}{\mathrm{d}t} = -\frac{\mathrm{d}I}{\mathrm{d}s} = \frac{1}{c}\frac{\omega_p^2}{\omega^2}\nu_{ei} I, \tag{2.1}$$

in which we recall that s is the curvilinear abscissa of the ray carrying the intensity I and ν_{ei} is the electron-ion collision frequency.

In this chapter, we will show a theoretical derivation of the inverse bremsstrahlung heating rate eq. (2.1) of a weakly coupled plasma. Since electron-ion are central in this phenomenon, the first step is the modelling of a single collision. Then, we will show how the effects of all binary collisions occuring in the plasma are summed up in the electron-ion collision frequency

ν_{ei}. Finally, we will demonstrate how the oscillating E-field of an external electromagnetic wave heats the plasma. The last subsection of this chapter will be concerned with the derivation of the Landau collision operator, upon which Fokker-Planck codes are often based. This explains why chapters 3 and 4 of this thesis use a simulation technique that is not based upon a Landau collision operator.

Though the theoretical developments of this chapter can mostly be found in textbooks [Delcroix & Bers, 1963, Eliezer, 2002, Reif, 2009], they are often fragmented. Furthermore, a detailled derivation of the heating rate will emphasize all the assumptions that have to be made to reach the usual formula of the inverse bremsstrahlung heating rate.

2.1 Binary collisions

The first step in the modelling of electron-ion collision is to consider a single binary collision event. We consider two point particles 1 and 2 of masses m_1 and m_2, charges q_1 and q_2, whose positions are referenced by $\boldsymbol{r}_1$ and $\boldsymbol{r}_2$. They are under the influence of a central potential $V_{12}(|\boldsymbol{r}|)$, where $\boldsymbol{r} = \boldsymbol{r}_1 - \boldsymbol{r}_2$.

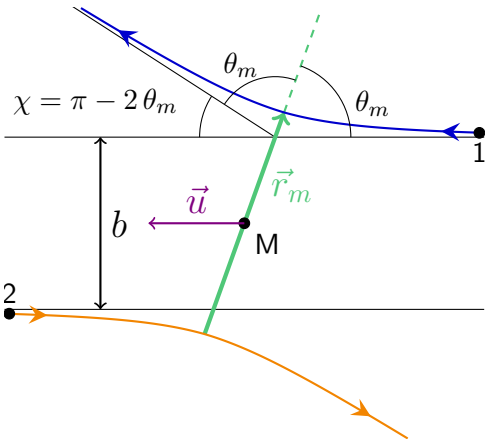

Figure 2.1: Schematic representation of the collision between two particles, 1 and 2. The points labelled 1 and 2 are the particle positions long before the collision. M is the center of mass of the two particles. The minimal distance r_m is characterized by an angle θ_m. In this illustration, the particles repulse each other (for example two electrons), and have the same mass.

The position of the center of mass of the system M is given by

$$\boldsymbol{r}_M = \frac{m_1\,\boldsymbol{r}_1 + m_2\,\boldsymbol{r}_2}{m_1 + m_2}. \tag{2.2}$$

Since the potential is central, the trajectories of both particles are contained inside a plane. A schematic representation of the collision which introduces useful notations is given in Fig. 2.1. In the center of mass reference frame, and using $\boldsymbol{r} = \begin{pmatrix} r\cos\theta \\ r\sin\theta \end{pmatrix}$,

$$\boldsymbol{v}_1 = -\frac{m_2}{m_1+m_2}\begin{pmatrix} \dot{r}\,\cos\theta - r\,\dot{\theta}\,\sin\theta \\ \dot{r}\,\sin\theta + r\,\dot{\theta}\,\cos\theta \end{pmatrix} \quad \text{and} \quad \boldsymbol{v}_2 = \frac{m_1}{m_1+m_2}\begin{pmatrix} \dot{r}\,\cos\theta - r\,\dot{\theta}\,\sin\theta \\ \dot{r}\,\sin\theta + r\,\dot{\theta}\,\cos\theta \end{pmatrix}. \tag{2.3}$$

Using, the reduced mass $m_{12} = m_1\, m_2/(m_1 + m_2)$, the total kinetic energy is therefore

$$\frac{1}{2}\, m_1\, v_1^2 + \frac{1}{2}\, m_2\, v_2^2 = \frac{1}{2}\, m_{12}\, \left(\dot{r}^2 + r^2\, \dot{\theta}^2\right), \tag{2.4}$$

and the angular momentum of the system is

$$(\boldsymbol{r}_1 - \boldsymbol{r}_M) \wedge \boldsymbol{v}_1 + (\boldsymbol{r}_2 - \boldsymbol{r}_M) \wedge \boldsymbol{v}_2 = m_{12}\, r^2\, \dot{\theta}. \tag{2.5}$$

Since both particles interact only via a central potential, angular momentum and mechanical energy are conserved during the collision. Long before the collision, $\theta \approx \sin\theta \approx b/r$, so $\dot{\theta} \approx -b\,\dot{r}/r^2$, where b is the impact parameter defined in Fig. 2.1. At $t = -\infty$, $r^2\,\dot{\theta}^2$ can be neglected in eq. (2.4) compared to u^2, where u is the magnitude of $\boldsymbol{u} = \dot{\boldsymbol{r}}(t = -\infty)$, the initial relative velocity. Thus, the mechanical energy is $m_{12}\, u^2/2$, and the angular momentum is $m_{12}\, b\, u$. Furthermore, still at $t = -\infty$, the particles are infinitely far from each other, in which situation the potential is conventionally taken equal to 0. The conservation of total energy and of the angular momentum are then given by

$$\frac{1}{2}\, m_{12}\, u^2 = \frac{1}{2}\, m_{12}\, \left(\dot{r}^2 + r^2\, \dot{\theta}^2\right) + V_{12}(r), \tag{2.6}$$

and

$$m_{12}\, b\, u = m_{12}\, r^2\, \dot{\theta}. \tag{2.7}$$

The conservation of angular momentum eq. (2.7) can then be used to find $\dot{\theta}$, which can then be inserted into eq. (2.6) to yield

$$\dot{r}^2 = u^2\, \left(1 - \frac{b^2}{r^2} - \frac{2\, V_{12}(r)}{m_{12}\, u^2}\right). \tag{2.8}$$

When $\dot{r}$ is negative, the particles are closing in on each other, this is the first part of the collision. When $\dot{r}$ is positive, the particles are going away from each other after the collision. When $\dot{r}$ is zero, the distance between both particles is at its lowest value, r_m, and $\theta = \theta_m$. The angle θ_m is also given by

$$\theta_m = \int_{r_m}^{\infty} \frac{\mathrm{d}\theta}{\mathrm{d}r}\, \mathrm{d}r = \int_{r_m}^{\infty} \frac{\dot{\theta}}{\dot{r}}\, \mathrm{d}r = \int_{r_m}^{\infty} \frac{b\, \mathrm{d}r}{r^2\, \sqrt{1 - \dfrac{b^2}{r^2} - \dfrac{2\, V_{12}(r)}{m_{12}\, u^2}}}. \tag{2.9}$$

The differential cross-section[1] σ is defined by the proportion of particles with impact parameter between b and $b + \mathrm{d}b$ and azimuth between ϕ and $\phi + \mathrm{d}\phi$ that are scattered in a solid angle $\mathrm{d}\Omega$, see Fig. 2.2. This means

$$\sigma = \frac{b\, \mathrm{d}b\, \mathrm{d}\phi}{\mathrm{d}\Omega}. \tag{2.10}$$

The trajectory of the particles long after the collision is at an angle χ with the trajectory they would have had, did they not interact. Since the deviation angle is given by $\chi = \pi - 2\,\theta_m$ (cf.

[1] The notation $\dfrac{\mathrm{d}\sigma}{\mathrm{d}\Omega}$ is sometimes used for the differential cross-section, and $\sigma = \int \dfrac{\mathrm{d}\sigma}{\mathrm{d}\Omega}\, \mathrm{d}\Omega$ then refers to the total cross-section. Using the notations of this work, the total cross-section is $\sigma_0 = \int \sigma\, \mathrm{d}\Omega$

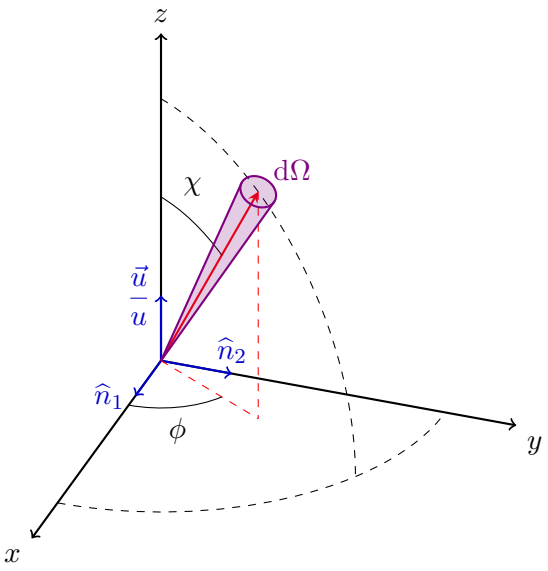

Figure 2.2: Spherical coordinates used for the definition of the cross-section. z is an axis along the direction of $\boldsymbol{u}$. x and y are two axes normal to z and to each other, with unit vectors $\widehat{\boldsymbol{n}}_1$ and $\widehat{\boldsymbol{n}}_2$ respectively. The deviation χ is the angle with $\boldsymbol{u}$, and ϕ is the azimuth. The differential solid angle $\mathrm{d}\Omega$ is defined from the angles χ and ϕ by $\mathrm{d}\Omega = \sin\chi\ \mathrm{d}\chi\ \mathrm{d}\phi$

Fig. 2.1), and since $\mathrm{d}\Omega = \sin\chi\ \mathrm{d}\chi\ \mathrm{d}\phi$, the differential cross-section can be written as

$$\sigma = \frac{b}{\sin\chi}\left(\frac{\partial b}{\partial\chi}\right)_u . \tag{2.11}$$

The relative velocity long after the collision $\widehat{\boldsymbol{u}}$ has the same magnitude u as before the collision, but is rotated by the deviation angle χ. Thus, the component along $\boldsymbol{u}$ of the velocity difference $\widehat{\boldsymbol{u}} - \boldsymbol{u}$ is $u\,(\cos\chi - 1)$. The fraction of the velocity difference that is not transferred to another direction is $(1 - \cos\chi)$. Integrating it over all possible collisions (*i.e.* all possible impact parameters and azimuth) yields the momentum transfer cross-section σ_1,

$$\sigma_1 = \int \sigma\,(1-\cos\chi)\ \mathrm{d}\Omega = 2\,\pi \int b\ \mathrm{d}b\,(1-\cos\chi) = 4\,\pi \int b\,\cos^2\theta_m\ \mathrm{d}b. \tag{2.12}$$

One case of particular interest in plasma physics is when particles interact via the Coulomb potential, $V_{12}(r) = q_1\,q_2/(4\,\pi\,\varepsilon_0\,r)$. In this case, the distance of closest approach r_m can be expressed directly, since it is the biggest root of the right side of eq. (2.8), so

$$r_m = \frac{q_1\,q_2}{4\,\pi\,\varepsilon_0\,m_{12}\,u^2} + \sqrt{\left(\frac{q_1\,q_2}{4\,\pi\,\varepsilon_0\,m_{12}\,u^2}\right)^2 + b^2}. \tag{2.13}$$

Then, θ_m is given by $\tan\theta_m = 1/\tan(\chi/2) = 4\,\pi\,\varepsilon_0\,m_{12}\,u^2\,b/q_1\,q_2$, which means

$$b = \frac{q_1\,q_2}{4\,\pi\,\varepsilon_0\,m_{12}\,u^2\,b\,\tan(\chi/2)}, \tag{2.14}$$

which can be inserted into eq. (2.11) to yield the differential cross section,

$$\sigma = \left(\frac{q_1\, q_2}{4\,\pi\,\varepsilon_0\, 2\, m_{12}\, u^2\, \sin^2(\chi/2)} \right)^2 . \tag{2.15}$$

This is why the momentum transfer cross section σ_1 can be recast as

$$\sigma_1 = \int_0^\infty \frac{b\ \mathrm{d}b}{1 + \left(\dfrac{4\,\pi\,\varepsilon_0\, m_{12}\, u^2\, b}{q_1\, q_2} \right)^2} . \tag{2.16}$$

This integral is divergent at $b = \infty$, for it scales as $\int \mathrm{d}b/b$, corresponding to a logarithmic divergence. This divergence is unphysical because, in a plasma, charges q_1 and q_2 evolve in a bath of other charged particles whose collective effect alter the simple view described here [Eliezer, 2002]. The simplest way to account for these collective effects is to set the upper bound of the integral to a certain value, $b_{\max}$. Physically, this means that when particles have an impact parameter greater than $b_{\max}$, they are assumed not to interact with each other, they are shielded from one another. A common choice for $b_{\max}$ in a plasma is the electron Debye length $\lambda_D = \sqrt{\varepsilon_0\, k_B T_e / n_e\, e^2}$. In this case,

$$\sigma_1 = 4\,\pi \left(\frac{q_1\, q_2}{4\,\pi\,\varepsilon_0\, m_{12}\, u^2} \right)^2 \ln \sqrt{1 + \left(4\,\pi\,\varepsilon_0\, \frac{m_{12}\, u^2\, b_{\max}}{q_1\, q_2} \right)^2} . \tag{2.17}$$

Additionally, the case $b = 0$ can also be pathological, in the opposite charges case. In this case, eq. (2.13) yields $r_m = 0$, which is problematic since the Coulomb potential diverges at $r_m = 0$. This happens because in using Coulomb potential, we have assumed that both particles are point-like, which is not true at very close range for ions due to un-ionized electrons cloud surrounding ions, and for electrons due to quantum effects. This has motivated the introduction of a second parameter $b_{\min}$, which replaces the lower bound of the integral in eq. (2.17). This yields

$$\sigma_1 = 4\,\pi \left(\frac{q_1\, q_2}{4\,\pi\,\varepsilon_0\, m_{12}\, u^2} \right)^2 \frac{1}{2} \ln \left[\frac{1 + \left(4\,\pi\,\varepsilon_0\, \dfrac{m_{12}\, u^2\, b_{\max}}{q_1\, q_2} \right)^2}{1 + \left(4\,\pi\,\varepsilon_0\, \dfrac{m_{12}\, u^2\, b_{\min}}{q_1\, q_2} \right)^2} \right] . \tag{2.18}$$

A common choice for $b_{\min}$ is the impact parameter $b_\perp$ that corresponds to $\chi = \pi/2$, or, since $\chi = \pi - 2\,\theta_m$, $\theta_m = \pi/4$ [Temko, 1957]. Inserting this into eq. (2.14) yields $b_\perp = q_1\, q_2 / 4\,\pi\,\varepsilon_0\, m_{12}\, u^2$, which can be inserted into eq. (2.18) to yield

$$\sigma_1 = 4\,\pi \left(\frac{q_1\, q_2}{4\,\pi\,\varepsilon_0\, m_{12}\, u^2} \right)^2 \ln \left(\frac{1}{\sqrt{2}} \sqrt{1 + \left(4\,\pi\,\varepsilon_0\, \frac{m_{12}\, u^2\, b_{\max}}{q_1\, q_2} \right)^2} \right) . \tag{2.19}$$

The choice of $b_{\min}$ and $b_{\max}$ has been discussed extensively in the literature [Filippov *et al.*, 2018, Lee & More, 1984, Skupsky, 1987]. Ways to resolve the divergence of the cross-section have also been proposed, for example by using a shielded potential [Liboff, 1959, Ordonez & Molina,

1994], by using the Lenard-Balescu collision operator [Balescu, 1960, Lennard, 1960], or by means of different techniques such as wave theory [Kihara & Aono, 1963] or dimensional continuation [Brown *et al.*, 2005].

To summarize, we just showed how divergence appears in the momentum transfer cross-section. Now we need to relate this cross section to the collision frequency that shows up in the inverse bremsstrahlung heating.

2.2 Emergence of the Coulomb logarithm in collision frequencies

Here, we show why the so called Coulomb logarithm appears in the derivation of the collision frequency. Following Baalrud [2012], we consider a uniform plasma containing two species labelled 1 and 2. The collision process between a particle of species 1 and a particle of species 2 is characterized by the differential cross-section σ and the solid angle of the collision Ω, defined from the deviation χ, and an azimuth ϕ, as described in the previous section and shown in Fig. 2.2. The momentum given by species 1 to species 2 is written

$$\boldsymbol{R}^{1-2} = \int_{\boldsymbol{v}_1} \mathrm{d}^3 v_1 \, m_1 \, \boldsymbol{v}_1 \, C_B(f_1,\, f_2), \tag{2.20}$$

where C_B is the Boltzmann collision operator, defined in a uniform plasma by

$$C_B(f_1,\, f_2) = n_1 \, n_2 \int_{\boldsymbol{v}_2} \int_{\Omega} \mathrm{d}^3 v_2 \; \mathrm{d}\Omega \, u \, \sigma \; \left(f_1(\widehat{\boldsymbol{v}}_1) \, f_2(\widehat{\boldsymbol{v}}_2) - f_1(\boldsymbol{v}_1) \, f_2(\boldsymbol{v}_2) \right), \tag{2.21}$$

in which f_1 and f_2 are the velocity distribution functions of species 1 and 2 respectively. Quantities with a hat correspond to the state well after the collision, and $\boldsymbol{u}$ is the relative velocity $\boldsymbol{v}_1 - \boldsymbol{v}_2$. The integration on the particle positions has already been performed, since the plasma is assumed to be uniform, and yielded the particle densities n_1 and n_2 as factors in eq. (2.21).

A derivation of the Boltzmann collision operator can be found in textbooks [Reif, 2009]. This derivation makes multiple hypothesis: (i) only binary collisions are considered, so collisions with three particles or more are neglected; (ii) any external force acting on the distribution f_1 has no effect on the scattering process; (iii) the variation of the velocity distribution functions is slow compared to the characteristic time of the scattering process; (iv) the positions of two particles are not correlated before the collision.

These assumptions are verified in weakly coupled plasmas, which are those of interest in ICF. However, in the context of inverse bremsstrahlung, *i.e.* with a laser electrical field as an external force, the modelling of the Coulomb logarithm can involve parameters of an external E-field of the laser (frequency, intensity), which violates hypothesis (ii).

There are also assumptions that have to be made on the scattering process itself. Indeed, the scattering process must conserve both momentum and energy. In the previous section, we considered that particles interacted via a potential during the collision, so this is verified. This can be used in eq. (2.20) to yield [Baalrud, 2012, Reif, 2009]

$$\boldsymbol{R}^{1-2} = n_1 \, n_2 \int \mathrm{d}^3 v_1 \; \mathrm{d}^3 v_2 \; \mathrm{d}\Omega \, m_1 \; (\widehat{\boldsymbol{v}}_1 - \boldsymbol{v}_1) \; \sigma \, u \, f_1(\boldsymbol{v}_1) \, f_2(\boldsymbol{v}_2). \tag{2.22}$$

When the differential cross-section σ is a function of u and the collision solid angle Ω only, such

as in the case of a Coulomb interaction eq. (2.15), the integration over $\boldsymbol{v}_1$ can be written over $\boldsymbol{u}$. To do so, the conservation of momentum $m_1\,\boldsymbol{v}_1 + m_2\,\boldsymbol{v}_2 = m_1\,\widehat{\boldsymbol{v}}_1 + m_2\,\widehat{\boldsymbol{v}}_2$ can be used in order to get $m_1\ (\widehat{\boldsymbol{v}}_1 - \boldsymbol{v}_1) = m_{12}\ (\widehat{\boldsymbol{u}} - \boldsymbol{u})$, where $m_{12} = m_1\,m_2/(m_1 + m_2)$. Thus,

$$\boldsymbol{R}^{1-2} = n_1\,n_2\,m_{12} \int \mathrm{d}^3u\ \mathrm{d}\Omega\,\sigma(u,\,\Omega)\,u\ (\widehat{\boldsymbol{u}} - \boldsymbol{u}) \int \mathrm{d}^3v_2\,f_1(\boldsymbol{u} + \boldsymbol{v}_2)\,f_2(\boldsymbol{v}_2). \tag{2.23}$$

We will now concentrate on the integration over Ω, that concerns only $\int \mathrm{d}\Omega\,\sigma(u,\,\Omega)\ (\widehat{\boldsymbol{u}} - \boldsymbol{u})$. Since $\widehat{\boldsymbol{u}}$ has the same magnitude as $\boldsymbol{u}$, but is rotated by an angle given by the deviation χ, it is possible to write $(\widehat{\boldsymbol{u}} - \boldsymbol{u})$ as $(\cos\chi - 1)\,\boldsymbol{u} + u\,\sin\chi\,\cos\phi\,\widehat{\boldsymbol{n}}_1 + u\,\sin\chi\,\sin\phi\,\widehat{\boldsymbol{n}}_2$, where $\widehat{\boldsymbol{n}}_1$ and $\widehat{\boldsymbol{n}}_2$ are unit vectors normal to $\boldsymbol{u}$ and to each other. Moreover, assuming σ does not depend on the azimuth ϕ, only the component of the integral along $\boldsymbol{u}$ remains,

$$\int \mathrm{d}\Omega\,\sigma(u,\chi)\ (\widehat{\boldsymbol{u}} - \boldsymbol{u}) = \int \mathrm{d}\Omega\,\sigma(u,\chi)\,(\cos\chi - 1)\,\boldsymbol{u} = -\boldsymbol{u}\,\sigma_1, \tag{2.24}$$

where σ_1 is the momentum transfer cross section that was defined in eq. (2.12). Furthermore, defining the cross-correlation of f_1 and f_2 by $F(\boldsymbol{u}) = \int \mathrm{d}^3v_2\,f_1(\boldsymbol{u} + \boldsymbol{v}_2)\,f_2(\boldsymbol{v}_2)$ allows eq. (2.23) to be recast as

$$\boldsymbol{R}^{1-2} = -n_1\,n_2\,m_{12} \int \mathrm{d}^3u\,\boldsymbol{u}\,u\,\sigma_1(u)\,F(\boldsymbol{u}). \tag{2.25}$$

To proceed any further, assumptions must be made on f_1 and f_2. In the context of inverse bremsstrahlung, a laser's periodic E-field is applied to the particles. The primary effect of this E-field is to induce a coherent oscillating motion of free electrons. Since all particles of one species have the same charge, they will all follow the same oscillation. Thus, the instantaneous velocity distribution is not centred, but drifted because of the oscillations. It therefore makes sense to consider drifted distributions, *i.e.* isotropic distributions with a drift velocity. The simplest case is to have both f_1 and f_2 be drifted Gaussian distribution,

$$f_1(\boldsymbol{v_1}) = \frac{1}{(2\,\pi\,v_{\mathrm{th1}}^2)^{3/2}}\,\exp\left(-\frac{|\boldsymbol{v} - \boldsymbol{v}_{\mathrm{d1}}|^2}{2\,v_{\mathrm{th1}}^2}\right), \quad f_2(\boldsymbol{v_2}) = \frac{1}{(2\,\pi\,v_{\mathrm{th2}}^2)^{3/2}}\,\exp\left(-\frac{|\boldsymbol{v} - \boldsymbol{v}_{\mathrm{d2}}|^2}{2\,v_{\mathrm{th2}}^2}\right) \tag{2.26}$$

where v_{th1} is the thermal velocity and $\boldsymbol{v}_{\mathrm{d1}}$ the drift velocity, respectively for species 2. In this case, F is also a Gaussian distribution, with thermal velocity $v_{\mathrm{th}} = \sqrt{v_{\mathrm{th1}}^2 + v_{\mathrm{th2}}^2}$, and drift velocity $\boldsymbol{v}_{\mathrm{d}} = \boldsymbol{v}_{\mathrm{d1}} - \boldsymbol{v}_{\mathrm{d2}}$. However, with other distribution shapes of interest as will be expanded on in chapter 4 with Langdon's Super-Gaussian [Langdon, 1980] for instance, F cannot be determined analytically, neither when f_1 and f_2 are both Super-Gaussian nor when one of them is Gaussian and the other Super-Gaussian.

Nevertheless, it is possible to take advantage of the fact that in a two component plasma, species 1 and 2 correspond to electrons and ions with a significant mass difference. The heavy ions can be considered almost motionless compared to the light electrons and therefore, the ion velocity distribution can be approximated by a Dirac distribution. In this case, F is simply the instantaneous electron velocity distribution, which is what we will be considering in the remainder of the reasoning.

More assumptions on F are necessary to carry on the computation of $\boldsymbol{R}^{1-2}$. In particular,

we will assume that, for a drift velocity $\boldsymbol{v}_\mathrm{d}$, there is a distribution f such that

$$F(\boldsymbol{u}) = f(|\boldsymbol{u} - \boldsymbol{v}_\mathrm{d}|, \theta, \phi) = f(|\boldsymbol{u} - \boldsymbol{v}_\mathrm{d}|, \theta), \tag{2.27}$$

where θ is the angle of $\boldsymbol{u}$ with $\boldsymbol{v}_d$, and ϕ is the azimuth, see Fig. 2.3. This leaves

$$\boldsymbol{R}^{1-2} = -n_1\, n_2\, m_{12} \int \mathrm{d}^3u\, \boldsymbol{u}\, u\, \sigma_1(u)\, f(|\boldsymbol{u} - \boldsymbol{v}_\mathrm{d}|, \theta). \tag{2.28}$$

Setting $\boldsymbol{w} = \boldsymbol{u} - \boldsymbol{v}_\mathrm{d}$ yields

$$\boldsymbol{R}^{1-2} = -n_1\, n_2\, m_{12} \int \mathrm{d}^3w\, (\boldsymbol{w} + \boldsymbol{v}_\mathrm{d})\, |\boldsymbol{w} + \boldsymbol{v}_\mathrm{d}|\, \sigma_1(|\boldsymbol{w} + \boldsymbol{v}_\mathrm{d}|)\, f(w, \theta). \tag{2.29}$$

We now use spherical coordinates as described in Fig. 2.3. The direction of $\boldsymbol{v}_\mathrm{d}$ is used as a reference (z axis in Fig. 2.3). The angle with $\boldsymbol{v}_\mathrm{d}$ is θ. The notation ϕ for the azimuth is kept from Fig. 2.2. Every factor only depends on w and θ, except for the direction factor $\boldsymbol{w} + \boldsymbol{v}_\mathrm{d}$, so only the component along $\boldsymbol{v}_\mathrm{d}$ will remain when integrating over the azimuth ϕ. This yields

$$\boldsymbol{R}^{1-2} = -2\,\pi\, n_1\, n_2\, m_{12}\, \boldsymbol{v}_\mathrm{d} \int \sqrt{w^2 + v_\mathrm{d}^2 + 2\, v_\mathrm{d}\, w\, \cos\theta}\, \left(1 + \frac{w}{v_\mathrm{d}}\cos\theta\right) \sigma_1\, f(w, \theta)\, w^2\, \sin\theta\, \mathrm{d}\theta\, \mathrm{d}w, \tag{2.30}$$

where σ_1 is a shorthand for $\sigma_1\left(\sqrt{w^2 + v_\mathrm{d}^2 + 2\, v_\mathrm{d}\, w\, \cos\theta}\right)$. To proceed further in the computation of $\boldsymbol{R}^{1-2}$, a specific cross-section must be used. Furthermore, the distribution must be independent of θ. This is a strong assumption that proved not to be correct in many situations investigated in our Classical Molecular Dynamics Simulation presented in chapter 4. However, this assumption is necessary to derive an analytical expression. With these assumptions,

$$\boldsymbol{R}^{1-2} = -8\,\pi^2\, n_1\, n_2\, m_{12}\, R_c^2\, v_\mathrm{th}^4\, \boldsymbol{v}_\mathrm{d} \int \frac{1 + \dfrac{w}{v_\mathrm{d}}\cos\theta}{u^3} \ln\left[\sqrt{\frac{1}{2} + \frac{1}{2}\left(\frac{b_\mathrm{max}\, u^2}{R_c\, v_\mathrm{th}^2}\right)^2}\right] f(w)\, w^2\, \mathrm{d}w\, \sin\theta\, \mathrm{d}\theta, \tag{2.31}$$

where $u = \sqrt{w^2 + v_\mathrm{d}^2 + 2\, v_\mathrm{d}\, w\, \cos\theta}$ and $R_c = q_1\, q_2 / 4\,\pi\,\varepsilon_0\, m_{12}\, v_\mathrm{th}^2$ is the Landau length, v_th being the thermal velocity of f, defined by $3v_\mathrm{th}^2 = 4\,\pi \int w^4\, f(w)\, \mathrm{d}w$.

2.2.1 Separate treatment of the Coulomb logarithm and the velocity distribution

The logarithmic term in the integral in eq. (2.31) is often treated separately from the rest, *i.e.* $\ln\left[\sqrt{\frac{1}{2} + \frac{1}{2}\left(\frac{b_\mathrm{max}\, u^2}{R_c\, v_\mathrm{th}^2}\right)^2}\right] = \ln\Lambda$ and $\ln\Lambda$ is assumed to be independent of w and θ, and is modelled separately. This makes the integrals in eq. (2.31) tractable. $\boldsymbol{R}^{1-2}$ can now be recast as

$$\boldsymbol{R}^{1-2} = -8\,\pi^2\, n_1\, n_2\, m_{12}\, R_c^2\, v_\mathrm{th}^4 \boldsymbol{v}_\mathrm{d} \ln\Lambda \int \frac{1 + \dfrac{w}{v_\mathrm{d}}\cos\theta}{\left(w^2 + v_\mathrm{d}^2 + 2\, v_\mathrm{d}\, w\, \cos\theta\right)^{3/2}} f(w)\, w^2\, \mathrm{d}w\, \sin\theta\, \mathrm{d}\theta. \tag{2.32}$$

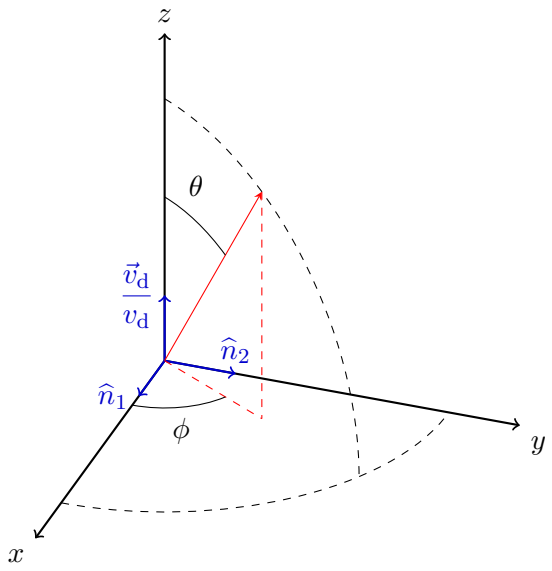

Figure 2.3: Spherical coordinates used in the computation of $\boldsymbol{R}^{1-2}$. z is an axis along the direction of $\boldsymbol{v}_\mathrm{d}$. x and y are two axes normal to z and to each other, with unit vectors $\widehat{\boldsymbol{n}}_1$ and $\widehat{\boldsymbol{n}}_2$. The angle with $\boldsymbol{v}_\mathrm{d}$ is θ, and ϕ is the azimuth.

The integral on θ can be performed, and yields

$$\boldsymbol{R}^{1-2} = -16\,\pi^2\,n_1\,n_2\,m_{12}\,R_c^2\,\frac{v_\mathrm{th}^4}{v_\mathrm{d}^3}\,\boldsymbol{v}_\mathrm{d}\,\ln\Lambda\int_0^{v_\mathrm{d}} f(w)\,w^2\,\mathrm{d}w. \tag{2.33}$$

The momentum collision frequency ν_{12} is defined as the proportion of the momentum density of species 1 that is given to species 2 through collisions, or

$$\boldsymbol{R}^{1-2} = -n_1\,m_1\,\nu_{12}\,\boldsymbol{v}_\mathrm{d}, \tag{2.34}$$

so that

$$\nu_{12} = 16\,\pi^2\,n_2\,\frac{m_{12}}{m_1}\,R_c^2\,\frac{v_\mathrm{th}^4}{v_\mathrm{d}^3}\,\ln\Lambda\int_0^{v_\mathrm{d}} f(w)\,w^2\,\mathrm{d}w \tag{2.35}$$

$$= \nu_{12}^0\,\ln\Lambda\,M(v_\mathrm{d},\,f), \tag{2.36}$$

where

$$\nu_{12}^0 = \frac{4\,\sqrt{2\,\pi}}{3}\,R_c^2\,v_\mathrm{th}\,n_2\,\frac{m_{12}}{m_1} \tag{2.37}$$

is the usual collision frequency prefactor, and

$$M(v_\mathrm{d},\,f) = 3\,(2\,\pi)^{3/2}\frac{v_\mathrm{th}^3}{v_\mathrm{d}^3}\int_0^{v_\mathrm{d}} f(w)\,w^2\,\mathrm{d}w, \tag{2.38}$$

is the absorption multiplier caused by the drift of f. This expression was obtained by Mulser *et al.* [2000], who applied it to an isotropic Gaussian distribution $f^G(v) = \exp(-v^2/2\,v_\mathrm{th}^2)/(2\,\pi\,v_\mathrm{th}^2)^{3/2}$,

which yields

$$M^G(\xi) = M(v_\mathrm{d},\, f^G) = \frac{3}{2}\left(\frac{\sqrt{2\,\pi}}{\xi^3}\,\mathrm{erf}\left(\frac{\xi}{\sqrt{2}}\right) - \frac{2}{\xi^2}\,\exp\left(-\frac{\xi^2}{2}\right)\right), \tag{2.39}$$

where $\mathrm{erf}(x) = 2/\sqrt{\pi}\int_0^x e^{-t^2}\,\mathrm{d}t$ is the error function, and $\xi = v_\mathrm{d}/v_\mathrm{th}$. $M^G(\xi)$ approaches 1 when ξ goes to 0, which yields the textbook collision frequency $\nu_{12} = \nu_{12}^0\,\ln\Lambda$.

The formula eq. (2.38) can also be applied to an isotropic Super-Gaussian distribution $f^{SG}(v) \propto \exp(-v^k)$ where $k > 0$ is the order of the Super-Gaussian. This yields

$$M^{SG}(\xi,\, k) = \frac{3\,(2\,\pi)^{3/2}}{4\,\pi\,\xi^3\,\Gamma(3/k)}\gamma\left(\frac{3}{k},\, \left(\frac{\xi}{\sqrt{3\Gamma(3/k)/\Gamma(5/k)}}\right)^k\right), \tag{2.40}$$

where Γ is Euler's gamma function, and $\gamma(s,\, x) = \int_0^x t^{s-1}\,e^{-t}\,\mathrm{d}t$ is the lower incomplete gamma function.

In a nutshell, the assumption for the sake of amenability is the separate modelling of the Coulomb logarithm that was necessary in order to obtain eq. (2.32). In the next subection, we will show that in the case of Gaussian distributions, this separate modelling is not necessary. This allows the derivation of a more consistent Coulomb logarithm that can be used in eq. (2.36).

2.2.2 Small drift compared to the thermal velocity: the Coulomb logarithm and velocity distribution can be treated together

In this part, we compute $\boldsymbol{R}^{1-2}$ from eq. (2.28) assuming an isotropic Gaussian distribution $f(|\boldsymbol{u} - \boldsymbol{v}_\mathrm{d}|\,,\theta) = \exp(-|\boldsymbol{u} - \boldsymbol{v}_\mathrm{d}|^2/2\,v_\mathrm{th}^2)/(2\,\pi\,v_\mathrm{th}^2)^{3/2}$. We will show that this strong assumption on the distribution allows to calculate $\boldsymbol{R}^{1-2}$ without separating the modelling of the Coulomb logarithm from the rest of the calculation as was necessary in the previous section. With a Gaussian distribution, eq. (2.28) is written

$$\boldsymbol{R}^{1-2} = -\frac{2\,\pi\,n_1\,n_2\,m_{12}}{(2\,\pi\,v_\mathrm{th}^2)^{3/2}}\int \mathrm{d}^3u\,\boldsymbol{u}\,u\,\sigma_1(u)\,\exp\left(-\frac{u^2 + v_\mathrm{d}^2 - 2\,u\,v_\mathrm{d}\,\cos\theta}{2\,v_\mathrm{th}^2}\right). \tag{2.41}$$

Since the only term that depends upon ϕ is $\boldsymbol{u}$, the integration over ϕ sums up to $\int \boldsymbol{u}\,\mathrm{d}\phi = 2\,\pi\,u\,\cos\theta\,\boldsymbol{v}_\mathrm{d}/v_\mathrm{d}$. The integration over θ can then be performed, and yield

$$\boldsymbol{R}^{1-2} = -\frac{2\,\pi\,n_1\,n_2\,m_{12}}{(2\,\pi\,v_\mathrm{th}^2)^{3/2}}\,\frac{\boldsymbol{v}_\mathrm{d}}{v_\mathrm{d}}\int v_\mathrm{th}^5\,\mathrm{d}\mu\,\mu^4\,\sigma_1(u)\,\frac{2}{\mu^2\,\xi^2}\,e^{-\frac{\mu^2+\xi^2}{2}}\,(\mu\,\xi\,\cosh(\mu\,\xi) - \sinh(\mu\,\xi)), \tag{2.42}$$

where $\mu = u/v_\mathrm{th}$ and $\xi = v_\mathrm{d}/v_\mathrm{th}$. The collision frequency ν_{12} can then be expressed as

$$\nu_{12} = \nu_{12}^0\,\frac{3}{4\,\pi\,R_c^2}\int \sigma_1(u)\,e^{-\frac{\mu^2+\xi^2}{2}}\left(\frac{\mu^3}{\xi^2}\,\cosh(\mu\,\xi) - \frac{\mu^2}{\xi^3}\,\sinh(\mu\,\xi)\right)\mathrm{d}\mu, \tag{2.43}$$

in which we recall $R_c = q_1\,q_2/4\,\pi\,\varepsilon_0\,m_1\,v_{\mathrm{th}}^2$ and $\nu_{12}^0 = 4\,\sqrt{2\,\pi}\,R_c^2\,v_{\mathrm{th}}\,n_2\,m_{12}/3\,m_1$. The trigonometric functions can be expanded in series to yield

$$\nu_{12} = \nu_{12}^0\,\frac{3}{2\,\pi\,R_c^2}\,e^{-\frac{\xi^2}{2}}\sum_{n=1}^{+\infty}\frac{n\,\xi^{2\,n-2}}{(2\,n+1)!}\int\sigma_1(u)\,\mu^{2\,n+3}\,e^{-\frac{\mu^2}{2}}\,\mathrm{d}\mu. \tag{2.44}$$

In the low laser intensity limit, $\xi = v_{\mathrm{d}}/v_{\mathrm{th}} \ll 1$, and so only the first term of the sum can be considered. Using the Coulomb momentum cross section eq. (2.19),

$$\nu_{12} = \nu_{12}^0\left[\sin\left(\frac{R_c}{2\,b_{\max}}\right)\left(\frac{\pi}{2} - \mathrm{Si}\left(\frac{R_c}{2\,b_{\max}}\right)\right) - \cos\left(\frac{R_c}{2\,b_{\max}}\right)\mathrm{Ci}\left(\frac{R_c}{2\,b_{\max}}\right) - \ln\sqrt{2}\right], \tag{2.45}$$

where $\mathrm{Si}(x) = \int_0^x \mathrm{d}t\,\sin(t)/t$ is the sine integral function, and $\mathrm{Ci}(x) = -\int_x^\infty \mathrm{d}t\,\cos(t)/t$ is the cosine integral function. This time, the logarithmic part of σ_1 has been kept in the integral eq. (2.44), as opposed to the method described for the transition between eq. (2.31) and eq. (2.32). A standard choice for $b_{\max}$ is the electron Debye length $\lambda_D = \sqrt{\varepsilon_0\,k_B T_e/n_e\,e^2}$ in which case $R_c/b_{\max}$ is the plasma coupling parameter $g = R_c/\lambda_D$. When the plasma is weakly coupled $g \ll 1$, a series expansion yields

$$\nu_{12} = \nu_{12}^0\left(\ln\left(\frac{\sqrt{2}\,e^{-\gamma}}{g}\right) + \mathcal{O}(g)\right), \tag{2.46}$$

in which γ is Euler's constant and we used the big O notation $\mathcal{O}$. Since $\sqrt{2}\,e^{-\gamma} \approx 0.794$, this is very close to other expressions found in the litterature, such as $\ln(0.765/g)$ obtained theoretically [Brown *et al.*, 2005, Kihara & Aono, 1963], or $\ln(1 + 0.7/g)$ obtained using Molecular Dynamic simulations [Dimonte & Daligault, 2008].

In a nutshell, assuming the distribution is Gaussian allows the exact Coulomb momentum cross-section to be used in order to derive a self consistent expression of the collision frequency and of the Coulombian logarithm without having to model it separately, as was needed in eq. (2.32). However, since the electron velocity distribution is known to be distorted by the laser E-field [Langdon, 1980, Milder *et al.*, 2021], we will have to resort to eq. (2.36) in order to take f into account in the modelling of the inverse bremsstrahlung heating rate.

2.3 Inverse bremsstrahlung heating rate

The average volumetric heating rate of electrons under the influence of an external E-field $\boldsymbol{E}$ is simply the Joule heating rate

$$\frac{3}{2}\,n_e\,\frac{\mathrm{d}k_B T_e}{\mathrm{d}t} = \boldsymbol{j}\cdot\boldsymbol{E}, \tag{2.47}$$

where $\boldsymbol{j} = -n_e\,e\,\boldsymbol{v}_e$ is the electron current density, $\boldsymbol{v}_e$ being the average electron velocity. In cases of interest, two forces are acting on these electrons: the periodic external E-field $\boldsymbol{E} = \boldsymbol{E}_0\,\cos\omega t$, and the collisions with ions, so that the evolution of the ensemble averaged velocity of electrons can be modelled as

$$m_e\,\frac{\mathrm{d}\boldsymbol{v}_e}{\mathrm{d}t} + m_e\,\nu_{ei}\,\boldsymbol{v}_e = -e\,\boldsymbol{E}_0\,\cos\omega t, \tag{2.48}$$

where we recall that ν_{ei} not only depends on the plasma parameters (Z, n_e, T_e), but also on v_e, as shown in eq. (2.36). Eq. (2.48) shows that $\boldsymbol{v}_e$ is always colinear to the E-field, so $\boldsymbol{j} \cdot \boldsymbol{E} = j\,E$. The equation on the average electron velocity eq. (2.48) can also be written using the current density,

$$\frac{\mathrm{d}\boldsymbol{j}}{\mathrm{d}t} = \varepsilon_0\,\omega_p^2\,\boldsymbol{E}_0\,\cos\omega t - \nu_{ei}\,\boldsymbol{j}, \tag{2.49}$$

in which $\omega_p^2 = n_e\,e^2/\varepsilon_0\,m_e$ is the plasma frequency. To determine $\boldsymbol{j}$, it is useful to recall that the plasmas of interest in this work are weakly coupled, $g \ll 1$, where $g = R_c/\lambda_D$ is the plasma coupling parameter, $R_c = Z\,e^2/4\,\pi\,\varepsilon_0\,k_B T_e$ being the Landau length and $\lambda_D = \sqrt{\varepsilon_0\,k_B T_e/n_e\,e^2}$ being the electron Debye length. This means that

$$\frac{\nu_{ei}}{\omega} = \frac{1}{3}\,\sqrt{\frac{2}{\pi}}\,g\,\sqrt{\frac{n_e}{n_c}}\,M(v_d,\,f)\,\ln\Lambda \ll 1, \tag{2.50}$$

in subcritical plasmas, and assuming the Coulomb logarithm and absorption multiplier are $\mathcal{O}(1)$. Since the time scale for the variation of $\boldsymbol{j}$ is ω, eq. (2.49) can be expanded using the small parameter ν_{ei}/ω, $\boldsymbol{j} = \boldsymbol{j}^0 + \boldsymbol{j}^1$, where $j^0\,\nu_{ei}/\omega$ is of the same order of magnitude as j^1, so $j^1 \ll j^0$. This yields

$$\frac{\mathrm{d}\boldsymbol{j}^0}{\mathrm{d}t} = \varepsilon_0\,\omega_p^2\,\boldsymbol{E}_0\,\cos\omega t, \tag{2.51}$$

$$\frac{\mathrm{d}\boldsymbol{j}^1}{\mathrm{d}t} = -\nu_{ei}\,\boldsymbol{j}^0, \tag{2.52}$$

and so

$$\boldsymbol{j}^0 = \varepsilon_0\,\frac{\omega_p^2}{\omega}\,\boldsymbol{E}_0\,\sin\omega t, \tag{2.53}$$

$$\frac{\mathrm{d}\boldsymbol{j}^1}{\mathrm{d}t} = -\nu_{ei}\,\varepsilon_0\,\frac{\omega_p^2}{\omega}\,\boldsymbol{E}_0\,\sin\omega t, \tag{2.54}$$

This can be inserted into eq. (2.47). Since the E-field is periodic, it makes sense to average the heating rate over one of its period. Finally,

$$\left\langle \frac{3}{2}\,n_e\,\frac{\mathrm{d}k_B T_e}{\mathrm{d}t} \right\rangle = \frac{\omega}{2\,\pi}\int_0^{2\,\pi/\omega} j\,E_0\,\cos\omega t\;\mathrm{d}t \tag{2.55}$$

$$= \frac{1}{2\,\pi}\int_0^{2\,\pi/\omega} \frac{\mathrm{d}j}{\mathrm{d}t}\,E_0\,\sin\omega t\;\mathrm{d}t \tag{2.56}$$

$$= \frac{1}{2\,\pi}\int_0^{2\,\pi/\omega} \varepsilon_0\,\omega_p^2\,E_0^2\,\sin\omega t\,\cos\omega t + \nu_{ei}\,\varepsilon_0\,\frac{\omega_p^2}{\omega}\,E_0^2\,\sin^2\omega t\;\mathrm{d}t \tag{2.57}$$

$$= n_e\,m_e\,v_{\mathrm{osc}}^2\,\frac{\omega}{2\,\pi}\int_0^{2\,\pi/\omega} \nu_{ei}(v_e(t))\,\sin^2\omega t\;\mathrm{d}t, \tag{2.58}$$

where $\boldsymbol{v}_{\mathrm{osc}} = e\,\boldsymbol{E}_0/m_e\,\omega$. The average velocity of the electrons is needed to evaluate the electron-ion collision frequency. It can be evaluated at zeroth order using $\boldsymbol{j}^0$ from eq. (2.53) as $\boldsymbol{v}_e = \boldsymbol{v}_{\mathrm{osc}}\,\sin\omega t$.

The most simple way to evaluate eq. (2.58) is simply to neglect the variation of ν_{ei} with v_e, and write $\nu_{ei} = \nu_{ei}^0\,\ln\Lambda$, where $\nu_{ei}^0 = 4\,\sqrt{2\,\pi}\,Z^2\,e^4\,n_i/(3\,\sqrt{m_e}(4\,\pi\,\varepsilon_0)^2(k_B T_e)^{3/2})$, and model $\ln\Lambda$

in such a way that it only depends on the plasma parameters. This yields

$$\left\langle \frac{3}{2} n_e \frac{\mathrm{d}k_B T_e}{\mathrm{d}t} \right\rangle = \frac{1}{2} n_e m_e v_{\mathrm{osc}}^2 \nu_{ei}^0 \ln\Lambda. \tag{2.59}$$

A more accurate way to evaluate the heating rate is to use eq. (2.36), $\nu_{12} = \nu_{12}^0 \ln\Lambda M(v_\mathrm{d}, f)$. The Coulomb logarithm is still modelled separately, even though it may depend on the drift velocity. Taking advantage of the fact M only depends on the magnitude of the drift, this yields

$$\left\langle \frac{3}{2} n_e \frac{\mathrm{d}k_B T_e}{\mathrm{d}t} \right\rangle = n_e m_e v_{\mathrm{osc}}^2 \nu_{ei}^0 \ln\Lambda \frac{2}{\pi} \int_0^{\pi/2} M(v_{\mathrm{osc}} \sin t, f) \sin^2 t \, \mathrm{d}t \tag{2.60}$$

$$= \frac{1}{2} n_e m_e v_{\mathrm{osc}}^2 \nu_{ei}^0 \ln\Lambda \bar{M}(v_{\mathrm{osc}}, f), \tag{2.61}$$

where $\bar{M}(v_{\mathrm{osc}}, f) = 4/\pi \int_0^{\pi/2} M(v_{\mathrm{osc}} \sin t, f) \sin^2 t \, \mathrm{d}t$ is the multiplier on the heating rate, to be compared with the modelling described by eq. (2.59). In the case where the electron velocity distribution f is a Gaussian, $\bar{M}$ can be computed analytically, and is given by

$$\bar{M}^G(\eta) = \frac{6}{\eta^2} \left({}_2F_2\left(\frac{1}{2}, \frac{1}{2}; 1, \frac{3}{2}; -\frac{\eta^2}{2}\right) - e^{-\frac{\eta^2}{4}} I_0\left(\frac{\eta^2}{4}\right) \right), \tag{2.62}$$

where $\eta = v_{\mathrm{osc}}/v_{\mathrm{th}}$, I_0 is the modified Bessel function of the first kind, and ${}_2F_2$ is a generalized hypergeometric function. Unfortunately, $\bar{M}^{SG} = \bar{M}(v_{\mathrm{osc}}, f^{SG})$ cannot be computed analytically. It can, however, be evaluated numerically as shown in Fig. 2.4, which compares M^G from eq. (2.39), M^{SG} from eq. (2.40), $\bar{M}^G$ from eq. (2.62) and $\bar{M}^{SG}$ for a range of $\eta = v_{\mathrm{osc}}/v_{\mathrm{th}}$. Clearly, $\bar{M}(\eta, f) \approx M(\eta, f)$ for small η, which is the expected result: at small oscillation amplitude, the averaging process does not have much of an impact on M.

In Fig. 2.4, it can be seen that the absorption multipliers, both instantaneous and cycle-averaged are independant of the shape of the distribution at high η. This seemingly weak dependance of the absorption multiplier on the distribution shape at high laser intensity might indicate that the anisotropic distribution shapes that are observed in our CMDS in chapter 4 at high laser intensity do not affect much the absorption multiplier.

At low η, the Gaussian absorption multiplier approaches 1, as described above. The Super-Gaussian absorption multiplier for $k = 5$ approaches 0.445, which is very close to Langdon's multiplier for $k = 5$. Indeed, in Langdon [1980]'s model, absorption is proportional to $f(0)$. Since the absorption multiplier uses the Gaussian case as a reference, it follows that the absorption multiplier should be $f(0)/f^G(0)$ to be consistent with Langdon's model. One of the key assumptions in this model is $\eta = v_{\mathrm{osc}}/v_{\mathrm{th}} \ll 1$, so this limit will be examined. Integrating the Taylor expansion of $f(w)$ at small w yields

$$\int_0^\xi f(w) w^2 \, \mathrm{d}w = \frac{\xi^3}{3} f(0) + \frac{\xi^4}{4} \partial_v f(0) + \mathcal{O}(\xi^5). \tag{2.63}$$

This can the be inserted into the definition of M eq. (2.38), and since $f^G(0) = (2\pi)^{-3/2}$,

$$M(\xi, f) = \frac{f(0)}{f^G(0)} + \frac{3}{4 f^G(0)} \xi \partial_v f(0) + \mathcal{O}(\xi^2). \tag{2.64}$$

Thus, for small ξ, $M(\xi, f) \approx f(0)/f^G(0)$, which explains why $M(0, f^{SG})$ is very close to the correction proposed by Matte *et al.* [1988] [2]

$$M_{\text{matte}}(k) = 1 - \frac{0.553}{1 + 0.27\left(\frac{1}{1.66}\left(\frac{3}{k-2} - 1\right)\right)^{1/0.724}}, \tag{2.65}$$

where k is the order of the Super-Gaussian f^{SG}.

All in all, we have showed how the inverse bremsstrahlung heating rate depends on the amplitude of the laser field and on the electron velocity distribution. The expression we derived, which was obtained by Mulser *et al.* [2000] is coherent with other expressions obtained from Fokker-Planck simulations [Langdon, 1980, Matte *et al.*, 1988]. However, the computation of M requires knowing the shape of the electron velocity distribution, which is not known in all situations. This is why we resorted to numerical simulations in order to confirm the validity of theoretical models and better characterize the shape of the electron velocity distribution when under the influence of a laser field. Before presenting the simulations we carried out in chapters 3 and 4, the next section will explain why Fokker-Planck simulations based on the Landau collision operator cannot fully capture the electron-ion collision frequency, which explains why we resorted to Molecular Dynamics simulations.

[2] Though this formula is not directly present in [Matte *et al.*, 1988], it can be obtained by extracting α from eq. (14) and inserting it into eq. (15), where both equation numbers refer to [Matte *et al.*, 1988]

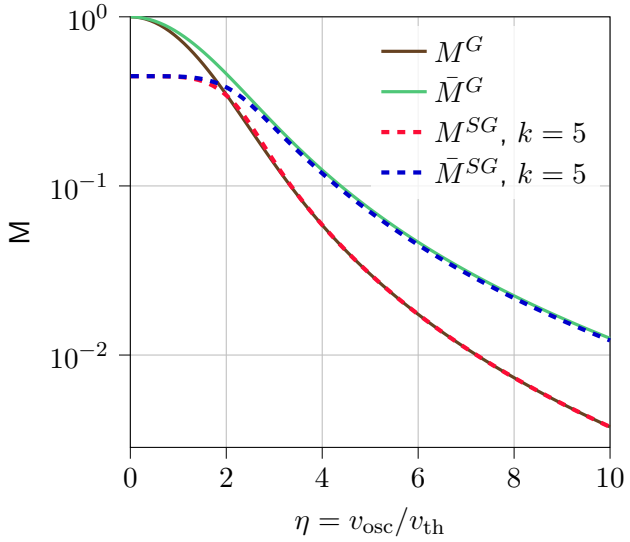

Figure 2.4: Instantaneous and cycle-averaged absorption multipliers for a Gaussian distribution and a Super-Gaussian ($k = 5$) distribution. At high η, the multiplier seems to be independant of the distribution shape. When η approaches 0, the cycle-averaged multipliers $\bar{M}^G$ and $\bar{M}^{SG}$ tend towards their instantaneous values, M^G and M^{SG} respectively. When $\eta = 0$, $M^G = 1$, since a non-drifted gaussian is our reference case, and $M^{SG} \approx 0.445$, which corresponds to Langdon's factor for k=5 [Langdon, 1980].

2.4 Landau collision operator

Most Fokker-Planck simulations [Ersfeld & Bell, 2000, Jones & Lee, 1982, Matte *et al.*, 1988], as well as theoretical models [Balescu, 1982, Chichkov *et al.*, 1992, Fourkal *et al.*, 2001, Langdon, 1980, Li & D., 1993, Porshnev *et al.*, 1993, 1996] dedicated to the study of non-Maxwellian behaviour of a plasma under the influence of a time varying E-field use the Landau collision operator, as opposed to the Boltzmann collision operator that was used in the previous sections. In this section, we will show how the Landau collision operator can be obtained from the Boltzmann collision operator and which assumptions are necessary. In particular, we will show that an expression of the Coulomb logarithm needs to be provided. Therefore, Fokker-Planck simulations cannot be used to get insight on the Coulomb logarithm, at variance with Classical Molecular Dynamic Simulations where the level of assumption is much lower and the trajectory of every particle is precisely described.

We recall the Boltzmann collision operator

$$C_B(f_1,\, f_2) = \int_{\boldsymbol{v}_2} \int_{\Omega} \mathrm{d}^3 v_2 \; \mathrm{d}\Omega \, \sigma(\boldsymbol{v}_1,\, \boldsymbol{v}_2 \to \widehat{\boldsymbol{v}}_1,\, \widehat{\boldsymbol{v}}_2)\, u \, \left(f_1(\widehat{\boldsymbol{v}}_1)\, f_2(\widehat{\boldsymbol{v}}_2) - f_1(\boldsymbol{v}_1)\, f_2(\boldsymbol{v}_2)\right), \tag{2.66}$$

where Ω is the solid angle of the collision, and $\boldsymbol{u} = \boldsymbol{v}_1 - \boldsymbol{v}_2$. The main assumption needed to derive the Landau collision operator is that collisions only slightly deviates the trajectory, *i.e.* the evolution of the velocity distribution is mainly a result of many small-angle of deviation collisions. This means that $\widehat{\boldsymbol{v}}_1$ is sufficiently close to $\boldsymbol{v}_1$ to use the Taylor expansion of f_1, and f_2. It is useful to notice that the conservation of momentum in a collision yields $m_1\,(\widehat{\boldsymbol{v}}_1 - \boldsymbol{v}_1) = -m_2\,(\widehat{\boldsymbol{v}}_2 - \boldsymbol{v}_2) = m_{12}\,(\widehat{\boldsymbol{u}} - \boldsymbol{u}) = m_{12}\,\Delta\boldsymbol{u}$. Additionally, we note $f_\alpha = f_\alpha\,(\boldsymbol{v}_\alpha)$, and $\widehat{f}_\alpha = f_\alpha\,(\widehat{\boldsymbol{v}}_\alpha)$

for $\alpha = 1, 2$, to clarify. The Taylor expansion of f_1 around $\boldsymbol{v}_1$ is

$$\widehat{f_1} = f_1 + \frac{m_{12}}{m_1}\,\Delta\boldsymbol{u}\cdot\partial_{\boldsymbol{v_1}} f_1 + \frac{m_{12}^2}{2\,m_1^2}\,(\Delta\boldsymbol{u}\otimes\Delta\boldsymbol{u}) : \boldsymbol{\Delta} f_1, \tag{2.67}$$

where $(\boldsymbol{X}\otimes\boldsymbol{Y})_{ij} = X_i\,Y_j$, $\boldsymbol{A} : \boldsymbol{B} = \sum_{i,j} A_{ij}\,B_{ij}$ and $(\boldsymbol{\Delta} f_1)_{ij} = \partial_{v_i v_j} f$ is the Laplacian of f_1. With the same expansion on f_2, it is possible to write

$$\widehat{f_1}\,\widehat{f_2} - f_1\,f_2 = m_{12}\,\Delta\boldsymbol{u}\cdot\boldsymbol{D} + \frac{m_{12}^2}{2}\,\Delta\boldsymbol{u}\otimes\Delta\boldsymbol{u} : \left[\left(\frac{1}{m_1}\,\partial_{\boldsymbol{v}_1} - \frac{1}{m_2}\,\partial_{\boldsymbol{v}_2}\right)\boldsymbol{D}\right] \tag{2.68}$$

where

$$\boldsymbol{D} = \frac{f_2}{m_1}\,\partial_{\boldsymbol{v}_1} f_1 - \frac{f_1}{m_2}\,\partial_{\boldsymbol{v}_2} f_2. \tag{2.69}$$

It is now possible to perform the integral on the collision solid angle. Indeed, only the differential cross section σ, and $\Delta\boldsymbol{u}$ depend on Ω. To perform the integral, we use the spherical coordinates described in Fig. 2.2 that are based on $\boldsymbol{u}$, χ the deviation angle from $\boldsymbol{u}$, and the azimuth ϕ. The differential cross-section σ usually does not depend on the azimuth. Therefore, the components of $\Delta\boldsymbol{u}$ normal to $\boldsymbol{u}$ will cancel when integrating over ϕ. The component of $\Delta\boldsymbol{u}$ along $\boldsymbol{u}$ is then $\boldsymbol{u}\,(\cos\chi - 1)$, and so

$$\int \mathrm{d}\Omega\,\Delta\boldsymbol{u}\,\sigma = -\boldsymbol{u}\int \mathrm{d}\Omega\,\sigma\,(1-\cos\chi) = -\boldsymbol{u}\,\sigma_1, \tag{2.70}$$

where σ_1 is the momentum transfer cross-section defined in eq. (2.12). In this same coordinate system,

$$\Delta\boldsymbol{u}\otimes\Delta\boldsymbol{u} = u^2\begin{pmatrix} (\cos\chi-1)^2 & (\cos\chi-1)\,\sin\chi\,\cos\phi & (\cos\chi-1)\,\sin\chi\,\sin\phi \\ (\cos\chi-1)\,\sin\chi\,\cos\phi & \sin^2\chi\,\cos^2\phi & \sin^2\chi\,\sin\phi\,\cos\phi \\ (\cos\chi-1)\,\sin\chi\,\sin\phi & \sin^2\chi\,\sin\phi\,\cos\phi & \sin^2\chi\,\sin^2\phi \end{pmatrix}. \tag{2.71}$$

Clearly, all the off-diagonal elements cancel out when integrated over ϕ. Additionally, the collisions were assumed to only slightly deviate the particles, so $(\cos\chi-1)^2 \approx 0$ et $\sin^2\chi \approx 2\,(1-\cos\chi)$ at the second order in χ, and thus

$$\int \mathrm{d}\Omega\,\sigma\,\Delta\boldsymbol{u}\otimes\Delta\boldsymbol{u} = u^2\,\sigma_1\begin{pmatrix}\mathbf{0} & 0 & 0\\ 0 & \mathbf{1} & 0\\ 0 & 0 & \mathbf{1}\end{pmatrix} = u^3\,\sigma_1\,\frac{u^2\,\boldsymbol{I}-\boldsymbol{u}\otimes\boldsymbol{u}}{u^3} = u^3\,\sigma_1\,\boldsymbol{w}, \tag{2.72}$$

where $\boldsymbol{w}$ is defined as $(u^2\,\boldsymbol{I}-\boldsymbol{u}\otimes\boldsymbol{u})\,/u^3$ and corresponds to the projection on the plane normal to $\boldsymbol{u}$, $\boldsymbol{I}$ being the identity matrix. The collision operator is now

$$C(f_1,\,f_2) = \int_{\boldsymbol{v}_2} \mathrm{d}^3 v_2\,\left[m_{12}\,u\,(-\sigma_1\,\boldsymbol{u})\cdot\boldsymbol{D} + \frac{m_{12}^2\,u}{2}(u^3\,\sigma_1\,\boldsymbol{w}) : \left[\left(\frac{1}{m_1}\,\partial_{\boldsymbol{v}_1} - \frac{1}{m_2}\,\partial_{\boldsymbol{v}_2}\right)\boldsymbol{D}\right]\right]. \tag{2.73}$$

It is useful to notice that $\partial_{\boldsymbol{u}} \cdot \boldsymbol{w} = -2\,\boldsymbol{u}/u^3$, so we substitute $\boldsymbol{u}$ by $-u^3\,\partial_{\boldsymbol{u}} \cdot \boldsymbol{w}/2$, yielding

$$C(f_1,\, f_2) = \frac{m_{12}}{2} \int_{\boldsymbol{v}_2} \mathrm{d}^3 v_2\, \sigma_1\, u^4 \left[(\partial_{\boldsymbol{u}} \cdot \boldsymbol{w}) \cdot \boldsymbol{D} + \frac{m_{12}}{m_1}\, \boldsymbol{w} : \partial_{\boldsymbol{v}_1} \boldsymbol{D} - \frac{m_{12}}{m_2}\, \boldsymbol{w} : \partial_{\boldsymbol{v}_2} \boldsymbol{D} \right]. \tag{2.74}$$

Since $\boldsymbol{w}$ only depends on $\boldsymbol{u}$, $(\partial_{\boldsymbol{v}_2} \cdot \boldsymbol{w}) = -(\partial_{\boldsymbol{u}} \cdot \boldsymbol{w}) = -(\partial_{\boldsymbol{v}_1} \cdot \boldsymbol{w})$. Using this and an integration by part on the last term of eq. (2.74) yield

$$C(f_1,\, f_2) = \frac{m_{12}}{2} \int_{\boldsymbol{v}_2} \mathrm{d}^3 v_2\, \sigma_1\, u^4 \left[(\partial_{\boldsymbol{v}_1} \cdot \boldsymbol{w}) \cdot \boldsymbol{D} + \frac{m_{12}}{m_1}\, \boldsymbol{w} : \partial_{\boldsymbol{v}_1} \boldsymbol{D} - \frac{m_{12}}{m_2}\, (\partial_{\boldsymbol{v}_1} \cdot \boldsymbol{w}) \cdot \boldsymbol{D} \right] \tag{2.75}$$

$$= \frac{m_{12}}{2} \int_{\boldsymbol{v}_2} \mathrm{d}^3 v_2\, \sigma_1\, u^4 \left[\left(1 - \frac{m_{12}}{m_2}\right) (\partial_{\boldsymbol{v}_1} \cdot \boldsymbol{w}) \cdot \boldsymbol{D} + \frac{m_{12}}{m_1}\, \boldsymbol{w} : \partial_{\boldsymbol{v}_1} \boldsymbol{D} \right] \tag{2.76}$$

$$= \frac{m_{12}^2}{2\,m_1} \int_{\boldsymbol{v}_2} \mathrm{d}^3 v_2\, \sigma_1\, u^4 \left[(\partial_{\boldsymbol{v}_1} \cdot \boldsymbol{w}) \cdot \boldsymbol{D} + \boldsymbol{w} : \partial_{\boldsymbol{v}_1} \boldsymbol{D} \right] \tag{2.77}$$

$$= \frac{m_{12}^2}{2\,m_1} \int_{\boldsymbol{v}_2} \mathrm{d}^3 v_2\, \sigma_1\, u^4\, \partial_{\boldsymbol{v}_1} \cdot (\boldsymbol{w}\boldsymbol{D}) \tag{2.78}$$

The case of interest here is when species 1 corresponds to electrons and species 2 to ions, with ions being much heavier than electrons. In this case, the second term of $\boldsymbol{D}$ can be neglected because $m_2 \gg m_1$, and ions are much slower than electrons, so $f_i \approx n_i\,\delta$ and $\boldsymbol{u} \approx \boldsymbol{v}_e$. Finally,

$$C(f_e) = \frac{n_i}{2}\, \sigma_1\,(v_e)\; v_e^4\, \partial_{\boldsymbol{v}_e} \cdot \frac{v_e^2\, \boldsymbol{I} - \boldsymbol{v}_e \otimes \boldsymbol{v}_e}{v_e^3}\, \partial_{\boldsymbol{v}_e} f_e, \tag{2.79}$$

where the notation $\sigma_1\,(v_e)$ emphasises that σ_1 depends on u which has been approximated by v_e here. The usual Landau collision operator is then obtained by using the Coulomb momentum cross-section eq. (2.19), in which the logarithmic term is treated as constant, like before, so $\sigma_1 = 4\,\pi\,(q_1\,q_2/m_{12}\,v_e^2)^2\,\ln\Lambda$, which yields

$$C(f_e) = 2\,\pi\,\frac{Z^2\,e^4\,n_i}{m_e^2}\,\ln\Lambda\,\partial_{\boldsymbol{v}_e} \cdot \frac{v_e^2\, \boldsymbol{I} - \boldsymbol{v}_e \otimes \boldsymbol{v}_e}{v_e^3}\, \partial_{\boldsymbol{v}_e} f_e. \tag{2.80}$$

This is the Landau collision operator that is the basis of what is used in Fokker-Planck codes. The precise expression may vary from code to code. It might also be based on a development of this operator in Legendre polynomials.

This calculation has shown why the momentum transfer cross-section has to be modelled in order to derive the Landau collision operator. We have shown in section 2.1 that this modelling requires modelling the potential between two particles, which is not straightforward in a plasma where both long-range collective effects and close-range effects have to be included. As a result, Fokker-Planck simulations that are based on eq. (2.80) cannot get insight on the Coulomb logarithm, which arises from σ_1. This is why we resorted to Classical Molecular Dynamics simulations, where collision processes are inherently taken into account.

Part II

Classical Molecular Dynamics Simulations

Chapter 3

Molecular Dynamics of low-Z plasmas

Contents

The following is the text of an article that was written during the thesis. It has been published by Physics of Plasmas (editor's pick) under the title "Classical molecular dynamic simulations and modeling of inverse bremsstrahlung heating in low Z weakly coupled plasmas" by R. Devriendt and O. Poujade, Physics of plasmas **29**, 073301 (2022) [Devriendt & Poujade, 2022].

Classical molecular-dynamics simulations (CMDS) have been conducted to investigate one of the main mechanism responsible for absorption of radiation by matter namely stimulated inverse bremsstrahlung. CMDS of two components plasmas (electrons and ions) for a large range of electron densities, electron temperatures, for ionization $Z = 1$, were carried out with 2 million particles using the code LAMMPS. A parameterized model (with 6 adjustable constants), which encompasses most theoretical models proposed in the past to quantify heating rate by stimulated inverse bremsstrahlung, serves as a reference for comparison to our simulations. CMDS results are precise enough to rule out elements of these past models such as coulomb logarithms depending solely on laser pulsation ω and not on intensity. The 6 constants of the parameterized model have been adjusted and the resulting model matches all our CMDS results and those of previous CMDS in the literature.

3.1 Introduction

Inverse bremsstrahlung (IB) is the process of absorption of a single photon by a free electron in the field of another particle (ion or neutral atom). It is the main source of absorption of laser light by matter for intensities less than 10^{16} W/cm^2. It is far from being the only effect responsible for laser absorption directly or indirectly. Non resonant ponderomotive effects (laser beam self-focusing, filamentation) or resonant ponderomotive effects (Brillouin, Raman, parametric decay and oscillating two-stream instabilities, two plasmon decay, Langmuir cascade, two phonon decay of phonon, etc) also contribute to absorption in their own way but IB is the most important.

This process of IB heating is modeled in several different ways in the extensive literature on the subject. Theoretical works are either based on a classical approach [Brantov *et al.*, 2003, Dawson & Oberman, 1962, Grinenko & Gericke, 2009, Johnston & Dawson, 1973, Jones & Lee, 1982, Landau & Teller, 1936, Mulser *et al.*, 2000, Silin, 1965, Skupsky, 1987] or upon a quantum approach[Brantov *et al.*, 2003, Grinenko & Gericke, 2009, Kull & Plagne, 2001, Moll *et al.*, 2012, Polishchuk & Meyer-Ter-Vehn, 1994, Rand, 1964, Schlessinger & Wright, 1979, Shima & Yatom, 1975, Silin & Uryupin, 1981, Skupsky, 1987]. In both cases, there does not seem to be a general agreement, and quantum model do not converge to the classical limit for vanishingly small values of $\hbar$. Few studies, such as [Brantov *et al.*, 2003, Bunkin *et al.*, 1973, Seely & Harris, 1973], even go so far as to take a critical look at some of them.

In order to challenge these theoretical results, numerical evaluations of IB heating has been carried out but mostly using Fokker-Planck (FP) simulations [Ersfeld & Bell, 2000, Le *et al.*, 2019, Matte *et al.*, 1984, Weng *et al.*, 2006, 2009]. These simulations require collision kernels to be specified which amounts to making assumptions at microscopic level.

Ab initio classical molecular dynamic simulation (CMDS) of IB are very few in the recent literature and this is one of the objective of this article, to strengthen the share of these CMDS with present high-performance-computing capabilities. The second objective is to provide a literal expression for the IB heating $\mathrm{d}(k_B T_e)/\mathrm{d}t$ and, as a corollary, for the electron-ion collision frequency in the IB process ν_{ei}^{IB} (there is no reason it should be the same as the electron-ion collision frequency within other mechanisms such as temperature relaxation ν_{ei}^{T} [Dimonte & Daligault, 2008] or velocity relaxation ν_{ei}^{V} [Shaffer & Baalrud, 2019], both of which will be described hereafter).

There are several different such expressions in the literature and we are now at a point where

it is possible to reliably discriminate these expressions by use of microscopic molecular dynamic simulations. Such a literal expression is of the essence when it comes to simulate the interaction of intense radiations with matter within complex flows using radiation-hydrodynamics codes [Lefebvre *et al.*, 2018, Marinak *et al.*, 2001, Zimmerman & Kruer, 1975], particle-in-cell codes [Derouillat *et al.*, 2018, Lefebvre *et al.*, 2003] or Fokker-Planck codes.

Most theoretical expressions of inverse-bremsstrahlung heating in the literature can be summarized in a single parameterized expression that will be presented in section 3.2. Numerical simulations dedicated to IB absorption in the literature will be presented in section 3.3. The classical modeling of a two component plasma described in our simulations and the description of our CMDS will be the subject of section 3.4 and section 3.5. Finally, results of our CMDS on situations without oscillating electric field will be compared to existing results [Dimonte & Daligault, 2008, Shaffer & Baalrud, 2019] to ascertain our simulation settings in section 3.6 and the determination of the adjustable constants of the parameterized model will be carried out in 3.7.

3.2 Theoretical modeling for inverse bremsstrahlung absorption in the literature

Classical solutions to this problem have been provided through different techniques in the literature. The oldest was by way of ballistic modeling as in Landau [Landau & Teller, 1936] or Mulser [Mulser *et al.*, 2000] where one considers the trajectory of one single electron in the field of a single screened scattering center. The second technique makes use of Vlasov equation, for irradiation frequencies near the plasma frequency, as in the work of Dawson, Oberman and Johnston [Dawson & Oberman, 1962, Dawson, 1964, Johnston & Dawson, 1973]. The last techniques consists in solving the Boltzmann equation with a Lenard-Balescu collision term in order to get a solution for a wider range of frequencies and intensities as in Silin's work [Silin, 1965]. This last method was also used by Jones and Lee [Jones & Lee, 1982] to discuss the evolution of the electron velocity distribution in a plasma heated by laser radiation. In a nutshell, these theoretical works all led to similar template formulas of the electron heating rate by inverse Bremsstrahlung

$$\frac{\mathrm{d}(k_B\,T_e)}{\mathrm{d}t} = \frac{2}{3n_e}\frac{\omega_p^2}{c\,\omega^2}\,\nu_{ei}^{\mathrm{IB}}\,I \tag{3.1}$$

where I and ω are respectively the radiation intensity and pulsation and ν_{ei}^{IB} is the electron-ion collision frequency for the IB process that is proportional to a Coulomb logarithm, $\ln(\Lambda_{\mathrm{ei}}^{\mathrm{IB}})$ as can be seen in the general formula eq. (3.2).

In this classical context, there is, of course, no dependence upon $\hbar$. All these analytical expressions have been derived assuming that electrons velocity distributions are Maxwellians. Collective effects are hidden in the Coulomb logarithm which is generically of the form $\ln(\Lambda) = \ln(b_{\max}/b_{\min})$ where, in the absence of irradiation ($I = 0$), $b_{\max}$ corresponds to the range of collective interactions (of order the Debye length $\lambda_D = \sqrt{\varepsilon_0 k_B T_e/e^2 n_e}$) and $b_{\min}$ corresponds to the shortest distance accessible to these charged particles (of order either the closest distance of approach, also known as the Landau length $R = Z\,e^2/4\pi\varepsilon_0\,k_B T_e$, or the de Broglie length). The fuzziness of the expression of $\ln(\Lambda)$ is characteristic of theoretical calculations or reasonings

where collective effects of all particles on all other is not properly addressed from first principles and relies on the assumption that it can, in a sense, be captured by studying the motion of one electron around one ion screened by the mean field of all other charged particles (all other electrons and ions) which is largely disputable.

The Coulomb logarithm in the absence of laser irradiation is well known for the temperature relaxation and velocity relaxation. It has been derived from first principles using dimensional regularization [Brown *et al.*, 2005] and was confirmed to a very good accuracy by CMDS [Dimonte & Daligault, 2008, Shaffer & Baalrud, 2019]. On the contrary, for a plasmas submitted to laser irradiation, none of the theoretical studies listed in previous sections [Brantov *et al.*, 2003, Dawson & Oberman, 1962, Johnston & Dawson, 1973, Jones & Lee, 1982, Landau & Teller, 1936, Mulser *et al.*, 2000, Silin, 1965, Skupsky, 1987] give any precise formulation of $\ln(\Lambda)$ apart from the generic $\ln(b_{\max}/b_{\min})$. Nevertheless, interesting suggestions have been pushed forward that can be put to the test of microscopic simulations.

Here we propose a parameterized formulation of the inverse-Bremsstrahlung electron-ion collision frequency with six constants, $(\boldsymbol{C_{abs}}, \boldsymbol{\eta}, \boldsymbol{\epsilon_\ell}, \boldsymbol{C_\ell}, \boldsymbol{\eta_\ell}, \boldsymbol{\delta})$ which correspond to variations found in the literature, to be adjusted by CMDS

$$\nu_{ei}^{IB} = \boldsymbol{C_{abs}}\, \nu_0[n_e, T_{\rm eff}(\boldsymbol{\eta}), Z]\, \ln(\Lambda_{ei}^{IB}), \tag{3.2}$$

$$\nu_0[n_e, T_e, Z] = \frac{4\sqrt{2\pi}\, e^4}{3\sqrt{m_e}\,(4\pi\epsilon_0)^2} \frac{n_e\, Z}{(k_B T_e)^{3/2}}, \tag{3.3}$$

$$T_{\rm eff}(x) = T_e + x\ m_e\, v_E^2/k_B, \tag{3.4}$$

$$\Lambda_{ei}^{IB} = \left[\boldsymbol{\epsilon_\ell} + \boldsymbol{C_\ell}\, \frac{4\,\pi\,\varepsilon_0^{\frac{3}{2}}\,(k_B T_{\rm eff}(\boldsymbol{\eta_\ell}))^{3/2}}{Z\, e^3\, \sqrt{n_e}}\right] \left(\frac{\omega_p}{\omega}\right)^{\boldsymbol{\delta}}, \tag{3.5}$$

where

$$v_E^2 = \left(\frac{e\tilde{E}}{m_e\omega}\right)^2 = \frac{e^2\,(I\,\lambda^2)}{2\,\pi^2\,\varepsilon_0\,c^3\,m_e^2} \tag{3.6}$$

is the quiver velocity which is the maximum velocity of the oscillating motion of free electrons due to the electric field time variation assumed to be monochromatic and linearly polarized of the form $\boldsymbol{E(t)} = \tilde{E}\, cos(\omega\, t + \Phi)\, \boldsymbol{n}$ where $\boldsymbol{n}$ is a unit vector along the polarization direction (in section 3.7.2 other polarizations will be considered).

The usual classical value of $\Lambda = b_{\max}/b_{\min}$ given by the ratio of the Debye length λ_D and the Landau length R is

$$\Lambda = \frac{4\,\pi\,\varepsilon_0^{\frac{3}{2}}\,(k_B T_{\rm e})^{3/2}}{Z\, e^3\, \sqrt{n_e}}. \tag{3.7}$$

It is found in eq. (3.5) that can be recast as

$$\Lambda_{ei}^{IB} = \left[\boldsymbol{\epsilon_\ell} + \boldsymbol{C_\ell}\, \frac{b_{\max}}{b_{\min}}\right] \left(\frac{\omega_p}{\omega}\right)^{\boldsymbol{\delta}} \tag{3.8}$$

and where T_e should be replaced by $T_{\rm eff}$ defined by eq. (3.4). The usual classical value of Λ is

recovered if one set $\boldsymbol{\epsilon_\ell} = 0$, $\boldsymbol{C_\ell} = 1$ and $\boldsymbol{\delta} = 0$.

The advantage of this parameterized formulation is that comparison with results of the literature can be made easier. In the following table A, values of these six parameters for different references in the literature are compared in various regimes

Ref	Validity	C_{abs}	η	ϵ_ℓ	C_ℓ	η_ℓ	δ
[Dawson & Oberman, 1962], [Johnston & Dawson, 1973]	LiHf	1	0	0	1	0	1
[Silin, 1965]	LiLf	1	0	0	1	0	0
[Silin, 1965]	LiHf (see section 3.9)	1	0	0	1	0	1
[Silin, 1965]	HiLf	(a)	0.221	0	1	0	0
[Jones & Lee, 1982]	Hi	(b)	0.221	0	1	0	1
[Skupsky, 1987]	Hf	1	0	0	1	0	1
[Mulser, 2020]	Hf	1	-	0	1	1/4	1
[Mulser *et al.*, 2000]	Hf	1	-	0	1	1	1
[Brantov *et al.*, 2003]	Hf	1	1/6	0	1	0	1
[Dimonte & Daligault, 2008], [Daligault & Dimonte, 2009]	$I = 0$	1	0	1	0.7	0	0

Table A: In this table, L and H stand for Low and High, i and f stand for intensity and frequency (for example, LiHf means Low intensity High frequency). This is an illustration of the fact that there are many different classical models in the literatures (different constants), and the list is not exhaustive. (a) grows like $(\ln(v_E/2v_{\text{th}})+1)$ where $v_{\text{th}} = \sqrt{k_B T_e/m_e}$, (b) grows like $(\ln(v_E/v_{\text{th}}))$. More details on the constants reported in this table can be found in section 3.10.

In the remainder of this chapter, the goal is to use molecular dynamic simulations to reach clear conclusions regarding values of these constants in order to discriminate between these models.

3.3 Numerical simulations dedicated to inverse bremsstrahlung absorption in the literature

In the molecular dynamic simulations described in this paper, a plasma is described at the atomic level. Every particles of a plasma, electrons and ions, are described classically by their position and velocity and evolve as time goes by with Newton's first law.

The physical quantities we are interested in – the electron-ion frequency, and in particular, the so called Coulomb logarithm that describes the manifestation of collective effects within the plasma – depend on two length scales that, in the context of weakly coupled plasma, are different by orders of magnitude. They are commonly called $b_{\min}$ and $b_{\max}$ and correspond, for the former, to the smaller distances of approach between electron and ions (a two-body effect) and, for the latter, to the Debye length (a collective effect). Therefore, in order to simulate these collisions and measure the Coulomb logarithm, it is of paramount importance to describe both scales precisely. Only molecular dynamics simulations allow for such a description. In the best case scenario, PIC simulations capture Debye length, $b_{\max}$, but under no circumstances can they capture $b_{\min}$.

In the literature, numerical simulations dedicated to inverse bremsstrahlung fall into three categories : particle-in-cell simulations (PIC), Fokker-Planck simulations (FPS) and molecular

dynamic simulations (either quantum molecular dynamic simulations, QMDS, or classical molecular dynamic simulations, CMDS).

In the context of inverse Bremsstrahlung, FPS have mostly been used to assess the effect of the laser on the free electron distribution [Weng *et al.*, 2006, 2009] which could turn from Maxwellian to super Gaussian of order 5 [Langdon, 1980] when the electron-electron collision frequency is much less that electron-ion collision frequency so that electron-electron collisions are not frequent enough to preserve the equilibrium shape. FP codes resolve the Boltzmann equation for single-particle velocity distribution function but it is well known that the collision source term in this equation depends on the two-particle distribution function which in turn depends on the three-particle distribution function and so on. This is the BBGKY hierarchy problem. In order to get a practical collision term it is mandatory, in this context of FP simulations, to make assumptions on the closure of this collision term [Langdon, 1980]. Therefore, these FP simulations are not able to let us gain full insight on microscopic quantities, such as collision-frequency or absorption, for their results rely heavily on the assumptions made on these very processes. PIC simulations are also plagued with the same issues.

The first CMDS in the context of IB [Pfalzner & Gibbon, 1998] was carried out for strongly coupled plasmas and high intensity drive (non linear) because it is a situation that does not require to many particles (between 20000 and 40000 limited by the computational power back in 1998) to get proper results. Pfalzner and Gibbon were able to produce deformation of the free electron distribution as predicted by Langdon [Langdon, 1980], though not in Langdon's condition which is $Z \gg 1$, and heating rate for $Z = 1$ for a coupled plasma of $\Gamma = 0.1$ and for v_E/v_{th} from 0.2 to 10.

In [David *et al.*, 2004], David, Spence and Hooker carried out many CMDS (with approximately 16000 particles) resulting in several points of heating rate (dT_e/dt) versus laser intensity (from 10^{12} to 10^{17} W/cm^2) for different plasma states (n_e, T_e) and compared their results to Polishchuk and Meyer-Ter-Vehn's quantum model [Polishchuk & Meyer-Ter-Vehn, 1994] but had to propose an alternative expression to get an agreement. We tested these numerical results against our parameterized model and showed that they are in agreement with our classical model.

The response of moderately to strongly coupled plasmas to a time varying electric field solicitation was studied using CMDS [Morozov *et al.*, 2005]. In order to mimic quantum behaviors, effective potentials, such as Deutsch or Kelbg potentials, were used as an alternative to Coulomb potential. These potentials were not meant to avoid spurious numerical effects, as in [Kuzmin & O'Neil, 2002] because of the divergent nature of the Coulomb potential at vanishingly small radii, but they depended on De-Broglie wavelengths in order to capture, in an effective way, the quantum delocalization of particles that are classically described as point-like.

Although not directly related to IB, CMDS reported in [Daligault & Dimonte, 2009, Dimonte & Daligault, 2008] were the starting point of this work and are relevant to our parameterized model. These articles report on CMDS used to measure $\ln(\Lambda_{ei}^T)$ with respect to a parameter g (which is nothing else than $\Gamma^{2/3}$ where Γ is the plasma parameter). An almost perfect agreement was found when compared to the BPS theory [Brown *et al.*, 2005]. For the sake of completeness, we have found the same agreement with our own CMDS against Dimonte and Daligault's [Daligault & Dimonte, 2009, Dimonte & Daligault, 2008] and against BPS (cf. Fig. 3.4 in the present article). The analytical expression of the electron-ion collision frequency in the context

of temperature relaxation is

$$\nu_{ei}^{T} = \nu_0[n_e, T_e, Z]\ \ln(\Lambda_{ei}^{T}), \tag{3.9}$$

$$\Lambda_{ei}^{T} = 1 + 0.7\,\frac{4\,\pi\,\varepsilon_0^{\frac{3}{2}}\,(k_B T_e)^{3/2}}{Z\,e^3\,\sqrt{n_e}}, \tag{3.10}$$

which, in the parameterized formalism, would correspond to $C_{\text{abs}} = 1$, $\eta = \eta_\ell = 0$ (for there is no quiver velocity in this context), $\epsilon_\ell = 1$ and $C_\ell = 0.7$.

In [Shaffer & Baalrud, 2019], Shaffer and Baalrud carried out velocity relaxation CMDS and found that the symmetry of charge was broken on the collision frequency at moderately to strong coupling. They found that for weakly coupled plasmas, CMDS with ions and positrons (positively charged electrons) and CMDS with ions and electrons (with statistically equivalent initial conditions) will evolve in a similar manner (statistically speaking). This is something we have found with or without electric field in our own CMDS. We have also checked that in the context of velocity relaxation, $\nu_{ei}^{V}(g) = \nu_{ei}^{T}(g)$ which means, in weakly coupled plasmas, from a CMDS stand point that $\Lambda_{ei}^{T} = \Lambda_{ei}^{V}$ (cf. Fig. 3.4 in the present article).

In this article, we will only deal with Z=1 plasmas. Higher Z plasmas will be the subject of a future publication where the velocity distribution alteration, as it was first predicted by Langdon [Langdon, 1980], will be central.

3.4 Classical modelling of a two component plasma

3.4.1 Equations of motion

Describing a classical plasma consists in solving the classical equations of motions for all particles in the plasma submitted to their mutual Coulomb interactions. In the actual simulations, a soft core Coulomb potential as been used (instead of the $1/r$ potential) to avoid numerical problems, whose discussion is deferred to section section 3.5.2 (Simulations Settings), without affecting physical results.

As long as the velocities involved are much less than the celerity of light c, the generated B-field is not strong enough to counteract onto the motion. In the context of inverse-Bremsstrahlung, one has to add the effect of an external varying electric field (corresponding to the laser). One can also neglect the electric field of the black-body radiation. Therefore, the equations of motions are as follow

$$m_e\,\frac{\mathrm{d}\boldsymbol{v}_{\mathrm{e}}^{(\alpha)}(t)}{\mathrm{d}t} = -\frac{e^2}{4\pi\varepsilon_0}\sum_{\beta\neq\alpha}\frac{\boldsymbol{n}_{\alpha\beta}}{|\boldsymbol{r}_{\mathrm{e}}^{(\alpha)} - \boldsymbol{r}_{\mathrm{e}}^{(\beta)}|^2} + \frac{Z\,e^2}{4\pi\varepsilon_0}\sum_{b}\frac{\boldsymbol{n}_{\alpha b}}{|\boldsymbol{r}_{\mathrm{e}}^{(\alpha)} - \boldsymbol{r}_{\mathrm{i}}^{(b)}|^2} - e\,\boldsymbol{E}(\boldsymbol{r}_{\mathrm{e}}^{(\alpha)}(t), t), \tag{3.11}$$

$$m_i\,\frac{\mathrm{d}\boldsymbol{v}_{\mathrm{i}}^{(a)}(t)}{\mathrm{d}t} = \frac{Z\,e^2}{4\pi\varepsilon_0}\sum_{\beta}\frac{\boldsymbol{n}_{a\beta}}{|\boldsymbol{r}_{\mathrm{i}}^{(a)} - \boldsymbol{r}_{\mathrm{e}}^{(\beta)}|^2} - \frac{Z^2\,e^2}{4\pi\varepsilon_0}\sum_{b\neq a}\frac{\boldsymbol{n}_{ab}}{|\boldsymbol{r}_{\mathrm{i}}^{(a)} - \boldsymbol{r}_{\mathrm{i}}^{(b)}|^2} + Z\,e\,\boldsymbol{E}(\boldsymbol{r}_{\mathrm{i}}^{(a)}(t), t), \tag{3.12}$$

where m_e and m_i are the mass respectively of one electron and one ion (only one population considered), Z is the charge of an individual ion ($+Z\,e$), $\boldsymbol{r}_{\mathrm{e}}^{(\alpha)}$ and $\boldsymbol{v}_{\mathrm{e}}^{(\alpha)}$ are the position and velocity of electrons (labeled with greek letters α, β, $\cdots$) and $\boldsymbol{r}_{\mathrm{i}}^{(a)}$ and $\boldsymbol{v}_{\mathrm{i}}^{(a)}$ are the position and velocity of ions (labeled with roman letters for a, b, $\cdots$). Unit vectors $\boldsymbol{n}_{xy}$ are directed

from particle (x) to particle (y) (where x and y can be the label of an electron or of an ion). These are the exact equations taken into account in the forthcoming classical molecular dynamic simulations (CMDS) of a classical two components plasma.

3.4.2 Nondimensionalization of the equations of motion for electrons

The following discussion is purely theoretical and aims to determine the important dimensionless parameters of the problem.

Owing to the mass difference between electrons and ions, $m_e \ll m_i$, the electrons can be assumed to collide on immobile ions to a very good approximation as long as

$$k\,T_i/m_i \ll k\,T_e/m_e. \tag{3.13}$$

In this limit, for theoretical purposes only and for the following reasoning, ions positions ($\boldsymbol{r}_\mathrm{i}$) can be considered frozen (time independent) in eq. (3.11). Keep in mind that our CMDS resolves both eqs. (3.11) and (3.12) without any approximations.

The characteristic geometrical length scale of a plasma is the typical distance between ions ℓ, the characteristic velocity is the thermal velocity v_th and therefore the typical duration τ should be such that

$$\ell = n_i^{-1/3}, \tag{3.14}$$

$$v_\mathrm{th} = \left(\frac{k_B\,T_e}{m_e}\right)^{\frac{1}{2}}, \tag{3.15}$$

$$\tau = \frac{\ell}{v_\mathrm{th}}, \tag{3.16}$$

where n_i is the ion density. Therefore, if one rescales lengths with ℓ and velocities with v_th, every plasmas will end up with typical distances between ions equal 1 and velocity distribution of electrons width of 1 as well. What happens to other length scales, such as those related to e-e, i-i and e-i radial distributions functions, or time scales such as inverse of collision frequencies, depends entirely upon non dimensional parameters to be found in the remainder of this section.

The electric field is assumed to be a pure monochromatic oscillation with pulsation $\omega = 2\,\pi\,c/\lambda$ (where λ is the actual wavelength of the laser) and it is further assumed to be spatially uniform. This is compatible with our goal to evaluate, in a numerical experiment, values of electron-ion frequency in IB processes which are local physical quantities. Assuming the electric field is uniform amount to saying that the vacuum celerity of light is infinite. Indeed, if ω is fixed and $c = +\infty$ therefore $\tilde{k} = \omega/c = 0$ that is to say, the wave length in this limit of c, $\tilde{\lambda} = +\infty$. Have we had less particles in our CMDS we could have claimed that the actual laser wave length, λ, is much larger than the simulation domain size L but this is not quite correct for 10^6 particles when one explores electronic densities as low as 10^{18} cm^{-3} for L becomes as large as 500 nm. We will consider that the actual $\boldsymbol{E}(\boldsymbol{x}, t)$ only depends on t within the restricted simulation domain (the electric field is spatially uniform within that simulation domain). This is the same hypothesis made by all theoretical developments to model inverse bremsstrahlung absorption [Brantov *et al.*, 2003, Dawson & Oberman, 1962, Johnston & Dawson, 1973, Jones & Lee, 1982, Landau & Teller, 1936, Mulser *et al.*, 2000, Silin, 1965, Skupsky, 1987]. Finally, the polarization can be either linear,

elliptical or circular such that

$$\boldsymbol{E}(t) = E_1 \cos(\omega\, t)\, \boldsymbol{n_1} + E_2 \sin(\omega\, t)\, \boldsymbol{n_2}\,, \tag{3.17}$$

with $\boldsymbol{n_1}$ and $\boldsymbol{n_2}$ two orthonormal vectors perpendicular to the direction of propagation.

Therefore, if $R = \ell\,\tilde{R}$, $r = \ell\,\tilde{r}$, $v = v_{\text{th}}\,\tilde{v}$, $t = \tau\,\tilde{t}$ (where $\tau = \ell/v_{\text{th}}$) and $E = (2\,I/c\,\varepsilon_0)^{1/2}\,\tilde{E}$, eq. (3.11) can be recast as

$$\frac{\mathrm{d}\tilde{\boldsymbol{v}}_{\text{e}}^{(\alpha)}}{\mathrm{d}\tilde{t}} = g_{\text{coul}} \left[\frac{1}{Z} \sum_{\beta\neq\alpha} \frac{\boldsymbol{n}_{\alpha\beta}}{|\tilde{\boldsymbol{r}}_{\text{e}}^{(\alpha)} - \tilde{\boldsymbol{r}}_{\text{e}}^{(\beta)}|^2} - \sum_b \frac{\boldsymbol{n}_{\alpha b}}{|\tilde{\boldsymbol{r}}_{\text{e}}^{(\alpha)} - \tilde{\boldsymbol{r}}_{\text{i}}^{(b)}|^2} \right] + g_{\text{osc}}\, \tilde{\boldsymbol{E}}(g_\omega\, \tilde{t}), \tag{3.18}$$

where

$$g_{\text{coul}} = \frac{Z\, e^2\, n_i^{1/3}}{4\,\pi\varepsilon_0\, k\, T_e}, \tag{3.19}$$

$$g_{\text{osc}} = \frac{e}{n_i^{1/3}\, k\, T_e} \sqrt{\frac{2\,I}{c\,\varepsilon_0}}, \tag{3.20}$$

$$g_\omega = \omega\,\tau. \tag{3.21}$$

This very simple analysis shows that plasmas with different temperatures, densities, laser sources may look different but as long as they have the same Z, g_{coul}, g_{osc} and g_ω, they are similar, that is to say, they will evolve identically when rescaled by the right length (ℓ), velocity (v_{th}) and time (τ) factor.

If eq. (3.18) is integrated with respect to nondimensional time $\tilde{t}$, the velocity evolves as

$$\tilde{v}_{\text{e}}^{(\alpha)}(\tilde{t}) = \tilde{v}_{\text{e}}^{(\alpha)}(0) + g_{\text{coul}} \int_0^{\tilde{t}} \left[\frac{1}{Z} \sum_{\beta\neq\alpha} \frac{\boldsymbol{n}_{\alpha\beta}}{|\tilde{\boldsymbol{r}}_{\text{e}}^{(\alpha)} - \tilde{\boldsymbol{r}}_{\text{e}}^{(\beta)}|^2} - \sum_b \frac{\boldsymbol{n}_{\alpha b}}{|\tilde{\boldsymbol{r}}_{\text{e}}^{(\alpha)} - \tilde{\boldsymbol{r}}_{\text{i}}^{(b)}|^2} \right] \mathrm{d}\tilde{\tau} + \frac{g_{\text{osc}}}{g_\omega}\, \tilde{\boldsymbol{E}}^{(-1)}(g_\omega\, \tilde{t}). \tag{3.22}$$

The first term in the right-hand-side of the equation is still piloted by g_{coul} but the second term, concerning the electric field, is now piloted by g_{osc}/g_ω which is exactly v_E/v_{th}.

Therefore, with no laser, $I = 0$ or $g_{\text{osc}} = 0$, all nondimensionalized physical quantities (such as a coulomb logarithm) should only depends on Z and g_{coul} (which is nothing else than the plasma parameter). This is indeed the case as reported from molecular dynamic simulations of temperature relaxation [Daligault & Dimonte, 2009, Dimonte & Daligault, 2008] (where g in these references is proportional to $g_{\text{coul}}^{3/2}$) and from theoretical studies [Brown *et al.*, 2005].

With radiation, meaning $g_{\text{osc}} \neq 0$, eq. (3.22) tells us that every nondimensionalized physical quantities that depends on velocity distribution (such as collision frequencies or absorption rate), should depend on Z, g_{coul} and $g_{\text{osc}}/g_\omega = v_E/v_{\text{th}}$ and not on Z, g_{coul} and g_{osc} as eq. (3.18) might have suggested. This will be highlighted in section 3.7.2.

3.5 Molecular dynamic simulations of a TCP with LAMMPS

3.5.1 LAMMPS code

LAMMPS [Thompson *et al.*, 2022] stands for Large-scale Atomic/Molecular Massively Parallel Simulator. It is a PPPM (Particle-Particle-Particle-Mesh algorithm to account for periodic domain) code that has been developed at Sandia National Laboratory (New Mexico) with computational cost $O(N \log N)$, where N is the number of particles simulated, as opposed to a PP (Particle-Particle) code with higher computational cost $O(N^2)$.

The computational cost of the simulations limits the simulation domain to a small fraction of the size of a real plasma. This is mitigated by simulating a cube with periodic boundary conditions in all three directions, which is a valid approximation provided the Debye sphere of a given particle does not intersect with the Debye sphere of its replicas.

That has two consequences. The first and most obvious one is the fact that a particle going out of the domain through a boundary is immediately reintegrated to the domain through the opposite boundary with the same velocity. This is the reason why the number of particles in the domain will remain constant as time goes by along with total energy. This is the characteristic of a microcanonical simulation. The second consequence has to do with the interaction of particles. For instance, if a particle A interacts with a particle B in the domain, it also interacts with its own infinite replicates (all the As) and the infinite replicates of particle B in the periodic domains. This infinite sum can be efficiently carried out by the technic of Ewald summation. The way this is handled in PPPM molecular dynamic simulations [Griebel *et al.*, 2007] is by optimizing this Ewald summation using a fine regular mesh in the CMDS domain that will be used to calculate the long range part the electric potential with periodic replicates using fast-Fourier-transform and the short range part of the potential by simply adding up the contributions of neighboring particles.

3.5.2 Simulations settings

The numerical domain is defined by a periodic box of size $L \times L \times L$ with N_{ion} ions of charge $+Z\,e$ and $Z\,N_{\text{ion}}$ electrons of charge $-e$. Here, we have tested both like-charges simulations (positive electrons and positive ions, as in [Dimonte & Daligault, 2008]) and opposed-charges simulations (negative electrons and positive ions) and found no difference for weakly coupled plasmas as reported in [Shaffer & Baalrud, 2019].

In CMDS, close encounters between negative electrons and positive ions, which are very unlikely for weakly coupled plasmas but can happen on very few occasions, would produce a non conservative energy event that would ruin the outcome of the simulation. In order to avoid these events, the potential used in our CMDS simulations with LAMMPS is a soft-core (SC) potential[Kuzmin & O'Neil, 2002]

$$V_{\text{SC}}(r) = \frac{q_1\,q_2}{4\pi\varepsilon_0}\frac{1}{\sqrt{r^2+a^2}} \tag{3.23}$$

which behaves as a pure Coulomb potential when $r \gg a$ and goes to a finite value $q_1\,q_2/(4\pi\varepsilon_0\,a)$ when $r \ll a$ (corresponding to a vanishingly small value of the electric field derived from that potential when $r \ll a$). Other soft core potentials exist in the literature, such as $\frac{q_1\,q_2}{4\pi\varepsilon_0}\frac{1}{r}\left(1-e^{-r/a}\right)$, but they are equivalent for the most part. If the soft-core radius a is small enough but non zero, it allows most particles to feel a pure Coulomb potential (because they are at a distance of one

another much greater than a most of the time) but for those few particles that venture too close to an opposite-charge particle (within a distance a) the SC potential leaves them fly-by (no interaction at distances much smaller than a). It drastically differs from the pure Coulomb potential that would increase and would capture both particles into such a small orbit around one another (with radius $\ll a$) that their velocity would skyrocket and violate the time-step limitation of the simulation. The value

$$a = 0.1 \text{ Å}, \tag{3.24}$$

set in all simulations at $T_e = 10$ eV that will be presented hereafter, was found to be small enough: it has been checked Fig. 3.1 that results presented do not depend on such a small value of a up to at least 0.1 Å (this was studied in [Pandit *et al.*, 2017]).

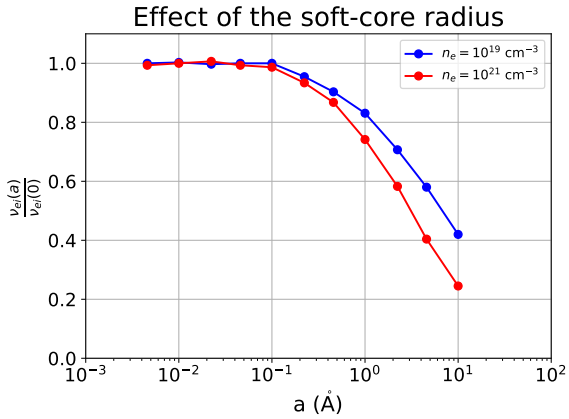

Figure 3.1: (color online) Evolution of the normalized electron-ion frequency with respect to the soft-core radius "a" for two plasma states with different electron densities ($n_e = 10^{19}$ and 10^{21} cm^{-3}) and for the same electron temperature $T_e = 10$ eV (which is the electron temperature used throughout this article). Each point in the viewgraph corresponds to the result of one CMDS. As long as $a \ll b_{\min}$, which is approximately $e^2/(4\pi\varepsilon_0 k_B T_e)$ in a classical treatment, simulations provide results that do not depend upon "a" with $\nu_{ei} = \nu_{ei}(0)$ ($\nu_{ei}(0) = 3.3$ ps^{-1} for $n_e = 10^{19}$ cm^{-3} and $\nu_{ei}(0) = 151$ ps^{-1} for $n_e = 10^{21}$ cm^{-3}). For $a \geq b_{\min}$, the electron-ion frequency $\nu_{ei}(a)$ decreases like $-\log(a)$ as a increases (it is a linear behavior in a semilog axis) because then, in the Coulomb logarithm, $b_{\min}$ is replaced by the soft-core radius "a" which becomes the lowest accessible length scale.

Our simulations are parameterized by the number of ions N_{ion} allowed to evolve (10^6 in our simulations), by Z, the degree of ionization of ions (one variety of ion with exactly one degree of ionization in our simulations, at variance with real life plasmas where there are several varieties of ions, each with possibly several degrees of ionization) and by n_e, the electron density. These three parameters defined the size L of the numerical domain by

$$L = \left(\frac{Z\, N_{\text{ion}}}{n_e} \right)^{1/3}. \tag{3.25}$$

Initially, the positions of electrons and ions are randomly distributed throughout the simulation domain with a uniform law. Moreover, velocities of these particles are also randomly distributed with a Maxwellian distribution, at T_e for electrons and T_i for ions. Of course, these initializations are not physical since the actual radial distribution function $g(r)$, also known as

the pair correlation function, is not constant even in a weakly coupled plasma. Therefore, before each simulation, the code is launched for a period during which particles equilibrates and spatial and velocity distributions converge towards their physical state. The spatial distribution of electrons and ions becomes such that the Coulomb potential between ions and electrons, $V_{\rm ei}$, reaches a minimum. The usual procedure is to apply a thermostat at the target electronic temperature $T_e^{(0)}$ (it is a canonical simulation) and let the system evolve until $V_{\rm ei}$ reaches a minimum. Here, we have found that a well chosen succession of microcanonical simulations (MS) would get us faster to the equilibrium spatial distribution at $T_e^{(0)}$. This is just an empirical observation and in no way an explanation. The way we proceed is as follows. The first of these MS starts at the target electronic temperature $T_1(0) = T_e^{(0)}$ and, as time unfold, T_e increases while $V_{\rm ei}$ decreases and we terminate this first MS at the time $\tau_{\rm MS}$ when the electron temperature as increased by 10%: $T_1(\tau_{\rm MS}) = T_e(\tau_{\rm MS}) = 1.1 \times T_e^{(0)}$ (this threshold of 10% was found to be a good numerical compromise). The second MS starts with the resulting spatial distribution of the first MS but with a velocity distribution rescaled at $T_2(0) = T_e^{(0)}$ and it is carried out for the same amount of time ($\tau_{\rm MS}$) and it results that $T_e^{(0)} < T_2(\tau_{\rm MS}) < T_1(\tau_{\rm MS})$. The same procedure is repeated several times. The n'th iteration starts with the resulting spatial distribution of the $(n-1)$'th and with a velocity distribution rescaled at $T_n(0) = T_e^{(0)}$ and, after a time $\tau_{\rm MS}$, it results that $T_e^{(0)} < T_n(\tau_{\rm MS}) < T_{n-1}(\tau_{\rm MS}) < \cdots < T_1(\tau_{\rm MS}) = 1.1 \times T_e^{(0)}$ (where n is the number of time this procedure is repeated). As n increases, T_e varies less and less with time (dT_e/dt is smaller and smaller at each successive MS) because V_{ei} is closer to its equilibrium value. After enough iterations, the resulting spatial distribution corresponds to $V_{\rm ei}$ that has relaxed to a minimum for $T_e = T_e^{(0)}$.

A quantity defined in terms of quadrupole moments of the plasma distribution is introduced in section section 3.6.1 in order to monitor the evolution of the spatial distribution quantitatively in a different way than by inspecting the evolution of the inter-potential.

In order to accurately capture the physics of the plasmas of interest, simulations are constrained by a number of assumptions. First, relativistic effects are not included, so the electron temperature should not be too high ($k_B\,T_e \ll m_e\,c^2$=511 keV) which is always satisfied in ICF plasmas.

Furthermore, for the periodic boundary condition not to affect the physics of the plasma, every particle should be screened from its replicas, i.e. the size of the domain should be greater than twice the Debye length of the particles. As long as $T_i < \bar{Z}T_e$, which will always be the case in the configurations we consider, the Debye length of the ions is smaller than that of the electrons, so the most constraining condition is $2\lambda_D < L$, that is to say, $2(\varepsilon_0\,k_B\,T_e/n_e\,e^2)^{1/2} < (Z\,N_{\rm ion}/n_e)^{1/3}$ which translates roughly to

$$N_{\rm ion} > \frac{1}{2\pi\,(Z+1)^{3/2}}\,\frac{1}{g}. \tag{3.26}$$

The smaller g (coupling parameter), the larger the number of particles in the simulation ($(Z+1)\,N_{\rm ion}$), the more computationally costly the simulation. One can then evaluate the cost of one time iteration depending upon the numerical scheme. In a nutshell, it scales like $O(N_{\rm ion}\log N_{\rm ion}) \sim g^{-1}\log g$ for a PPPM code such as LAMMPS.

The time step of a simulation must be such that for all particles and at all time, the variation of the acceleration of a particle between two time step should not vary more than a fraction

($\ll 1$) of its value or energy might be lost in the process causing spurious effects. For that matter, the most stringent constraint is exerted by electrons, which are the lightest and most mobile particles (compared to the heaviest ions). On average, they travel at velocities of order $v_{\rm th} \sim (k_B\,T_e/m_e)^{1/2}$. The distance of closest approach to one another or to an ion is given by $b_{\rm min} \sim e^2/4\pi\varepsilon_0\,k_B\,T_e$. The time step should then be of order $dt \sim b_{\rm min}/v_{\rm th}$, that is to say

$$dt \sim \frac{e^2\,\sqrt{m_e}}{4\pi\varepsilon_0\,(k_B\,T_e)^{3/2}} \tag{3.27}$$

The purpose of all our simulations is to precisely quantify the time of the exponential relaxation (either for temperature of for drift velocity) that is to say $\tau_{ei}^{p,E} = 1/\nu_{ei}^{p,E}$. Therefore, simulations must last for a suitable fraction of $1/\nu_{ei}^{p,E}$. This is why, the number of iterations should scale like $N_{\rm iter}^{p,E} \sim 1/(dt\,\nu_{ei}^{p,E})$, that is to say

$$N_{\rm iter}^{p,E} \sim \frac{(4\pi\varepsilon_0\,k_B\,T_e)^3}{n_e Z e^6} \sim Z\,g^{-2}. \tag{3.28}$$

The computational cost of a simulation is therefore given by the product of the number of iteration, $N_{\rm iter}$, times the computational cost of one iteration. For a PPPM code such as LAMMPS, it scales like $Z\,g^{-3}\log g$. Therefore, the weaker the plasma coupling, the more costly the simulation.

3.6 Simulations without time varying external electric field

Before carrying out MD simulations dedicated to inverse bremsstrahlung (IB), we have tested the simulation suite on well established configurations. We have been able to reproduce existing results with our MD simulations in temperature relaxation [Daligault & Dimonte, 2009, Dimonte & Daligault, 2008] and velocity relaxation [Shaffer & Baalrud, 2019].

3.6.1 Relaxation towards a physical initial plasma state monitored by the quadrupole moment of charges distribution

One of the key problem in molecular dynamic simulation is to obtain a physical initial plasma configuration. Velocities of each particles within a simulated plasma at local thermal equilibrium at temperature T can easily be randomly generated following the Maxwell distribution $\exp(-\frac{m\,v^2}{2\,k_B\,T})$. Positions, on the contrary, are more difficult to generate. Charged particles within a plasma are not randomly distributed following a uniform distribution (where every position would be equally likely) since like charges tend not to get too close to each other, at variance with opposed charges. In order to quantify the deviation to spatial uniform distribution one uses radial distribution functions, $g_{ei}(r)$, $g_{ii}(r)$, $g_{ee}(r)$, defined by the distribution of distances, respectively, between each pair of electron-ion (ei), ion-ion (ii) or electron-electron (ee).

In practice, particles positions are initially distributed randomly and uniformly in a CMDS. Simulations (without laser) are then run for a certain duration τ_{eq} at the end of which particles reach their physical spatial distribution with the right radial distribution functions. It is suggested in the literature [Shaffer & Baalrud, 2019] that τ_{eq} should be approximately $60\,\omega_{pe}^{-1}$ by inspecting the evolution of radial distribution functions as time goes by.

Here, we describe a scalar quantity whose time evolution allows to precisely grasp the relaxation of the uniform distribution towards the physical distribution. Any positions distribution of particles $\{\boldsymbol{x}^{(\alpha)}\}_{\alpha\in[1,N]}$ (where N is the number of particles in the CMDS, α the label of one given particle with charge q_α) can be characterized by its multipoles, the first two being the dipole (rank one tensor) and the quadrupole (rank two tensor). The averaged dipole per particle, D_i, is defined by

$$D_i = \frac{1}{N_e} \sum_\alpha q_\alpha \, x_i^{(\alpha)}, \tag{3.29}$$

and the averaged quadrupole per particle, Q_{ij}, is defined by

$$Q_{ij} = \frac{1}{N_e} \sum_\alpha q_\alpha \left(x_i^{(\alpha)} x_j^{(\alpha)} - \frac{\delta_{ij}}{3} |\boldsymbol{x}^{(\alpha)}|^2 \right). \tag{3.30}$$

Hidden in these multipoles is the information of the position distribution which is exactly what one needs to construct a scalar that could be monitored as time unfolds to observe the relaxation of positions distribution.

For a two components plasma, one can show that the dipole $\boldsymbol{D}$ evolves as the position of the centre of mass of the electron. Indeed, since

$$D_i = -e \sum_{\alpha_e} x_i^{(\alpha_e)} + Z\, e \sum_{\alpha_{\text{ion}}} x_i^{(\alpha_{\text{ion}})} \tag{3.31}$$

and since the total momentum of the plasma can be set to zero, for it is a conserved quantity, then the centre of mass position of the plasma,

$$m_e \sum_{\alpha_e} x_j^{(\alpha_e)} + m_i \sum_{\alpha_{\text{ion}}} x_i^{(\alpha_{\text{ion}})}, \tag{3.32}$$

is constant and can be set to zero without loss of generality. Therefore,

$$D_i = -\frac{e}{N_e} (1 - Z\frac{m_e}{m_i}) \sum_{\alpha_e} x_i^{(\alpha_e)}. \tag{3.33}$$

If N_e is the number of electrons in the domain, the centre of mass of the electron, $\sum_{\alpha_e} x_i^{(\alpha_e)}$ is roughly in the centre of the domain within non coherent thermal position fluctuations of order $\ell/\sqrt{N_e}$ decreasing as N_e is increased. Therefore, no interesting information can be extracted from the only scalar that can be made out of the dipole $\boldsymbol{D}$ which is $|\boldsymbol{D}|^2$.

On the contrary, no such simplifications can be carried out on the quadrupole and the remaining question is how to construct an interesting scalar out of the quadrupole tensor ? The quadrupole is traceless by construction, therefore the trace of the quadrupole, which is the simple way to get a scalar (that is a rank 0 tensor) from a rank 2 tensor, is not an option. On the other hand, one can square the quadrupole and get the trace, $\text{Tr}(\boldsymbol{Q}^2) = Q_{kj}Q_{kj}$, which is homogeneous to a length to the fourth power, that we can divide by the averaged length between electrons for

instance ($n_e^{-1/3}$) at the fourth power to get a non-dimensional scalar,

$$\mathcal{Q} = n_e^{\frac{4}{3}} \operatorname{Tr}(\boldsymbol{Q}^2) = n_e^{\frac{4}{3}} \sum_{jk} Q_{kj}^2, \tag{3.34}$$

that can be compared between different plasma state (cf. Fig. 3.2).

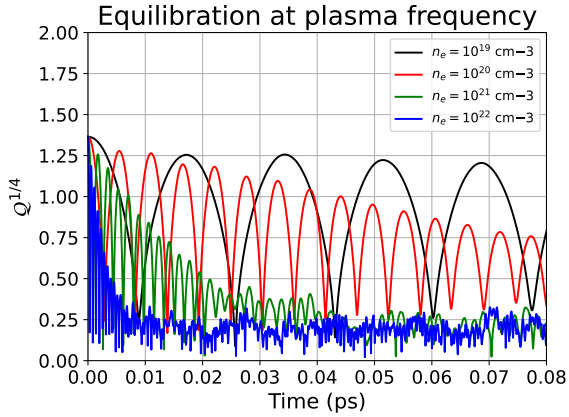

Figure 3.2: (color online) Evolution of the quadrupole, through $\mathcal{Q}^{1/4}$ (where $\mathcal{Q}$ is defined in eq. (3.34)), with respect to time for four different plasma states, with $n_e = 10^{19}$, 10^{20}, 10^{21} or 10^{22} cm^{-3} initialized with random position distribution (uniform law) and Maxwellian velocity distribution corresponding to T =10 eV. The coherent oscillations observed for the four cases correspond to Langmuir waves at different plasma frequencies $\omega_p = \sqrt{n_e\, e^2/\varepsilon_0\, m_e}$ owing to different electronic densities. These coherent waves are progressively damped as the plasma evolves towards its statistically stationary state.

The behavior depicted on Fig. Fig. 3.2 is typical of a plasma initialized ($t = 0$) with a uniform spatial random distribution. For different initial electron densities, but for the same initial $T_e = 10$ eV, the quantity $\mathcal{Q}$ undergoes a damped oscillation at the plasma frequency due to the fact that the initial spatial distribution is not physical and correspond to a perturbation with respect to its physical (equilibrium) counterpart. This perturbation is subsequently ($t > 0$) damped out through plasma waves. Once these coherent oscillations reach a sufficiently low level, corresponding to the amplitude of the incoherent thermal fluctuations [that can be seen for $t > 0.01$ ps on the blue curve ($n_e = 10^{22}$ cm^{-3}) or for $t > 0.04$ ps on the green curve ($n_e = 10^{21}$ cm^{-3}) on Fig. Fig. 3.2], one can be confident that the spatial distribution reaches an equilibrium state.

Once this physical state is reached, it constitutes the initial state of temperature relaxation (TR) simulations or velocity relaxation (VR) simulations, which were both carried out in order to compare our methodology with existing, well documented studies, and foremost, it constitutes the initial state of our inverse bremsstrahlung heating (IBH) simulations which are the core material of this publication.

3.6.2 Temperature relaxation (TR) and velocity relaxation (VR)

The initialization previously described brings the electrons (at a density n_e) and the ions (at a density $n_i = Z\, n_e$) in a physical configuration (spatial distribution) at $T_e = T_i$ (velocity distribution). For (TR) simulations, one additionally requires that T_i be different than T_e in order

to measure the relaxation rate to an equilibrium temperature. This can simply be done by only modifying the ions velocity distribution with $T_i > T_e$ or $T_i < T_e$.

If the plasma, initialized this way, evolves freely, both temperatures will eventually equalize after a while when thermal equilibrium is reached. Both temperatures will reach the common equilibrium value following and exponential relaxation with time constant of order $1/\nu_{ei}^T$ defined by the energy electron-ion frequency

$$\nu_{ei}^T = \frac{m_e}{m_i}\,\nu_0\,\ln\left(\Lambda_{ei}^T\right) \tag{3.35}$$

characterizing the rate at which energy of an electron is significantly altered in its scattered motion through the plasma.

For a weakly-coupled plasma, the potential energy of the ee, ii and ei interactions are negligible compared to kinetic energy and, therefore, $n_eT_e + n_iT_i$ is constant throughout the evolution to a very good approximation. This can be used to eliminate T_i from the evolution equation of the electron temperature

$$\frac{dT_e}{dt} = -\nu_{ei}^T(T_e - T_i). \tag{3.36}$$

From the fit of the solution of the resulting equation with the $T_e(t)$ relaxation time history in the CMDS, one can deduce, see [Dimonte & Daligault, 2008] for more details, the value of ν_{ei}^T and therefore that of $\ln\left(\Lambda_{ei}^T\right)$ for any given value of g (compatible with the constraints of CMDS).

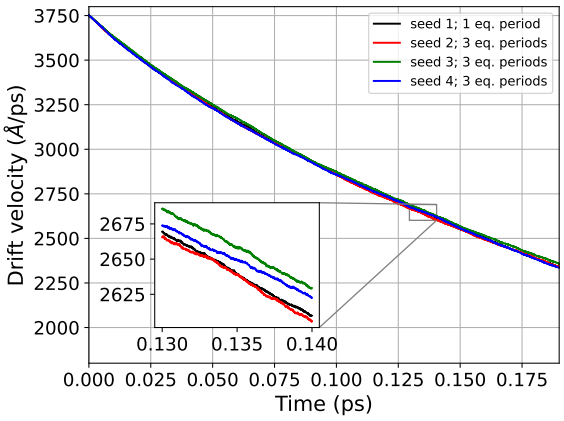

Figure 3.3: (color online) Evolutions of the drift velocity of a plasma initially at $n_e = 10^{19}$ cm^{-3}, T =10 eV and $Z = 1$, for 4 different equilibrations where the electron population has initially been given an ensemble velocity (drift velocity) where $v_d = 0.1v_{th}$. The drift velocity is decreasing in the same way for the 4 different initializations.

For (VR) simulations, both the relaxed spatial distributions and the velocity distribution for ions and electrons are left unchanged. Therefore $T_e = T_i$, but a drift velocity component, $\boldsymbol{V}_d$, is added to every electrons so that the initial velocity of any single electron in a VR simulations is of the form $\boldsymbol{v}_\alpha = \boldsymbol{V}_d + \boldsymbol{v}'_\alpha$ (α being the label of the electron under consideration) where $\boldsymbol{v}'_\alpha$ is distributed according to a Maxwellian of temperature T_e. Therefore, in velocity space, the distribution of the electrons in the plasma is a Maxwellian shifted by $\boldsymbol{V}_d$ from the origin.

With such an initialization, the electrons will flow through the web of ions with a drift velocity

that will exponentially decrease as time goes by following

$$\frac{\mathrm{d}\boldsymbol{V}_d}{\mathrm{d}t} = -\nu_{ei}^V \boldsymbol{V}_d, \tag{3.37}$$

where

$$\nu_{ei}^V = \nu_0 \ln\left(\Lambda_{ei}^V\right), \tag{3.38}$$

which characterizes the rate at which the momentum of an electron is significantly modified by its motion through scattering particles (electrons or ions) in the plasma (cf. Fig. 3.3).

The comparison between eqs. (3.35) and (3.38) shows a factor m_e/m_i between ν_{ei}^T and ν_{ei}^V. This is due to the fact that a single collision of an electron (small mass) against an ion (large mass, $m_i \gg m_e$) is enough to affect momentum (possible scattering of the electron in any direction) with almost no kinetic energy variation (elastic scattering) whereas it would require $\approx m_i/m_e > 2000$ collisions with ions to modify appreciably its kinetic energy. Molecular dynamics simulations of temperature relaxation are therefore more numerically costly for they need to be run for much longer time (m_i/m_e times as long) than velocity relaxation.

Extreme care should be brought to the choice of the initial V_d as compared to v_{th}. In order for the ν_{ei}^V measured in such simulation to be representative of the actual ν_{ei}^V of a plasma at local thermodynamic equilibrium (LTE) with $T_e = T_i = T$, the amplitude of the drift velocity V_d should be much less than v_{th} for the velocity distribution of electrons to appear centred in the laboratory frame where ions have no ensemble averaged velocity. If V_d were to be of order or greater than v_{th}, not only would the velocity distribution of electrons in the same reference frame appreciably be shifted (by V_d) but it would gradually turn into a centred Maxwellian of larger width for the excess kinetic energy brought by the coherent motion (V_d) would dissipate, by collisional processes, into internal energy thereby increasing the electron temperature (T_e) significantly.

The drawback is that taking $V_d \ll v_{\mathrm{th}}$ goes against signal to noise ratio. A molecular dynamic simulation being made of a limited number of particles, every averaged value, and the drift velocity is no exception, is subjected to statistical fluctuation, which is of order $v_{\mathrm{fluc}} \sim v_{\mathrm{th}}/\sqrt{N_{\mathrm{part}}}$ for drift velocities. Thus, in order to comply with the LTE constraint ($V_d \ll v_{\mathrm{th}}$) and still be able to get a sound measurement of the time history of V_d, which should not be buried under the statistical noise ($V_d \gg v_{\mathrm{fluc}}$), the drift velocity should verify $v_{\mathrm{fluc}} \ll V_d \ll v_{\mathrm{th}}$ to get a sufficient separation between v_{fluc} and v_{th}. Two orders of magnitude, requires $N_{\mathrm{part}} > 10^4$. All simulations presented in this article are carried out with 10^6 ions and as many electrons. For all VR simulations, one used an initial

$$V_d = 0.3\, v_{\mathrm{th}} \tag{3.39}$$

which turned out to be a good compromise between LTE and statistical fluctuations.

From the fit of the solution of that equation with the $\boldsymbol{V}_d(t)$ relaxation time history in the CMDS, one can deduce, see [Shaffer & Baalrud, 2019] for more details, the value of ν_{ei}^V and therefore that of $\ln\left(\Lambda_{ei}^V\right)$ for any given value of g (compatible with the constraints of CMDS).

Clearly, our results on Fig. 3.4 show very good agreement with results reported by [Dimonte & Daligault, 2008] also in agreement with theoretical results by [Brown *et al.*, 2005]. It is found

that $\nu_{\mathrm{ei}}^{(V)}$ satisfies

$$C_{\mathrm{abs}} = 1, \tag{3.40}$$
$$\eta = 0, \tag{3.41}$$
$$\epsilon_\ell = 1, \tag{3.42}$$
$$C_\ell = 0.7, \tag{3.43}$$
$$\eta_\ell = 0, \tag{3.44}$$

which are the values reported by [Dimonte & Daligault, 2008] for $\nu_{\mathrm{ei}}^{(T)}$. This shows that, in weakly-coupled plasmas, molecular dynamics simulations agree with

$$\ln\left(\Lambda_{ei}^{T}\right) = \ln\left(\Lambda_{ei}^{V}\right). \tag{3.45}$$

It is to be remembered, here (for $\nu_{\mathrm{ei}}^{(V)}$ and $\nu_{\mathrm{ei}}^{(T)}$), that $C_{\mathrm{abs}} = 1$ whereas in our IB molecular dynamic simulations, even at low intensity, we shall measure that it is consistent with half that value, but we will come back to that in section 3.7.2.

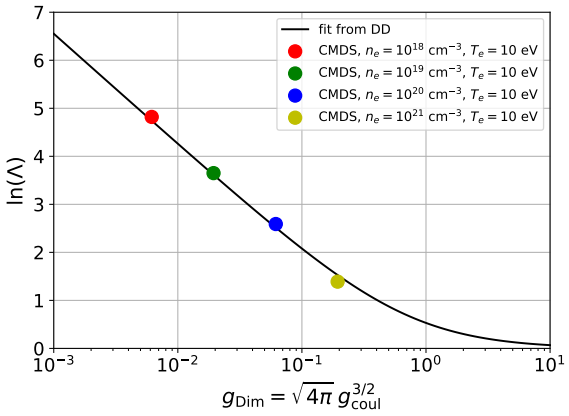

Figure 3.4: (color online) Plot of $\ln\left(\Lambda_{ei}^{E}\right) = \ln(1 + 0.7/g)$ from Daligault and Dimonte [Dimonte & Daligault, 2008] in black solid line with colored points from our LAMMPS CMDS with $T_e = 10$ eV and n_e varied in such a way as to span the g axis from 0.006 to 0.2 for VR relaxation. The green point corresponds to the simulation described in Fig. 3.3.

3.7 Simulations with time varying external electric field dedicated to inverse bremsstrahlung heating

3.7.1 Setup specific to IBH

In our molecular dynamic simulations, the spatial variation of the electric field of the laser is not taken into account as mentioned in section 3.4.2 and as it is the case in other such CMDS [David *et al.*, 2004, Pfalzner & Gibbon, 1998]. This means that in no way can our CMDS provide any information about the dispersion relation for wave vector $k \neq 0$.

In such simulations, the laser is mimicked by the uniform (in space) oscillating (in time)

electric field. The oscillation frequency is such that $f_\ell = c/\lambda_\ell$. The effect of the electric field is to force a coherent ensemble motion of electrons (and ions) with an oscillating velocity whose maximum is the quiver velocity defined by 3.6 (where $\omega = \omega_\ell = 2\pi\, f_\ell$ is the laser pulsation and $\widetilde{E}$ the maximum amplitude of the electric field generated by the laser).

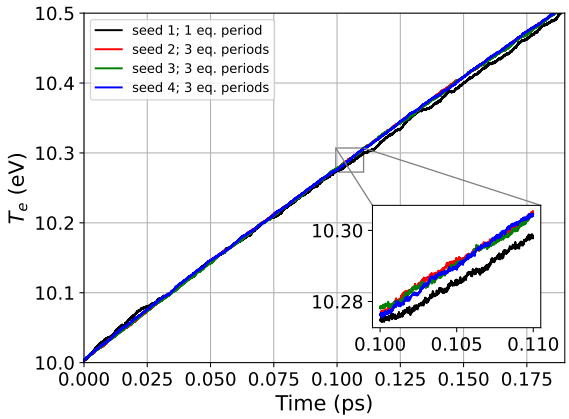

Figure 3.5: (color online) Evolution of the electronic temperature of a plasma initially at $n_e = 10^{19}$ cm^{-3}, T =10 eV and $Z = 1$, for 4 different equilibration processes, that is heated with a laser at $I = 10^{14}$ W/cm^2 and $\lambda = 351$ nm. The electronic temperature is increasing linearly, in the same way for the 4 different initializations, at a rate of 2.75 $\pm$ 0.05 eV/ps. Seed 1 to 4 correspond to different random series to generate the initial random velocities with maxwellian distribution. The number of equilibration periods corresponds to the number of time the equilibration process was carried out. Although, "long time" ($\approx$ 0.025 ps) fluctuation are clearly visible on the 1 equilibration period case, it does not affect the overall slope of the early linear increase of T_e as time goes by compared to 3 equilibration periods.

In the most general case, IBH simulations has to be initialized as VR simulations. Indeed, in the presence of an oscillating electric field, a coherent motion of the electrons (and ions) is set into play. There is an oscillating drift velocity created $\boldsymbol{V}_d(t)$ that verifies an equation similar to eq. (3.37) where the electric field sets in as

$$\frac{\mathrm{d}\boldsymbol{V}_d}{\mathrm{d}t} = -\nu_{ei}^p\, \boldsymbol{V}_d + \frac{e\,\boldsymbol{E}(t)}{m_e}, \tag{3.46}$$

and with initial condition $V_d = 0$. Assuming a varying electric field of the form eq. (3.17), the general solution of 3.46 at early time, when V_d is still small (with respect to v_{th}), is $\boldsymbol{V}_d(t) = \frac{e}{m_e\,\omega}(E_1 \sin(\omega t)\,\boldsymbol{n}_1 - E_2 \cos(\omega t)\,\boldsymbol{n}_2) + \boldsymbol{V}_d^0$ where $\boldsymbol{V}_d^0$ is a possible constant vector of integration. Since initially $\boldsymbol{V}_d(0) = 0$, it yields $\boldsymbol{V}_d^0 = (e\,E_2/m_e\,\omega)\,\boldsymbol{n}_2$. When averaging the resulting $\boldsymbol{V}_d(t)$ over one laser period, it is found that $\langle \boldsymbol{V}_d(t) \rangle = \boldsymbol{V}_d^0 = (e\,E_2/m_e\,\omega)\,\boldsymbol{n}_2$ since $\langle \cos(\omega t) \rangle = \langle \sin(\omega t) \rangle = 0$. Therefore, once the electric field is set on, there is an immediate drift velocity in the most general case (when $E_2 \neq 0$).

This drift velocity relaxes with time but, as it does so, it although heats the electron population as described earlier in section 3.6.2 in the part concerning VR. This heating interferes with the one we want to monitor exclusively namely the inverse bremsstrahlung heating. In order to circumvent that issue, an initial drift velocity on the population of electron has to be enforced to compensate exactly for the one that will be triggered by the electric field. This is why, initially,

one must set

$$\boldsymbol{V}_d(t=0) = -(e\,E_2/m_e\,\omega)\,\boldsymbol{n}_2. \tag{3.47}$$

Once this is done, one can clearly appreciate the precision of the evolution of a typical electronic temperature history of one of our CMDS. In Fig. 3.5, one displays the evolution of a typical electron temperature time history, $T_e(t)$ (calculated by summing the individual kinetic energies of every electron in the reference frame of the oscillating electric field), for four different CMDS with the same plasma and electric field parameters but originating from four different initializations such as described earlier in section 3.6.1. Clearly, with $N_{\rm ion} = 10^6$, the thermal fluctuation is barely noticeable which makes the measurement of the slope, $\mathrm{d}T_e/\mathrm{d}t$, very precise. This slope, also known as the heating rate, can be compared to the parameterized model eqs. (3.2) to (3.5) when included in eq. (3.1).

This is the important information we gather from these simulations in order to display CMDS measurements versus theoretical models such as those in Fig. 3.6 for instance. In this example, indeed, each black point corresponds to a full CMDS of $N_{\rm ion} = 10^6$ ions and $N_{\rm elec} = 10^6$ electrons over roughly 10^6 iterations with time steps around 10^{-7} ps with $n_e = 10^{19}$ cm^{-3}, $T_e = 10$ eV with an oscillating electric field corresponding to $\lambda_\ell = 351$ nm at intensities ranging from 10^{13} to 10^{18} W/cm^2.

The heating rate is calculated by a linear regression of the CMDS electronic temperature history between $t = 0$ (corresponding to the instant the irradiation is turned on) and $t = t_{\rm fit}$, when the temperature deviates from a straight line by more than 0.1 % (calculated from a least squared fit). Therefore, what we call $\mathrm{d}T_e/\mathrm{d}t$ is the value at early time when (i) T_e is still equal to its initial value (heating over a sufficiently long period may increase that temperature drastically) and (ii) the velocity distribution is still Maxwellian which may change as time unfold. This is a deliberate choice to be coherent with assumptions made by all theoretical investigations on IB heating [Brantov *et al.*, 2003, Dawson & Oberman, 1962, Johnston & Dawson, 1973, Jones & Lee, 1982, Landau & Teller, 1936, Mulser *et al.*, 2000, Silin, 1965, Skupsky, 1987] (Maxwellian distribution is one of these important assumptions).

3.7.2 Comparison between CMDS and the parameterized model

On one single set of CMDS, corresponding to a plasma state with $n_e = 10^{19}$ cm^{-3}, $T_e = 10$ eV, where the wavelength of the electric field is fixed to $\lambda_\ell = 351$ nm but where the intensity is varied, it is possible to adjust values of some constants of the parameterized model.

On each viewgraph in Fig. 3.6, the 11 black points correspond to different values of the intensity evenly distributed in logarithmic scale (2 points per decade). Various settings of the parameterized model are plotted against our CMDS data. Viewgraph (a) demonstrates that the value $\eta = 1/6$ is, without a doubt, the only one compatible with molecular dynamics results. Viewgraph (c), also demonstrates that the value $\eta_\ell = 1/6$ is the only one compatible with the CMDS data.

This particular value $\eta = \eta_\ell = 1/6$ is interesting for it is the precise value one would have found have we assumed that the coherent wiggly motion of electrons due to the electric field oscillation was like an effective thermal motion that superimpose to the actual random thermal motion. This idea is not new for it is present in various earlier works such as [Brantov *et al.*,

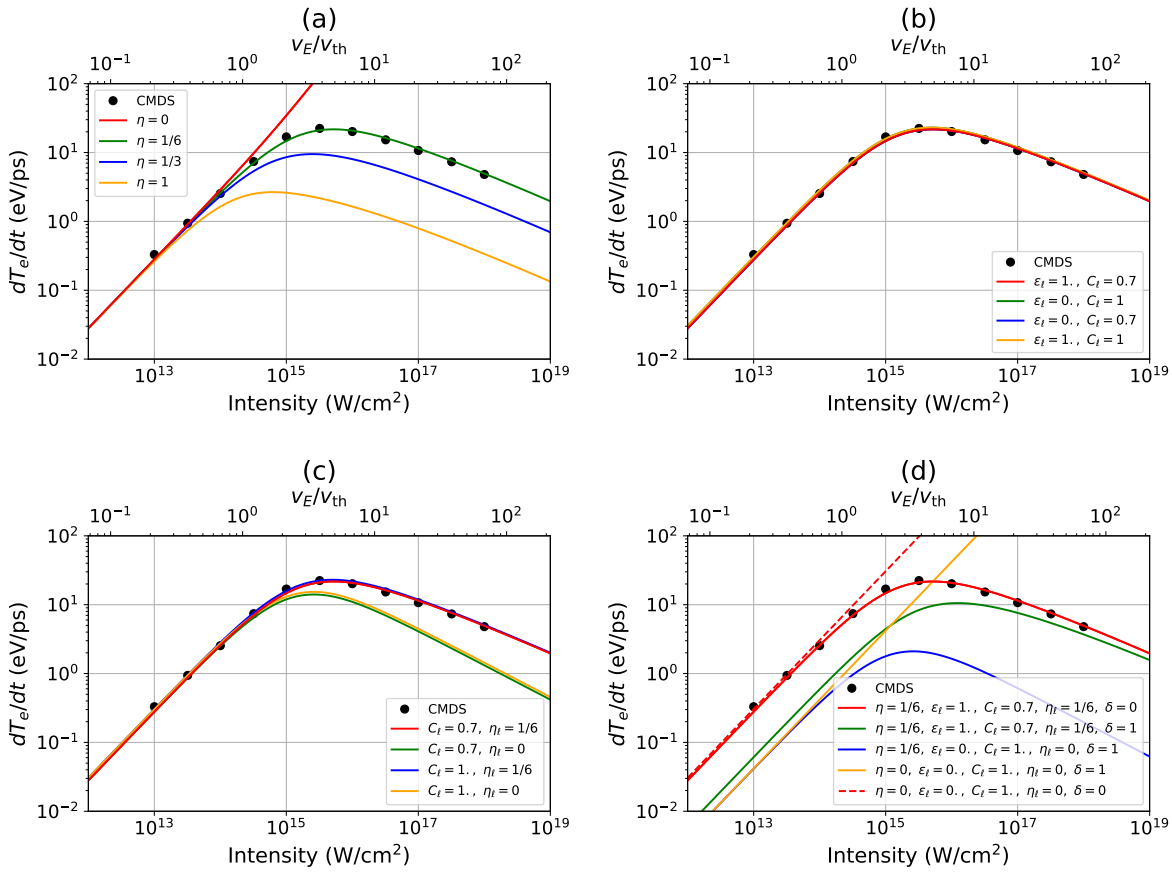

Figure 3.6: (color online) Comparison of CMDS results (for $n_e = 10^{19}$ cm^{-3}, $T_e = 10$ eV and $\lambda_\ell = 351$ nm) with the parameterized model for different adjustable constants variations. The important effect of η is evaluated in figure (a). Figure (b) shows that the effect of ε_ℓ and C_ℓ are not very important within these reasonable limits. Figure (c) confirms the small effect of C_ℓ but shows the important effect of η_ℓ. Finally, figure (d) shows the importance of δ. The value $\delta = 1$, put to the fore by most classical theories, is ruled out by CMDS. The default values of the six parameters are those of eqs. (3.48) to (3.53).

2003] and [Faehl & Roderick, 1978]. Since the actual velocity of a single electron is made out of a random thermal velocity $\boldsymbol{v}'$ and of a coherent oscillation velocity $\boldsymbol{v}_E$, it can be recast as $\boldsymbol{v} = \boldsymbol{v}' + \boldsymbol{v}_E$. From there, one can deduce $\boldsymbol{v}^2 = \boldsymbol{v}'^2 + \boldsymbol{v}_E^2 + 2\,\boldsymbol{v}' \cdot \boldsymbol{v}_E$ and since $\boldsymbol{v}'$ and $\boldsymbol{v}_E$ are uncorrelated, the average over one cycle of oscillation yields $\langle \boldsymbol{v}^2 \rangle = 3\,v_{\rm th}^2 + v_E^2/2 = 3\,(v_{\rm th}^2 + v_E^2/6)$ since $\langle \boldsymbol{v}'^2 \rangle = 3k_B T_e/m_e = 3\,v_{\rm th}^2$ and $\langle \boldsymbol{v}_E^2 \rangle = v_E^2/2$ (average over 1 cycle of a squared sine is half its amplitude). One recognizes the factor 1/6 between $v_{\rm th}^2$ and v_E^2.

Viewgraph (b) of Fig. 3.6, shows that, within reasonable bounds ($\varepsilon_\ell = 0$ and $C_\ell = 1$ for most models [Brantov *et al.*, 2003, Dawson & Oberman, 1962, Johnston & Dawson, 1973, Jones & Lee, 1982, Landau & Teller, 1936, Mulser *et al.*, 2000, Silin, 1965, Skupsky, 1987] and $\varepsilon_\ell = 1$ and $C_\ell = 0.7$ for [Daligault & Dimonte, 2009, Dimonte & Daligault, 2008]) it is difficult to discriminate between values of ε_ℓ and C_ℓ with our CMDS. Nevertheless, one has chosen to fix $\varepsilon_\ell = 1$ and $C_\ell = 0.7$ to be coherent with [Brown *et al.*, 2005, Daligault & Dimonte, 2009, Dimonte & Daligault, 2008] in the limit of vanishingly small intensities.

Viewgraph (d) of Fig. 3.6 displays several settings of the parameterized model with the best

3.7. Simulations with time varying external electric field dedicated to inverse bremsstrahlung heating

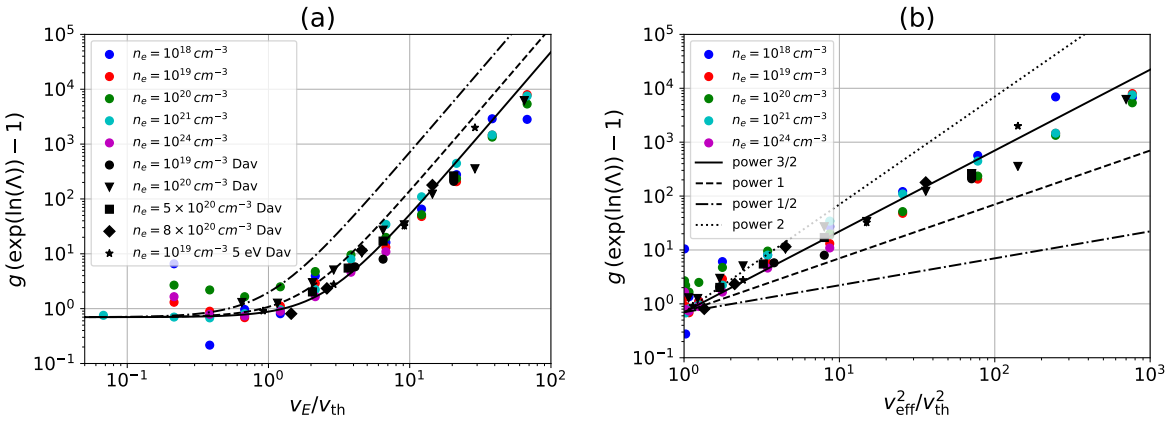

Figure 3.7: (color online) Points represent CMDS simulations from different origins. Colored points, with $\lambda = 351$ nm, for CMDS from the present study and black points, with $\lambda = 1060$ nm, from [David *et al.*, 2004]. On viewgraph (a), these points collapse with $g\,(\exp(\ln(\Lambda)) - 1) \propto (1 + \eta_\ell\, v^2_{\rm eff}/v^2_{\rm th}))^{3/2}$ for $\eta_\ell = 1/6$ in black solid line (dashed line corresponds to $\eta_\ell = 1/3$ and dashed-point line corresponds to $\eta = 1$). On viewgraph (b), molecular dynamics simulations points collapse with $g\,(\exp(\ln(\Lambda)) - 1) \propto (v^2_{\rm eff}/v^2_{\rm th}))^n$ with $n = 3/2$, expected by Mulser [Mulser, 2020, Mulser *et al.*, 2000], that cannot be mistaken with $n = 0$ which is what most other past models advocate [Dawson & Oberman, 1962, Johnston & Dawson, 1973, Jones & Lee, 1982, Landau & Teller, 1936, Silin, 1965, Skupsky, 1987].

match to the CMDS data in red and with models from [Johnston & Dawson, 1973, Jones & Lee, 1982, Silin, 1965] in blue and [Skupsky, 1987] in orange. The variation of the parameter δ clearly shows that $\delta = 1$ is incompatible with CMDS data. The value $\delta = 0$, not content with being in agreement with CMDS data, is also consistent from a theoretical point of view because one expect $\ln(\Lambda^{IB}_{ei})$ to converge towards $\ln(\Lambda^{V}_{ei}) = \ln(\Lambda^{T}_{ei})$ in the vanishingly small intensity limit. In this same limit, if one considers the case $\delta = 1$, one is left with a dependency upon the laser pulsation in the coulombian logarithm whereas the oscillating electric field is almost turned off and that does not make sense.

It is possible to inspect the structure of $\ln(\Lambda^{\rm IB}_{ei})$ by dividing off the prefactor eq. (3.3) to the CMDS heating rate and taking the exponential in order to get $\Lambda^{\rm IB}_{ei}$. This is what was carried out and reported on Fig. 3.7. On viewgraph (a), the parameterized model was plotted for three different values of η_ℓ (entering the expression of $\Lambda^{\rm IB}_{ei}$ in eq. (3.5)) and clearly, even if the collapse of CMDS points is not perfect – but it should be reminded that it is done on the exponential of $\ln(\Lambda^{\rm IB}_{ei})$, that is to say the exponential of CMDS results which increases drastically the uncertainty – viewgraph (a) points toward $\eta_\ell = 1/6$. Moreover, viewgraph (b) shows a clear behaviour of $\Lambda^{\rm IB}_{ei}$ in $(v_E/v_{\rm th})^3$ as explained by Mulser in [Mulser, 2020, Mulser *et al.*, 2000]. All points, including [David *et al.*, 2004], collapse to the $I^{3/2} \propto v_E^3$ behaviour which strongly support that T_e in the Coulomb logarithm should be replaced by $T_{\rm eff}$ of eq. (3.4).

It should be reminded here that only monochromatic oscillations of the electric field are considered. The question to be answered here is whether pulsation should enter the formal expression of the heating rate through the quiver velocity or could it steps in on its own, as reported by many publication starting from [Dawson & Oberman, 1962, Dawson, 1964]. This idea is encapsulated in the constant δ of the parameterized model that is non-zero in many publications as described in Table table A. In order to get an answer to that interrogation, several CMDS have been carried out in the present study (Fig. 3.8), maintaining the initial plasma state

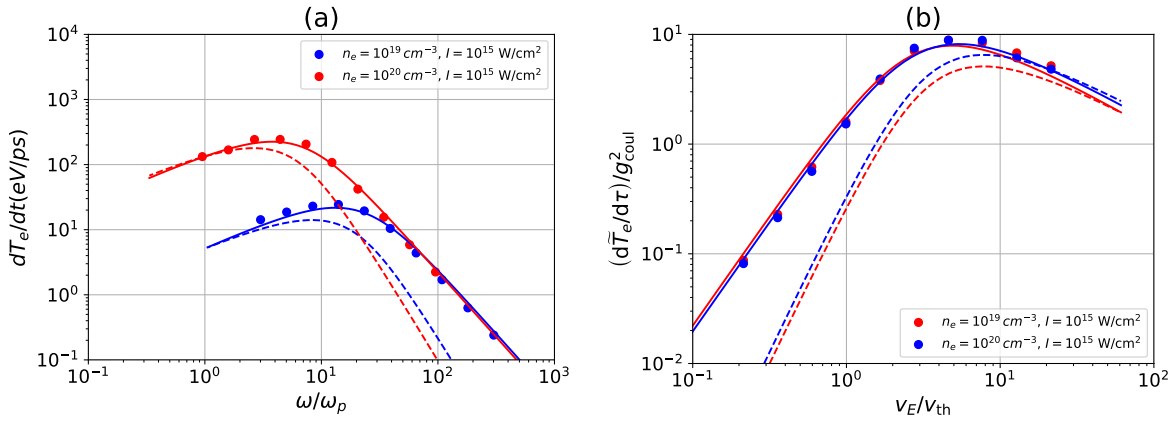

Figure 3.8: (color online) (a) Heating rate versus pulsation in unit of plasma pulsation (ω_p) and (b) adimensionalized heating rate versus adimensionalized quiver velocity. Colored dots correspond to CMDS results at a fixed intensity of 10^{15} W/cm^2 for various laser pulsation (corresponding to wavelengths ranging from 35 to 3500 nm). Solid lines correspond to the best parameterized model with $\delta = 0$ and dashed line with $\delta = 1$.

and the intensity of the irradiation constant and varying only its pulsation (for λ ranging from 30 nm to 3000 nm). In viewgraph (a) results are presented as a function of ω/ω_p and shows that all points considered here are under-critical. This set of simulations, again, strongly supports $\delta = 0$ and viewgraph (b) shows that variations with respect to ω only shows up through $v_E/v_{\rm th}$ as expected from nondimensionalized equations in Section 3.4.2.

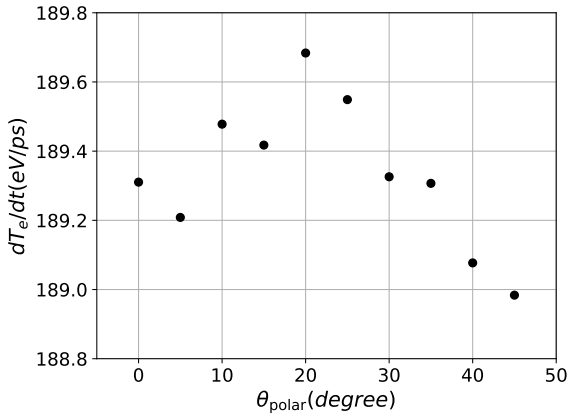

Figure 3.9: Effect of polarization on the heating rate for a plasma at $n_e = 10^{20}$ cm^{-3} and $T_e = 10$ eV and for an intensity of 10^{15} W/cm^2 at 351 nm. The variations observed are of statistical nature due to the finite number of particles in our simulations. As $\theta_{\rm polar}$ is varied, the heating rate does remain constant to within 0.15 % for CMDS carried out with 10^6 ions.

Effects of polarization on heating at a given intensity has also been investigated in the present study (Fig. 3.9). From eq. (3.17), the expression of $\langle E^2(t)\rangle$, where $\langle\,\rangle$ is the time average over one laser period, is $E_1^2\langle cos^2(\omega t)\rangle + E_2^2\langle sin^2(\omega t)\rangle$ and since $\langle cos^2(\omega t)\rangle = \langle sin^2(\omega t)\rangle = 1/2$, it follows $\langle E^2(t)\rangle = (E_1^2+E_2^2)/2$. Let us define, $\theta_{\rm polar}$ such that $E_1 = E_0\,\cos(\theta_{\rm polar})$ and $E_2 = E_0\,\sin(\theta_{\rm polar})$. This yields $\langle E^2(t)\rangle = E_0^2/2$ whatever $\theta_{\rm polar}$. Therefore, by varying $\theta_{\rm polar}$ one spans all possible

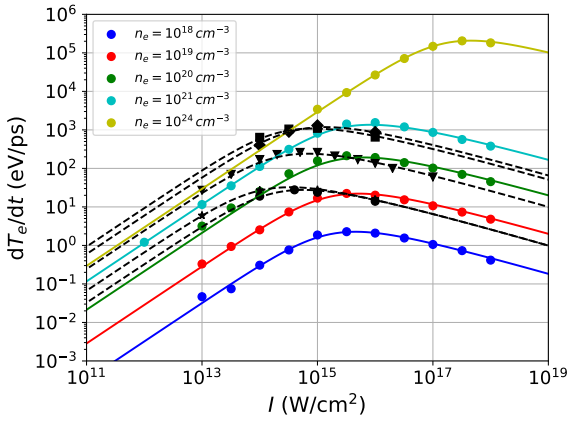

Figure 3.10: (color online) The colored dots represents initial dT_e/dt versus laser intensity for plasmas initially at $T_e = 10$ eV at different electronic densities (10^{18}, 10^{19}, 10^{21}, 10^{21} and 10^{24} cm^{-3}) extracted from our CMDS along with CMDS of David et. al. [David *et al.*, 2004] that are represented by black squares, triangles and stars. Solid colored curves represent the parametrized model for a wavelength of 351 nm, with adjustable constants fixed to the values reported on eqs. (3.48) to (3.53), at the corresponding n_e and T_e. Dashed black curves represent the parametrized model for a wavelength of 1060 nm (which is used in [David *et al.*, 2004]), with adjustable constants fixed to the exact same values eqs. (3.48) to (3.53).

polarizations while keeping the intensity constant. A rectilinear polarization corresponds to $\theta_{\text{polar}} = 0°$, a circular polarization corresponds to $\theta_{\text{polar}} = 45°$ and all other elliptical polarizations range between 0 and 45°. The result in Fig. 3.9 shows that there is no dependence of the heating rate upon polarization as seen from CMDS, at least, for low Z plasma.

n_e (cm^{-3})	T_e (eV)	λ (nm)	I (W/cm^{-2})	C_{abs}	data
10^{18}	10	351	varI	0.48	Fig. 3.10
10^{19}	10	351	varI	0.56	Fig. 3.10
10^{20}	10	351	varI	0.60	Fig. 3.10
10^{21}	10	351	varI	0.54	Fig. 3.10
10^{24}	10	351	varI	0.44	Fig. 3.10
10^{19}	10	varλ	10^{15}	0.55	Fig. 3.8
10^{20}	10	varλ	10^{15}	0.65	Fig. 3.8

Table B: In this table, values of C_{abs} are reported for different series of CMDS either by maintaining a constant laser wavelength of 351 nm and varying the intensity from 10^{14} W/cm^2 to 10^{18} W/cm^2 (varI) or by maintaining the intensity constant at 10^{15} W/cm^2 and varying the wavelength from 35 to 3500 nm (varλ).

The last point that needs to be addressed is the value of the overall factor C_{abs} in the parameterized model eqs. (3.2) to (3.5). The way it is done in our numerical experiments is that this adjustable constant is calculated by fitting the parameterized model (with $\eta = \eta_\ell = 1/6$, $\varepsilon_\ell = 1$, $C_\ell = 0.7$ and $\delta = 0$) to each set of CMDS data at constant n_e, T_e. There were two kinds of data sets : those (i) maintaining the laser wavelength constant and varying the laser intensity Fig. 3.10 and those (ii) maintaining the laser intensity constant and varying the laser wavelength Fig. 3.8. Values of C_{abs} were found to be scattered around 0.55 within a standard deviation of 0.07 as computed from table B. Therefore, in a nutshell, that analysis as enabled to fix the six

free parameters to the following values

$$C_{\text{abs}} = 0.55 \pm 0.07, \tag{3.48}$$
$$\eta = 1/6, \tag{3.49}$$
$$\epsilon_\ell = 1, \tag{3.50}$$
$$C_\ell = 0.7, \tag{3.51}$$
$$\eta_\ell = 1/6, \tag{3.52}$$
$$\delta = 0. \tag{3.53}$$

Our CMDS results for velocity relaxation (for $I = 0$), in Fig. 3.4, match theoretical results [Brown *et al.*, 2005] and molecular dynamic simulations by Dimonte and Daligault [Daligault & Dimonte, 2009, Dimonte & Daligault, 2008] with $C_{\text{abs}} = 1$. One cannot provide solid explanation as to what might be causing this variation of C_{abs} from 1 when $I = 0$ W/cm^2 to 0.55 when I is a least above 10^{13} W/cm^2 (which is the intensity domain we have been able to probe in our CMDS) but if one goes back to eq. (3.18), one can, however, notice that the limit $I = 0$ (no-radiation limit) is reached when $g_{\text{osc}} \ll g_{\text{coul}}$ which can be recast as

$$I \ll \frac{e^2\, c}{8\pi\,(4\pi\varepsilon_0)}\, Z^{2/3}\, n_e^{4/3}, \tag{3.54}$$

that, interestingly enough, does not depend on T_e but only on n_e and Z. As an example, for $n_e = 10^{22}$ cm^{-3} and $Z = 1$, it amounts to saying that the no-radiation limit is bound to the domain $I \ll 5.95 \times 10^{12}$ W/cm^2. A change in behavior (that could explain the C_{abs} shift from 0.55 to 1) may therefore appear below this intensity. We have not been able to assess this domain because it would have required running CMDS over prohibitively long times to overcome the loss of signal to noise ratio (The small T_e increase, due to small intensities, is buried under the thermal fluctuations of T_e due to the limited number of particles in the CMDS).

3.8 Conclusion

The heating rate due to laser absorption by inverse bremsstrahlung is evaluated using the parameterized model described in eqs. (3.2) to (3.5), which takes into account most models proposed in the literature (cf. table A) with appropriate parameter values ($\boldsymbol{C_{\text{abs}}}, \boldsymbol{\eta}, \boldsymbol{\epsilon_\ell}, \boldsymbol{C_\ell}, \boldsymbol{\eta_\ell}, \boldsymbol{\delta}$).

It was compared to results from classical molecular dynamic simulations (CMDS) carried out with LAMMPS [Thompson *et al.*, 2022]. These simulations where shown to be in very good agreement with previous CMDS (with [Daligault & Dimonte, 2009, Dimonte & Daligault, 2008] for velocity relaxation and with [David *et al.*, 2004] for inverse bremsstrahlung). CMDS presented here were carried out for a wide class of weak to moderate plasma coupling, for a wide variation of laser intensities (five orders of magnitude) for a fixed pulsation or for a wide variation of pulsations (two decades) for a fixed intensity.

It was found that CMDS do not back up the rule, first put to the forth by Dawson & Oberman [1962], Dawson [1964] and derived by Silin [1965] for low intensity irradiation (as described in our section 3.9), that ω_p in the expression of the Coulomb logarithm should be replaced by ω when $\omega \gg \omega_p$ or equivalently $\delta = 1$ in our parametrized model. From a theoretical stand point, it

tends to show that modeling the inverse bremsstrahlung heating should be done self-consistently by taking into account collective effects from first principles rather than assuming that they can be evaluated separately through a coulomb logarithm depending on ad-hoc choices of short and long range characteristic lengths ($b_{\min}$ and $b_{\min}$).

Our classical molecular dynamic simulations of inverse bremsstrahlung heating are consistent with the parametrized model set to $\eta = \eta_\ell = 1/6$, $\epsilon_\ell = 1$, $C_\ell = 0.7$, $\delta = 0$ and $C_{\rm abs} = 0.55$ which also matches previous CMDS by David *et al.* [2004].

3.9 Appendix A: Silin's formula at low intensity

In his seminal paper, Silin [1965] did not derive explicitly a formula for the electron-ion frequency in the process of IB at low irradiation intensity. In [Decker *et al.*, 1994], the authors said : "*He [Silin] presented a general expression for the collision frequency in terms of complicated integrals. In the limit $v_E/v_{\rm th} \ll 1$ a closed form expression can be obtained and it is identical to that from the Dawson-Oberman model*". This is the calculation of this limit, from the *complicated integrals*, that we present in this appendix.

From eq. (3.8) of [Silin, 1965], instead of taking the limit of supra-critical plasma ($n_e \gg n_c$ or equivalently $\omega \ll \omega_p$ as in eq. (3.2) in [Silin, 1965]) we take the low intensity limit, that is to say $\rho \ll 1$ in eq. (3.9) which corresponds to $e\,E_0/m\omega\,v_T \ll 1$ in eq. (3.8) of [Silin, 1965].

The electron-ion collision frequency in the process of inverse-Bremsstrahlung heating is given by

$$\nu = \frac{16NiZ^2e^2\omega^3m_e}{e\,E_0^3}\left[R\left(\frac{eE_0}{m\omega v_T},\frac{v_Tk_{\max}}{\omega}\right) - R\left(\frac{eE_0}{m\omega v_T},\frac{v_Tk_{\min}}{\omega}\right)\right], \tag{3.55}$$

where the function R is defined by

$$\begin{aligned} R(\rho,x) = \rho\int_0^x \mathrm{d}z\int_0^\infty \mathrm{d}y\, J_0(2\rho z\sin(y/2)) \\ \times\left[e^{-x^2y^2/2} + \frac{1}{2}\,Ei\left(-\frac{x^2y^2}{2}\right)\right. \\ \left. -e^{-z^2y^2/2} - \frac{1}{2}\,Ei\left(-\frac{z^2y^2}{2}\right)\right]. \end{aligned} \tag{3.56}$$

In the limit ρ small, $J_0(x)$ can be expanded as $1 - x^2$ at second order. If J_0 is replaced by its first order, that is 1, in eq. (3.56), then it is straightforward to show that $R = 0$. Therefore, the first non vanishing term of the development of R is due to the second order of the development of J_0. Therefore,

$$\begin{aligned} R(\rho,x) \approx -4\rho^3\int_0^x \mathrm{d}z\, z^2\int_0^\infty \mathrm{d}y\sin^2(y/2)) \\ \times\left[e^{-x^2y^2/2} + \frac{1}{2}\,Ei\left(-\frac{x^2y^2}{2}\right) - e^{-z^2y^2/2}\right. \\ \left. -\frac{1}{2}\,Ei\left(-\frac{z^2y^2}{2}\right)\right]. \end{aligned} \tag{3.57}$$

Since

$$\int_0^\infty \mathrm{d}y \sin^2(y/2)) \left[e^{-x^2y^2/2} + \frac{1}{2}\,\mathrm{Ei}\left(-\frac{x^2y^2}{2}\right)\right] = \frac{\pi}{4}\mathrm{Erf}\left(\frac{1}{\sqrt{2}x}\right) - \frac{\sqrt{2\pi}}{4}\frac{e^{-\frac{1}{\sqrt{2}x}}}{x}, \tag{3.58}$$

the last integral, over z, in eq. (3.57) can be recast as

$$R(\rho,x) \approx -4\rho^3 \int_0^x \mathrm{d}z\, z^2 \left(\frac{\pi}{4}\mathrm{Erf}\left(\frac{1}{\sqrt{2}x}\right) - \frac{\sqrt{2\pi}}{4}\frac{e^{-\frac{1}{\sqrt{2}x}}}{x} - \frac{\pi}{4}\mathrm{Erf}\left(\frac{1}{\sqrt{2}z}\right) + \frac{\sqrt{2\pi}}{4}\frac{e^{-\frac{1}{\sqrt{2}z}}}{z}\right), \tag{3.59}$$

and yields

$$R(\rho,x) \approx -\frac{\rho^3}{12}\sqrt{\frac{\pi}{2}}\,\mathrm{Ei}\left(-\frac{1}{2x^2}\right). \tag{3.60}$$

One can then write the collision in the inverse Bremsstrahlung context as

$$\nu = \frac{1}{2}\nu_0 \left[\mathrm{Ei}\left(-\frac{\omega^2}{2v_T^2 k_{\min}^2}\right) - \mathrm{Ei}\left(-\frac{\omega^2}{2v_T^2 k_{\max}^2}\right)\right] \tag{3.61}$$

and since $k_{\min} = 2\pi/b_{\max}$ and $k_{\max} = 2\pi/b_{\min}$ (where $b_{\max}$ and $b_{\min}$ are not deduced from first principle as in BPS but just cut-off of the theory), one can specified $2v_T^2 k_{\min}^2$ to be ω_p^2 and then $2v_T^2 k_{\max}^2 = 2v_T^2 k_{\min}^2 (k_{\max}^2/k_{\min}^2) = \omega_p^2\,\Lambda^2$. The final result is

$$\nu = \nu_0\,\ln(\Lambda_{\mathrm{Sil}}) \tag{3.62}$$

where

$$\ln(\Lambda_{\mathrm{Sil}}) = \frac{1}{2}\left[\mathrm{Ei}\left(-\frac{\omega^2}{\omega_p^2}\right) - \mathrm{Ei}\left(-\frac{\omega^2}{\omega_p^2\,\Lambda^2}\right)\right] \tag{3.63}$$

is displayed in Fig. 3.11. The coulomb logarithm from Silin $\ln(\Lambda_{\mathrm{Sil}}) = \ln(\Lambda)$ when $\omega \ll \omega_p$ (in the over-critical regime, which corresponds to eq. (3.12) in [Silin, 1965]) and it goes to $\ln(\Lambda_{\mathrm{Sil}}) = \ln(\Lambda\frac{\omega_p}{\omega}\,e^{-\gamma/2})$ when $\omega \gg \omega_p$ (in the super-critical regime, of interest to ICF) where $\gamma \approx 0.577$ is the Euler constant. It is interesting to note that if one write

$$\Lambda = b_{\max}/b_{\min} = v_{\mathrm{th}}\,k_{\max}/\omega_p, \tag{3.64}$$

the $\Lambda_{\mathrm{Sil}} = \Lambda\frac{\omega_p}{\omega}$ when $\omega \gg \omega_p$ amounts to replacing ω_p in eq. (3.64) by ω which is exactly what is done in Dawson-Oberman [Dawson & Oberman, 1962] in eq. (26), in Johnston-Dawson [Johnston & Dawson, 1973] just below eq. (1.b), in Jones-Lee [Jones & Lee, 1982] above eq. (28) "the small wave number cut-off is ω/v_{th}", in Skupsky [Skupsky, 1987] with its explicit prescription in eq. (3.a) and in Mulser et. al. [Mulser *et al.*, 2000] in eq. (15) and eq. (16).

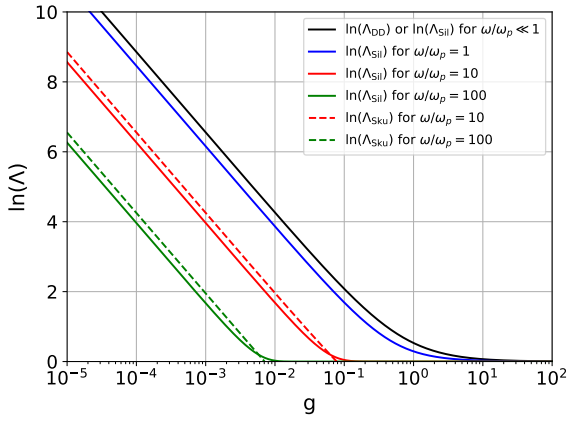

Figure 3.11: (color online) Plot of $\ln(\Lambda_{\rm Sil})$ using $\Lambda = \Lambda_{\rm DD} = (1 + 0.7/g)$ from Daligault and Dimonte [Dimonte & Daligault, 2008] for various values of ω/ω_p and compared to Skupsky's prescription which consists in replacing ω_p by ω in $\Lambda = \frac{b_{\rm max}}{b_{\rm min}} = \frac{v_{\rm th}\, k_{\rm max}}{\omega_p}$ as soon as $\omega > \omega_p$. Clearly Skupsky's prescription is close to Silin results but none of these theoretical predictions match molecular dynamics simulation results.

3.10 Appendix B: Details on the constants reported in table A

In Dawson-Oberman [Dawson & Oberman, 1962] or Johnston-Dawson [Johnston & Dawson, 1973], the collision frequency is provided in the low intensity ($v_E \ll v_{\rm th}$) and high frequency ($\omega \gg \omega_p$) limit, $C = 1$ and $\ln(\Lambda_{ei}^{(IB)}) = \ln(\Lambda\,\omega/\omega_p) - \gamma$ where $\gamma \approx 0.577$ is the Euler constant. Skupsky [Skupsky, 1987], in its development about classic plasmas (as opposed to quantum), used similar Coulomb logarithm of the form $\ln(\Lambda_{ei}^{(IB)}) = \ln(\Lambda\,\omega/\omega_p)$ in the high frequency limit.

In Silin [Silin, 1965], for the low intensity ($v_E \ll v_{\rm th}$) and low frequency ($\omega \ll \omega_p$) limit, it is found that $C = 1$ and $\ln(\Lambda_{ei}^{(IB)}) = \ln(\Lambda)$ and for the high frequency limit ($\omega \gg \omega_p$) it is found that $C = 1$ and $\ln(\Lambda_{ei}^{(IB)}) \approx \ln(\Lambda\,\omega/\omega_p)$ (cf. appendix section 3.9). In the high intensity ($v_E \gg v_{\rm th}$) and low frequency ($\omega \ll \omega_p$) limit (eq. eq. (3.13) from [Silin, 1965]), it is found that $\nu = 16 N_i e_i^2 m\omega^3/eE_0^3\{\ln(v_E/2v_{\rm th}) + 1\}\ln(\Lambda)$ which, in our notation, should correspond to eq. (3.12) of [Silin, 1965] where v_T^2 is replaced by the high intensity limit $\eta\, v_E^2$ that yields to $\nu = 4\sqrt{2\pi} N_i e_i^2 m\omega^3/3e\,\eta^{3/2} E_0^3\{\ln(v_E/2v_{\rm th}) + 1\}\ln(\Lambda)$ implying $\eta = (4\sqrt{2\pi}/3/16)^{2/3} \approx 0.221$ reported in the fourth line of table table A.

In Jones-Lee [Jones & Lee, 1982], for high intensities ($v_E \gg v_{\rm th}$) it is found (eq. (63) in [Jones & Lee, 1982]) that the prefactor is the same as in Silin [Silin, 1965] but with $\ln(\Lambda_{ei}^{(IB)}) = \ln(\Lambda\,\omega_p/\omega)$ and a slightly different logarithmic factor depending upon v_E namely $\ln(v_E/v_{\rm th})$ instead of $\ln(v_E/2v_{\rm th})$.

In Mulser[Mulser, 2020], in eq. (7.71) when $\omega \gg \omega_p$, $\ln(\Lambda_{ei}^{(IB)}) = \ln(\Lambda\,\omega_p/\omega)$ with $(v_{\rm th}^2)^{3/2}$ in $b_{\rm max}$ replaced by $(v_{\rm th}^2 + v_E^2/4)^{3/2}$ or by $(v_{\rm th}^2 + v_E^2)^{3/2}$ in [Mulser *et al.*, 2000].

In Brantov et al. [Brantov *et al.*, 2003], what is called the effective collision in eqs.(19) or (20) of this reference, sums up to $C = (v_{\rm th}^2/(v_{\rm th}^2 + v_E^2/6))^{3/2}$ or $C = (v_{\rm th}^2/(v_{\rm th}^2 + v_E^2 * 0.3))^{3/2}$ in our notations and $\ln(\Lambda_{ei}^{(IB)}) = \ln(\Lambda\,\omega_p/\omega)$ when $\omega \gg \omega_p$ in eq.(3) of [Brantov *et al.*, 2003].

Chapter 4

Molecular Dynamics Simulations of moderate-Z plasmas

Contents

The following is the text of an article in preparation entitled "Classical molecular dynamic simulation to assess the non-Maxwellian behavior of inverse bremsstrahlung heating in weakly coupled plasmas" by R. Devriendt and O. Poujade.

4.1 Introduction

Collisional absorption of laser radiation by a plasma through the process of inverse bremsstrahlung is dominant for intensities less than $10^{15}\,\mathrm{W/cm^2}$. A precise modelling of this physical effect in

radiation-hydrodynamics codes [Lefebvre *et al.*, 2018, Marinak *et al.*, 2001] is paramount to designing inertial confinement fusion experiments [Betti & Hurricane, 2016] in order to reach the goal of thermonuclear ignition.

When a monochromatic electromagnetic wave (laser) of pulsation ω and intensity I propagates through a plasma of electronic density n_e and temperature T_e, electrons undergo an oscillating coherent motion at the same pulsation superimposed to their random thermal motion of characteristic velocity $v_{\text{th}} = \sqrt{k_B T_e / m_e}$. The velocity amplitude of this collective motion is given by $v_{\text{osc}} = e\,E/m_e\,\omega$ known as the quiver velocity where $E = \sqrt{2\,I/c\,\varepsilon_0}$ is the amplitude of the electric field of the wave. Then, some of the energy carried by the electromagnetic wave is transferred to electrons and ions thermal energies (random motion kinetic energy) by means of their random scatterings. Obviously, this process affects the electron velocity distribution (EVD). It modifies the width of its Maxwellian shape, since the electron temperature increases, but it can also modify the overall shape, turning the Maxwellian into a drastically different distribution, such as a Supergaussian as predicted theoretically by Langdon [1980]. It happens when electron-electron (e-e) collisions are not efficient enough to damp any deviations from the Maxwellian.

Langdon [1980] devised a nondimensional parameter

$$\alpha = Z\,\frac{v_{\text{osc}}^2}{v_{\text{th}}^2} = Z\,\frac{2\,e^2\,I}{c\,\varepsilon_0\,m_e\,\omega^2\,k_B T_e}, \tag{4.1}$$

such that e-e collisions are negligible when $\alpha \gg 1$. Solving Boltzmann equation with a Fokker-Planck collision term, assuming $v_{\text{osc}}/v_{\text{th}} \ll 1$ and neglecting e-e collisions (therefore assuming $Z \gg 1$ because of eq. (4.1)), Langdon showed that the EVD of such a plasma submitted to an oscillating electric field, reaches an asymptotic self similar state described by a Supergaussian EVD

$$f_e^{SG}(\boldsymbol{v}) \propto \exp(-v^k) \tag{4.2}$$

as will be described in more detail in section 4.5 of this paper. The parameter k is called the order of the Supergaussian and it tends asymptotically and monotonically towards a value depending upon α comprised between $k = 2$ (when $\alpha = 0$) and $k = 5$ (when $\alpha \gg 1$) according to Langdon's derivation. This deformation may result in a reduction of absorption by a significant factor when compared to the case $\alpha = 0$ (still assuming $v_{\text{osc}}/v_{\text{th}} \ll 1$). Subsequently, Fokker-Planck simulations (FPS) confirmed [Jones & Lee, 1982, Weng *et al.*, 2006] Langdon's finding, and the authors of these simulations proposed [Matte *et al.*, 1988, Weng *et al.*, 2009] a fit for the order of the EVD, namely $k(\alpha)$, as well as the reduction in absorption relative to a Maxwellian EVD, namely $R(\alpha)$, as functions of α.

Other shapes of EVDs have been suggested in the literature. A sum of a Supergaussian with a Maxwellian tail [Fourkal *et al.*, 2001] was put forward for low laser intensities because e-e collisions could become more important than e-i collisions for the population of electrons lying in the supra-thermal tail of the EVD. As an other example, for high laser intensity ($v_{\text{osc}}/v_{\text{th}} \gg 1$), it is expected [Ferrante *et al.*, 2001] that temperatures parallel and perpendicular to the electric field polarization grow at different rates. This could result in two-temperature oscillating Maxwellian [Chichkov *et al.*, 1992, Pfalzner, 1992] or Supergaussian [Porshnev *et al.*, 1996] EVDs.

Recent, high energy density experiments confirmed [Liu *et al.*, 1994, Milder *et al.*, 2021,

2020, Turnbull *et al.*, 2020] that non-Maxwellian distributions do form in laser induced plasmas. Observations of these EVDs have proved that shapes are clearly non-Maxwellian and look a lot like supergaussians [Langdon, 1980] but they are not precise enough to discriminate all shapes proposed in the theoretical literature.

In classical molecular dynamics simulations (CMDS), which are numerical simulations at the microscopic scale, EVD distortion was also observed by Pfalzner & Gibbon [1998] for $Z = 1$. Nevertheless, that distortion was not observed in Langdon's conditions requiring [Langdon, 1980] both $v_{\mathrm{osc}}/v_{\mathrm{th}} \ll 1$ and $Z\,v_{\mathrm{osc}}^2/v_{\mathrm{th}}^2 \gg 1$ which can only be fulfilled if $Z \gg 1$. It was observed at $v_{\mathrm{osc}}/v_{\mathrm{th}} \gg 1$, which is the only possibility to get $\alpha \gg 1$ with a $Z = 1$ plasma. Moreover, the EVD unveiled in Pfalzner & Gibbon [1998] was averaged over one laser cycle. Therefore, the distortion can either be due to the averaging process that results in a non-Maxwellian averaged EVD out of an oscillating instantaneous Maxwellian EVD or because the instantaneous EVD itself is already distorted. The cycle-averaged EVD is different from the instantaneous EVD for it integrates the coherent oscillating motion of the EVD in phase space (velocity space) produced by the varying electric field. A clear distinction between instantaneous and cycle-averaged EVD is therefore of the essence, as shown in section 4.10.

Ersfeld & Bell [2000] studied the anisotropy of the instantaneous distribution at high laser intensity using a Fokker-Planck code (FP) with high-order Legendre polynomials. The isotropic, cycle averaged and exact distribution yielded similar heating rate. However, in Fokker-Planck codes, collisions have to be modelled and an analytical expression of the coulomb logarithm, as a function of plasma state parameters (electronic density, temperature, etc.), has to be provided as an input data. This is not the case in CMDS where collisions are inherently taken into account.

In this work, we will study the distortion of the instantaneous distribution at higher $Z = 10$ using classical molecular dynamic simulations in order to probe Langdon's insight for a large range of $v_{\mathrm{osc}}/v_{\mathrm{th}}$, and the effect of this distortion on the electron heating rate. We will first start by detailing the setup of our CMDS simulations, before showing CMDS results of plasmas with $v_{\mathrm{osc}}/v_{\mathrm{th}} \ll 1$ and $Z v_{\mathrm{osc}}^2/v_{\mathrm{th}}^2 \gg 1$, which are the exact conditions predicted by Langdon to observe non-Maxwellian EVDs. We will then present CMDS at high laser intensity, *i.e.* $v_{\mathrm{osc}}/v_{\mathrm{th}} > 1$, in order to extend Langdon's results. We will then reproduce recent experimental results [Milder *et al.*, 2021], where the sum of a Maxwellian and a Supergaussian was measured. In section 4.6, we will compare the order of the distribution as a function of $v_{\mathrm{osc}}/v_{\mathrm{th}}$ from our CMDS simulations with the predictions of Matte *et al.* [1988]. Finally, we will look at how the distortion of the EVD affects the heating rate. To do so, we will first shortly recall the absorption model developed in chapter 2 before testing it against our CMDS.

4.2 Classical molecular dynamic simulations setup

We carried out classical molecular dynamic simulations (CMDS) of a two components plasma (electrons and one kind of ions with ionization $Z = 10$) using the code LAMMPS [Thompson *et al.*, 2022]. Large simulations with $4 \cdot 10^5$ electrons and $4 \cdot 10^4$ ions where carried out in our study contrasting with 10^4 particles in Pfalzner & Gibbon [1998] or in David *et al.* [2004]. In CMDS, particles are described by their charges, positions and velocities and evolve according to Newton's law. Electrostatic Coulomb forces between each individual particles (electron-electron, ion-ion and electron-ion) are taken into account and for the problem at hand, namely radiation

absorption by inverse bremsstrahlung, an external oscillating electric field with its interaction with each charges of the simulated plasma is taken into account.

Since the pure Coulomb potential is not valid at very short range where the electronic structure of the ion should be taken into account, particles in CMDS interact with each other via a modified Coulomb potential. A soft core was added [Beutler *et al.*, 1994] to the Coulomb potential in such a way that the interaction potential between two generic charges q_1 and q_2 is

$$\phi(r) = \frac{q_1\, q_2}{4\,\pi\,\varepsilon_0\,\sqrt{r_c^2 + r^2}}, \tag{4.3}$$

where r is the distance between q_1 and q_2 and r_c is the approximate distance below which the pure Coulomb potential ceased to be meaningful. We chose $r_c = 0.1\,\text{Å}$ and checked that our results were not dependent on the particular choice of r_c provided it is small enough. Additionally, periodic boundary conditions were used to simulate an infinite uniform plasma and this is why LAMMPS' Particle-Particle Particle-Mesh (PPPM) algorithm was used to compute interactions with domain replicas.

Particular care was given to the production of the initial states of our CMDS. Equilibrium EVD and ion velocity distributions can be generated easily, since they are known to be Maxwellian at thermodynamic equilibrium, contrary to the equilibrium spatial distributions. In order to circumvent this problem, particles were initially distributed at random in the simulation domain. Using a thermostat in LAMMPS, they were then left to relax until equilibrium was reached. To speed up this relaxation, the ion and electron temperatures were regularly rescaled to their desired values. This phase lasted for a few electron-ion collision times, until a steady state was reached, which was monitored via the potential energy of the system, the ion and electron temperatures, the EVD and the quadrupole (see chapter 3).

In order to encompass both subcritical and critical plasmas, where $n_c = 9 \times 10^{21}\,\text{cm}^{-3}$ for $\lambda = 351\,\text{nm}$, one initial state was generated with $n_e = 10^{20}\,\text{cm}^{-3}$ (corresponding to $n_e < n_c$) and another one with $n_e = 10^{22}\,\text{cm}^{-3}$ (corresponding to $n_e \sim n_c$). The choice of initial T_e for both initialization was set by the choice of the plasma coupling parameter [Dimonte & Daligault, 2008], (see Chapter 3)

$$g = \frac{Z\,e^3\,\sqrt{n_e}}{4\,\pi\,(\varepsilon_0\,k_B T_e)^{3/2}}, \tag{4.4}$$

that we fixed to the same value ($g \ll 1$ for a weakly coupled plasma) for comparison purposes. The chosen value, $g = 0.05$, is a compromise between plasma weakness, for which one would advocate for small values of g, and not-too-high-numerical-cost, for which one would advocate for high values of g (see section 3.5.2). This is why we generated two initial conditions

$$n_e = 10^{20}\,\text{cm}^{-3},\ k_B T_e = 100\,\text{eV},\ Z = 10, \tag{4.5}$$

$$n_e = 10^{22}\,\text{cm}^{-3},\ k_B T_e = 500\,\text{eV},\ Z = 10. \tag{4.6}$$

For both initial conditions, multiple initial states were generated, in order to reduce the effect of statistical fluctuations on our results.

In our CMDS, a time varying, spatially uniform, external electric field mimics the effect of a laser in a small simulation volume. It is periodic in time and polarization is linear. The spatial uniformity of the electric field means that effects arising from the spatial periodicity of the laser,

such as the dispersion relation, are not captured by such CMDS (it was also the case in Pfalzner & Gibbon [1998] and David *et al.* [2004]).

In chapter 3, which was dedicated to $Z = 1$ weakly coupled plasma, we have devised a parametrized model for electron-ion collision frequency in the IB heating process with constants adjusted by CMDS (for $Z = 1$ plasmas). The model is given by eqs. (3.2) to (3.5), which we recall here for convenience

$$\nu_{ei}^{IB} = \boldsymbol{C_{abs}}\, \nu_0[n_e,\, T_{\text{eff}}(\boldsymbol{\eta}),\, Z]\, \ln(\Lambda_{ei}^{IB}), \tag{4.7}$$

$$\nu_0[n_e,\, T_e,\, Z] = \frac{4\,\sqrt{2\,\pi}\,e^4}{3\,\sqrt{m_e}\,(4\,\pi\,\epsilon_0)^2}\,\frac{n_e\,Z}{(k_B T_e)^{3/2}}, \tag{4.8}$$

$$T_{\text{eff}}(x) = T_e + x\; m_e\, v_E^2/k_B, \tag{4.9}$$

$$\Lambda_{ei}^{IB} = \left[\boldsymbol{\epsilon_\ell} + \boldsymbol{C_\ell}\,\frac{4\,\pi\,\varepsilon_0^{\frac{3}{2}}\,(k_B T_{\text{eff}}(\boldsymbol{\eta_\ell}))^{3/2}}{Z\,e^3\,\sqrt{n_e}}\right]\,\left(\frac{\omega_p}{\omega}\right)^{\boldsymbol{\delta}}, \tag{4.10}$$

with adjusted constants given in eqs. (3.49) to (3.53) as

$$\eta = 1/6, \tag{4.11}$$

$$\epsilon_\ell = 1, \tag{4.12}$$

$$C_\ell = 0.7, \tag{4.13}$$

$$\eta_\ell = 1/6, \tag{4.14}$$

$$\delta = 0. \tag{4.15}$$

In Fig. 4.1, this parametrized model, with constants adjusted for $Z = 1$, is compared to CMDS results (red and blue points) for the $Z = 10$ plasmas described in eq. (4.5) and eq. (4.6). The points correspond to measurement of the heating rate at early time, when the EVDs are still Maxwellian, because the parametrized model has been devised from different theoretical models assuming Maxwellian EVDs. Clearly, with the same parameters devised from $Z = 1$ simulations, the agreement is still very good for $Z = 10$ plasmas at early time. This last precision is of course very important for the remaining of this paper will deal with late time evolution of $Z = 10$ plasmas where EVDs turn non-Maxwellian.

Ideally, one would like to produce fits for $k(\alpha)$ and $R(\alpha)$ out of our CMDS and compare them with those obtained in Matte *et al.* [1988] by FP simulations in the case of uniform plasmas. As mentioned by these authors, in the absence of sink mechanism (which is the case for FPS of uniform plasmas and also for our CMDS) the value of α, defined in eq. (4.1), is not constant and decreases as the electron temperature of the plasma (T_e) increases due to the laser heating at constant intensity. This is the reason why, in the fitted functions k and R provided by Matte *et al.* [1988], the values of α are not the initial values but the end-of-the-simulation value (when the self-similar behaviour is achieved). The problem we observed in our CMDS is that the time it takes for the EVD to reach the self-similar regime increases with laser intensity. As a result, for a given CMDS duration, this limits the range of α where it is possible to observe that self-similar evolution of the EVD. Hence, our simulations were carried out in the range

$$0.1 < v_{\text{osc}}/v_{\text{th}}^0 < 5, \tag{4.16}$$

where v_{th}^0 is the initial thermal velocity. Increasing the intensity further ($v_{\text{osc}}/v_{\text{th}}^0 > 5$) would have a high numerical cost because a smaller timestep would be needed to accurately capture high velocity electrons and the number of time iterations would jump drastically. On the contrary, reducing the intensity ($v_{\text{osc}}/v_{\text{th}}^0 < 0.1$) would come into conflict with signal to noise ratio in the CMDS because heating rate would be too small and buried under thermal fluctuations.

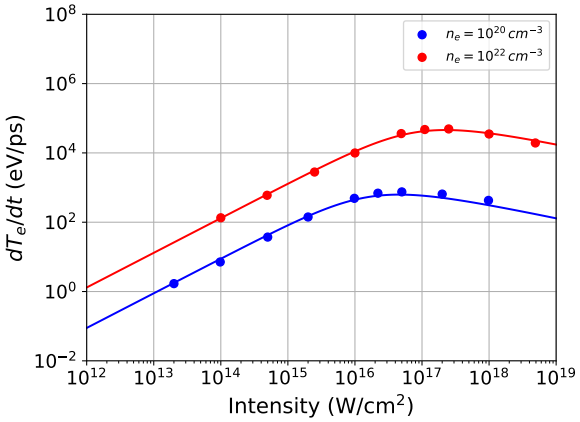

Figure 4.1: Heating rate for both plasmas described in eq. (4.5) and eq. (4.6) at different intensities measured at early time to ensure that EVDs have not yet transitioned to non-Maxwellian which is the hypothesis of the parametrized model developed in chapter 3. The coefficients of the model are those adjusted in chapter 3 by CMDSs at $Z = 1$ and one can see that the agreement is excellent even for $Z = 10$.

4.3 Langdon effect impacts the instantaneous distribution

In order to assess the effects of an oscillating electric field on a plasma EVD, it is important to introduce two distributions of practical interest for the description of the results presented in this work. The first one, the isotropic distribution, corresponds to the isotropic part of the 3D distribution. It is that isotropic distribution that was inferred by Langdon in its seminal paper [Langdon, 1980]. The second one, the projected distribution, is particularly useful when 3D distributions are anisotropic.

In order to precisely define these two distributions, let us call the 3D distribution

$$f_e(\boldsymbol{v}) \tag{4.17}$$

such that $f_e(\boldsymbol{v})\ \mathrm{d}^3\boldsymbol{v}$ corresponds to the number of electrons of velocity $\boldsymbol{v}$ within $\mathrm{d}^3\boldsymbol{v}$. It can be computed in CMDS by sampling the whole 3D velocity space in small 3D sampling-cubes and by counting the number of particles with velocities in each of these sampling-cubes. However, it requires a very high number of particles to be accurate in a large velocity domain and is therefore unpractical.

The isotropic distribution is computed from the 3D distribution $f_e(\boldsymbol{v})$, where the velocity vector can be recast as $\boldsymbol{v} = v\,\boldsymbol{\Omega}$, by fixing the modulus v and averaging over all directions $\boldsymbol{\Omega}$ and

defined as

$$f_e^0(v) = \frac{1}{4\,\pi} \int f_e\,(\boldsymbol{v})\ \mathrm{d}^2\Omega. \tag{4.18}$$

It is used in Fokker-Planck codes, and is especially useful when the 3D distribution is close to isotropic which is the assumption in Langdon [1980]'s and Matte *et al.* [1988]'s results. However, the laser electric field inherently introduces anisotropy in the 3D distribution as will be shown in section 4.4. It is thus appropriate to consider a last category of distributions.

The projected distributions are obtained by integrating the 3D distribution over the two dimensions perpendicular to the axis of projection. As an example, the projected distribution on the x-axis requires to integrate over y and z such that

$$f_x(v_x) = \int f_e(v_x,\, v_y,\, v_z)\ \mathrm{d}v_y\ \mathrm{d}v_z. \tag{4.19}$$

Because we only consider linear polarization, two projections are of interest: along the direction of the electric field, and perpendicularly. Indeed, the projected distribution is expected to be the same along any of the directions perpendicular to the electric field. In the rest of this paper quantities along the direction of the electric field will be referred to as parallel ($/\!/$) and quantities referred to as perpendicular ($\perp$) are in a direction perpendicular to the electric field.

In the perspective of describing non-Maxwellian effects displayed by our CMDS, we first tried to ascertain the degree of distortion of instantaneous EVDs. Indeed, time-averaged EVDs, often reported in the literature, can be distorted by two mechanisms.

The first one, that we call the *sweeping mechanism*, can cause an instantaneous Maxwellian EVD to become non-Maxwellian in the one-cycle-averaging process because of its oscillation in $\boldsymbol{v}$-space around the origin due to the collective oscillation triggered by the oscillating electric-field. This effect can indeed modify collisional absorption as pointed out by Mulser *et al.* [2000]. We also insist on that particular point in 4.10, where the order of the averaged distribution is shown to be significantly larger than that of the instantaneous distribution, even at low laser intensity.

The second mechanism, that we call the *intrinsic mechanism*, has to do with the fact that the forced oscillation of the electrons with respect to the ions (which remain motionless to a very good approximation) that adds up to the random thermal motion, modifies the ratio of slow ($v \ll v_{\mathrm{th}}$) to fast electrons ($v \gg v_{\mathrm{th}}$) in the oscillating reference frame, that is to say, the instantaneous shape of the EVD. Indeed, depending upon the intensity and therefore the amplitude of v_{osc} with respect to v_{th}, electrons with initial thermal velocity comprised between $-v_{\mathrm{osc}}$ and $+v_{\mathrm{osc}}$ along the polarization direction for instance, will have, at one moment during the cycle of an oscillation, a very small velocity in the ion reference frame. This is the condition for an important cross section of collision with ions and therefore the condition for an increased slowing down.

In order to remove the *sweeping* mechanism, isotropic and projected distributions were extracted out of our CMDSs in the oscillating reference frame.

In the conditions of the Langdon effect, *i.e.* $v_{\mathrm{osc}}/v_T \ll 1$ and $Zv_{\mathrm{osc}}/v_T \gg 1$, our CMDS display deformations of the instantaneous distribution function (therefore due to the *intrinsic* mechanism). In Fig. 4.2 the projected distribution on the parallel direction (to the laser polarization) $f_{/\!/}$ is plotted. It clearly shows that a projected Maxwellian (which is a Maxwellian) does not fit the projected CMDS distribution. This is why we tested other theoretical distributions

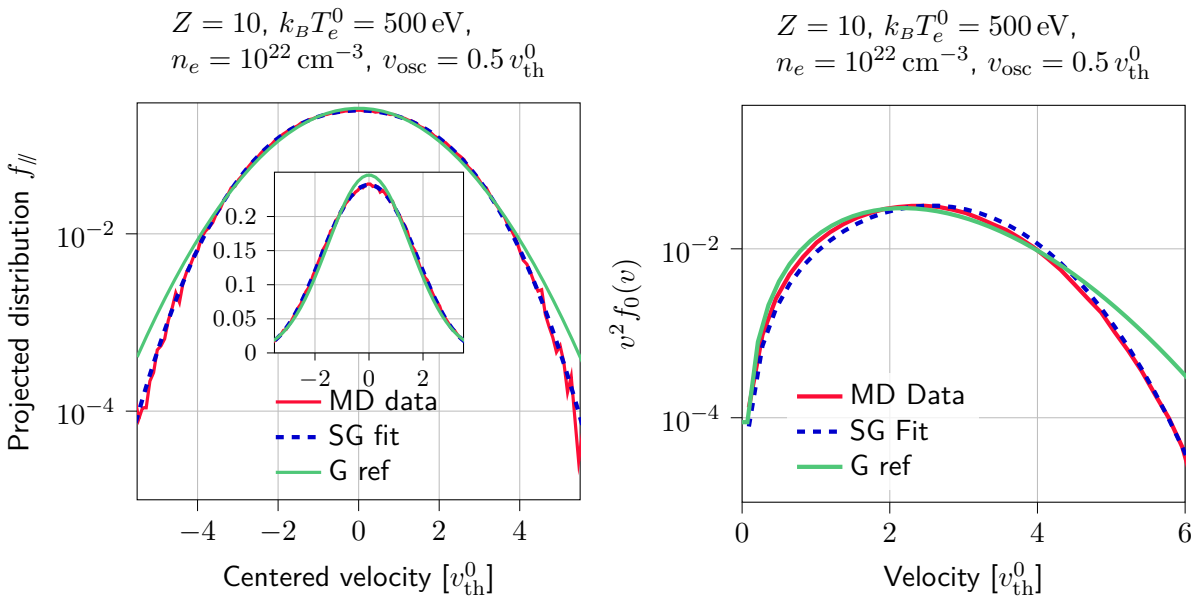

Figure 4.2: Instantaneous projected (left) and isotropic (right) electron distribution function $f_{/\!/}$ after 450 laser cycles. The simulation from which this result originates was set with $Z = 10$, $T_e^0 = 500\,\mathrm{eV}$, $n_e = 10^{22}\,\mathrm{cm}^{-3}$ and $v_{\mathrm{osc}} = 0.5\,v_{\mathrm{th}}^{(0)}$. As predicted by Langdon, the distribution function is closer to a Supergaussian than to a Maxwellian. The best Supergaussian fit corresponds to an order $k = 2.69$ at variance with predictions from Matte *et al.* [1988].

described in section 4.11.

A projected Supergaussian eq. (4.37), fits both its bulk and tail for $k = 2.69$ at $v_{\mathrm{osc}}/v_{\mathrm{th}} = 0.5$ after 450 laser cycles, well in the self-similar regime (one recalls that k is the Supergaussian order of the 3D distribution). At smaller laser intensities ($v_{\mathrm{osc}}/v_{\mathrm{th}} = 0.1$), the projected CMDS distribution was also well fitted by a projected Supergaussian, albeit with an order closer to 2. In both cases, the measured Supergaussian order on our CMDS is less than the very popular predictions by Matte *et al.* [1988]. The discussion on this discrepancy is deferred to section 4.6 for it requires more elements that will be presented in the following sections. Notwithstanding this quantitative issue, the result presented in Fig. 4.2 is, to our knowledge, the first observation in CMDS of non-Maxwellian effects on instantaneous EVDs in Langdon's conditions.

4.4 Extension to Langdon prediction at high laser intensity

4.4.1 Anisotropy

In agreement with previous works [Chichkov *et al.*, 1992, Ferrante *et al.*, 2001, Pfalzner, 1992], our CMDS show the isotropy of the distribution is not preserved at increasing laser intensities. Indeed, at moderate or high laser intensities ($v_{\mathrm{osc}} \geq v_{\mathrm{th}}$), our CMDS show that electron temperatures become anisotropic.

In Fig. 4.3, the evolution of the temperatures // and $\perp$ to the polarization is plotted for multiple laser intensities, or equivalently for multiple initial values of $v_{\mathrm{osc}}/v_{\mathrm{th}}$. In simulations where $v_{\mathrm{osc}} > v_{\mathrm{th}}$, it can be seen that the temperature in the direction of the polarization rises faster than in the other directions. The different temperatures $k_B T_{/\!/} = m_e \langle v'^2_{/\!/} \rangle / 2$ and $k_B T_{\perp} = m_e \langle v'^2_{\perp} \rangle / 2$

(where $\boldsymbol{v}'$ is the fluctuating velocity of an electron around the average velocity of the whole electron population and $\langle . \rangle$ is the ensemble average over that whole electron population) can be accounted for in the distribution while still preserving the Supergaussian shape that we observed at lower laser intensities with the single-order-anisotropic Supergaussian distribution defined by eq. (4.36). This expression has been suggested by theoretical models [Porshnev *et al.*, 1996] although the order was fixed and not variable as it is assumed here. With the appropriate temperatures, the projections of the single-order-anisotropic Supergaussian distribution, computed in eq. (4.37), both $/\!/$ and $\perp$ to the electric field, closely fit with the CMDS projected distributions $f_{/\!/}$ and $f_{\perp}$.

At even higher laser intensity ($v_{\text{osc}} \geq 2.2\, v_{\text{th}}$), a single-order-anisotropic Supergaussian distribution cannot fit both $f_{/\!/}$ and $f_{\perp}$ simultaneously anymore. Indeed, as an illustration, the parallel and perpendicular instantaneous projected distributions of our CMDS data are plotted (solid line) on the same viewgraph in Fig. 4.4. It is a critical plasma ($n_e \approx n_c$) irradiated by a laser of intensity such that $v_{\text{osc}} = 5\, v_{\text{th}}$. The projected distribution $f_{\perp}$ is well-fitted by a projected SG eq. (4.37) with $k = 3.5$. However, unlike at lower laser intensity, the distribution projected along the direction of the electric field, $f_{/\!/}$ is well-fitted by a projected SG with a different order, $k = 6$. The anisotropic SG shape, eq. (4.36) is not sufficient to describe the 3D distribution, since the Supergaussian order k depends on the direction.

A quantitative indicator of this anisotropy is the kurtosis of the projected distributions. It is defined by

$$\text{Kurt}_{\mu} = \frac{1}{v_{\text{th}_{\mu}}^4} \int (v - \langle v_{\mu} \rangle)^4 \, f_{\mu}(v) \, \mathrm{d}v, \tag{4.20}$$

where $\mu \in \{x,\, y,\, z\}$ is the projection direction and $\langle v_{\mu} \rangle$ is the collective averaged velocity (due to the oscillation of the electric field). Any projected distribution of a Maxwellian distribution (which is itself a Maxwellian distribution) has a kurtosis of 3 regardless of the projection direction. For the single-order-anisotropic Supergaussian (SOA) distribution, defined in eq. (4.36), the kurtosis of its projected distribution is independent of the projected direction μ, and

$$\text{Kurt}_{\mu}^{\text{SOA}} = \frac{9\,\Gamma(3/k)\,\Gamma(7/k)}{5\,\Gamma(5/k)^2}. \tag{4.21}$$

That kurtosis equals 3 when the order $k = 2$ (for a pure Maxwellian). As one can notice, the kurtosis of a projected single-order-anisotropic Supergaussian distribution is only a function of the order k of the distribution even when the temperature is anisotropic. Since there is a one to one relation between the order k of the EVD and the kurtosis of its projected distribution, eq. (4.21) can be reversed numerically and used to compute the order of the distribution, assuming the shape of the distribution is eq. (4.36). The order of the CMDS distribution can thus be computed in two ways: either by fitting the CMDS projected distribution to a projected Supergaussian eq. (4.37) or by calculating the CMDS projected distribution kurtosis and using the inverse of relation eq. (4.21). The projection can be carried out along the electric field or perpendicular to it. In Fig. 4.3, we show that for $v_{\text{osc}}/v_{\text{th}}$ large enough (at high intensity), parallel and perpendicular CMDS projected distribution are different both in temperature and order. As depicted in Fig. 4.5, the kurtosis analysis leads to the same conclusion. It allows to assess the evolution of the order of the parallel and perpendicular projected distribution as time goes by. In Fig. 4.5, the evolution of $\text{Kurt}_{/\!/}$ and $\text{Kurt}_{\perp}$ is plotted for multiple laser intensities. The kurtosis can be read on the left vertical axis and the order of the projected Supergaussian can be read on the right vertical axis.

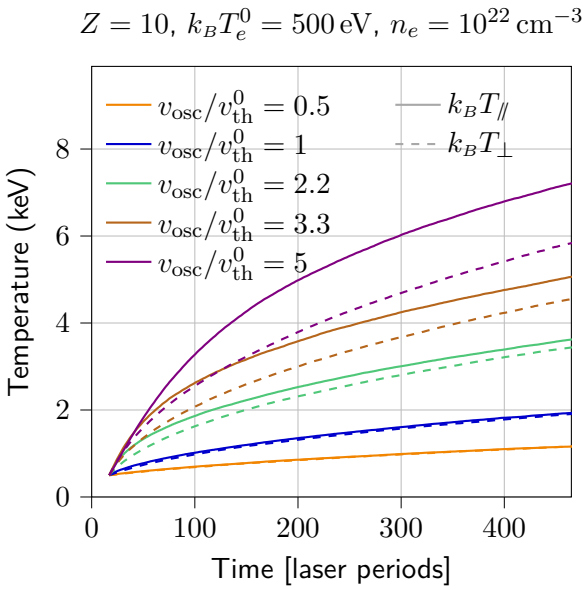

Figure 4.3: Evolution of electronic temperatures $k_B T_\perp$ and $k_B T_{/\!/}$ for different v_{osc}. These simulations start from $T_e^0 = 500\,\mathrm{eV}$ and $n_e = 10^{22}\,\mathrm{cm}^{-3}$. The temperature is defined by $k_B T_\perp = m_e\,(\bar{v_\perp^2} - \bar{v_\perp}^2)$, resp. $k_B T_{/\!/}$. The temperature is the same in every direction perpendicular to the electric field, except for statistical fluctuations. When $v_{\mathrm{osc}} > v_{\mathrm{th}}$, the temperature becomes anisotropic, with the temperature in the direction of the laser rising faster then the other directions.

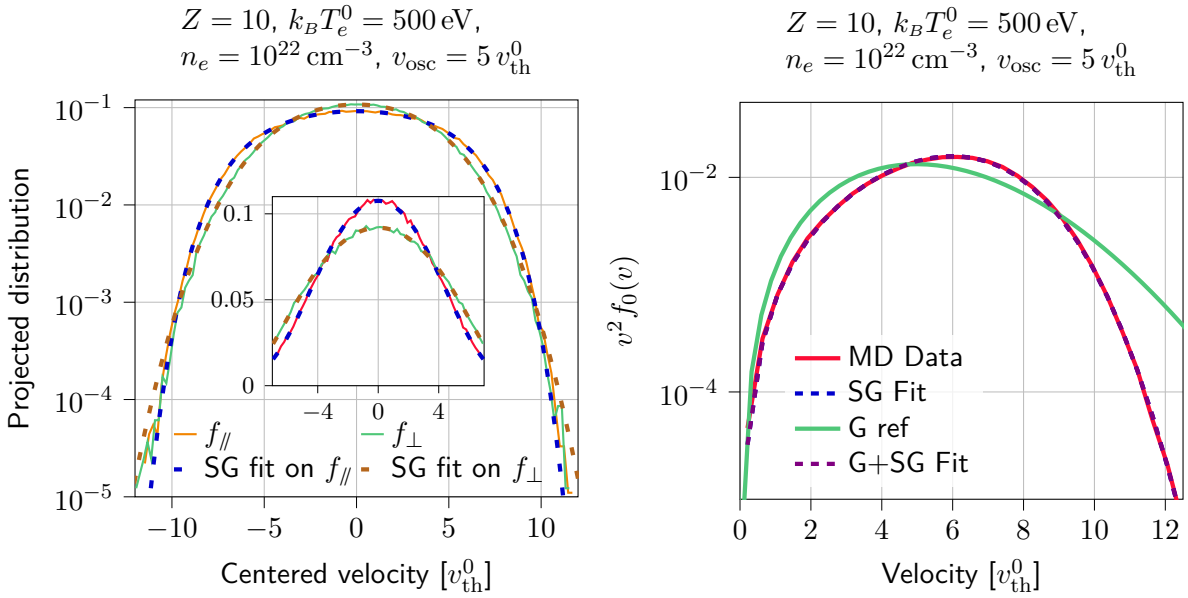

Figure 4.4: (color online) Centered projected (left) and isotropic (right) distributions after 450 laser cycles. This simulation started with $T_e^0 = 500\,\mathrm{eV}$, $n_e = 10^{22}\,\mathrm{cm}^{-3}$, and $v_{\mathrm{osc}}/v_{\mathrm{th}}^0 = 5$. Both projected distributions are well fitted by projected SG, but with different order and thermal velocity. The best fit of $f_{/\!/}$ on eq. (4.37) gives $v_{T/\!/} = 3.78 v_{\mathrm{th}}^{(0)}$ and $k_{/\!/} = 6.22$. In a perpendicular direction, $v_{T\perp} = 3.41 v_{\mathrm{th}}^{(0)}$ and $k_\perp = 3.22$. This graph shows the distribution anisotropy both in temperature and order. The distribution eq. (4.36) can, when projected, fit both $f_{/\!/}$ and $f_\perp$ separately, but not at the same time, since $k_{/\!/} \neq k_\perp$.

It is interesting to notice that for high intensities, the asymptotic perpendicular Supergaussian order does not depend on intensity, at variance with the asymptotic parallel Supergaussian order increasing with intensity.

4.4.2 Supergaussian order can exceed Langdon's prediction

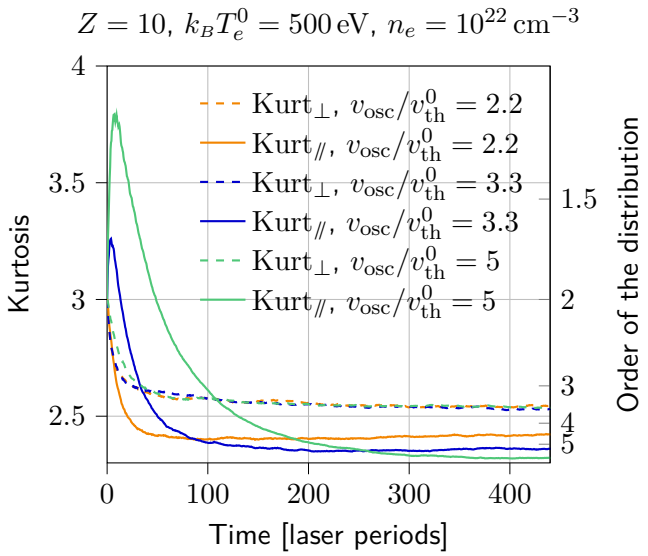

Figure 4.5: $\mathrm{Kurt}_{/\!/}$ and $\mathrm{Kurt}_\perp$ for different v_{osc} (left axis). On the right axis is the corresponding SG order given by Eq. eq. (4.21). As mentioned before, eq. (4.21) assumes the distribution is eq. (4.36). These simulations start from $k_B T_e^0 = 500\,\mathrm{eV}$ and $n_e = 10^{22}\,\mathrm{cm}^{-3}$. When $v_{\mathrm{osc}} > v_{\mathrm{th}}$, the kurtosis becomes anisotropic. This is not compatible with a Supergaussian distribution such as eq. (4.36).

After only a few laser cycles, for high intensities ($v_{\mathrm{osc}} \geq v_{\mathrm{th}}$), the kurtosis can temporarily exceed 3 as can be seen in Fig. 4.5. It implies, temporarily, that EVD projected Supergaussian orders can be smaller than 2 before evolving toward a self-similar state. However, we have no reason to expect the distribution to fit a Supergaussian shape before a self-similar state is reached, and so the computed order should be taken with caution. By examining the projected distribution at these instants in Fig. 4.6, it is possible to see that the increase of kurtosis is mainly caused by a high-velocity tail. Indeed, since the kurtosis is computed from the fourth power of the deviation to the mean, it is very sensitive to values far from the mean. The behaviour of the distribution agrees with the sum of two Maxwellian distributions with different temperatures. Nevertheless, fitting the central part of the distribution at these instants to a projected SG eq. (4.37) still yields orders smaller than 2, although not as small as what the kurtosis predicts. All in all, in the transient regime, the small orders assessed from the kurtosis are evidence for abundance of suprathermal electrons (strong tails in the EVD).

In the self-similar regime, when the kurtosis levelled off, a very good agreement was observed between the distribution order computed from the kurtosis eq. (4.21) and the order obtained by fitting the projected distribution. The kurtosis can thus be used quantitatively to evaluate the order of the projected distribution. In Fig. 4.7, one can see that the asymptotic value of the kurtosis decreases with increasing laser intensity. This corresponds to higher and higher SG orders. In particular, the SG order can become higher than 5 unlike Langdon's prediction which

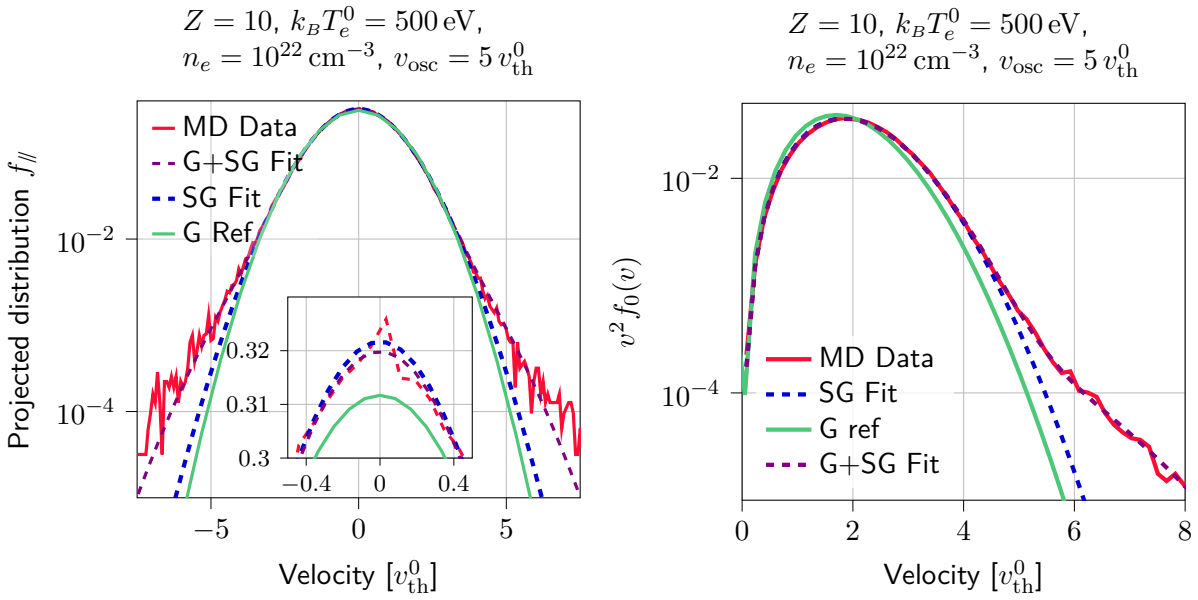

Figure 4.6: Instantaneous projected (left) and isotropic (right) electron distribution function $f_{/\!/}$ integrated on both directions perpendicular to the laser field after 8.5 laser cycles. This simulation started with $T_e^0 = 500\,\mathrm{eV}$, $n_e = 1 \times 10^{22}\,\mathrm{cm}^{-3}$ and $v_{\mathrm{osc}} = 5\,v_{\mathrm{th}}^0$. The best SG eq. (4.37) fit has $k = 1.75$ and $v_{\mathrm{th}} = 1.28\,v_{\mathrm{th}}^0$. For reference, the Gaussian with $v_{\mathrm{th}} = 1.28\,v_{\mathrm{th}}^0$ is plotted in green. The best fit on the projection of eq. (4.39) has $A = -1.24$, $v_{\mathrm{th}}^G = 1.87\,v_{\mathrm{th}}^0$, $v_{\mathrm{th}}^{SG} = 1.18\,v_{\mathrm{th}}^0$, and $k = 1.97$. The order of the best SG fit is less than two, but more than the prediction with $\mathrm{Kurt}_{/\!/}$. It only captures the behaviour of $f_{/\!/}$ in the bulk ($v < v_{\mathrm{th}}$). As shown by the fit on a sum of a Gaussian and SG, $f_{/\!/}$ behaves like the sum of two Gaussian distribution with different temperatures.

is illustrated in Fig. 4.4.

This anisotropy is further shown in Fig. 4.8, in which the density of the projected distribution is plotted for multiple projection direction, defined by their angle with the laser electric field. The bulk part of the distribution, in blue in Fig. 4.8, is well reproduced by Supergaussian models. This is because the different temperatures in different directions are taken into account in both models. However, the tail of the distribution is clearly not as well reproduced by the models. Indeed, the Maxwellian model ($k = 2$) has a tail higher than the CMDS data. The Supergaussian model is very accurate for the projection along the direction of the electric field, since $k_{/\!/}$ was used in the model. However, along the direction perpendicular to the laser electric field, the data has a bigger tail than the SG model, this corresponds to $k_\perp < k_{/\!/}$.

In a nutshell, we observed three kinds of anisotropy in the distribution at high v_{osc}: the coherent oscillating movement of the electrons which causes anisotropy in the laboratory frame, the temperature anisotropy, and the anisotropy of the Supergaussian order.

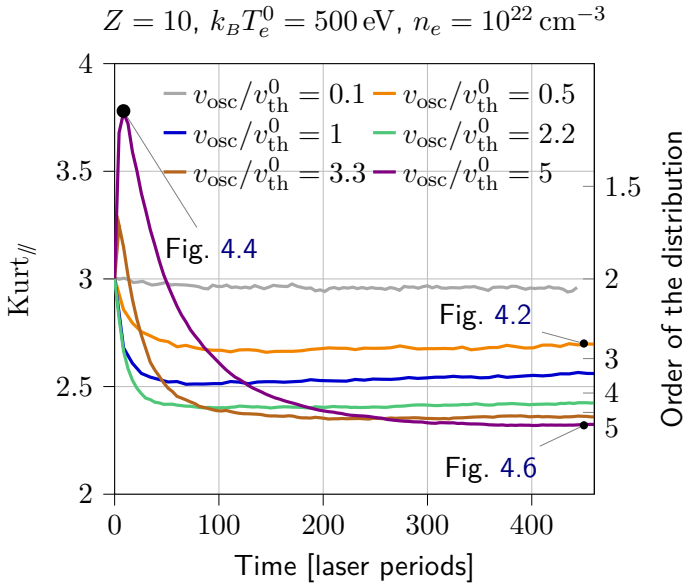

Figure 4.7: Evolution of $\mathrm{Kurt}_{/\!/}$ for multiple v_{osc} (left axis). On the right axis is the corresponding SG order given by eq. (4.21). These simulations start from $k_B T_e^0 = 500\,\mathrm{eV}$ and $n_e = 10^{22}\,\mathrm{cm}^{-3}$. The laser is linearly polarized in the z direction. When $v_{\mathrm{osc}} > 3.3 v_{\mathrm{th}}$, a transient effect in which the order of the distribution becomes lower than 2 is observed. However, in the asymptotic behaviour of the kurtosis, which corresponds to a self-similar state of the distribution, the order seems to increase with increasing laser intensity.

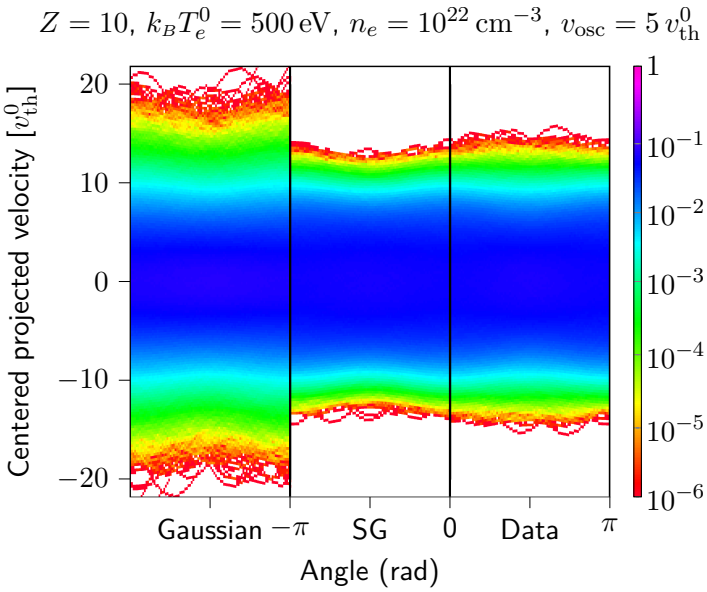

Figure 4.8: Density of the projected distributions as a function of the angle of the projection to the electric field. The angle of projection is periodicized between 0 and π. The projected velocity is centered to remove the oscillation due to the laser electric field. The density is given by the color. For comparison, the same graph is plotted for the Maxwellian and Supergaussian eq. (4.36) models. For both models, since the projection along an arbitrary direction is not known, the distributions were sampled, and then projected. The number of samples used was the same as the number of electrons in our simulations ($4 \cdot 10^5$). The Maxwellian and Supergaussian thermal velocities were chosen so as to keep the same temperature as the data, so $v_{\mathrm{th}/\!/} = 4.57$ and $v_{\mathrm{th}\perp} = 4.27$. The MD data has $k_{/\!/} = 5.85$ and $k_\perp = 3.38$. The order of the SG here is $k_{/\!/}$.

4.5 Conditions for Supergaussian distributions with Maxwellian tails

Fokker-Planck (FP) codes solve an equation based on the Boltzmann equation, which is, for a uniform plasma submitted to an external electric field,

$$\partial_t f_e - \frac{e}{m_e}\,\boldsymbol{E}\cdot\partial_{\boldsymbol{v}} f_e = C_{ee}(f_e) + C_{ei}(f_e), \tag{4.22}$$

where C_{ee} and C_{ei} are the electron-electron and electron-ion collision operators (usually in the form Landau collision operators [Jones & Lee, 1982, Langdon, 1980]). Both collision terms are modelled and depends on theoretical assumptions unlike in CMDS. In this modelling process, assumptions have to be made on collision mechanism and the influence of collective effects, in particular, through Coulomb logarithms. They are given as input data to the FP code.

Solutions of the Boltzmann equation eq. (4.22) are developed in Legendre polynomials and only the first few terms are usually considered in FP codes. Langdon [1980] retained only the slowly-varying (compared to the electric field) part of f_e^0 averaged over a laser period. The resulting equation is

$$\partial_t f_e^0 = \frac{A\,v_{\mathrm{osc}}^2}{3}\,\frac{1}{v^2}\,\partial_v \frac{1}{v}\,\partial_v f_e^0, \tag{4.23}$$

where $A = 2\,\pi\,n_e\,Z\,e^4\,\ln\Lambda/(m_e^2\,(4\,\pi\,\varepsilon_0)^2)$. Balescu [1982] derived the same equation by considering the oscillating reference frame of the electrons to separate the slow and fast varying parts of f_e^0. This equation admits the self similar state $f_e^0 \propto \exp(-(v/v_{\mathrm{th}})^5)$, where the thermal velocity v_{th} scales nonlinearly with time because of heating. In the limit $Z v_{\mathrm{osc}}/v_{\mathrm{th}} \ll 1$, electron-electron collisions are dominant ($C_{ee} \gg C_{ei}$) therefore f_e^0 remains Maxwellian. Fokker-Planck simulations were carried out [Matte *et al.*, 1988] in order to compute the general case taking into account both collision terms C_{ee} and C_{ei}. An empirical fit on the order of the Supergaussian distribution with respect to $\alpha = Z\,v_{\mathrm{osc}}^2/v_{\mathrm{th}}^2$ was proposed,

$$k(\alpha) = 2 + \frac{3}{1 + \dfrac{1.66}{\alpha^{0.724}}}, \tag{4.24}$$

along with the reduction in laser absorption due to the distortion of the distribution

$$R(\alpha) = 1 - \frac{1}{(1 + (0.27/\alpha)^{0.75}}. \tag{4.25}$$

A model was proposed by Fourkal *et al.* [2001] where the distribution can become a sum of a Maxwellian distribution and a Supergaussian distribution. The low-velocity (with respect to the thermal velocity) part of the distribution is expected to be distorted by the Langdon effect thus becoming supergaussian, but the dynamics of the high-velocity part of the distribution are dominated by electron-electron collisions. These collisions tend to relax the distribution towards a Maxwellian, in the electrons oscillating frame. Taking both of these effects into account, the distribution has the appearance of an oscillating Supergaussian with a Maxwellian tail. This model was shown to be in agreement with experimental measurements of the isotropic distribution function [Milder *et al.*, 2021].

Although the exact experimental conditions were too numerically costly to replicate ($Z = 36$ for most shots), we carried out simulations in similar conditions of electronic density ($n_e \approx 4 \times 10^{20}\,\mathrm{cm}^{-3}$ in the experiments, and $n_e = 10^{20}\,\mathrm{cm}^{-3}$ in our CMDS) and electronic temperature ($k_B T_e = 0.5 - 1\,\mathrm{keV}$ in the experiments, while our simulations start with $k_B T_e^0 = 100\,\mathrm{eV}$, but the electrons heats up to 900 eV in our CMDS), but with $Z = 10$. In Fig. 4.9, we do observe an isotropic distribution that is a Supergaussian at low velocities with a Maxwellian tail. However, the conditions were slightly different than the conditions in Milder *et al.* [2021]. Besides the difference in Z and n_e, they had $v_{\mathrm{osc}} \sim 0.5 v_{\mathrm{th}}$, while the Maxwellian tail only appear at $v_{\mathrm{osc}} > v_{\mathrm{th}}$ in our simulations. We did not observe the Maxwellian tail for $v_{\mathrm{osc}} < v_{\mathrm{th}}$, nor for $n_e > n_c$.

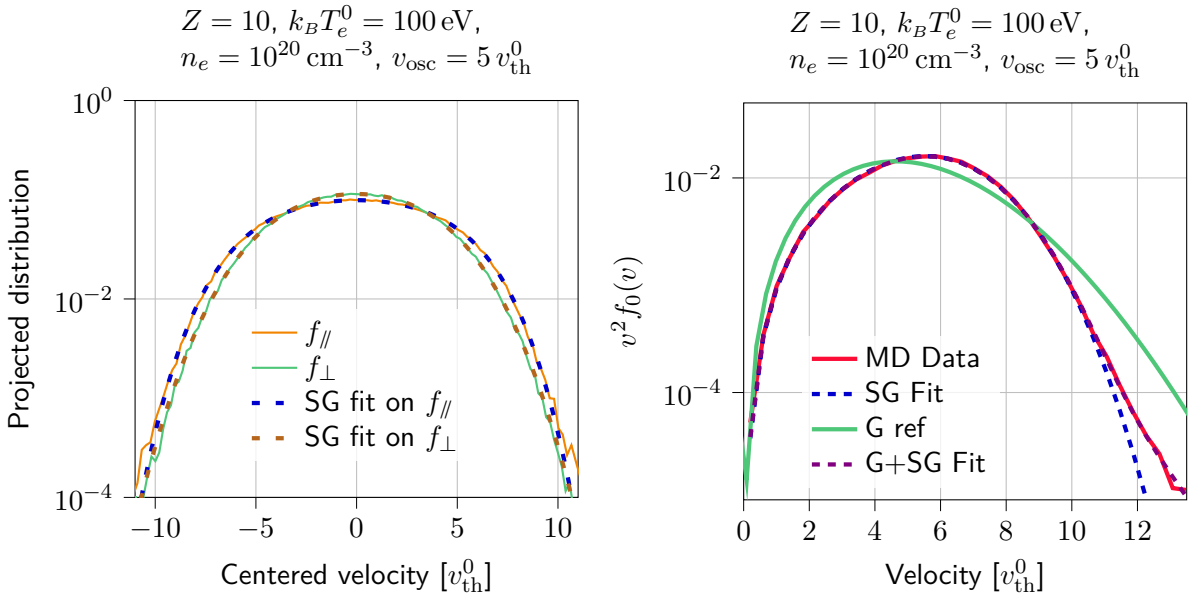

Figure 4.9: Instantaneous projected (left) and isotropic (right) distribution after 2963.2 laser cycles (solid blue line). The best Supergaussian ($k = 3.53$) fit is in red dashed, and the best fit of the sum of a Maxwellian and Supergaussian eq. (4.39) is in purple dashed. This simulation started from $k_B T_e^0 = 100\,\mathrm{eV}$ and $n_e = 10^{20}\,\mathrm{cm}^{-3}$, and $v_{\mathrm{osc}}/v_{\mathrm{th}}^0 = 3.3$. The low velocity part of the distribution is very well fitted by a Supergaussian distribution. However, the tail of the distribution behaves like a Maxwellian. The best fit has the same temperature for the Maxwellian and the Supergaussian distribution. The distribution corresponds to that predicted by Fourkal *et al.* [2001], albeit in different conditions, since $v_{\mathrm{osc}} > v_{\mathrm{th}}$ here. The Supergaussian order measured here ($k = 3.53$) corresponds to neither of the Supergaussian orders measured from the projected distributions ($k_{/\!/} = 4.43$ in the direction of the E-field and $k_\perp = 3.08$ in the perpendicular directions).

4.6 The order of the distribution as a function of $v_{\mathrm{osc}}/v_{\mathrm{th}}$

We established that in our simulations, the self similar state of the projected distributions can always be fitted by a projected Supergaussian distribution eq. (4.37), though different orders have to be specified in the parallel or perpendicular direction (with respect to polarization). In Fig. 4.10, the top viewgraphs correspond to the evolution of the Supergaussian order of the projected distributions and the bottom viewgraphs to the evolution of isotropic distribution. Each curve in each viewgraph corresponds to the evolution of the Supergaussian order of a single CMDS starting as a Maxwellian (with order 2 on the vertical axis). The initial value of $v_{\mathrm{osc}}/v_{\mathrm{th}}$

can be read on the horizontal axis of order 2. On each curve, the laser intensity is kept constant and $v_{\mathrm{osc}}/v_{\mathrm{th}}$ decreases as time goes by because electrons heat up. Therefore, on each curve, the time evolution is from right to left. Since simulations do not reach a steady state, the order keeps evolving as the simulation proceed. As a reference, Matte's formula, given in eq. (4.24) for the order of the distribution, is plotted in solid black.

One can see in Fig. 4.10 top left viewgraph that parallel-projected-distributions-order can overshoot Matte's prediction unlike perpendicular-projected-distribution-order that seems to remain well under. There seems to be a change in behaviour at early time when $v_{\mathrm{osc}}/v_{\mathrm{th}} > 2.2$. Above this threshold, the parallel-projected-distribution-order seems to dive first (with orders less than 2 which indicates the creation of a supra-thermal electron tail) before rising rapidly and reaching the self-similar behaviour. There seems to be a dependency of $k_{/\!/}(v_{\mathrm{osc}}/v_{\mathrm{th}})$ upon the electronic density when comparing the top right and top left viewgraphs in Fig. 4.10. On the contrary, $k_{\perp}(v_{\mathrm{osc}}/v_{\mathrm{th}})$ is much less affected by a change in electronic density.

In regards to isotropic distribution order, in Fig. 4.10 bottom viewgraphs, one can clearly see that CMDS, for $n_e \approx n_c \approx 10^{22}\,\mathrm{cm}^{-3}$, predict a self-similar regime with an order that is close but slightly less than Matte's prediction ($\approx 10\%$ less). The same early time change in behaviour depicted before with projected-distributions is still visible. However, when it comes to $n_e \approx 0.01\,n_c$, the order in the self-similar regime is much less than Matte's prediction ($\approx 50\%$ less) and this is due to the fact that $k_{/\!/}(v_{\mathrm{osc}}/v_{\mathrm{th}})$ is less at smaller electronic density.

The discrepancy between our observations and the prediction of Matte *et al.* [1988] may be explained by the fact that Matte used Fokker-Planck simulations where EVD shapes are constrained by the limited development in Legendre polynomials in FP codes. Another sticking point concerns collisions that have to be modelled. In particular, the Coulomb logarithm $\ln\Lambda$ that appears in the electron-ion collision frequency, in eq. (4.26) for instance, has to be provided as an input to FP simulations, which is not the case in CMDS.

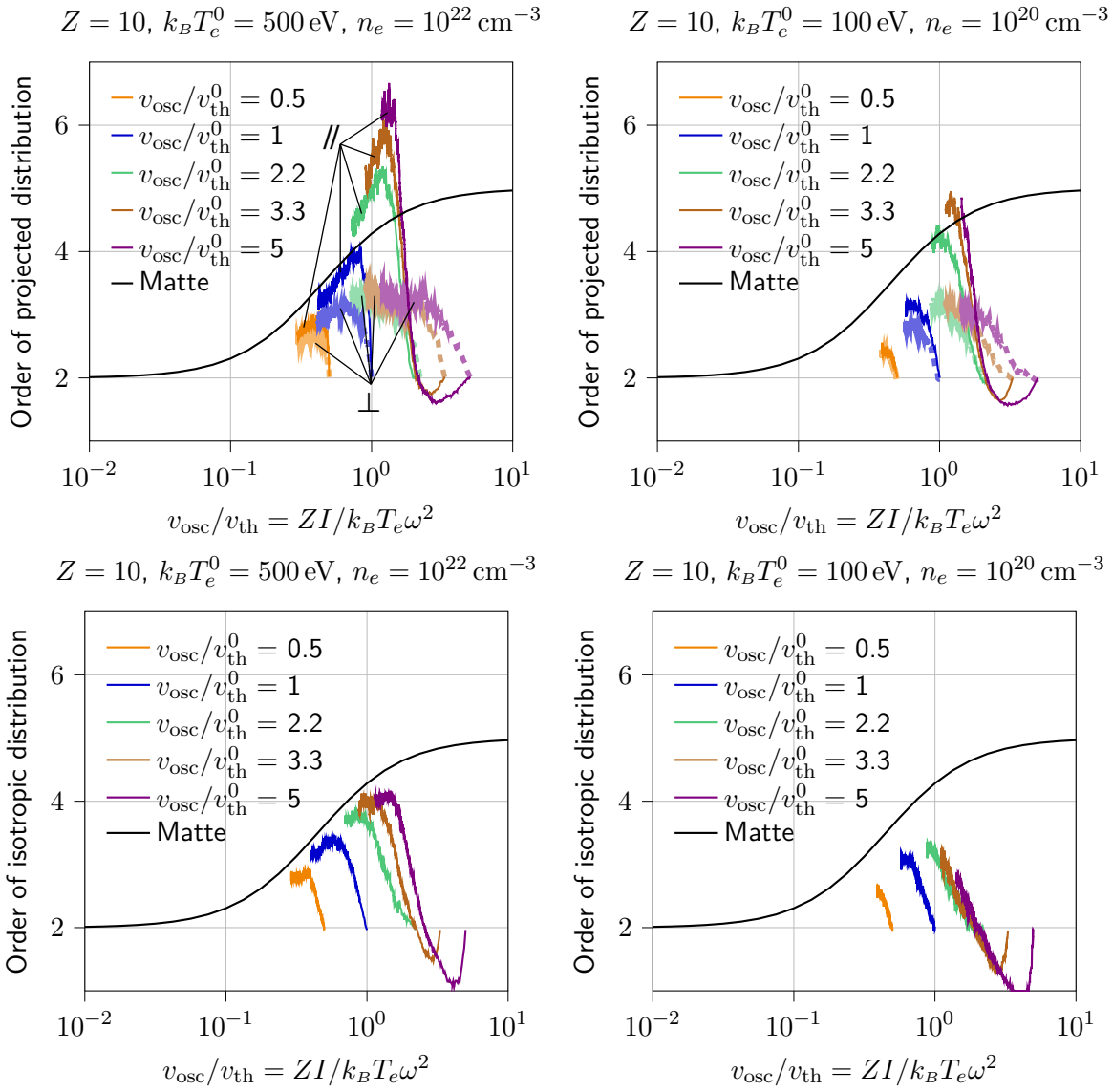

Figure 4.10: Supergaussian order as a function of $v_{\text{osc}}/v_{\text{th}}$ for multiple laser intensities. The top viewgraphs correspond to projected-distribution-order. The dashed lines correspond to perpendicular projected-distribution (with respect to the electric field), and the solid lines correspond to the parallel projected-distribution. The bottom viewgraphs correspond to isotropic-distribution-order. In each viewgraph, all curve of a given color correspond to the same CMDS (one color corresponds to one laser intensity that is kept constant during the simulation). The fact that $v_{\text{osc}}/v_{\text{th}}$ decreases during a simulation is due to the fact that T_e increases due to the IB heating. The black line on each viewgraph is Matte's prediction. These simulations all begin with the state(eq. (4.5) or eq. (4.6) with a Maxwellian EVD (order = 2).

4.7 Absorption model for a Supergaussian distribution

Here, we recall shortly the absorption model that was detailed in chapter 2. Mulser *et al.* [2000] used a ballistic model to derive the following expression for the instantaneous e-i collision frequency

$$\nu_{ei}(v_\mathrm{d}) = \frac{Z^2\, e^4\, n_i\, \ln\Lambda}{4\,\pi\,\varepsilon_0^2\, m_e^2\, v_\mathrm{d}^3} \int_0^{v_d} 4\,\pi\, v_e^2\, f_e(v_e)\, \mathrm{d}v_e, \tag{4.26}$$

where the electron population has an average relative velocity v_d with respect to the ion population. This is why, in the case of IB heating, when the electrons are under the influence of a periodic electric field, one can assume that v_d corresponds to the electrons oscillating velocity. Assuming the laser electric field is given by $\boldsymbol{E}\cos\omega t$, the electrons' cycle averaged heating rate is

$$\langle \boldsymbol{j}\cdot\boldsymbol{E}\,\cos(\omega t)\rangle = n_e\, e \frac{\omega}{2\,\pi} \int_0^{2\,\pi/\omega} \boldsymbol{v}\cdot\boldsymbol{E}\,\cos(\omega t)\,\mathrm{d}t, \tag{4.27}$$

where $\boldsymbol{v}$ is the average electron velocity. Let us consider the Drude model that describes the evolution of the ensemble velocity, $\boldsymbol{v}$, of a free electron gas

$$\frac{\mathrm{d}\boldsymbol{v}}{\mathrm{d}t} = \frac{-e\,\boldsymbol{E}}{m_e}\,\cos(\omega t) - \nu_{ei}\,\boldsymbol{v}. \tag{4.28}$$

After integrating by parts, the average heating rate can be expressed, with respect to ν_{ei}, as

$$\langle \boldsymbol{j}\cdot\boldsymbol{E}\,\cos(\omega t)\rangle = n_e\, m_e\, v_\mathrm{osc}\, \frac{\omega}{2\,\pi} \int_0^{2\,\pi/\omega} \nu_{ei}(v)\, v\,\sin(\omega t)\,\mathrm{d}t. \tag{4.29}$$

Inserting eq. (4.26) in eq. (4.29), with an isotropic Supergaussian distribution (4.35) for f_e yields

$$\langle \boldsymbol{j}\cdot\boldsymbol{E}\,\cos(\omega t)\rangle = n_e\, \frac{1}{2}\, m_e\, v_\mathrm{osc}^2\, \nu_{ei}^0\, \ln\Lambda\, R(\eta,\, k), \tag{4.30}$$

where $\nu_{ei}^0 = (4\,\sqrt{2\,\pi}Z\,e^4\,n_e)/(3\,\sqrt{m_e}(4\,\pi\,\varepsilon_0)^2 k_B T_e^{3/2})$, and

$$R(\eta,\, k) = \int_0^{\pi/2} \frac{12\,\gamma\left(\frac{3}{k},\, \left(\eta\,\sqrt{\frac{\Gamma(5/k)}{3\,\Gamma(3/k)}}\,\sin(t)\right)^k\right)}{\Gamma(3/k)\,\sqrt{2\,\pi}\,\eta^3\,\sin(t)}\,\mathrm{d}t, \tag{4.31}$$

where $\gamma(a,\, z) = \int_0^z t^{a-1}\,\exp(-t)\,\mathrm{d}t$ is the incomplete lower gamma function, $\eta = v_\mathrm{osc}/v_\mathrm{th}$ and k is the order of the Supergaussian distribution. This equation assumes the Coulomb logarithm can be left out of the time average, which means it should be independent from the laser intensity. This is not the case in practice, but this approximation allows the Coulomb logarithm to be modelled separately.

Although eq. (4.31) can be computed numerically, it is not very convenient to use as is. It still does retains useful properties, due to the way it was derived. The first of these properties is that when $k = 2$, i.e. the distribution is Maxwellian, it yields similar values to a previous model

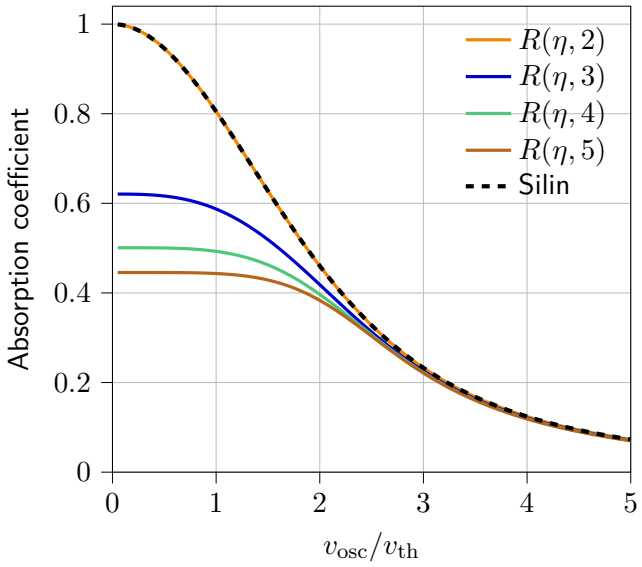

Figure 4.11: Absorption coefficient of our model as a function of $v_{\mathrm{osc}}/v_{\mathrm{th}}$ for multiple distribution shapes. Silin [1965]'s model is plotted in dotted black for reference. For small η, the line corresponding to Langdon's case ($k = 5$) has a value very close to the absorption reduction predicted by Langdon (0.445).

that assumed a Maxwellian distribution, proposed by Silin [1965], as shown in Fig. 4.11. Furthermore, in simple kinetic models, such as Langdon's, the laser absorption is directly proportional [Langdon, 1980] to $f_e(0)$. The term we propose here is consistent with that approach, since a Taylor expansion for small η (which is one of Langdon's assumptions) yields

$$R(\eta,\, k) \approx \sqrt{\frac{\pi}{6}}\, \frac{k\,\Gamma(5/k)^{3/2}}{3\,\Gamma(3/k)^{5/2}} = \frac{f_e^{SG}(0)}{f_e^{G}(0)}. \tag{4.32}$$

Matte *et al.* [1988]'s model also very closely agrees with this. Although the model we propose is valid at high laser intensities (high η), it does rely on a drifted isotropic Supergaussian distribution. This means that the temperature anisotropy as well as other anisotropy effects that we observed in our CMDS are not taken into account and yet, we are going to show that the agreement with CMDS results are quite correct in the following section.

4.8 Comparison of the absorption model to CMDS

In this section, we present preliminary results of a comparison between our model and numerical results from CMDS, shown in Fig. 4.12. The heating rate in our model is given by

$$\frac{\mathrm{d}k_B T_e}{\mathrm{d}t} = C_{\mathrm{abs}}\, \frac{m_e}{3}\, v_{\mathrm{osc}}^2\, \nu_{ei}^0\, \ln\Lambda\, R(\eta,\, k), \tag{4.33}$$

that is to say, the parametrized model, devised from $Z = 1$ simulations in chapter 3, multiplied by the non-Maxwellian multiplier R defined in eq. (4.31) and approximated in eq. (4.32). This is what is referred to as "model of this work" in Fig. 4.12. The coefficient C_{abs} was set to its value 0.55 from chapter 3.

The MD heating rate was computed from the variation of temperature in a given amount of laser cycles. Taking more cycles into account reduces noise, but produces inaccurate results

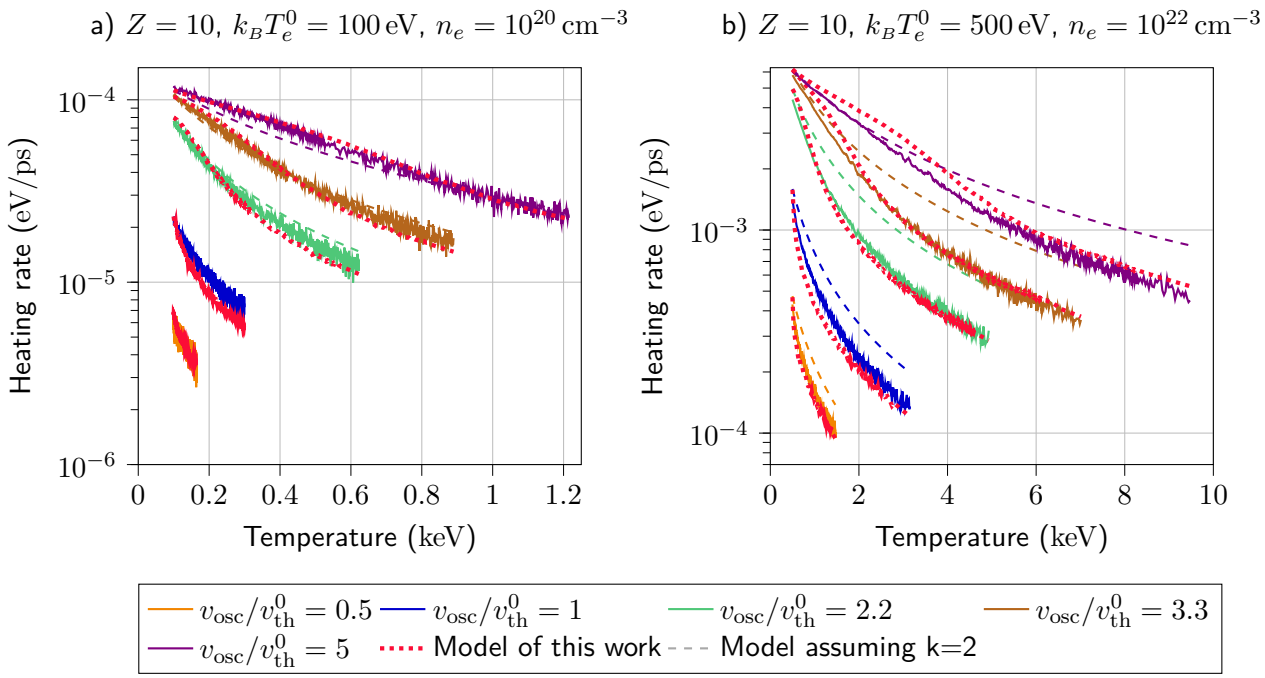

Figure 4.12: Heating rate as a function of temperature for multiple laser intensities and initial conditions. Initial conditions are a) $n_e = 10^{20}\,\mathrm{cm}^{-3}$ and $k_B T_e = 100\,\mathrm{eV}$, and b) $n_e = 10^{22}\,\mathrm{cm}^{-3}$ and $k_B T_e = 500\,\mathrm{eV}$. The CMDS heating rate is computed on 5 laser cycles. Each color corresponds to a value of v_{osc}/v_{th}. For each color (except red), solid lines correspond to simulation data, and dashed lines were computed from the model developed in chapter 3, which does not take into account distortion of the electron velocity distribution. The model proposed in this work eq. (4.33) is in red dotted for all intensities, but for each case, it is very close to MD data, at least asymptotically. After a transient regime, when the distribution has reached a self-similar state, the heating rate is well reproduced by our model, especially in the second case.

when the heating rate changes very fast, which is the case at the beginning of the simulations. In Fig. 4.12, the computed $\mathrm{d}k_B T_e/\,\mathrm{d}t$ on our CMDS was carried out over 5 laser periods. The left viewgraph corresponds to $n_e \approx 0.01\,n_c$ and the right viewgraph to $n_e \approx n_c$. The maxwellian model and the model with the non-maxwellian multiplier are plotted over CMDS results.

The MD data and both models are all close together at early time in simulations. This is expected, since the distribution is actually Maxwellian. At late time, when a self-similar state is reached, the model with non-Maxwellian multiplier is very close to CMDS data in both cases. Surprisingly enough, the absorption does not seem to be affected noticeably in the subcritical case $n_e = 10^{20}\,\mathrm{cm}^{-3}$. However, in the case $n_e = 10^{22}\,\mathrm{cm}^{-3}$, the MD heating rate is significantly lower than in the Maxwellian case. The transient regime, between early time and late time self-similar regime, is difficult to model accurately.

4.9 Conclusion

We observed the distortion of the EVD in moderate-Z plasmas for a wide range of laser intensities. At low laser intensity, we were able to observe the distortion predicted by Langdon [1980] on the instantaneous EVD, which had yet to be done in CMDS with $v_{osc} < v_{th}$ and $Z > 1$. At

higher laser intensity, we observed and characterized the distribution of the EVD. In particular, the distribution projected along the direction of the laser polarization was observed to reach a Supergaussian order higher than 5, which was the highest order possible in Langdon's predictions. We observed Supergaussian distributions with Maxwellian tail in conditions close to experimental conditions [Milder *et al.*, 2021]. Then, we showed that the behaviour of the isotropic part of the Supergaussian is qualitatively similar to the predictions of Matte *et al.* [1988], but with a Supergaussian order slightly small from a quantitative point of view. Finally, we showed results of the modification of the heating rate due to the distortion of the EVD. Though these results have to be taken with caution because they are preliminary, they showed the heating rate of the subcritical plasma we considered seems unaffected by the distortion of the EVD. The heating rate of the critical plasma we simulated is affected, and the reduction of absorption seems to be consistent with the non-Maxwellian model of absorption detailed in chapter 2.

4.10 Appendix A: Difference between instantaneous and cycle-averaged distributions

In the literature [Langdon, 1980, Matte *et al.*, 1988], electron velocity distributions (EVD) are presented after being averaged over one laser cycle. The averaging process itself distorts the shape of a the averaged distribution when the instantaneous distribution is subjected to oscillation in phase space (due to an oscillating electric field or any other cause of oscillation of the averaged velocity).

The cycle averaged-distribution of an oscillating population of electron, with instantaneous velocity distribution f_e in the oscillating frame, is given by

$$\langle f_e(\boldsymbol{v})\rangle = \frac{1}{2\,\pi}\int_0^{2\,\pi} f_e(\boldsymbol{v} + \boldsymbol{v}_{\rm osc}\,\sin t)\;\mathrm{d}t. \tag{4.34}$$

When $v_{\rm osc}$ vanishes, the averaged distribution is the same as the instantaneous distribution. In Fig. 4.13, we have assumed that f_e was a pure Maxwellian. Clearly, when $v_{\rm osc} = 0.1\,v_{\rm th}$, the difference between the projected-averaged and the projected-instantaneous distribution is barely visible. However when $v_{\rm osc}$ approaches $0.5\,v_{\rm th}$, the difference becomes noticeable and the projected-averaged distribution exhibits a flat top that could be interpreted as a Supergaussian. When $v_{\rm osc} \gg v_{\rm th}$ the projected-averaged distribution exhibits a concavity for $v \ll v_{\rm osc}$ with a maximum around $v \approx v_{\rm osc}$.

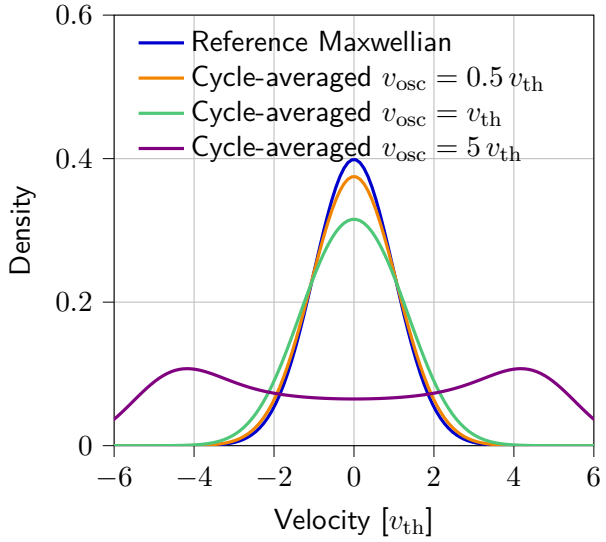

Figure 4.13: Effect of the averaging process on a Maxwellian distribution. The initial distribution is a Maxwellian in blue. The other curves correspond to the average of this distribution oscillating for multiple oscillation amplitudes ($v_{\rm osc}$). For $v_{\rm osc} = 0.5v_{\rm th}$, the averaged is close to the initial Maxwellian, but for $v_{\rm osc} = 0.5v_{\rm th}$ the distribution is very far from the Gaussian. Fitting these distribution by projected Supergaussian yield a thermal velocity of $1.06v_{\rm th}$ and $k = 2.02$ for $v_{\rm osc} = 0.5v_{\rm th}$; and a thermal velociy of $1.22v_{\rm th}$ and $k = 2.35$ in the case where $v_{\rm osc} = v_{\rm th}$. This demonstrates the effect of the *sweeping* mechanism on the Supergaussian order.

4.11 Appendix B: Expressions for various useful Supergaussian distributions and their projection

The non-Maxwellian expression of the EVD, first devised by Langdon [1980] then taken up by Jones & Lee [1982], Matte *et al.* [1988] and many others, is that of an isotropic Supergaussian (ISG) given by

$$f_e^{\rm ISG}(\boldsymbol{v}) = \frac{k\,\Gamma(5/k)^{3/2}}{4\,\pi\,v_{\rm th}^3\,\Gamma(3/k)^{5/2}\,3^{3/2}} \exp\left[-\left(\frac{v}{v_{\rm I}}\right)^k\right], \tag{4.35}$$

where the velocity $v = (v_x^2 + v_y^2 + v_z^2)^{1/2}$, the width sprawl $v_{\rm I} = v_{\rm th} \times (3\,\Gamma(3/k)/\Gamma(5/k))^{1/2}$ and where k is the order of the distribution. In the theoretical derivation of this expression by Langdon, isotropy was hypothesized. But as shown in section 4.4 of the present article, our CMDS show that EVDs can become anisotropic for different reasons.

At moderate intensities, CMDS illustrate that different temperatures can build up in both parallel and perpendicular directions while keeping a common order k in all directions (the reference being the direction of polarization). Therefore a single-order-anisotropic Supergaussian (SOA) distribution written as

$$f_e^{\rm SOA}(\boldsymbol{v}) = C\,\exp\left[-\left(\frac{v_x^2}{v_{{\rm S}x}^2} + \frac{v_y^2}{v_{{\rm S}y}^2} + \frac{v_z^2}{v_{{\rm S}z}^2}\right)^{k/2}\right], \tag{4.36}$$

is enough to describe such non-Maxwellian EVDs. In eq. (4.36), C is a normalization constant and the width sprawl $v_{{\rm S}\mu}^2 = v_{{\rm th}\mu} \times (3\,\Gamma(3/k)/\Gamma(5/k))^{1/2}$ where $\mu \in \{x,\, y,\, z\}$. When projected on

the μ-axis, in the sense of eq. (4.19), this distribution becomes

$$f_\mu^{\mathrm{SOA}}(v_\mu) = \frac{\sqrt{\Gamma(5/k)}}{2\sqrt{3}v_{\mathrm{th}}\Gamma(3/k)^{3/2}}\,\gamma\left(\frac{2}{k},\left(\frac{v_\mu}{v_{\mathrm{S}\mu}}\right)^k\right), \tag{4.37}$$

where $\gamma(a,z) = \int_0^z t^{a-1}\exp(-t)\,\mathrm{d}t$ is the incomplete lower gamma function. In the case of a 3D Maxwellian distribution, for which $k = 2$ in eq. (4.36), the projection is trivially a Maxwellian with the same temperature as that along the projected axis.

Since our CMDS seems to show that, at high intensities, even the order seems to be anisotropic (see Fig. 4.10) it would have been interesting to postulate a many-order-anisotropic Supergaussian (MOA) distribution of the form

$$f_e^{\mathrm{MOA}}(\boldsymbol{v}) = C\,\exp\left[-\left(\frac{v_x}{v_{\mathrm{M}x}}\right)^{k_x} - \left(\frac{v_y}{v_{\mathrm{M}y}}\right)^{k_y} - \left(\frac{v_z}{v_{\mathrm{M}z}}\right)^{k_z}\right], \tag{4.38}$$

but we were unable to find a practical formula for any of its projected distribution (such as eq. (4.37) for eq. (4.36)).

Finally, using particle-in-cell simulations, Fourkal *et al.* [2001] found that the non-Maxwellian behaviour of EVDs in a plasma submitted to an intense monochromatic radiation (laser) had one more feature that was not described by Langdon's seminal paper [Langdon, 1980]. Although the bulk of the EVD is well described by a Supergaussian, its tail (for $v \gg v_{\mathrm{th}}$) was found to match a Maxwellian. This is a characteristic that we can observe in our CMDS and this is the reason why it is listed in this section. It is represented by a Supergaussian-Maxwellian tail (SGM) function of the form

$$f_e^{\mathrm{SGM}}(\boldsymbol{v}) = \eta\, f_e^{\mathrm{M}}(\boldsymbol{v}) + (1-\eta)\, f_e^{\mathrm{ISG}}(\boldsymbol{v}), \tag{4.39}$$

where η is a parameter that characterizes the weight of the Maxwellian distribution.

4.11. Appendix B: Expressions for various useful Supergaussian distributions and their projection

Part III

Experimental campaing at the GCLT facility

Chapter 5

Setup of the experiment

Contents

This chapter describes the experimental campaign that took place in october 2021 at the GCLT facility (portable laser shock generator, *Générateur de Chocs Lasers Transportable* in French) as part of this work, in order to study the absorption and reflection of a laser by a plasma. We will start with a state of the art of similar experiments in section 5.1. The following section will then describe the setup of the campaign at the GCLT in detail.

5.1 Slab reflection and absorption experiments: state of the art

As explained in chapter 1, lasers beams irradiate either the cavity in indirect-drive ICF, or the spherical capsule in direct-drive ICF. Non planar target shapes such as cavities [Földes *et al.*, 1987] and spheres [Bach *et al.*, 1983] introduce many geometric features that can affect laser absorption. Any complicated target (sphere, cylinder, rugby-shaped) can locally, as any surface, be considered planar. This is the reason why we chose planar targets for our campaign, in addition to the fact that they are very simple to fabricate.

Thus, our review of the state of the art is limited to plane geometry. In the 1970s and the 1980s, specular reflection and scattering of a laser by a plane foil has been extensively studied for a wide range of materials and laser characteristics (wavelength, pulse duration, intensity).

The absorption and reflection of an intense laser by matter have been the subject of a number of experiments for more than 60 years, see table A on page 115 for a list of publications on the matter. For the most part, this literature review will be restricted to pulse durations between 0.1 and 8 nanoseconds, and laser intensities under 10^{14} W/cm^2 since these are parameters that were accessible on the GCLT facility. See section 5.2.1 for a more complete description of the facility.

Absorption and reflection depend on many experimental parameters including, but not limited to the material and the shape and rugosity of the target, the laser wavelength, its polarisation, the temporal shaping of the pulse, the size of the focal spot as well as the spatial intensity profile. These can all modify laser absorption and reflection.

5.1.1 The energy balance

A few definitions are useful before proceeding further. Fig. 5.1 shows a schematic representation of laser light hitting a plane target. The incident intensity is split into backscattered, absorbed, and scattered intensity. This is summarized in

$$I_{\text{inc}} = I_{\text{abs}} + I_{\text{bs}} + I_{\text{scat}}. \tag{5.1}$$

The backscattered light is mainly due to parametric instabilities such as Stimulated Brillouin Scattering (SBS) and Stimulated Raman Scattering (SRS). The scattered light include specular reflection as well as light scattered in other directions due to rugosity for instance. In the literature, this balance is often time-integrated over the duration of the incident pulse, which yields $E \propto \int I \, \mathrm{d}t$. Defining the absorption coefficient as $A = E_{\text{abs}}/E_{\text{inc}}$, the reflection coefficient as $R = E_{\text{scat}}/E_{\text{inc}}$ and the backscatter coefficient as $E_{\text{bs}}/E_{\text{inc}}$. The integration of eq. (5.1) with respect to time yields $1 = A + B + R$. Since $A = 1 - B - R$, a better characterization of reflected light leads to a better characterization of absorbed light, provided B can be estimated or otherwise measured. When backscattered light can be neglected, $A = 1 - R$. Measuring R becomes equivalent to measuring A. When the time-resolved intensity profiles are measured, they can be used to define the instantaneous absorption and reflection coefficients $A(t) = I_{\text{abs}}/I_{\text{inc}}$ and $R(t) = I_{\text{scat}}/I_{\text{inc}}$.

When the laser incidence is normal, the backscattered light and specular reflection overlap. They can still be distinguished from one another using spectroscopy, since reflected light is blue-shifted while SBS tends to be red-shifted. Indeed, light backscattered by SBS is subjected to the Doppler effect, and thus may be overall blue-shifted, if the plasma is fast enough. Because of the SBS process, this light cannot be as blue-shifted as specularly reflected light, and so reflected and SBS light can be distinguished by spectroscopy. However, spectroscopy was not used in all the experiments at normal incidence that will be discussed here, for example [Arad *et al.*, 1980].

5.1.2 Scattered light and specular reflection

The part of scattered light that is in the specular reflection may vary during the laser pulse. Indeed, the surface on which the laser is reflected is not guaranteed to stay parallel to the initial target surface for the whole duration of the pulse. In particular, non-uniformities in the spatial profile of the incident beam can lead to a deformation of the target surface [Desai *et al.*, 1994]. As a result, light can be scattered in the whole half space in which the plasma expands.

Ref	Wavelength (µm)	Target material	Intensity (TW/cm^2)	Duration (ns)	Focal spot diameter (µm)	Incidence (°)
Anthes *et al.* [1979]	1.064	Al, Fe, Au	10-100	8	100	17
Arad *et al.* [1980]	1.064	Al, Au	10-10^4	3	10	0
Dahmani [1993]	1.064	C coated Al, Si coated CH_2	10-1000	0.7	44	-
Desai *et al.* [1994]	1.064	Cu, glass	1-20	5	160	22.5
Eidmann *et al.* [1984]	1.3	$C_6H_7O_{11}N_3$, $C_{16}O_3H_{14}$	0.1-10^4	0.28	60, 400	0
Garban-Labaune *et al.* [1982]	1.064, 0.53, 0.26	$C_{10}H_8O_4$	0.02-1000	0.1, 2	50	0
Krokhin *et al.* [1975]	1.064	Al, $(CH_2)_n$	60, 70	3	40	0, 45
Mead *et al.* [1983]	0.53	Be, Au	30-5000	0.6-0.7	40-460	0-60
Meyer *et al.* [1982]	1.064	Al	5-500	0.8	60-500	0
Nishimura *et al.* [1980]	10.6	CD_2	0.3-2.6	3	200	35
Nishimura *et al.* [1981]	10.6, 1.064, 0.53	Au and $(CH_2)_n$ coated Al	1-300	0.5, 1	10	27, 45
Offenberger *et al.* [1986]	0.268	Al	0.1-100	1	170-340	0, 45
Ripin *et al.* [1980]	1.064	CH	3-700	3	35, 230, 450	6
Rupasov *et al.* [1973]	1.064	Be, Al, Cu, Zn, Ta, Pb, Al, $(CH_2)_n$	0.05-5	4	60	9
Seka *et al.* [1982]	0.35	CH, Ni, Au	20-3000	0.09, 0.45	100, 800	0, 10
Simpson *et al.* [1990]	0.527	Au	50-350	0.5-1.5	200	-
Young & Estabrook [1994]	1.064	CH	140	1	100, 200, 500	0

Table A: Summary of experimental conditions of previous experimental works that studied the absorption and reflection of an intense laser by a plane target. Though it is not explicitly stated in most of these papers, the date of the experiments is such that most probably did not use beam smoothing techniques.

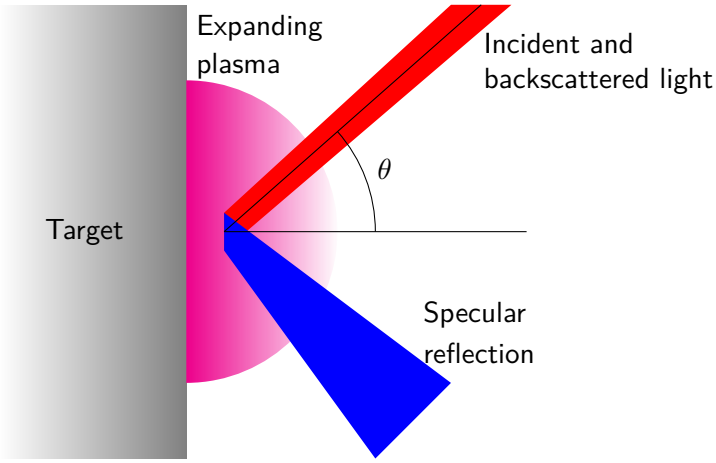

Figure 5.1: Representation of a laser hitting a plane target at an angle, and its specular reflection. The incidence θ is defined as the angle between the target normal and the incident beam. When the incidence is normal ($\theta = 0°$), the specular reflection is superimposed with the backscattered light. This simplified representation only shows the specular reflection. In practice, part of the light is scattered in the 2π half-space opposite to the target. The effects of this on the experiment are discussed insection 5.1.2.

Krokhin *et al.* [1975] measured the directivity of reflected light, both at normal and 45° incidence. Though the scattering pattern was elongated in the direction of specular reflection, they found that the scattered energy integrated in all directions was significantly higher than the specularly reflected energy collected in a cone with the same solid angle as the focusing system, for example from $R = 0.65\%$ to $R = 3\%$ in one of their shot. In other words, assuming the reflected light is scattered in a cone that has the same solid angle as the incident light induces a significant error in the energy balance. It is important to take into account light scattered in the whole half plane in which the plasma expands, or at least a larger solid angle than that of incident light. The directivity profiles of Krokhin *et al.* [1975] were confirmed by Ripin *et al.* [1980]. Nishimura *et al.* [1980] studied the directivity profiles for 35° incidence and showed the directivity of reflected light depends on the polarization of incident light.

The importance of scattered light was confirmed by Garban-Labaune *et al.* [1982], who measured more scattered light with an integrating sphere than reflected back into the optics, at normal incidence, $\lambda = 1.06\,\mu m$, and for intensities less than $10^{14}\,W/cm^2$. However, the light reflected back into the optics include SBS as well as specular reflection, so the exact difference between scattered light and specularly reflected light was not known. Finally, Desai *et al.* [1994] measured the reflection coefficient for multiple collection angle, and multiple intensities. They found that even the qualitative behaviour of the reflectivity with respect to laser intensity depended on the angle of collection. The wide scattering of the reflected laser light was in part explained by distortions of the plasma critical surface which were suggested to arise as a result of non-uniform laser irradiation.

As a result, experiments in which only the specular reflection is collected [Dahmani, 1993, Offenberger *et al.*, 1986], where the solid angle of collection is not always given, are not guaranteed to actually measure all the scattered light.

All in all, these experiments emphasize two points:

- the need to measure the reflectivity coefficient with an angle of collection as wide as possible,

- the importance of using smoothing techniques such as polarization smoothing and random phase plates that enhance laser power uniformity in the focal spot.

Another advantage of using smoothed laser beams, besides a better control of the laser intensity on target and a more specular reflection, is that random phase plates and polarization smoothing have been shown to greatly reduce SBS [Seka *et al.*, 2002b].

5.1.3 The integrated absorption coefficient

There is a general agreement in the literature that the integrated absorption coefficient decreases, when the laser intensity increases from 0.1 and 100 TW/cm^2, independantly of the target material and of the other laser parameters. This is supported by multiple experiments where an integrating sphere was used to measure the whole scattered power, and the light backscattered through the optics was measured separately [Anthes *et al.*, 1979, Arad *et al.*, 1980, Eidmann *et al.*, 1984, Meyer *et al.*, 1982, Nishimura *et al.*, 1981, Simpson *et al.*, 1990], as well as when only the backscattered light and specular reflection were measured [Dahmani, 1993, Offenberger *et al.*, 1986]. However, the exact values of absorption, reflection and backscattered light may fluctuate because they strongly depend on the other laser parameters (wavelength, pulse duration) as well as the angle of incidence.

The dependance of laser absorption upon the angle of incidence between the target and incident laser beam has been shown [Mead *et al.*, 1983] to be in agreement with theoretical predictions [Kruer, 1988, Scheiner & Schmitt, 2019], in which the reflection coefficient is expected to behave like $\exp(-K\cos^3\theta)$ where θ is the angle of incidence and where K depends on laser parameters (intensity, wavelength) and target material properties.

Experiments carried out with carbon, silicium, aluminium, iron and gold targets [Anthes *et al.*, 1979, Dahmani, 1993] revealed that the integrated reflection coefficient does not depend much on the target material for intensities lower than 100 TW/cm^2. This is apparent in Fig. 5.2, which is from Dahmani [1993]. The target material [Arad *et al.*, 1980, Mead *et al.*, 1983] does make a difference in energy absorption at higher intensities. The coefficient of energy absorption was found to decrease with increasing laser intensities in these experiments, though the numerical value varied from experiment to experiment. This is not surprising, since parameters known to affect energy absorption, such as the angle of incidence, were not the same in all these experiments.

5.1.4 The instantaneous absorption coefficient

It is known [Turnbull *et al.*, 2015] that the instantaneous reflectivity coefficient varies during the pulse in ICF experiments. Specifically, the reflection is significant at the beginning of the pulse, before rapidly decaying. The instantaneous reflection coefficient then increases again and even reaches values higher than the initial reflectivity.

Several experiments [Garban-Labaune *et al.*, 1982, Seka *et al.*, 2002a] indicated that the instantaneous reflection coefficient also varied in plane foil configurations. This was done by showing that the integrated reflection coefficient depends on the duration of the pulse. Seka *et al.* [2002a] showed an increase in the coefficient of absorption from 0.8 to approximately 0.95 at intensities below 100 TW/cm^2 when the pulse duration increased from 100 ps to 450 ps, at a wavelength of 0.35 µm. At a wavelength of 1.06 µm, Garban-Labaune *et al.* [1982] measured an increase of the absorption coefficient between 0.1 and 0.3 when the pulse duration was increased

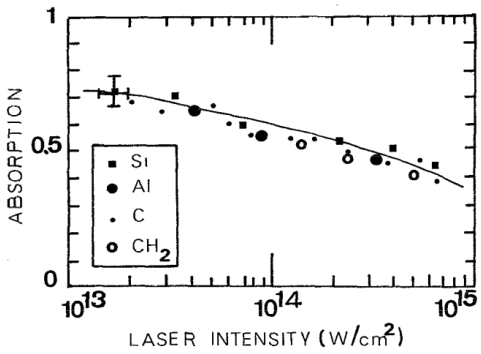

Figure 5.2: Integrated reflectivity coefficient with respect to laser intensity for multiple target materials. The linearly polarized laser had $\lambda = 1.064\,\mu m$. Further details of the experimental setup can be found in table A. Image credit: Dahmani [1993].

from 100 ps to 2.5 ns for intensities between 0.2 and 200 TW/cm^2. These two experiments confirm that the reflection coefficient of a laser induced plasma is not constant during the laser pulse. This emphasizes the importance of time-resolved reflectivity measurements.

Rupasov *et al.* [1973] measured the time-resolved reflected pulse, which appeared to have a different time profile than the incident pulse, specifically the power peaked earlier in the reflected pulse than the incident pulse. However, since the incident intensity is constantly varying, it is not possible to reach a self similar state, such as those for which theoretical models exist [Manheimer, 1982, Mora & Pellat, 1979]. This has guided us to use pulse shapes with intensities as constant as possible during our campaign at the GCLT facility, so that our results can be more easily compared to theoretical models of the literature.

5.2 Setup of the experimental campaign on GCLT

As part of this thesis, an experimental campaign took place at the GCLT facility at CEA DAM in october 2021. Though details will be given in what follows, the basic principle of the experiment is represented in Fig. 5.3. A high intensity laser (1) is focused by a f/6 lens on a plane foil of metal (2), with 45° between the incident laser and the normal of the target. The incident and specularly reflected radiation are measured (time-resolved profile, integrated energy) in (3) and (4) respectively, so as to obtain information on the reflectivity of the target. The specularly reflected radiation is collected by a f/2 lens. A CCD (5) and a streak (6) camera are used to record images of the plasma. In Fig. 5.4 are shown pictures of the experimental chamber, and of both cameras.

5.2.1 The laser facility

The GCLT facility houses a Nd:Glass laser ($\lambda = 1.053\,\mu m$) that is capable of delivering up to 40J of energy in a single pulse, with a duration between 4 and 100 ns that can be shaped at will. The laser chain, shown in Fig. 5.5 consists of two amplification stages and some diagnostics on the laser pulse before being directed to the experimental chamber. After the first amplification stage, the laser is split into two beams, going through the second amplification stage separately. The beams are recombined right before going out towards the experimental chamber. At this

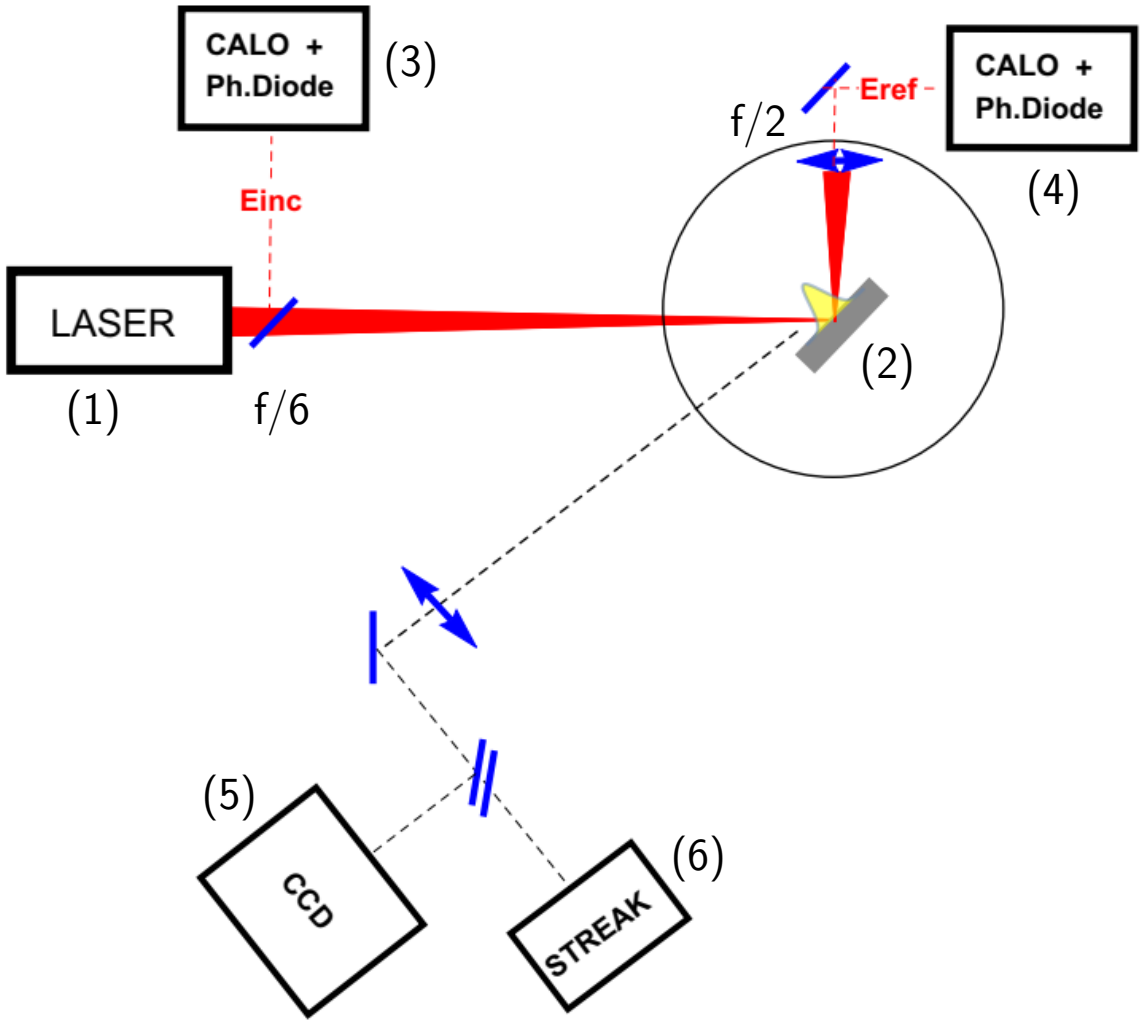

Figure 5.3: Diagram of the experimental setup. The laser (1) is focused on the target (2) with 45° incidence. Both the incident and the specularly reflected energy and temporal profile are measured by a calorimeter and a photodiode, (3) for the incident light and (4) for the reflected light. The plasma is observed by a CCD (5) and streak camera (6).

point, the two beams polarizations are normal to each other, so they do not interfere with one another. However, each beam has its own speckle pattern, which leads to a reduction in speckle contrast [Tsubakimoto *et al.*, 1992]. This process is known as polarization smoothing, and aims to make the intensity profile on target more uniform.

Random phase plates [Burckhardt, 1970, Kato *et al.*, 1984] are also used to smooth the spatial profile of laser intensity. A random phase plate is an array of cells, each of which transmits the laser beam while applying a phase shift of either 0 or π. It is associated to a focal spot diameter: we used focal spot diameters of 429, 250, and 86 µm. These diameters were measured so that 81% of the total laser energy is within the focal spot. In the rest of this work, all incident energies are corrected to exclude energy outside the focal spot. In Fig. 5.6 are shown the spatial intensity profiles associated with each phase plate. The 429 µm spot has the most uniform profile, but is associated with the lowest laser intensity, for a given energy. The 250 and 86 µm focal spot

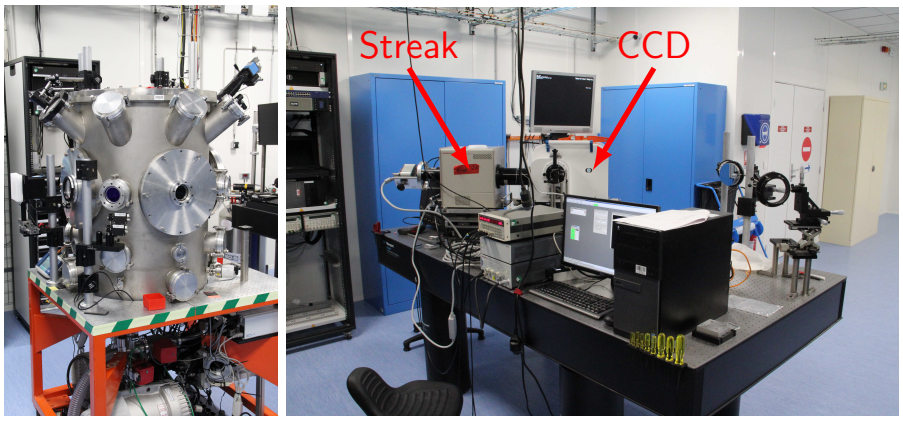

Figure 5.4: Pictures of the experimental chamber (left) and of the streak and CCD cameras (right).

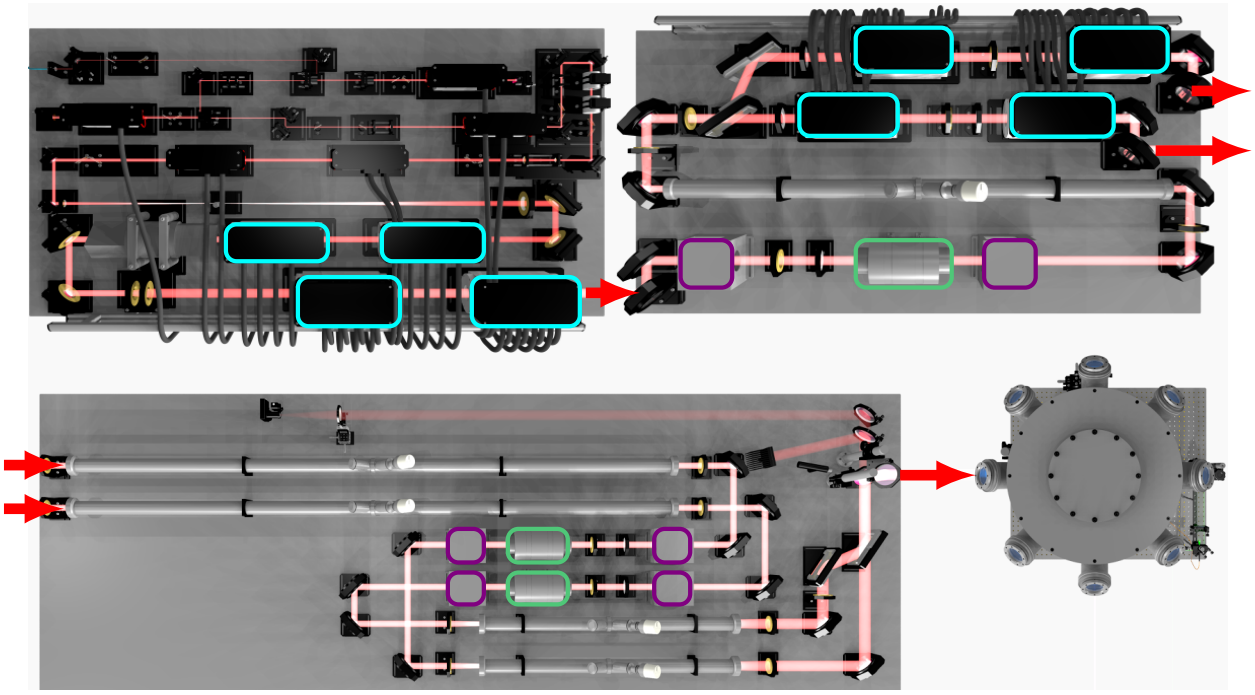

Figure 5.5: View of the two GCLT laser chain. The top part of the diagram contains the two stages of amplification. The bottom part contains diagnostics on the laser pulse, as well as the recombination of the two beams and the chamber. The elements outlined in cyan are Nd:glass amplification cristals. The elements outlined in green are Faraday rotators. Together with the elements outlined in violet, which are polarizers, they prevent light from backscattering through the laser chain. Image Credit: Emilien Lescoute (CEA/DAM).

diameters made it possible to expand the accessible range of intensities, but at the cost of less uniform focal spots.

This is because the size of a focal spot varies as $\lambda f/d$, where f is the focal length, λ the laser wavelength and d is the size of a cell of the random phase plate. This shows that a smaller focal spot for fixed λ and f means larger d. Thus, a small focal spot is associated with large cells in the random phase plate, and since the size of the beam before the phase plate is also fixed, the beam can pass through less cells, and so there are less speckles, which leads to lower intensity uniformity at the focal spot.

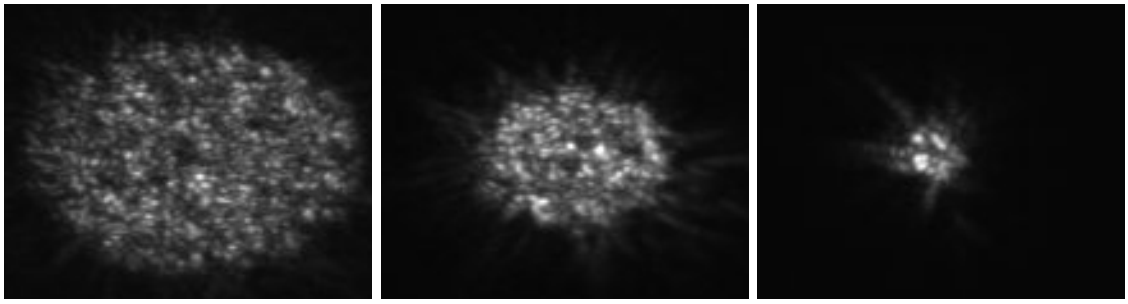

Figure 5.6: Imaging of the focal spot on target (with 45° incidence), with the 429 µm (left), 250 µm (center) and 86 µm (right) phase plates. The space scale is the same for all three graphs. The focal spot is elliptic because of the incidence. The size of the focal spot normal to the laser axis corresponds to the height of the focal spot in the graphs. It is apparent that the larger the focal spot, the more uniform it is.

5.2.2 The laser pulses

As part of the experimental campaign, four pulse shapes were considered, samples of which are shown in Fig. 5.7.

- **Short Single Pulse** (SSP): it is a pulse of constant intensity for 4 ns, which was used for the majority of the shots. Two settings of energy were used, 10 J and 20 J. One advantage of a step pulse is that since the incident intensity is almost constant for its whole duration, a steady (or at least self-similar) state can develop inside the plasma, at variance with Gaussian pulses, in which the incident intensity is constantly varying, so no steady state can develop.

- **Long Single Pulse** (LSP): it is a pulse of constant intensity lasting for 10 ns, which was used in order to study the behaviour of the reflected light on a longer timescale. 40 J were delivered over 10 ns.

- **Staircase Pulse** (STP): it is a pulse which starts out like the SSP, but switches to a higher intensity for four more nanoseconds at the end. The STP is an attempt to mimic typical ICF laser pulses, where intensity rises twice during the pulse to deliver two shocks, though the intensity reached at the GCLT facility are lower than intensities used in actual ICF experiments. 10 J were delivered over the first 4 ns of the pulse, and 20 J over the next 4 ns.

- **Double Step Pulse** (DSP): it is a pulse composed of a first SSP step, and, after a delay of 20 ns, a second SSP identical to the first one. This pulse allowed us to get more data on

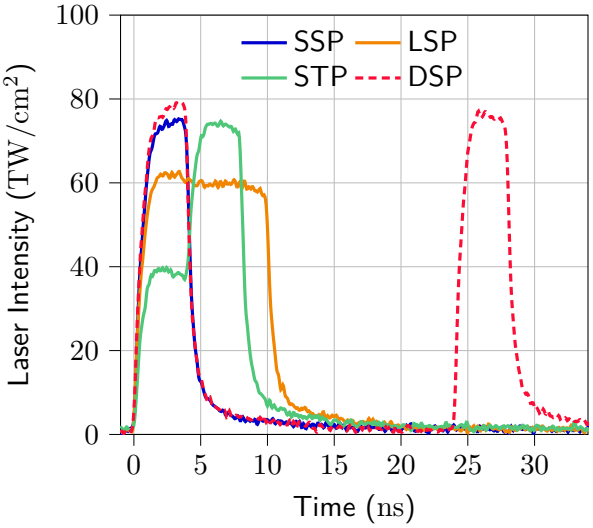

Figure 5.7: Typical laser pulses for all the shapes employed during the campaign. The energies on target experienced small shot-to-shot variations. For these pulses, the energies on target are 19.2 J for the step pulse (SSP), 38 J for the long step pulse (LSP), 29.98 J for the staircase pulse (STP), and 38.8 J in the double step pulse (DSP), of which 19.83 J in the first pulse, and 18.97 in the second one. The rise time is on the order of a nanosecond for all pulse shapes. However, the extinction after the pulse is not as short, and in particular, the extinction between the two steps of the double step is not total.

the SSP, since the first pulse of DSP is SSP, while the second pulse served as a probe on the plasma induced by the first pulse in order to assess the absorption of laser in a plasma bubble. Due to technical constraints, the intensity extinction between the two steps is not perfect, as shown in Fig. 5.7.

Table B sums up the intensities that were reached, between 1.7×10^{13} and 8.6×10^{13} TW/cm^2. Having intensities less than 10^{14} W/cm^2 means that we expect very little backscattered light (SBS and SRS), which was confirmed by radiation hydrodynamics simulations with TROLL. This means that I_{bs} can be neglected from eq. (5.1). Thus, most of the intensity that is not absorbed by the target is specularly reflected, the difference being energy scattered in other directions.

5.2.3 Targets and Diagnostic

All targets are plane foils of a pure element (except for plastic targets, which are made of carbon and hydrogen), placed inside a vacuum chamber with a pressure less than 10^{-3} bar. Elements shot are Al, Ti, Fe, Cu, Ag, Au, Pb, Si, V, Zn, Mo, Sn, Ta, W, Bi, and CH, shown in Fig. 5.8.

Size of focal spot	10 J over 4 ns	20 J over 4 ns	40 J over 10 ns
86 µm	4.3×10^{13} W/cm^2	8.6×10^{13} W/cm^2	6.9×10^{13} W/cm^2
250 µm	5.1×10^{12} W/cm^2	1.0×10^{13} W/cm^2	8.1×10^{12} W/cm^2
429 µm	1.7×10^{12} W/cm^2	3.5×10^{12} W/cm^2	2.7×10^{12} W/cm^2

Table B: Intensity reached for different phase plates and pulse characteristics. For all these pulses, the intensity is constant for the whole duration of the pulse. The staircase pulse shape is equivalent to a (10 J, 4 ns) step immediately followed by a (20 J, 4 ns) step.

When possible, we aimed to test multiple elements in each column of the periodic table, to assess whether their behaviour is related to the outermost electronic configuration. Additionnally, there were two kinds of iron and gold targets, smooth surface ($a_{rms} \approx 0.1\,\mu m$) called laminated and rough surface ($a_{rms} \approx 1\,\mu m$) called hard. Multiple shots on both types of target using the 10 J SSP have been carried out and we observed no significant difference beyond the shot-to-shot variations. That indicates the influence of target rugosity on our experiments was not significant, at least for low laser intensity shots.

The energy as well as the pulse shape of the incident laser irradiating the plane target are monitored by diverting 0.1% of its energy shortly before it reaches the experimental chamber, and measuring the energy and profile of this fraction, in (3) in Fig. 5.3 using both a photodiode and a calorimeter. The absolute energy measurement is then corrected to only include the energy in the focal spot. The specular reflection is collected by a lens inside the chamber and concentrated outside the chamber where it was analyzed using also a calorimeter and a photodiode (4) in Fig. 5.3. The f/2 collecting lens had a coating to minimize reflection at 1053 nm. The calorimeter provided an absolute integrated measure of the reflected energy, while the photodiode provided a relative time-resolved measure of the intensity collected.

TODO emsision du plasma, pas plasma Additionally, the plasma induced by the laser pulse was monitored with a streak camera and a CCD camera, respectively (5) and (6) in Fig. 5.3. The corresponding fields of view on the plasma are represented in Fig. 5.9. The streak camera observes a single axis, but is resolved in time. The operating principle of a streak camera is shown in Fig. 5.10. The plasma is observed through a thin slit(100 µm here). Photons emitted by the plasma are converted to photoelectrons by a photocathode. These photoelectrons are then projected onto a fluorescent screen. An electric field is applied to the electron beam before it reaches the screen. This electric field shifts the positions of the electrons. The electric field varies during the shot, and so the relation between the electrons shift and time is known. The result is a 2D picture, where one axis is space (the slit), and the other is time (the electrons shift).

The streak camera's slit was directed to image the axis of the plasma created by the irradiation of the target (normal to the foil). It provided a time-resolved imagery of a 10-µm wide slice of the plasma. The streak camera could be set for 10, 20 and 50 ns acquisition duration.

The CCD camera provided 2D images of the plasma self emission seen from the side. The CCD was able to take 16 pictures during a shot with 3 ns of exposure for each picture. The start time of exposure can be set independantly for each of the 16 pictures. This means that, for example, the camera could be set to take one picture every nanosecond. This setting was used for few shots, however, in most of them, the camera was set to take one picture every 3 ns, so the exposure of one picture started when the exposure of the previous picture ended. An example of CCD data is shown in Fig. 5.11, and cuts of the data are shown in Fig. 5.12. The plasma can be seen expanding from the target. Each camera has a different sensibility, so a normalization step is required in order to compare the CCD images with each other. This normalization is performed by using an image with a static laser used to light up the camera.

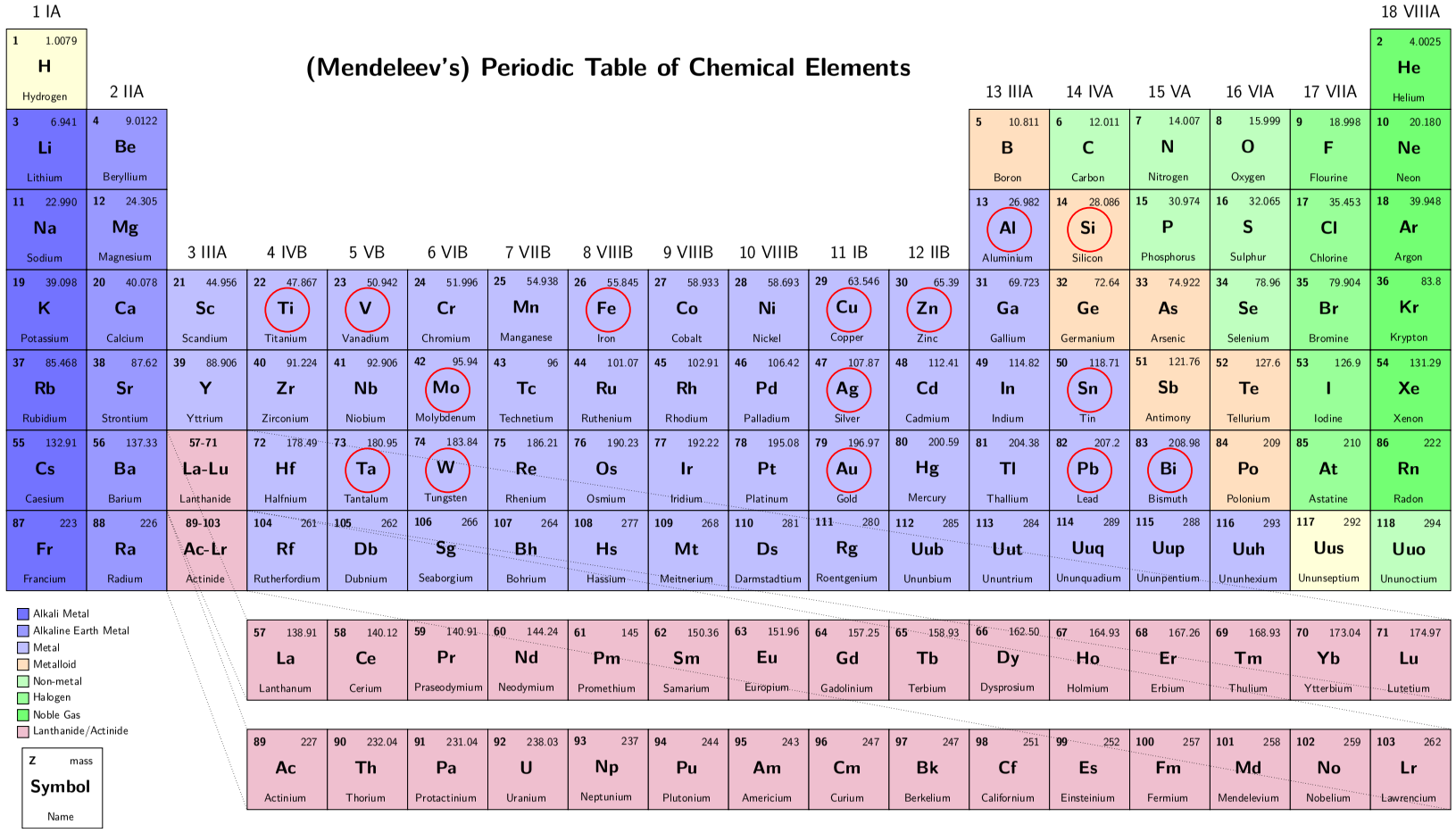

Figure 5.8: Periodic table of elements. The elements that were shot during the campaign are circled in red. Gold is the material that was shot the most, because of its common use as hohlraum material in ICF. When possible, we tried to shot multiple materials of the same column, for example copper and silver for gold, to test whether materials in the same column have similar properties.

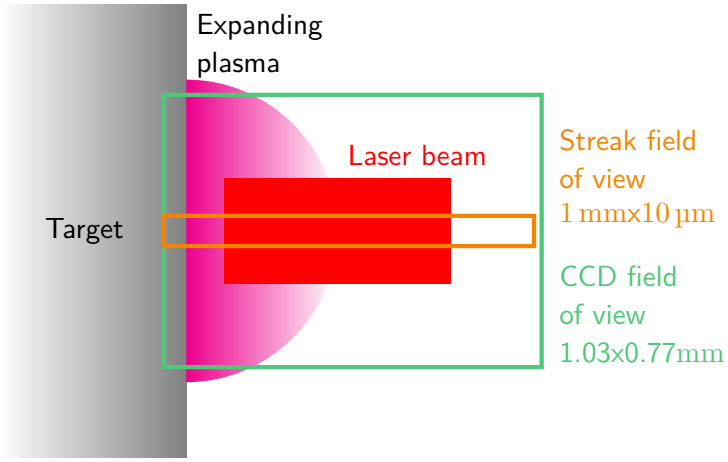

Figure 5.9: Representation of the fields of view of the streak and CCD cameras (not to scale). The laser does make a 45° angle with the target normal, but it is in the direction of the depth of the fields of view of the cameras, and so it cannot be seen in this representation. The lenses between the plasma and the cameras have a magnification of 10, so 100 µm wide slit of the streak camera corresponds to a 10 µm wide view of the plasma.

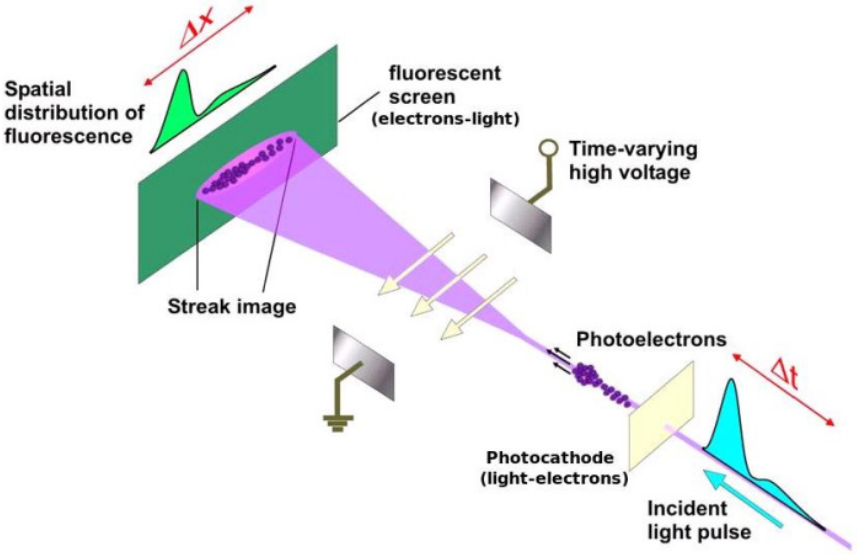

Figure 5.10: Working principle of a streak camera. Image credit: Mahgoub *et al.* [2012]

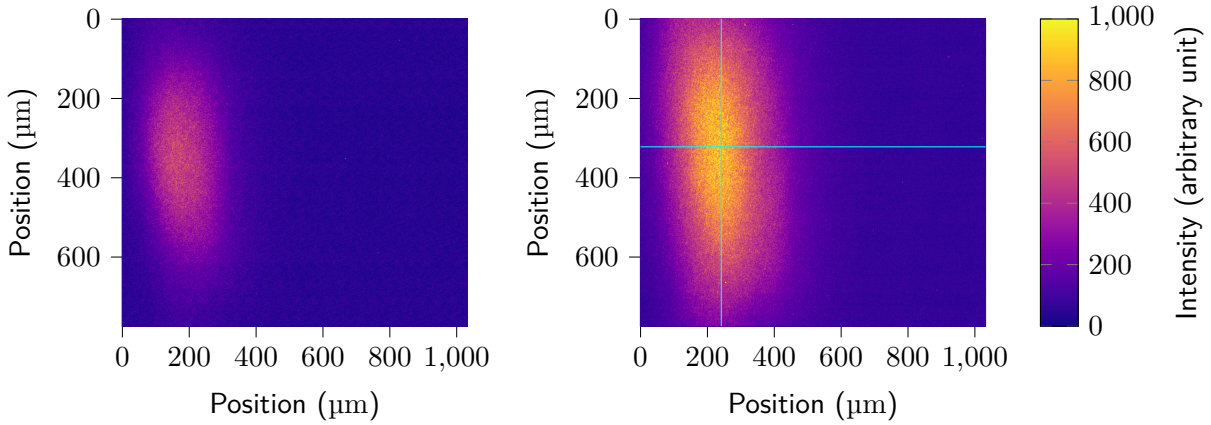

Figure 5.11: CCD images from a shot using the SSP, and $I = 8.6 \times 10^{13}\,\mathrm{W/cm^2}$. The CCD pictures are taken with 3 ns exposure. The left image is earlier during the shot than the right image. The target is seen from the side, it is on the left side of the picture, see Fig. 5.9 for the position of the field of view relative to the laser. The color scale is the same for both images. The orange feature corresponds to the self-emission of the plasma. The cyan lines indicate the cuts that are shown in Fig. 5.12

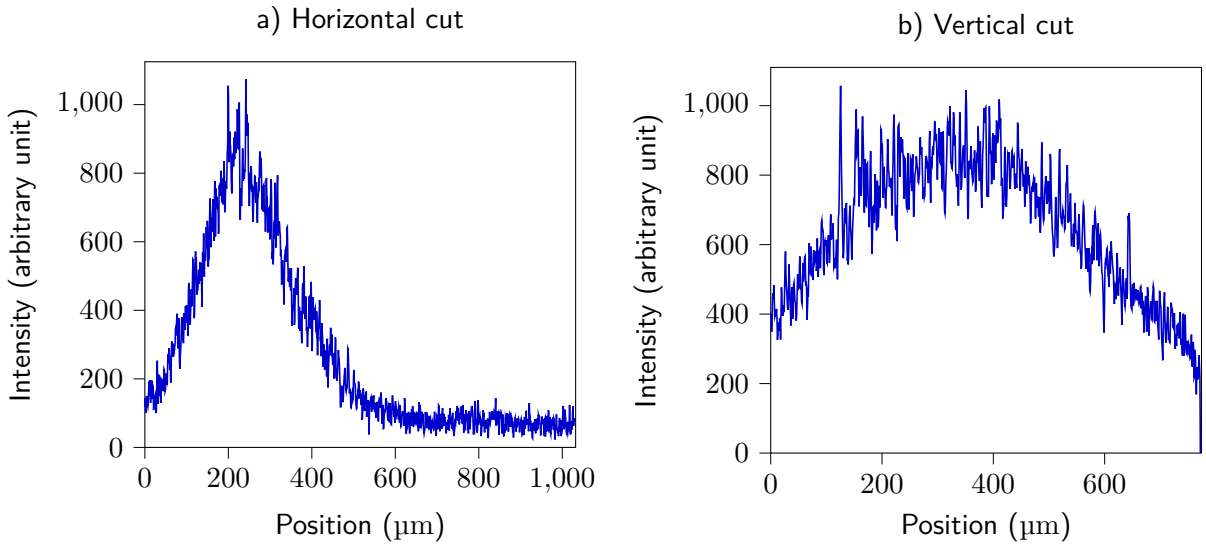

Figure 5.12: CCD cuts from the image shown in Fig. 5.11 corresponding to the cyan lines showed on the right image of Fig. 5.11.

Chapter 6

Experimental results and interpretation with the radiation hydrodynamics code TROLL

Contents

The results of the experimental campaign are presented in this chapter. For each pulse shape, the temporal profile of the reflected power is commented. The influence of target material is analysed, and the variations of the reflected power profiles with laser intensity is discussed (when multiple incident laser intensities are available). In section 6.1.5, a selection of streak images are presented and commented. In section 6.1.6, a simple theoretical model is used to better understand the results shown in the previous sections.

Finally, in section 6.2, the first results of radiation hydrodynamics simulations using the code TROLL are presented. Since the inverse bremsstrahlung absorption model devised in chapter 3 was implemented in TROLL, the comparison of experimental results with simulations can be used in order to get experimental measurements of the main constant of the parametrized models, C_{abs} (see eqs. (3.2) to (3.5)). The results presented here are preliminary because at the time of

writing this thesis, several sources of uncertainty, discussed in this chapter, have not yet been fully addressed.

6.1 Experimental results

6.1.1 Single step pulse (SSP)

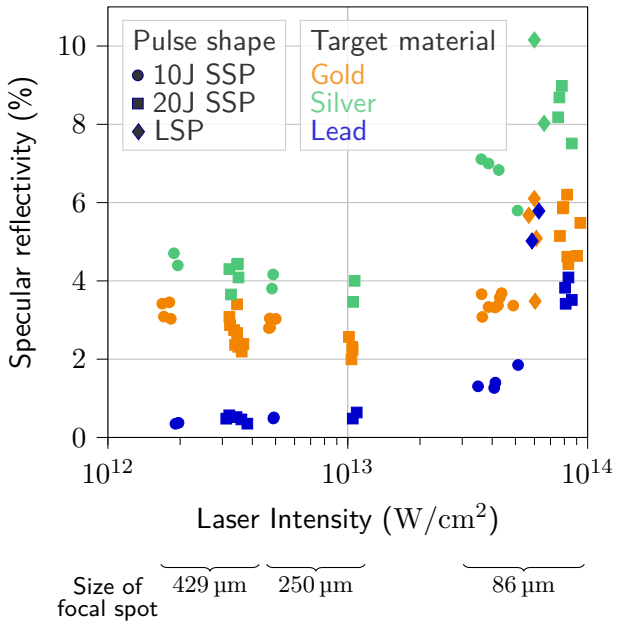

Figure 6.1: Integrated specular reflectivity versus shot intensity for multiple materials. For every shot, the laser pulse is approximately square and lasts 4 ns, *i.e.* the pulse is a step, or a double step. The reflectivity is integrated on the first 20 ns of the shot, so as to include residual laser energy hitting the target after the main pulse. Shots on gold are plotted in orange, shots on silver are plotted in green and shots on lead are plotted in blue. Other materials are not plotted for clarity, but follow the same trend: reflectivity almost constant for intensities $\leq 1.0 \times 10^{13}\,\mathrm{W/cm^2}$, and a higher reflectivity for intensities $\geq 1.0 \times 10^{13}\,\mathrm{W/cm^2}$. The exact value of the reflectivity for intensities $\leq 1.0 \times 10^{13}\,\mathrm{W/cm^2}$ as well as the trend for higher intensities are material-dependant.

In Fig. 6.1 is plotted the integrated reflectivity as a function of the laser intensity on target for multiple materials. The specular reflectivity is higher at high laser intensities. This is in accordance with previous results [Arad *et al.*, 1980, Eidmann *et al.*, 1984, Simpson *et al.*, 1990], where the energy absorbed decreases with increasing laser intensity. To investigate this behaviour, it is useful to observe the temporal profiles of reflected power with respect to time, for multiple laser intensities.

Indeed, Fig. 6.2 shows that this sharp rise in reflectivity is linked with a change of the reflected power temporal profile. For intensities $\leq 10^{13}\,\mathrm{W/cm^2}$, the reflected power on gold (left graph) decreases as time goes by. The rise of the integrated reflectivity in Fig. 6.1 for higher intensities is correlated with a rise of the reflected signal during the pulse, as opposed to the decreasing signal at low intensities. All materials tested during the campaign, except for lead which will be detailed further, exhibit the same qualitative behaviour, though it is not shown here for all

materials to avoid cluttering the graph. The slope of the reflected power during the pulse varies from material to material, but its sign is the same for all materials inspected, at a given intensity.

As shown in the right graph of Fig. 6.2, lead has a different behaviour compared to all other materials that were used. Indeed, it consistently had the lowest reflectivity of all materials as can be seen against gold and silver in Fig. 6.1. The reflected power versus time for lead also has a different shape compared to other materials, especially at high intensity. This may be linked to the fact that lead has the highest Z of all the materials tested at high intensity. The only material tested with higher Z is bismuth, but all shots involving bismuth targets were carried out at low intensity, where the reflected power for all materials has the same qualitative profile, which did not allow us to get a clearer insight on the subject.

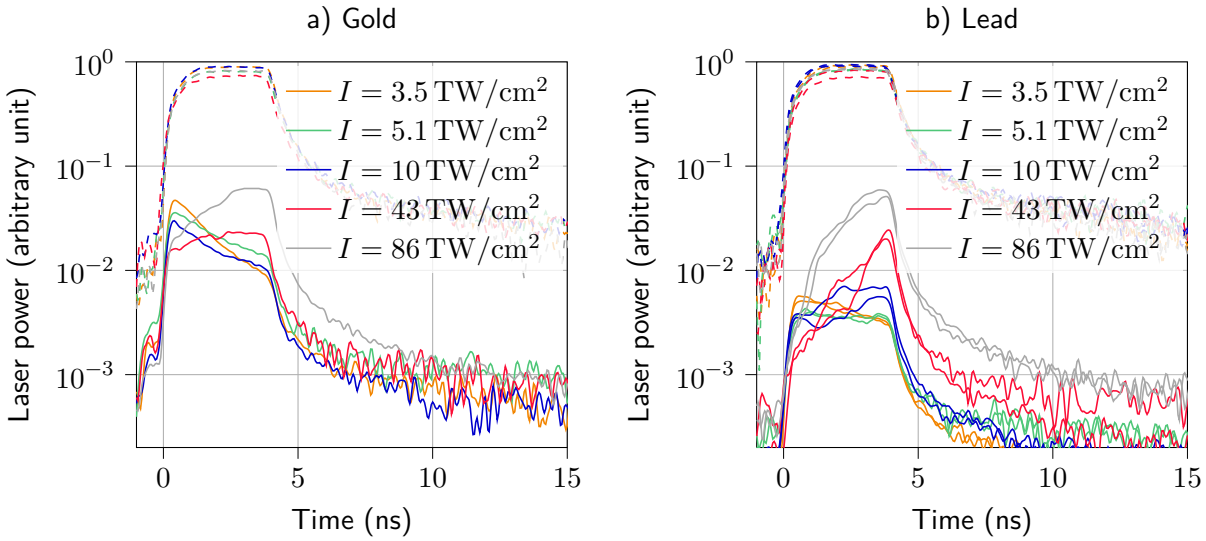

Figure 6.2: Power incident (dashed) and reflected (solid) versus time for multiple intensities, for two materials: gold (left) and lead (right). The laser power is normalized so that all the incident pulses have the same maximum level, otherwise the incident power would not be the same for 10 J and 20 J pulses. For each shot, the corresponding reflected power is the solid line of the same color. See table B for the focal spot size and energy corresponding to each intensity. For lead, two shots are plotted (in the same color) for each intensity, to show repeatability.

6.1.2 Long Single pulse (LSP)

To further investigate the rising reflected power during the pulse that was observed at high intensities with the LSP, we used the long single pulse shape. Because of technical constraints, it was not possible to simply extend the 20 J - 4 ns pulse to 10 ns. Instead, 40 J were delivered over 10 ns, so the intensity reached was $6.9 \times 10^{13}\,\mathrm{W/cm^2}$ (the 86 µm phase plate was used to investigate high intensities), which is slightly less than the $6.4 \times 10^{13}\,\mathrm{W/cm^2}$ intensity that was reached during the 20 J - 4 ns step pulse.

The reflected power for this pulse shape is presented in Fig. 6.3. Though only silver, gold and lead shots are presented so as not to clutter the graph, results for all materials are similar: the reflected power either levels off or rises slowly. It is interesting to note that the behaviour of lead in this graph is very similar to that of gold and silver, except at the very beginning of the pulse.

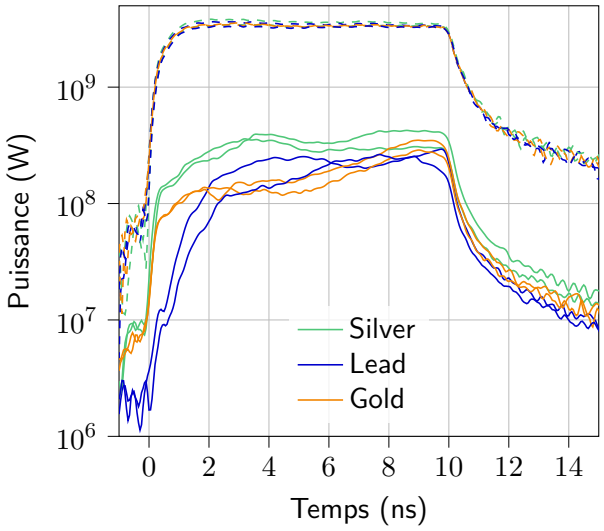

Figure 6.3: Power incident (dashed) and reflected (solid) versus time for multiple intensities, for silver, gold and lead targets. Multiple shots are shown for each material to demonstrate the shot to shot repeatability. The first four nanoseconds of the reflected profiles are very similar to the $I = 86\,\mathrm{TW/cm^2}$ shots in Fig. 6.2, which is expected since the laser profile is similar, only with a slightly lower intensity ($I = 69\,\mathrm{TW/cm^2}$). The reflected power on silver and lead does seem to reach a steady state, and stay constant for the last 5 ns of the pulse.

This might mean that at high laser intensity, lead behaves like other materials with a time delay. Further investigations into this matter are required to reach a definite conclusion, and to explain the behaviour of lead at low laser intensities.

6.1.3 Double step pulse (DSP)

The DSP was used to assess the absorption of laser light (the second pulse) on a preformed plasma (induced by the first pulse). A selection of these results are presented in Fig. 6.4 for a 86 µm focal spot. The materials not shown in these graphs behave similarly to gold, with a reflected power constant or slightly decreasing during the second pulse, but the exact numerical values of the reflected power and its slope vary with the material. Similar shots were carried out at a lower intensity, with a 429 µm focal spot. These results are not shown here since all materials behave similarly to gold in Fig. 6.4.

At higher laser intensities, with a 86 µm focal spot, the behaviour of reflected power for aluminium, iron and copper targets differed from other materials, as shown in Fig. 6.4. Indeed, a spike in reflected power occured near the end of the pulse. This is repeatable even though the amplitude of this spike differs from shot to shot, using the same laser pulse and material. However, this spike occured to different degrees in all shots on aluminium, iron and copper for the 2 x (10 J, 4 ns) pulse shape.

6.1.4 Staircase pulse (STP)

In ICF experiments, laser pulses are shaped to produce two shocks or more (see Fig. 1.8 for typical ICF pulses). Here, we mimicked this shape in our experiments with a succession of two intensity rises, the staircase pulse shape (see Fig. 5.7). We found that the behaviour of the reflectivity

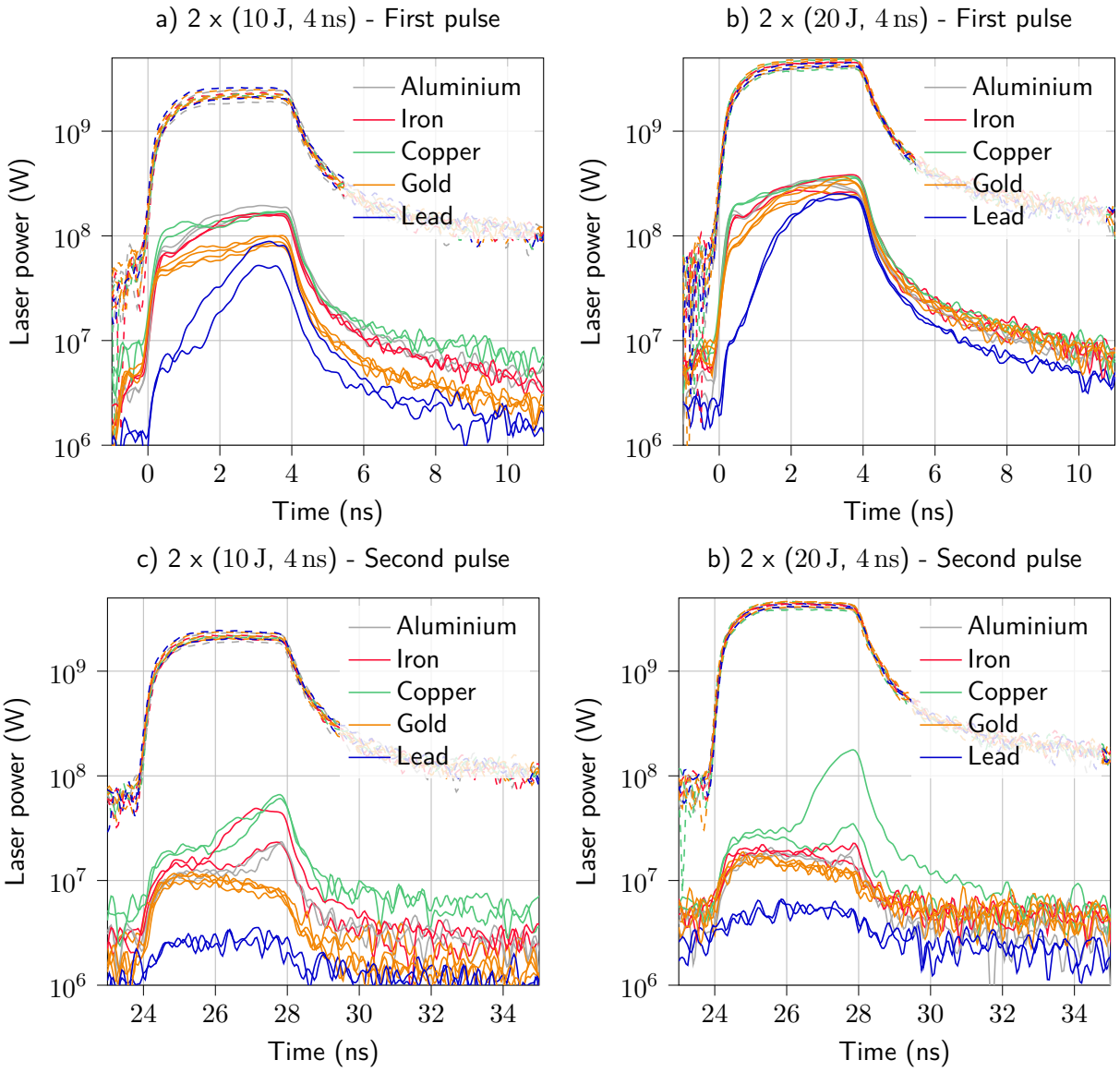

Figure 6.4: Power incident (dashed) and reflected (solid) versus time for multiple target materials: Al, Fe, Cu, Au, Pb. All graphs use the double step pulse and have a 86 µm focal spot, the difference being the shots plotted a) and c) use two 10 J steps, and b) and d) use two 20 J steps. For each shot, the corresponding reflected power is the solid line of the same color. Multiple shots are shown for each material, to show repeatability. Multiple behaviours can be distinguished. Reflected power during the first pulse is similar to the $I = 86\,\mathrm{TW/cm^2}$ in Fig. 6.1. Reflected power by lead and gold are almost constant during the second pulse, for both energies. For copper, iron and aluminium, a spike in reflected power seems to occur near the end of the pulse. The amplitude of the spike seems to vary from shot to shot, especially for copper in d), but the spike itself is always noticeable.

was not significantly affected by the second rise as shown in Fig. 6.5, though the reflected power doubles in a very short time, which is coherent with the fact that the incident power doubles in this same time span. However, with the 429 µm focal spot, the reflected power in the second part of the pulse seems to decrease with a slope comparable to that in the first part of the pulse. With the 86 µm focal spot, we observed a behaviour similar to the LSP, specifically the reflected

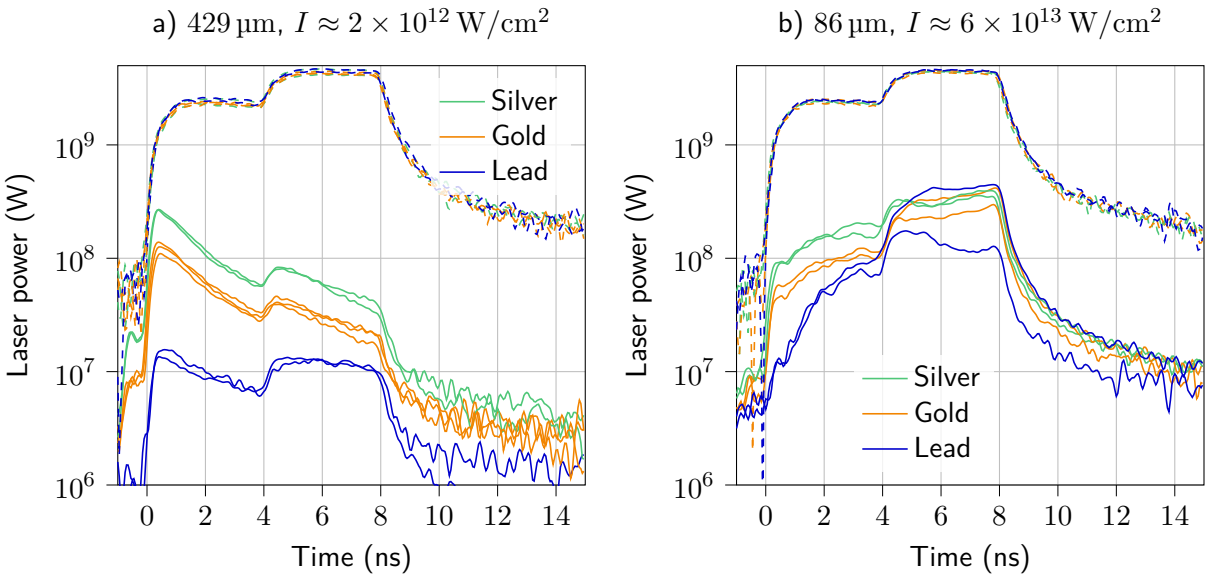

Figure 6.5: Power incident (dashed) and reflected (solid) versus time for silver, gold and lead target, for the staircase pulse shape, and a 429 µm focal spot (left) and a 86 um focal spot (right). The values on top of the graphs give the magnitude of the intensity reached during each shot. For each shot, the corresponding reflected power is the solid line of the same color. Multiple shots are shown for each material, to show repeatability. The first half of the pulse is identical to the 10 J single step pulse, so it follows that the reflected power is the same as in Fig. 6.2. In the second half of the pulse and for the 429 µm focal spot, the reflectivity does not seem to change behaviour, and still seem to decrease with the same slope. Since the incident power doubles at mid-pulse, the reflected power also doubles. For the 86 µm focal spot, the behaviour of the reflected power is reminiscent of the behaviour during the long pulse, which was shown in Fig. 6.3, where the reflected power reaches a steady value.

power was either approximately constant or slowly rising in the second half of the pulse.

6.1.5 Streak Data

The streak images can be used to obtain information on the plasma. In Fig. 6.6 are shown a selection of streak images for shots with $I = 8.6 \times 10^{13}$ W/cm^2 on different materials. Multiple features can be distinguished in the images: during the laser pulse, the plasma is at its brightest, and the bright area expands very fast. The edge of this feature is labelled "plasma-vacuum interface" in Fig. 6.6. At the end of the laser pulse, it is possible to see a very sharp front, especially for materials with high Z. This front is outlined in the streak image of the shot on gold in Fig. 6.6. This effect may be related to atomic physics, since the sharpness of the front indicates a very short characteristic time, too short to be related to any hydrodynamic phenomenon in the plasma. Another possible cause of this sharp front is second harmonic generation that could occur in the plasma. Since the laser has $\lambda = 1.053$ µm, the second harmonic has $\lambda = 526.5$ nm, and is in the bandwidth of the streak camera. The sharp extinction seen in streak images would then correspond to the extinction of the laser. This effect remains to be investigated. Finally, after the laser extinction, the hot plasma expands into the chamber. This is labelled "plasma expansion" in Fig. 6.6.

In Fig. 6.7, streak images of shot using the DSP are shown. These images show the interaction of a laser pulse with a plasma bubble, which was induced by the first pulse. The images show that

for all materials, the second pulse is much brighter than the first. If second harmonic generation does occur in the plasma, this could mean that the conditions for this are more favorable in the plasma bubble than during the first pulse. The bright spot associated to the second pulse is also further to the right of the images, which corresponds to further away from the initial target surface. This means that the laser mainly interacts with the plasma bubble, and only a fraction of the second pulse reaches the initial target surface. This seems to indicates that the second pulse is absorbed on its path traversing the subcritical plasma bubble, as opposed to the first pulse, which is mainly absorbed near the critical density of the plasma.

6.1.6 Behaviour of reflected power

Here, we use a simple theoretical model to explain the behaviour of the reflected power at low intensities. To simplify, we assume that the laser is normally incident on the target. The plasma flows is thus planar. It is known [Manheimer, 1982, Mora & Pellat, 1979] that it reaches a steady state where the electronic density decreases exponentially in the subcritical part of the plasma,

$$\frac{n_e}{n_c} = \exp\left(-x/\ell\right), \tag{6.1}$$

where x is a spatial coordinate away from the critical surface, $n_c = \varepsilon_0 m_e \omega^2/e^2$ is the critical electron density and $\ell = c_T t$ is the gradient length of n_e, in which $c_T = \sqrt{ZkT_c/m_i}$ is the isothermal sound speed at the critical surface, which scales with the square root of the temperature at the critical surface T_c.

The streak profiles presented in Fig. 6.8 show an exponential decay of the intensity at the plasma-vacuum interface (position 500 to 900 µm approximately). Though they are not shown in this graph so as not to clutter it, all other materials also exhibit an exponential profile. Assuming the degree of ionization and the electronic temperature are uniform in the underdense plasma, the streak measurement mainly depends on the density. This would indicate that experimental data is consistent with the model we propose. However, this must be taken with extreme caution, since we have no direct way of assessing whether the degree of ionization and electronic temperature are actually uniform. We make this assumption here to qualitatively explain the behaviour of the reflectivity.

The reflection coefficient of an electromagnetic wave normally incident in an exponential profile of electronic densitywith gradient length ℓ is [Eliezer, 2002]

$$R = \exp\left(-\frac{8}{3}\frac{\nu_{ei}^c\,\ell}{c}\right), \tag{6.2}$$

where ν_{ei}^c is the electron-ion momentum collision frequency at the critical surface. Ignoring the variation of the Coulomb logarithm, ν_{ei}^c scales with $Z\,n_c/T_c^{3/2}$. We also recall that in Manheimer [1982]'s model, $\ell = c_T\,t$. Finally,

$$\ln R \propto -\nu_{ei}^c\,c_T\,t \propto -Z\,n_c\,t/T_c \tag{6.3}$$

When the plasma expansion is in a steady state, T_c can be determined by writing the energy balance at the critical surface [Manheimer, 1982], which yields $k_B T_c = m_i\,(I/4\,\rho_c)^{2/3}/Z$, where I is the laser intensity and ρ_c is the density at the critical surface, which is proportional to

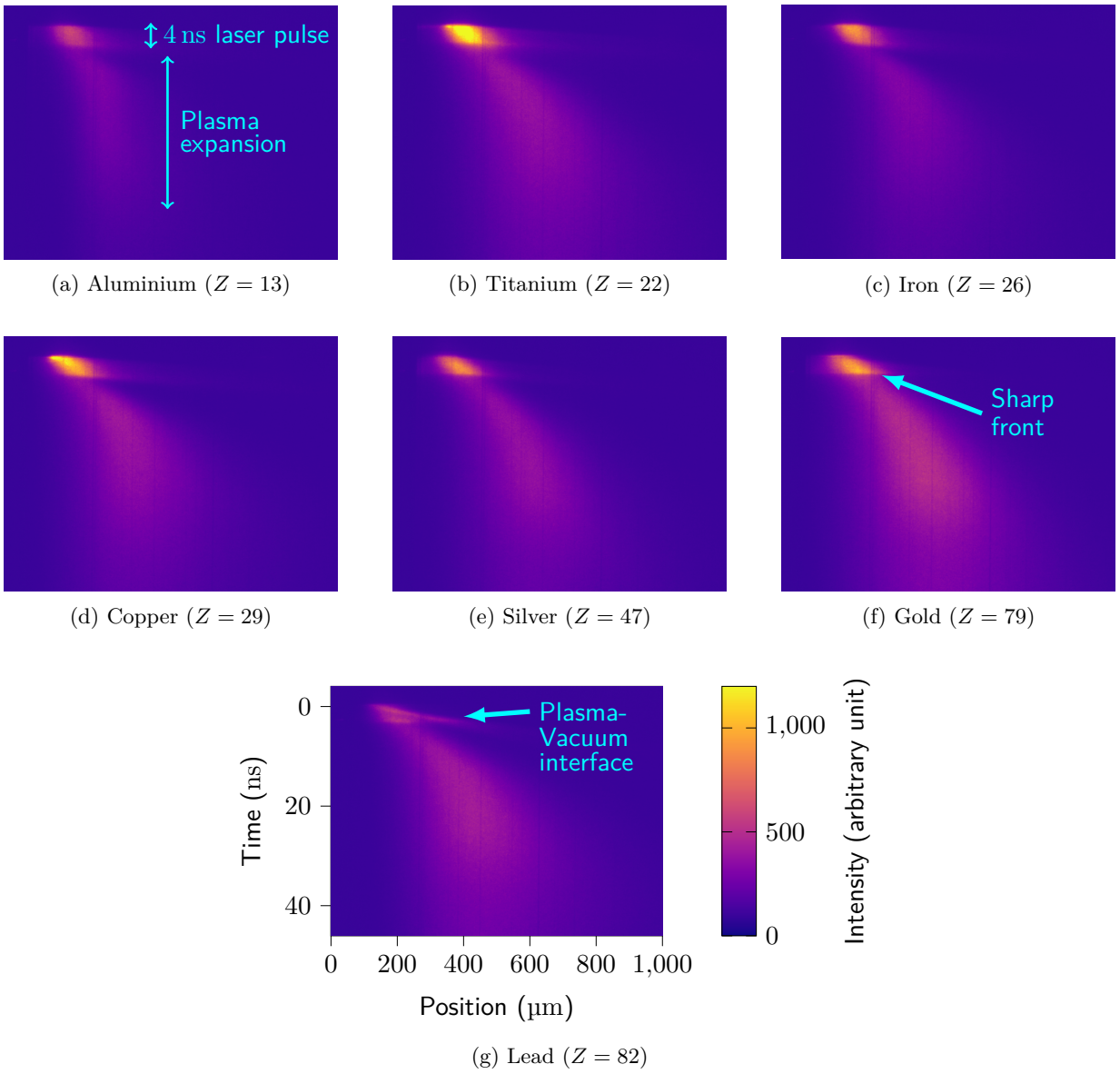

(a) Aluminium ($Z = 13$)

(b) Titanium ($Z = 22$)

(c) Iron ($Z = 26$)

(d) Copper ($Z = 29$)

(e) Silver ($Z = 47$)

(f) Gold ($Z = 79$)

(g) Lead ($Z = 82$)

Figure 6.6: Streak images of the plasma for shots on different targets. These shots all had $I = 8.6 \times 10^{13}\,\mathrm{W/cm^2}$, which corresponds to a 4 ns, 20 J pulse. The vertical axis of the images is time. The initial time is on top of the pictures, increases when going down. The streak was set to a 50 ns sweep time for these shots. The horizontal axis is the axis of the plasma. The target is on the left side of the images. The false color indicates the intensity of visible and near visible radiation from the plasma self emission. The time, space and color scales are the same for every picture. In every image, the plasma induced by the 4 ns laser pulse is the orange zone on the top left. The 50 ns sweep time makes it possible to see the expanding and cooling plasma afterwards. At high Z, a very sharp front forms right when the laser is shut down.

the critical electronic density n_c. Inserting this into eq. (6.3) yields $\ln R \propto I^{-2/3}\,\lambda^{-10/3}\,t$, since $n_c \propto \lambda^{-2}$. This explains both why the reflection coefficient decreases with time (at constant incident power), as well as why the reflected power increases with laser intensity. However, this model does not explain our observations for the reflected power at high intensity.

The fact that the reflected power is rising with time at high laser intensity may be explained by the fact that the plasma flow has not yet reached a steady state, which is a key assumption

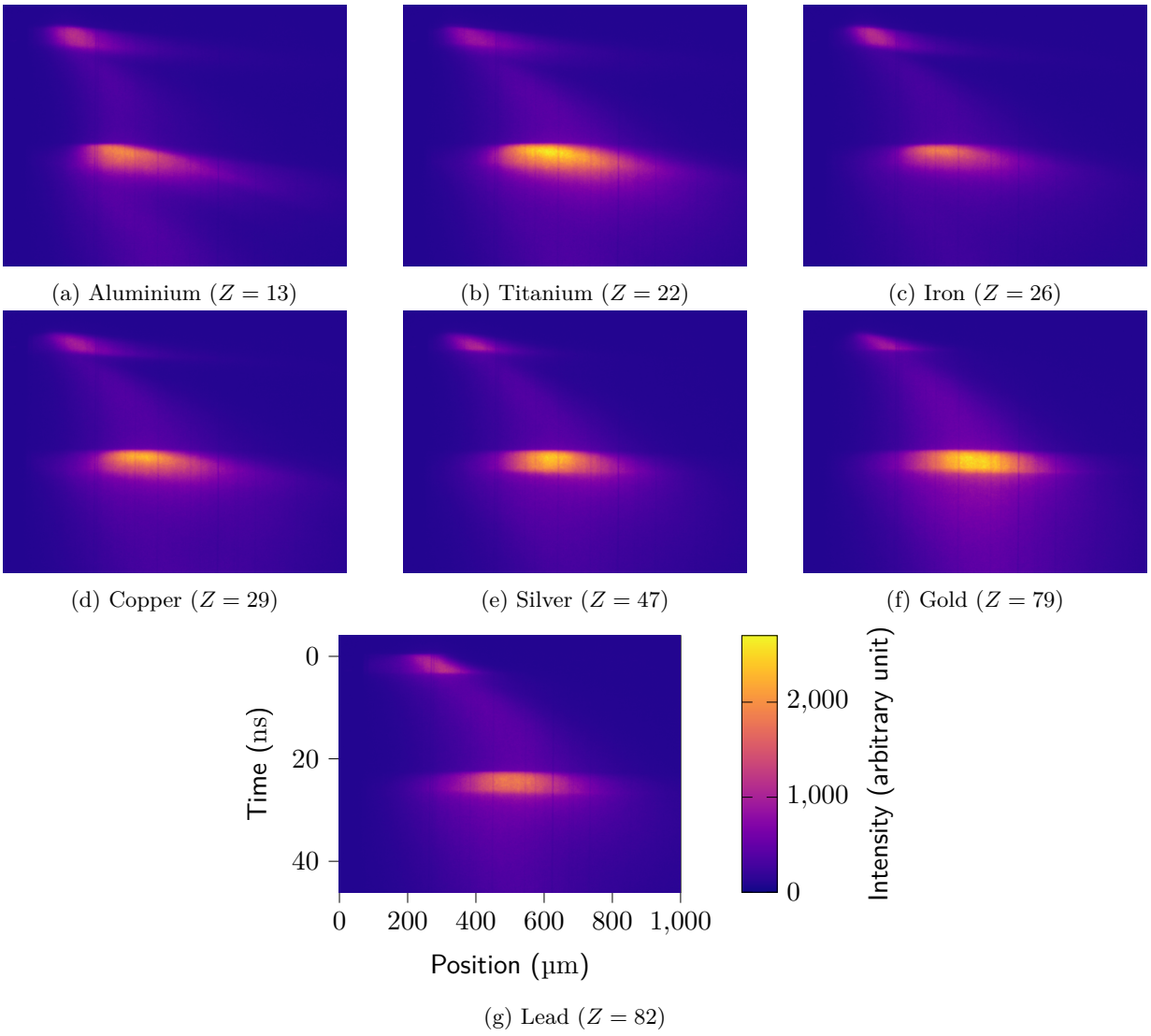

(a) Aluminium ($Z = 13$) (b) Titanium ($Z = 22$) (c) Iron ($Z = 26$)

(d) Copper ($Z = 29$) (e) Silver ($Z = 47$) (f) Gold ($Z = 79$)

(g) Lead ($Z = 82$)

Figure 6.7: Streak images of the plasma for shots on different targets. These shots all had $I = 8.6 \times 10^{13}\,\mathrm{W/cm^2}$, and correspond to a DSP with two 4 ns, 20 J pulses. The vertical axis of the images is time. The initial time is on top of the pictures, increases when going down. The streak was set to a 50 ns sweep time for these shots. The horizontal axis is the axis of the plasma. The target is on the left side of the images. The false color indicates the intensity of visible and near visible radiation from self emission. The time, space and color scales are the same for every picture. However, the color scale is not the same as in Fig. 6.6. This means that, even though the first 24 ns of the shots are the same, some features of the plasma were visible in Fig. 6.6, and are not visible here. The gain of the streak camera was unchanged between the shots shown in Fig. 6.6 and the shots presented in this figure, so the different color scale was needed because the plasma is more bright during the second pulse than during the first.

[Manheimer, 1982, Mora & Pellat, 1979] in the model presented here. Indeed, though the incident intensity is as constant as possible for the duration of the pulse, Figs. 5.7 and 6.1 show that there is still a non-negligible rise time. At least for the first part of the pulse, the incident intensity is rising, so the temperature at the critical density can also be expected to rise.

Assuming eq. (6.2) still stands, a rising reflectivity coefficient can be explained by the ratio $Z\,n_c\ell/T_c^{3/2}$ decreasing with time. Another possibility is that eq. (6.2) is not valid anymore, possibly because 3D effects become non negligible when the focal spot becomes small, while the

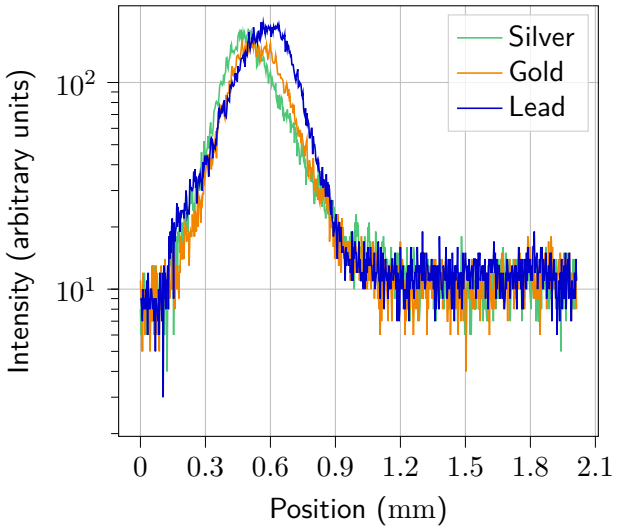

Figure 6.8: Spatial profiles of streak images for silver, gold and lead at $t = 2.9\,\text{ns}$ during a single pulse shape, with 20 J energy, and 429 µm focal spot. The integration time is 0.02 ns. However, in all materials, an exponential decay on the right side (*i.e.* where the plasma expands) can clearly be seen.

theoretical model is limited to one dimension. To further study the results in a 2D configuration, we carried out radiation hydrodynamics simulations, which are presented in the following section.

6.2 Radiation hydrodynamics simulations

6.2.1 Simulation setup

Two dimensional axisymmetric radiation hydrodynamic simulations were carried out using the code TROLL [Lefebvre *et al.*, 2018], in which was implemented the model eq. (3.2) described in chapter 3 and reproduced in eqs. (6.4) to (6.7). A brief presentation of radiation hydrodynamics codes was given in chapter 1. The simulations that are presented here constitute a preliminary work. In particular, all the simulations presented here reproduce shots that used the 20J SSP laser pulse. Furthermore, four target materials (Al, Cu, Au and Pb) out of the sixteen that were used during the experimental campaign have been the object of simulations so far.

The simulations presented here are 2D axisymmetric. Of course, 3D simulations would be more suited because one beam with 45° incidence is a purely 3D configuration. This is something to be done in the future, but because of time constraints, we restricted ourselves to 2D simulations. 2D planar simulations were unable to reproduce experimental results because the focal spot has the shape of a line, instead of the elliptic focal spot in our experiments, see Fig. 5.6 for images of the focal spot in our experiments and Fig. 6.9 for representations of the configurations. The hydrodynamics of the resulting plasma is very different from reality. We found that this significantly altered the simulations results, in particular the slope of the reflected power with respect to time during the simulation were steeper than in the experimental data. Using a 2D axisymmetric configuration, it is possible to simulate a circular focal spot, which is close enough to the elliptic experimental focal spot that we expect to be able to reproduce the level of reflection during the experiments.

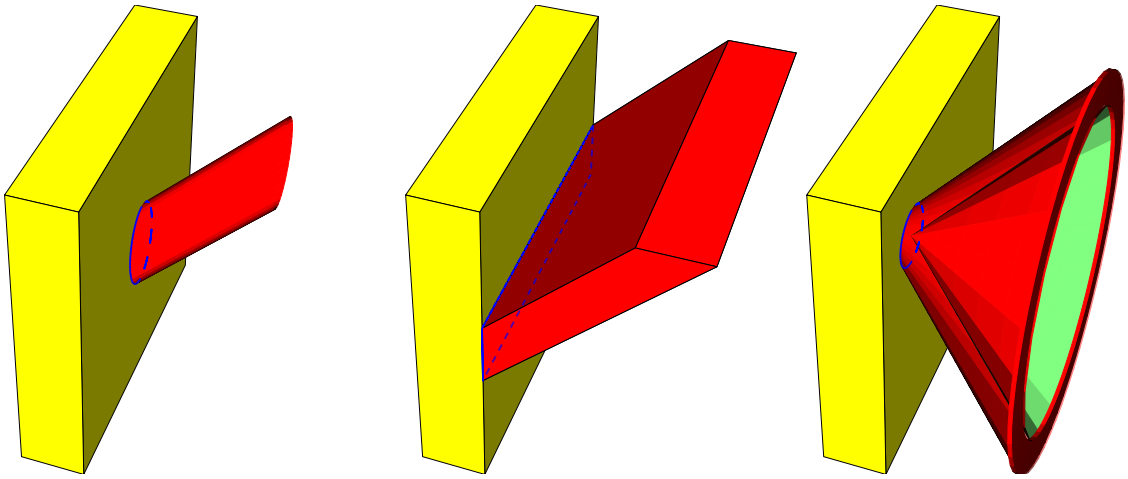

(a) Experimental (b) 2D plane (c) 2D axisymmetric

Figure 6.9: 3D representations of the experimental configuration (left), the 2D plane simulations configuration (middle) and the 2D axisymmetric simulations (right). In the 2D axisymmetric configuration, the interior of the cone is green to signify that there is no laser there. Indeed, the laser beams form a ring that gets smaller as they approach the slab, to finally converge into a circular focal spot. The shape of the focal spot is highlighted in blue in all three configurations. It is an ellipse in the experimental configuration, an infinite rectangle in the 2D plane configuration and a circle in the 2D axisymmetric configuration.

In simulations, the laser is propagated using a ray-tracing algorithm, as described in chapter 1. The angle of incidence is 45°, as in the experiments. However, the axisymmetric nature of the simulations means that the incident laser beam actually formed a ring. The laser pointing was adjusted so as to reproduce the experimental focal spot diameter on target. In the preliminary results that are presented, only a 20 J SSP is used. The ray-tracing algorithm computes the trajectory of each ray, as well as the power it carries. Every ray is either fully absorbed, or it exits the simulation domain with a power intensity. The sum of all the outgoing power exiting the simulation domain is what we will refer to as reflected power in the simulations. This means that all the energy reflected is measured, in contrast with experiments, where only the power collected by the lens could be measured (see Fig. 5.3). In the preliminary simulations presented here, the uncollected reflected power in experiments is neglected. The simulations we carried out use the inverse bremsstrahlung absorption model that was developed with Molecular Dynamic simulations in chapter 3. It is as follows (see eqs. (3.2) to (3.5))

$$\nu_{ei}^{IB} = \boldsymbol{C_{abs}}\, \nu_0[n_e,\, T_{\text{eff}}(\boldsymbol{\eta}),\, Z]\, \ln(\Lambda_{ei}^{IB}), \tag{6.4}$$

$$\nu_0[n_e,\, T_e,\, Z] = \frac{4\,\sqrt{2\pi}\,e^4}{3\,\sqrt{m_e}\,(4\pi\epsilon_0)^2}\,\frac{n_e\,Z}{(k_B T_e)^{3/2}}, \tag{6.5}$$

$$T_{\text{eff}}(x) = T_e + x\, m_e\, v_E^2/k_B, \tag{6.6}$$

$$\Lambda_{ei}^{IB} = \left[\boldsymbol{\epsilon_\ell} + \boldsymbol{C_\ell}\,\frac{4\,\pi\,\varepsilon_0^{\frac{3}{2}}\,(k_B T_{\text{eff}}(\boldsymbol{\eta_\ell}))^{3/2}}{Z\,e^3\,\sqrt{n_e}}\right]\,\left(\frac{\omega_p}{\omega}\right)^{\boldsymbol{\delta}}, \tag{6.7}$$

where the notations were introduced in section 3.2, and we recall that $C_{\text{abs}}, \eta, \epsilon_\ell, C_\ell, \eta_\ell, \delta$ are adjustable constants of the model. The coefficient C_{abs} is the one with the most effect on the

absorption which is the reason why we only varied this parameter in our simulations. The values of the other parameters of eq. (6.4) used in our simulations are those determined from Molecular Dynamics simulations in eqs. (3.49) to (3.53), which we recall here for convenience:

$$\eta = 1/6, \tag{6.8}$$
$$\epsilon_\ell = 1, \tag{6.9}$$
$$C_\ell = 0.7, \tag{6.10}$$
$$\eta_\ell = 1/6, \tag{6.11}$$
$$\delta = 0. \tag{6.12}$$

Fig. 6.10 shows a colormap of the electronic density at $t = 3.5\,\mathrm{ns}$. It also shows the basic setup of the simulations: the target is on the left side, in yellow, and the focal spot is at the bottom left of the picture.

In Fig. 6.11 are shown the simulated electronic density and temperature profiles on the expanding plasma axis at multiple times during the pulse. The electronic temperature is roughly uniform at each instant, which support the use of the theoretical models [Manheimer, 1982, Mora & Pellat, 1979] in section 6.1.6. The electronic density exhibits a decaying exponential profile, which also supports the use of these models. However, a density "bump" develops during the laser pulse at very low densities, close to $n_e/n_c = 10^{-3}$. This feature stems from the fact that our simulations use hydrodynamics equations, which are not valid in these low density areas where kinetic equations would be more appropriate. Along with the fact that the vacuum is simulated by a very low density gas-fill, this indicates the density feature is actually a shock that forms at the plasma-vacuum interface. In our simulations, this feature propagates roughly at the plasma isothermal sound speed c_T. Since $c_T = \sqrt{Z\,k_B T_c/m_i}$, it can be computed from simulations, and it takes values of few hundreds of µm/ns depending on the precise values of T_c and Z considered. Meanwhile, the velocity of this feature can be inferred from Fig. 6.11, where it is seen to cross 900 µm in 3.5 ns, meaning $c_T \approx 250\,\mu\mathrm{m/ns}$. As outlined in streak images of all materials Fig. 6.6, a plasma-vacuum interface feature seems to propagate at a speed of a few hundreds of µm/ns. Obviously, this connection must be taken with extreme caution and remains to be investigated.

6.2.2 Calibration of the absorption model by comparison between experimental results and simulations

A selection of experimental reflected powers compared to simulated reflected power (with various values of the main parameterized model coefficient C_{abs}) is shown in Figs. 6.12 to 6.14. As mentioned in the previous section, we found the slope of the reflected power with respect to time to depend on the dimensionality of the simulations, *i.e.* the slope varied between 2D plane and 2D axisymmetric simulations. We thus expect full 3D simulations to be necessary to reproduce precisely the slope of the reflected power versus time. However, we were able to roughly calibrate the value of C_{abs} from the level of reflectivity because it is very sensible to C_{abs}, as shown in Figs. 6.12 to 6.14.

The best value of C_{abs} is comprised between 0.5 and 0.75 at low intensity ($3.5\,\mathrm{TW/cm^2}$, in Fig. 6.12) for all materials but lead. The fact that it is compatible with CMDS results ($C_{\mathrm{abs}} = 0.55 \pm 0.07$ at one sigma) for most materials was expected because the inverse bremsstrahlung

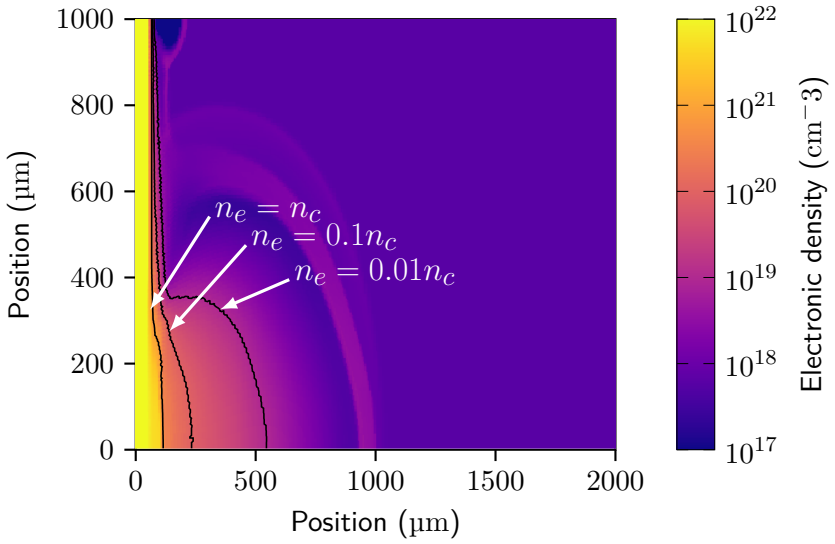

Figure 6.10: Simulated electronic density at $t = 3.5\,\text{ns}$ for a 20 J SSP shot on a gold target. The diameter of the focal spot was 250 µm, which corresponds to an intensity of $1.0 \times 10^{13}\,\text{W/cm}^2$. The rise of the density that can be seen at 500 µm on the axis is a purely numerical effect. Indeed, in this region, the density of the plasma is so low that hydrodynamic equations are not appropriate, the regime is kinetic.

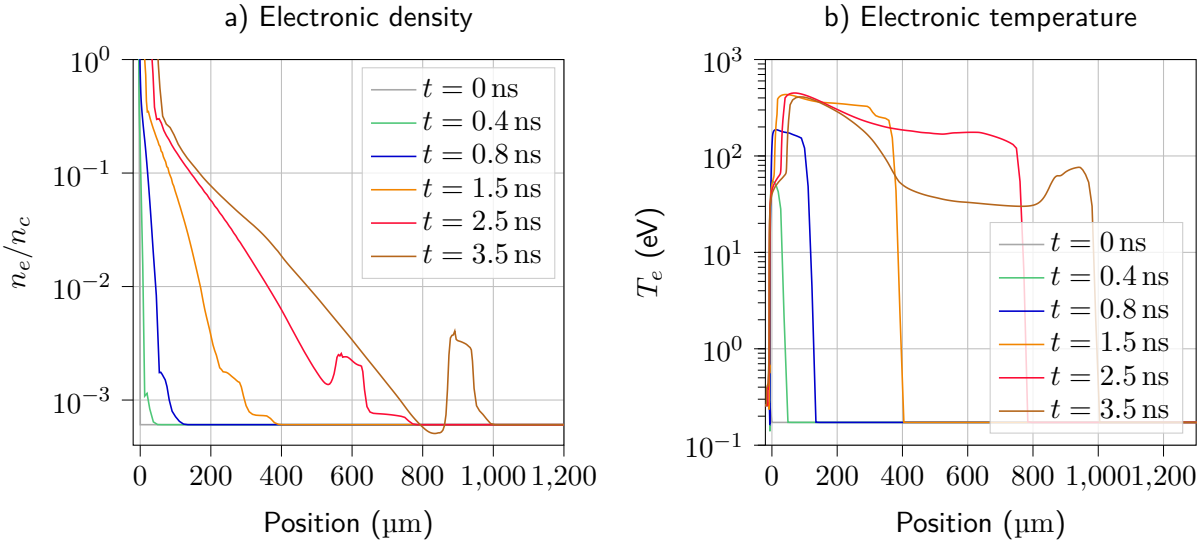

Figure 6.11: Simulated electronic density (left) and electronic temperature (right) at multiple times for the same simulation as in Fig. 6.10, so The diameter of the focal spot was 250 µm, which corresponds to an intensity of $1.0 \times 10^{13}\,\text{W/cm}^2$.

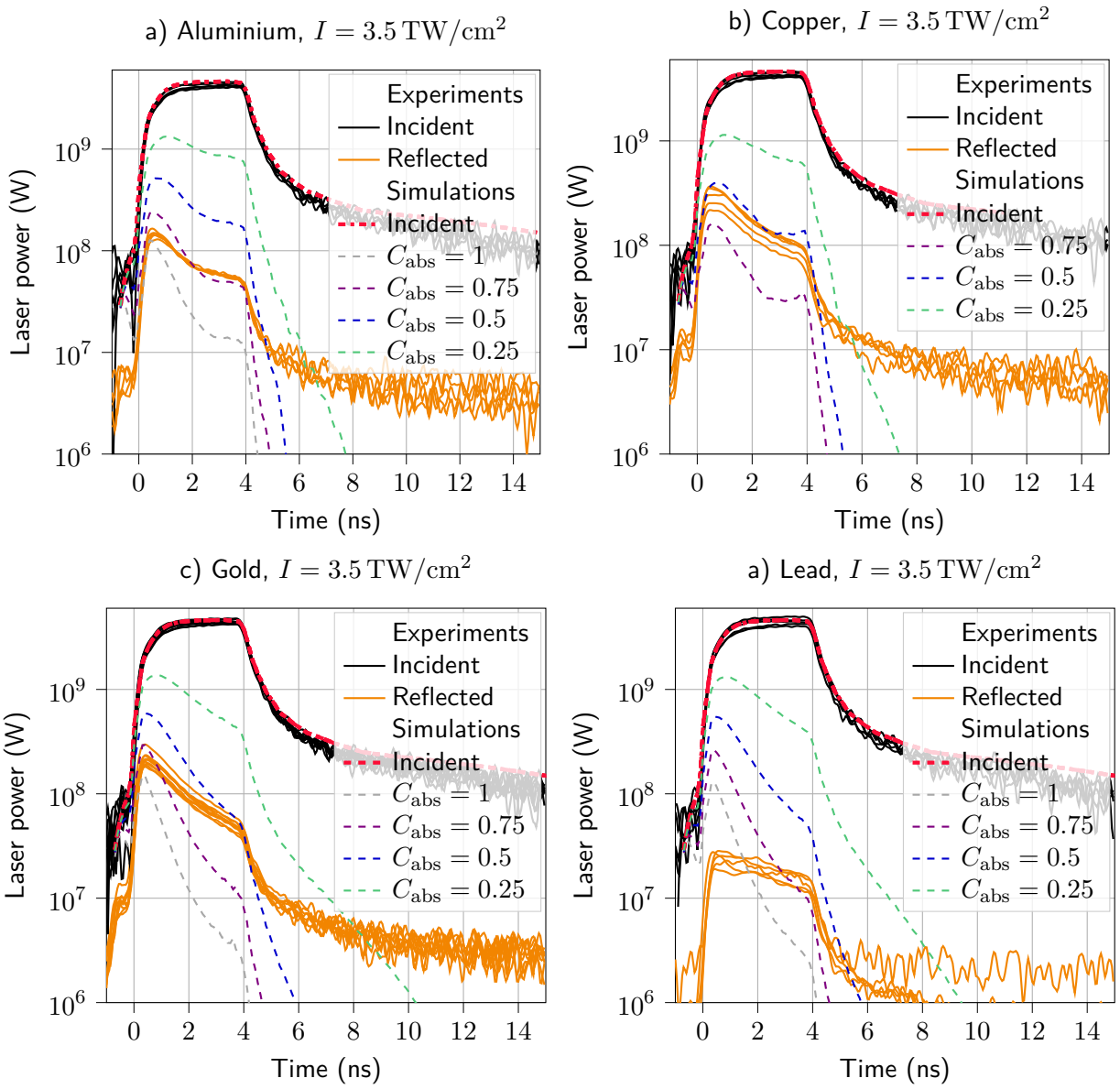

Figure 6.12: Simulated and experimental incident and reflected laser powers for a 20J SSP, for different materials and C_{abs}. Solid lines are experimental profiles and dashed or dash-dotted lines are simulated profiles. When multiple experimental shots are available, they are all plotted with the same color in order to show the reproducibility of the data.

absorption parameterized model was derived from $Z = 1$ simulations. In this situation, effects of the electron velocity distribution distortion, studied in chapter 4, are not included and should not be important at low intensities. In contrast, what was not expected is the particular behavior of lead which is an open problem. Indeed, lead ($Z = 81$) behaves very similarly to gold ($Z = 79$) in TROLL simulations, but this is not the case in experiments. Including models derived from CMDS for intermediate to high Z plasmas (such as the one described in chapter 4) will be the object of future investigations.

In table A are shown the optimal values of C_{abs} determined by comparison of the level of reflection with the experimental data.

Material	$I = 3.5\,\text{TW/cm}^2$	$I = 10\,\text{TW/cm}^2$	$I = 86\,\text{TW/cm}^2$
Gold	0.5-0.75	0.75-1	>1
Aluminium	0.75	1	1
Copper	0.5	0.75	0.75

Table A: Optimal value of the absorption coefficient C_{abs} for most shots simulated. Results for lead are not in this table since the experimental and simulated profiles of reflected power are so different from each other.

In Fig. 6.12 are shown a selection of simulated profiles of reflect power (in dashed lines) and compares them with the experimental profiles (in solid lines), for multiple materials. The behaviour of aluminium is well-reproduced by the code, and the absorption coefficient C_{abs} mostly serves to adjust the level of the profile. The graphs for $I = 10\,\text{TW/cm}^2$, in Fig. 6.13 reveal the experimental temporal profile of reflected power is almost the same as for $I = 3.5\,\text{TW/cm}^2$ for aluminium, copper and gold. However, in simulations, for a given C_{abs}, there is more reflected power for $I = 10\,\text{TW/cm}^2$ than for $I = 3.5\,\text{TW/cm}^2$. This explain why optimal C_{abs} values are higher for $I = 10\,\text{TW/cm}^2$ than for $I = 3.5\,\text{TW/cm}^2$ in table A.

The behaviour of copper, shown in the top right of Figs. 6.12 and 6.13 is more difficult to reproduce in simulations. Indeed, though the experimental shapes of reflected power are similar to those of aluminium, the same is not true for the simulated profiles. Indeed, the simulated reflected power increases at the end of the pulse. The magnitude of this increase seems to be related to both the C_{abs} and the laser intensity, though this behaviour is still the object of investigations.

In the case of gold, shown in the bottom left of Fig. 6.12, the level of reflected power at the beginning of the pulse is quite well reproduced by $C_{\text{abs}} = 0.75$ (in dashed violet), however, the slope of the profile is higher than in the experiments. Furthermore, modifying C_{abs} mostly seems to change the reflected power at the beginning of the pulse, and not the slope. This is shown by the simulation at $C_{\text{abs}} = 0.5$, in dashed blue, which reproduces the experimental reflected power at the end of the pulse, but overshoots it at the beginning of the pulse. Thus, there is a value of C_{abs} between 0.75 and 0.5 which would reproduce the integrated reflectivity observed experimentally, but not the profile of the reflected power. At $I = 10\,\text{TW/cm}^2$, in the bottom left of Fig. 6.13 this reasoning still holds, except with different values of C_{abs}: a value between 0.75 and 1 is necessary to reproduce the integrated reflected power.

Lead behaved unlike any other materials in our experiments. This is evidenced by its small integrated reflectivity coefficient (shown in Fig. 6.1), as well as by the temporal profile of reflected

power, which was already shown and discussed in Fig. 6.2. However, lead in simulations behaves similarly to gold, as shown in the bottom right of Fig. 6.12. Such a big difference in the temporal profile seems to indicate that there are some missing physics in the radiation hydrodynamic code that prevents us from predicting the right behaviour for lead. Beyond the inverse bremsstrahlung absorption model, further investigations into the equation of states and atomic physics models specific to lead would be necessary in order to understand what is observed in the experiments.

Finally, results of simulations with $I = 86\,\mathrm{TW/cm^2}$ are shown in Fig. 6.14. In the left graph, which corresponds to copper, it is shown that the temporal profile of reflected power at low C_{abs} (0.75 and less) is the same as the shape appearing for copper in the top right of Fig. 6.12. However, this does not correspond to the shape of the experimental reflected power with respect to time. Further study is required in order to better understand this behaviour.

Simulations were carried out for gold at $I = 86\,\mathrm{TW/cm^2}$. In the right graph of Fig. 6.14, the temporal profile of the reflected power seems stable in simulations, but is rising in experiments. Additionally, simulations overpredict the reflected power at all times, which would indicate that a larger C_{abs} is needed in order to reproduce experiments.

All in all, 2D axisymmetric radiation hydrodynamic simulations were able to reproduce the reflected power in experiments at low intensity ($I = 3.5\,\mathrm{TW/cm^2}$) and low Z (aluminium and copper). For higher Z (gold and lead), and higher intensities ($I = 10\,\mathrm{TW/cm^2}$ and $I = 86\,\mathrm{TW/cm^2}$), simulations struggle to reproduce experiments. There are multiple possible explanations for this. First, we expect high-intensity shots to have much more 3D effects than lower intensity, because they have a smaller and less uniform focal spot (see Fig. 5.6). In the case of high-Z materials, there are multiple effects that may affect the absorption and thus make the absorption model invalid, such as partially ionized atoms. Atomic physics effects may explain the large discrepancy in the behaviour of lead between simulations and experiments.

6.2.3 Simulation of streak data

Radiation hydrodynamics simulations directly provide data on the reflected laser intensity with respect to time, so the comparison with experimental data is straightforward. The same is not true for the comparison of experimental data of the streak and CCD cameras. Indeed, since these cameras are sensitive to visible and near-visible light, the images collected give information on the self-emission of the plasma in this particular spectral domain. However, most of the radiation has to propagate through the plasma first, before reaching the camera. During this propagation, part of the radiation may be absorbed, see Fig. 6.15, so what the camera collects is not simply the radiation emitted by the plasma, but the part of it that managed to propagate through the plasma.

This information is not directly computed during hydrodynamics simulations. However, this can be computed by using a particle transport code such as the 3D multigroup Monte Carlo code DIANE [Poujade *et al.*, 2017, Riz, 2000, Riz & Chiche, 2003]. This code solves a transport equation for the photons, including source terms and absorption in the plasma. Thus, it can simulate the radiation emitted by the plasma. We used this code to simulate the streak imaging of our experiments.

The basic equation for the propagation of radiation is of the form

$$\frac{\mathrm{d}I}{\mathrm{d}s}\left(\nu,\, s\right) = \mathcal{S}\left(\nu,\, n_e,\, T_r\right) - \sigma\left(\nu,\, n_e,\, T_r\right)\, I\left(\nu,\, s\right), \tag{6.13}$$

where I is the intensity, s the curvilinear abscissa of the propagation of the ray, $\mathcal{S}$ is the emissivity of the material and σ is the coefficient of absorption. The emissivity $\mathcal{S}$ as well as the absorption coefficient σ are tabulated values that depend on the plasma conditions as well as the frequency considered.

In Fig. 6.16 is shown a simulated streak image on the right side and the corresponding experimental streak image on the left side. The expansion speed of the most emissive part of the plasma, highlighted by the cyan lines in Fig. 6.16, seems to be well reproduced by simulations and is of the order of 20 µm/ns. However, the extension of the emissive zone of the plasma, roughly corresponding to the width of the orange spot is underestimated by simulations. As mentioned previously, the speed of the "bump" feature in Fig. 6.10 seems to correspond with the speed of the plasma-vacuum interface in the streak camera, which would that the extension of the plasma is well reproduced by simulations. This means that the discrepancy between the experimental and simulated streak images might come from uncertainties in the electronic temperature, or in the emissivity or opacity of the plasma. Indeed, there are effects, such as non-local electron transport which are not taken into account in the simulations presented here, but may impact the plasma temperature. These remain to be investigated. Concerning the plasma emissivity and opacity, the usual purpose of DIANE in the context of ICF experiments is to simulate X-ray imaging. The code therefore uses opacities and emissivities dedicated to photon energies $> 10\,\mathrm{eV}$, whereas the streak and CCD camera in our experiments collected light in the visible and near-visible domain (photon energy between 2 and 3 eV). Simulations using appropriate opacities and emissivities would be needed to complete this preliminary work.

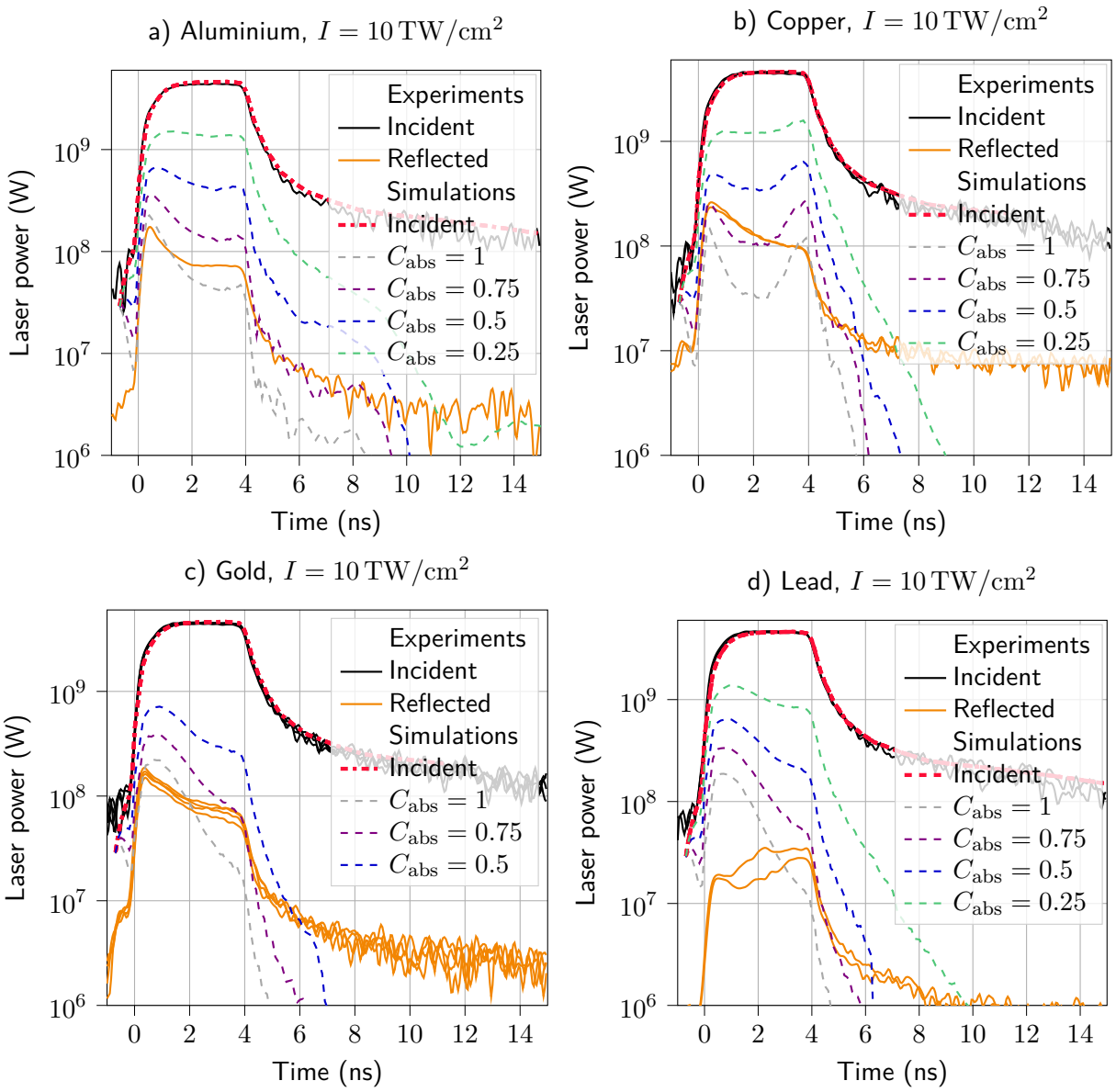

Figure 6.13: Simulated and experimental incident and reflected laser powers for a 20J SSP, for different materials and C_{abs}. Solid lines are experimental profiles and dashed or dash-dotted lines are simulated profiles. When multiple experimental shots are available, they are all plotted with the same color in order to show the reproducibility of the data.

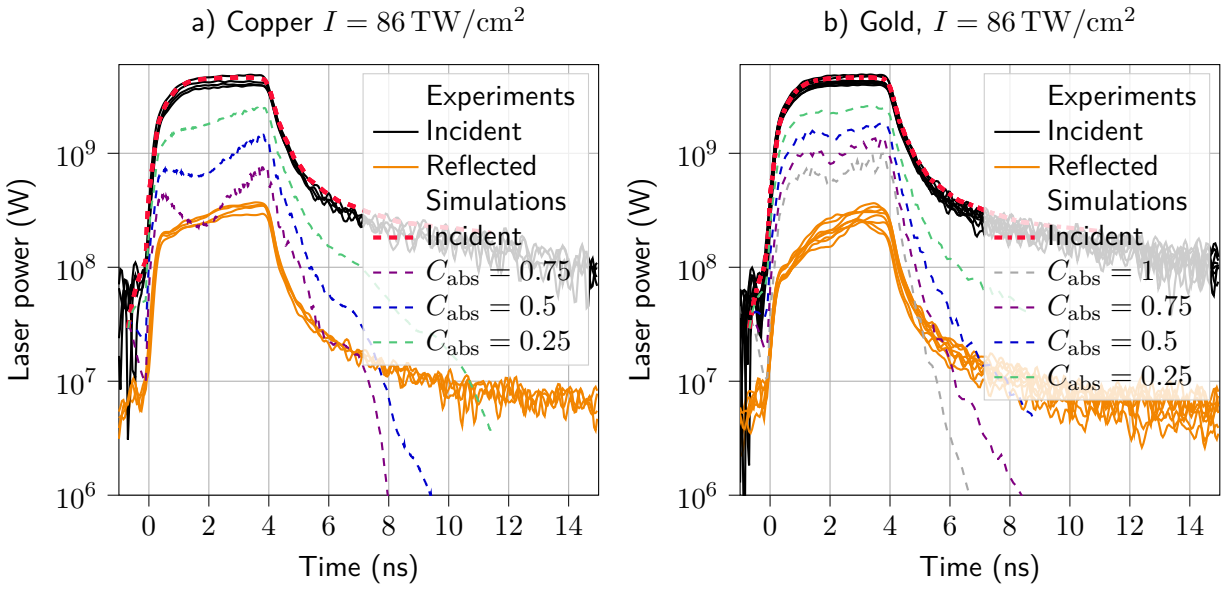

Figure 6.14: Simulated and experimental incident and reflected laser powers for a 20J SSP with a 86 µm diameter focal spot, which corresponds to $I = 86\,\mathrm{TW/cm^2}$, for multiple values of C_{abs}. Solid lines are experimental profiles and dashed or dash-dotted lines are simulated profiles. When multiple experimental shots are available, they are all plotted with the same color in order to show the reproducibility of the data. The case of copper (left graph) shows that C_{abs} can have a large influence on the shape of the temporal profile of reflected power. In the case of gold (right graph), the temporal shape is roughly similar in simulations and experiments, but the level of reflection is too high , which would indicate the necessity of a larger C_{abs}.

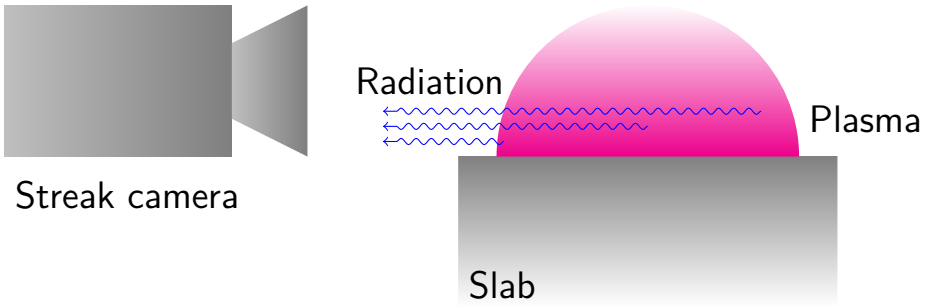

Figure 6.15: Representation of some radiation collected by the streak camera. When the radiation propagates through the plasma, part of it may be absorbed, so it is not collected by the camera.

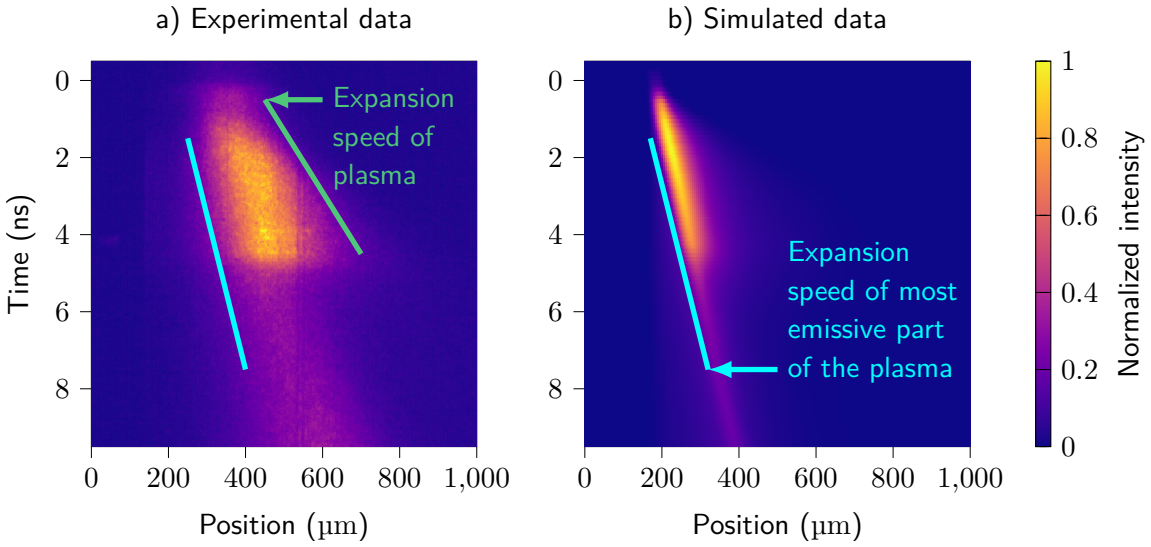

Figure 6.16: Experimental (right) and simulated (left) streak data for a 20 J SSP shot on a gold target. The diameter of the focal spot was 250 µm, which corresponds to an intensity of 1.0×10^{13} W/cm^2. The time and space scales are the same for both pictures. The acquisition duration of the experimental data was 20 ns, but it was cropped to match the simulated data. Streak images of the plasma for shots on different targets. For each picture, the intensity is normalized to the maximum of intensity of that picture. The cyan lines are aids to the eye to show the speed of the most emissive part of the plasma. In the left image, the green line shows the expansion speed of the plasma-vacuum interface.

6.3 Conclusion

In this chapter, we have presented experimental data for the reflection of a laser on a slab. The integrated specular reflectivities we observed were consistent with previous experiments. All the materials we used as targets during the campaign behaved similarly, except for lead. Indeed, the reflectivity of lead was lower than that of all other materials, especially at low laser intensity. Experiments using a longer laser pulse (10 ns compared to 4 ns previously) showed that at high laser intensity, lead seems to behave like the other materials, with a time delay. Further investigations into the reflectivity of lead would be needed to explain this behaviour.

We presented streak images of some experiments. Some features of the plasma are recognizable on the images. However, for any quantitative analysis, it has to be kept in mind that the streak camera was sensible to visible and near visible light. This means that laser-plasma interactions such as second harmonic generation may be seen on the streak images. We expect these non-linear interaction to be particularly significant in the interpretation of DSP (double single pulse) experiments images, since the second laser pulse interacts with an underdense plasma, which is a condition favourable to the development of many laser-plasma instabilities.

In the second part of this chapter, we presented preliminary 2D axisymmetric TROLL simulations that reproduce the experimental configuration of the campaign. The simulations were able to roughly reproduce the level of reflectivity of low-Z targets during low-intensity experiments, but struggled to reproduce the shape of the temporal reflectivity profile of high-Z targets at low intensity, and of all targets at high intensity. There are multiple issues to be investigated which could explain this. First, full 3D simulations might be needed in order to accurately reproduce these reflected power shapes. There are also uncertainties on the electronic temperature and degree of ionization in simulations, which both affect inverse bremsstrahlung absorption, per eq. (1.55). Indeed, the spatial profile of T_e inside the plasma during the experiments is affected by thermal conduction, and the simulations presented here all used a flux-limited Spitzer-Harm model. Using a model that includes non-local effects might be needed in order to accurately reproduce the shape of the reflected power with respect to time. Atomic physics effects not described in simulations may also be at play, especially in the case of lead ($Z = 81$), whose behaviour is similar to that of gold ($Z = 79$) in the simulations but not in the experiments. Even concerning other materials, atomic physics effects might impact the profile of Z inside the plasma, so more accurate models might be needed in order to reproduce the experimental shape of the reflected power in simulations. Still, we were able to roughly calibrate the absorption model developed in chapter 3 from the comparison of experimental levels of reflectivity (irrespective of the shape) with TROLL simulations that used this model. The value we obtained is in agreement with that obtained from CMDS.

However, many more issues remains to be investigated. In particular, the simulation of streak images was not able to reproduce the extension of the plasma, which may be explained by the fact that the opacities and emissivities used in DIANE simulations are most accurate in the X-ray range of frequency, whereas the streak camera collected visible and near-visible light. Undescribed atomic physics effects, in addition to laser-plasma instabilities (such as second harmonic generation) might also be at play here. Both of these may need to be investigated in order to be able to accurately reproduce streak images from the simulations.

Finally, the inverse bremsstrahlung absorption model used in these preliminary simulations

was developed at $Z = 1$, therefore including high-Z effects such as the distortion of the distribution shown in chapter 4 and multiple ion species might be necessary in order to accurately reproduce experimental data. The results of radiation hydrodynamics codes with the hybrid inverse bremsstrahlung absorption model (described in this chapter) would need to be compared with results using other absorption models.

Conclusion

This work contributes to improving the modelling of laser absorption by inverse bremsstrahlung (IB) in weakly coupled plasmas. This was achieved by a twofold approach. The first step consisted in Classical Molecular Dynamics Simulations (CMDS) to discriminate past models from the literature and to calibrate a hybrid model devised during the course of this work. Then, results of radiation hydrodynamics simulations, implementing the aforementioned hybrid model, were compared to actual experimental data gathered during an experimental campaign carried out as part of this thesis.

The broad context of this work, indirect-drive Inertial Confinement Fusion (ICF) was first introduced. A state of the art on current ICF experiments showed that laser absorption may not be faithfully described by radiation hydrodynamics simulations used for the design process and as a tool for post-shot modelling. In this work, we focused on the most important absorption mechanism, Inverse Bremsstrahlung (IB) absorption. The modelling of laser propagation and IB absorption in codes was then expanded upon, in order to show what approximations are made in the physical models implemented in radiation hydrodynamics codes. A theoretical derivation of the Coulomb logarithm was developed. It highlighted the fact that collective effects are not treated self-consistently from a theoretical point of view. They are notoriously difficult to take into account, which explains the coexistence of so many different Coulomb logarithm models in the literature. To discriminate theoretical models of IB absorption and Coulomb logarithm, we resorted to microscopic numerical simulations.

We showed that Fokker-Planck (FP) simulations, which have extensively been used in the past to describe IB heating cannot be carried out to capture any quantitative information about the Coulomb logarithm. In the FP simulation framework, an expression of the Coulomb logarithm must precisely be supplied as an input data. Particle-in-Cell (PIC) simulations suffer from the same drawback. This is the reason why we resorted to classical molecular dynamics simulations, where trajectories of individual particles of the plasma (electrons and ions) in the field of all others are calculated using classical Newton's laws. Collective effects are therefore inherently included. We used the classical molecular dynamics code LAMMPS to measure the heating rate and Coulomb logarithm for the process of IB, first for low-Z weakly coupled plasmas. A hybrid model with six adjustable parameters was proposed. It encompasses multiple models from the literature. This model was tested out against data obtained from CMDS and most of its adjustable parameters have been calibrated precisely enough to rule out certain categories of IB heating models from the literature along with their associated Coulomb logarithm.

We then carried out CMDS of IB heating in moderate-Z plasmas where electron velocity distributions (EVDs) could be distorted from their equilibrium Maxwellian shapes, as predicted by Langdon. We were able to make the first observation, in CMDS, of non-Maxwellian effects on instantaneous EVDs in Langdon's conditions. Moreover, anisotropy of EVDs were measured at high intensity as predicted theoretically. We observed that the Super Gaussian order of the EVDs parallel to the polarization of the laser E-field could exceed 5 (which is the limit inferred by Langdon) whereas the perpendicular order seems to remain below that limit. Depending on the plasma state and the laser intensity, isotropic or anisotropic Super-Gaussian EVDs or Super-Gaussian + Maxwellian EVDs were observed. The isotropic part of EVDs varies qualitatively as Matte *et al.* predicted, but slightly differently from a quantitative point of view with respect to intensity as measured by our CMDS. A fit of parallel and perpendicular orders with respect to the laser intensity has been proposed.

In order to get experimental values of some of the parameters of the hybrid model devised in this work, an experimental campaign was conducted at the GCLT facility at CEA/DAM. Each experiment used a laser with $\lambda = 1.053\,\mu\text{m}$ to deliver 10 to 40 J of energy on a slab. Sixteen elements of the periodic table were used during the campaign, including materials of interest to ICF such as gold. A review of similar slab experiments carried out in the past outlined the importance of measuring the instantaneous, as opposed to the integrated, reflection coefficient. The relative simplicity of these dedicated experiments allowed to shoot with different laser pulses and intensities, sometimes several times with the same configuration for repeatability purposes.

A selection of experimental results on the reflectivity of the laser induced plasma were presented. A physical model was proposed to try and qualitatively explain these results. Then, preliminary results of 2D axisymmetric radiation hydrodynamics simulations using TROLL were carried out in order to reproduce the experimental configuration. The hybrid model devised from CMDS was implemented in TROLL, and the comparison of simulation results with experimental data was used to calibrate, experimentally this time, the hybrid model. It was shown that, in preliminary simulations, the hybrid model with CMDS adjusted constants seemed to reproduce experimental data for low-Z materials and moderate laser intensity ($I = 3.5\,\text{TW/cm}^2$), but it struggled with high-Z materials and higher laser intensities ($I \geq 10\,\text{TW/cm}^2$). Uncertainties that could affect laser absorption remain on the reproduction of experimental plasma parameters (n_e, T_e, Z) by simulations. These uncertainties could be reduced by the use of full 3D simulations and of other physical models (non-local thermal conduction, atomic physics models, etc.) than those used in the preliminary simulations presented here. Finally, the hybrid model was developed with $Z = 1$, so high-Z effects such as multi-ion species and the structure of bound electrons around ions were not taken into account. Further CMDS in these situations may be required in order to develop a model that is able to reproduce high-Z experimental data.

Perspectives

Though the distortion of the electron velocity distribution that occurs at high-Z in a laser-irradiated plasma has been discussed, a predictive model for the shape of the distribution has not yet been proposed. Moreover, only two components with structureless ions plasmas were considered in this work, whereas in ICF experiments, hohlraum plasmas have multiple species of ions with extended bound electron structure. Additional CMDS would be required to assess

their effects on the heating rate.

The post-processing of the experimental data gathered during the campaign at the GCLT facility is still in progress. Notably, full 3D hydrodynamics simulations of all experimental configurations tested with all sixteen target materials would help to better calibrate the hybrid model. Discrepancies in the spatial extension of a bright area in simulated and experimental streak images is still an open question, though the dimensionality of the simulations may account for some of the difference. Simulating the CCD images, to see whether they coincide with the experimental images is also something that remains to be done.

List of scientific communications

Publications

- O. Poujade, M.A. Barrios, S. Baton, C. Blancard, R. Devriendt and M. Primout, *Rayleigh-Taylor mixing may account for the poisition anomaly in NIF microdot spectroscopy experiments*, Physics of plasmas **28**, 042704 (2021)
- R. Devriendt and O. Poujade, *Classical molecular dynamic simulations and modelling of inverse-bremsstrahlung heating in low Z weakly-coupled plasmas*, Physics of plasmas **29**, 073301 (2022) and editor's pick
- R. Devriendt and O. Poujade, *Non-Maxwellian electron velocity distribution in molecular dynamic simulations of weakly-coupled plasmas*, *in preparation*

Conferences

- Poster, High Energy Density Science Summer School 2019, San Diego, CA, USA: from July 29^{th} to August 8^{th}.
- Poster, Forum Interactions Laser Plasma, 2019, Fréjus, France
- Oral presentation, Forum Interactions Laser Plasma 2021, Belgodère, France
- Oral presentation, Direct Drive and Fast Ignition Workshop 2022, Madrid, Spain

Summary in French

Cette thèse s'inscrit dans le contexte de la Fusion par Confinement Inertiel (FCI). Le principe de la FCI est de compresser rapidement une petite capsule remplie de combustible fusible afin d'atteindre des conditions propices à la fusion thermonucléaire. Cette compression est réalisée à l'aide de faisceaux lasers intenses, qui peuvent directement irradier la capsule ou bien être utilisés indirectement pour produire des rayons X dans une cavité, lesquels irradient et compressent la capsule. Dans les deux cas, l'absorption de faisceaux laser est critique à la FCI. Une bonne compréhension des mécanismes d'absorption est donc indispensable à la FCI.

Des expériences de FCI sont réalisées sur l'installation NIF (*National Ignition Facility*) aux USA depuis plus de 10 ans, et pourtant, de nombreux problèmes liés à l'absorption échappent à notre compréhension. Des simulations numériques utilisant des codes d'hydrodynamique radiative comme TROLL au CEA ou HYDRA au LLNL (*Lawrence Livermore National Laboratory*) aux USA ont été menées pour préparer et reproduire ces expériences. Le début de cette thèse, consacré à l'introduction de la FCI ainsi qu'à l'état de l'art des expériences récentes de FCI, a montré que, dans la littérature, la description de l'absorption laser dans les codes n'est pas complètement fidèle aux expériences.

C'est pourquoi, dans cette thèse, nous nous intéressons à un des mécanismes principaux d'absorption d'un laser par un plasma : l'absorption par Bremsstrahlung Inverse (BI). Lorsqu'une onde électromagnétique traverse un plasma, son champ électrique est la cause d'un mouvement cohérent d'oscillation des électrons libres du plasma. Les ions du plasma ne sont que peu affectés par le champ électrique, en raison du rapport de masse entre électrons et ions. Les collisions entre les électrons oscillants et les ions peuvent transférer une partie de l'énergie de l'onde électromagnétique au plasma. La description de la modélisation de la propagation d'un laser et de son absorption par BI dans les codes d'hydrodynamique radiative a permis de mettre en évidence les approximations présentes dans les modèles physiques implémentés dans ces codes. Cette description a également montré l'émergence de la fréquence d'interaction entre les électrons et les ions, appelée fréquence de collision électron-ion. Cette fréquence est un paramètre de première importance dans la description du chauffage par BI, et a été largement étudiée dans la littérature depuis les années 1950. Pourtant, un consensus sur sa modélisation n'a pas encore émergé. Une dérivation théorique du taux de chauffage par BI présentée dans cette thèse a permis de montrer la difficulté de la prise en compte des effets collectifs, qui apparaissent par le biais du logarithme Coulombien. Cette complexité explique la coexistence de multiples modèles de logarithme Coulombien, et donc de chauffage par BI dans la littérature. Afin de discriminer ces

modèles, nous avons utilisé des simulations numériques microscopiques.

Nous avons montré que les simulations Fokker-Planck (FP), largement utilisées dans la littérature pour mesurer le chauffage par BI, ne peuvent pas capturer d'information quantitative sur le logarithme Coulombien. En effet, une expression du logarithme Coulombien doit être donnée en entrée de ces simulations. Les codes PIC (*Particle-in-Cell*) ont la même limitation. C'est pourquoi nous avons utilisé des Simulations de Dynamique Moléculaire Classique (SDMC). En effet, dans ces simulations, les trajectoires de toutes les particules du plasma sont calculées avec les lois de Newton, en prenant en compte l'interaction de chaque particule avec toutes les autres ainsi que le champ électrique du laser. La prise en compte de toutes les interactions (et les capacités finies de calcul) ont pour inconvénient de limiter ces simulations à de très petits volumes. En revanche, pour la même raison, les SDMC prennent en compte les effets collectifs et sont parfaitement adaptées à la mesure de quantités locales, comme le taux de chauffage par BI.

Dans cette thèse, plusieurs séries de SDMC ont été menées afin de mesurer le taux de chauffage par BI pour une vaste gamme d'états plasma et de paramètres laser. Dans un premier temps, nous avons simulé des plasmas faiblement couplés avec degré d'ionisation $Z = 1$ dans des situations où la distribution de vitesse des électrons est Maxwellienne. C'est une hypothèse des modèles théoriques de chauffage par BI de la littérature auxquels nous avons confronté nos SDMC. Pour ce faire, nous avons proposé un modèle hybride à six paramètres ajustables qui englobe la plupart des modèles de la littérature. Les paramètres de ce modèle ont été calibrés à l'aide de nos SDMC, de manière suffisamment précise pour rejeter certains modèles de logarithme Coulombien de la littérature.

Dans un deuxième temps, nous avons simulé le chauffage par BI dans des plasmas modérement ionisés ($Z = 10$), dans lesquels la distribution de vitesse des électrons (DVE) peut s'écarter de sa forme Maxwellienne d'équilibre. En effet, Langdon a prédit que la DVE moyennée sur une période laser peut devenir Super-Gaussienne ($f_e(v) \propto \exp(-v^k)$ où $k \geq 2$ est l'ordre de la distribution), ce que nous avons observé pour la première fois dans des SDMC dans les conditions de Langdon sur la DVE instantanée. De plus, nous avons pu voir l'anisotropie de la distribution à forte intensité laser, ce qui avait été prédit théoriquement. L'ordre Super-Gaussien de la DVE projetée sur la direction parallèle au champ électrique dépasse 5 (qui était la valeur maximale prédite par Langdon), tandis que l'ordre de la DVE projetée sur une direction perpendiculaire au champ électrique reste en dessous de cette limite. Sous certaines conditions, nous avons observé des distributions correspondant à la somme d'une Maxwellienne et d'une Super-Gaussienne, ce qui est en accord avec des mesures expérimentales de la forme de la DVE. L'ordre de la partie isotrope de la DVE correspond qualitativement aux prédictions de Matte *et al.* mais est légèrement inférieur d'un point de vue quantitatif.

Afin d'obtenir des valeurs expérimentales des paramètres du modèle hybride pour le chauffage par BI, une campagne expérimentale a été menée sur l'installation GCLT au CEA/DAM dans le cadre de cette thèse. Un laser de longueur d'onde 1.053 µm délivrant entre 10 et 40J d'énergie dans un faisceau, avec une durée d'impulsion comprise entre 4 et 30ns a été tiré sur des plaques planes à 45°. Seize éléments purs du tableau périodique ont été utilisés comme cibles durant la campagne, dont certains d'intérêt direct pour la FCI, comme l'or. Un état de l'art d'expériences similaires dans la littérature a mis en avant l'importance de mesurer la réflexion instantanée, et non intégrée sur l'impulsion laser. La relative simplicité de la configuration expérimentale a permis d'utiliser plusieurs formes d'impulsion laser, et plusieurs niveaux d'intensité, ainsi que de

réaliser plusieurs tirs identiques pour évaluer la répétabilité des expériences.

Une sélection de résultats expérimentaux ont été présentés dans cette thèse. Nous avons présenté des simulations 2D axisymétriques d'hydrodynamique radiative réalisées avec le code TROLL dans lequel le modèle hybride d'absorption par BI développé au cours de cette thèse a été implémenté. La comparaison de ces simulations avec les résultats expérimentaux a permis de calibrer, expérimentalement cette fois, le modèle hybride. Nous avons montré que la calibration expérimentale donne des résultats semblables à la calibration à partir des SDMC pour les matériaux à faible Z et à intensité laser modérée ($I = 3.5\,\mathrm{TW/cm^2}$). Le modèle hybride semble cependant avoir des difficultés à reproduire les résultats expérimentaux à Z élevé et intensité laser plus importante ($I > 10\,\mathrm{TW/cm^2}$). Des incertitudes qui pourraient affecter l'absorption laser persistent sur la bonne reproduction des paramètres plasma (n_e, T_e, Z) expérimentaux par les simulations. Ces incertitudes pourraient être réduites par des simulations 3D, ainsi que par l'utilisation d'autres modèles physiques (conduction thermique non locale, modèle de physique atomique, etc.) que ceux utilisés dans les simulations préliminaires présentées ici. Nous rappelons enfin que le modèle hybride, développé à partir de SDMC réalisées à $Z = 1$, n'inclut pas les effets spécifiques liés à un Z élevé, tel que la présence de plusieurs espèces d'ions et la structure du cortège des électrons liés. D'autres SDMC prenant en compte ces effets pourraient être nécessaires pour développer un modèle d'absorption par BI qui peut reproduire les données expérimentales à Z élevé.

Bibliography

Angulo, C., Arnould, M., Rayet, M., Descouvemont, P., Baye, D., Leclercq-Willain, C., Coc, A., Barhoumi, S., Aguer, P., Rolfs, C., Kunz, R., Hammer, J., Mayer, A., Paradellis, T., Kossionides, S., Chronidou, C., Spyrou, K., Degl'Innocenti, S., Fiorentini, G., Ricci, B., Zavatarelli, S., Providencia, C., Wolters, H., Soares, J., Grama, C., Rahighi, J., Shotter, A. & Lamehi Rachti, M., *A compilation of charged-particle induced thermonuclear reaction rates*, Nuclear Physics A, vol. 656, 1: 3 (1999) 10

Anthes, J. P., Palmer, M. A., Gusinow, M. A. & Matzen, M. K., *Absorption of laser radiation by Al, Fe, and Au planar metallic targets*, Applied Physics Letters, vol. 34, 12: 841 (1979) 115, 117

Arad, B., Eliezer, S., Gazit, Y., Jackel, S., Karmi, Y., Loebenstein, H. M. & Zigler, A., *Laser light absorption in long-pulse high-irradiance experiments*, Applied Physics Letters, vol. 37, 9: 774 (1980) 114, 115, 117, 128

Atzeni, S. & Meyer-ter Vehn, J., *The physics of inertial fusion: beam plasma interaction, hydrodynamics, hot dense matter*, OUP Oxford (2004) 7, 8, 9, 10, 11, 32

Baalrud, S. D., *Transport coefficients in strongly coupled plasmas*, Physics of Plasmas, vol. 19, 3: 030701 (2012) 44

Bach, D. R., Casperson, D. E., Forslund, D. W., Gitomer, S. J., Goldstone, P. D., Hauer, A., Kephart, J. F., Kindel, J. M., Kristal, R., Kyrala, G. A., Mitchell, K. B., van Hulsteyn, D. B. & Williams, A. H., *Intensity-Dependent Absorption in 10.6-Mm Laser-Illuminated Spheres*, Physical Review Letters, vol. 50, 26: 2082 (1983) 113

Balescu, R., *Irreversible processes in ionized gases*, The Physics of Fluids, vol. 3, 1: 52 (1960) 44

Balescu, R., *Heating of electrons and ions by inverse bremsstrahlung absorption: A self-similar tate of the plasma*, Journal of Plasma Physics, vol. 27, 3: 553 (1982) 53, 100

Berzak Hopkins, L. F., Meezan, N. B., Le Pape, S., Divol, L., Mackinnon, A. J., Ho, D. D., Hohenberger, M., Jones, O. S., Kyrala, G., Milovich, J. L., Pak, A., Ralph, J. E., Ross, J. S., Benedetti, L. R., Biener, J., Bionta, R., Bond, E., Bradley, D., Caggiano, J., Callahan, D., Cerjan, C., Church, J., Clark, D., Döppner, T., Dylla-Spears, R., Eckart, M., Edgell, D., Field, J., Fittinghoff, D. N., Gatu Johnson, M., Grim, G., Guler, N., Haan, S., Hamza, A., Hartouni,

E. P., Hatarik, R., Herrmann, H. W., Hinkel, D., Hoover, D., Huang, H., Izumi, N., Khan, S., Kozioziemski, B., Kroll, J., Ma, T., MacPhee, A., McNaney, J., Merrill, F., Moody, J., Nikroo, A., Patel, P., Robey, H. F., Rygg, J. R., Sater, J., Sayre, D., Schneider, M., Sepke, S., Stadermann, M., Stoeffl, W., Thomas, C., Town, R. P. J., Volegov, P. L., Wild, C., Wilde, C., Woerner, E., Yeamans, C., Yoxall, B., Kilkenny, J., Landen, O. L., Hsing, W. & Edwards, M. J., *First High-Convergence Cryogenic Implosion in a Near-Vacuum Hohlraum*, Physical Review Letters, vol. 114, 17: 175001 (2015) 16, 35, 36

Betti, R. & Hurricane, O. A., *Inertial-confinement fusion with lasers*, Nature Physics, vol. 12, 5: 435 (2016) 11, 12, 88

Beutler, T. C., Mark, A. E., van Schaik, R. C., Gerber, P. R. & van Gunsteren, W. F., *Avoiding singularities and numerical instabilities in free energy calculations based on molecular simulations*, Chemical Physics Letters, vol. 222, 6: 529 (1994) 90

Bhandarkar, S., Baumann, T., Alfonso, N., Thomas, C., Baker, K., Moore, A., Larson, C., Bennett, D., Sain, J. & Nikroo, A., *Fabrication of low-density foam liners in hohlraums for nif targets*, Fusion Science and Technology, vol. 73, 2: 194 (2018) 16

Blatt, J. M. & Weisskopf, V. F., *Theoretical nuclear physics*, Courier Corporation (1991) 8

Born, M. & Wolf, E., *Principles of Optics: Electromagnetic Theory of Propagation, Interference and Diffraction of Light*, Pergamon Press (1959) 23

Bosch, H.-S. & Hale, G., *Improved formulas for fusion cross-sections and thermal reactivities*, Nuclear Fusion, vol. 32, 4: 611 (1992) 10

Braginskii, S., *Transport properties in a plasma*, Review of plasma physics, vol. 1: 216 (1965) 21

Brantov, A., Rozmus, W., Sydora, R., Capjack, C. E., Bychenkov, V. Y. & Tikhonchuk, V. T., *Enhanced inverse bremsstrahlung heating rates in a strong laser field*, Physics of Plasmas, vol. 10, 8: 3385 (2003) 60, 62, 63, 66, 78, 79, 86

Brown, L., Preston, D. & Singletonjr, R., *Charged particle motion in a highly ionized plasma*, Physics Reports, vol. 410, 4: 237 (2005) 44, 49, 62, 64, 67, 75, 79, 83

Bunkin, F. B., Kazakov, A. E. & Fedorov, M. V., *Interaction of intense optical radiation with free electrons (non relativistic case)*, Sovi. Phys. Usp., vol. 15: 416 (1973) 60

Burckhardt, C. B., *Use of a random phase mask for the recording of fourier transform holograms of data masks*, Appl. Opt., vol. 9, 3: 695 (1970) 119

Callahan, D. A., Hurricane, O. A., Hinkel, D. E., Döppner, T., Ma, T., Park, H.-S., Barrios Garcia, M. A., Berzak Hopkins, L. F., Casey, D. T., Cerjan, C. J., Dewald, E. L., Dittrich, T. R., Edwards, M. J., Haan, S. W., Hamza, A. V., Kline, J. L., Knauer, J. P., Kritcher, A. L., Landen, O. L., LePape, S., MacPhee, A. G., Milovich, J. L., Nikroo, A., Pak, A. E., Patel, P. K., Rygg, J. R., Ralph, J. E., Salmonson, J. D., Spears, B. K., Springer, P. T., Tommasini, R., Benedetti, L. R., Bionta, R. M., Bond, E. J., Bradley, D. K., Caggiano, J. A., Field, J. E., Fittinghoff, D. N., Frenje, J., Gatu Johnson, M., Grim, G. P., Hatarik, R., Merrill, F. E.,

Nagel, S. R., Izumi, N., Khan, S. F., Town, R. P. J., Sayre, D. B., Volegov, P. & Wilde, C. H., *Higher velocity, high-foot implosions on the National Ignition Facility lasera)*, Physics of Plasmas, vol. 22, 5: 056314 (2015) 13

Casey, D. T., MacGowan, B. J., Sater, J. D., Zylstra, A. B., Landen, O. L., Milovich, J., Hurricane, O. A., Kritcher, A. L., Hohenberger, M., Baker, K., Le Pape, S., Döppner, T., Weber, C., Huang, H., Kong, C., Biener, J., Young, C. V., Haan, S., Nora, R. C., Ross, S., Robey, H., Stadermann, M., Nikroo, A., Callahan, D. A., Bionta, R. M., Hahn, K. D., Moore, A. S., Schlossberg, D., Bruhn, M., Sequoia, K., Rice, N., Farrell, M. & Wild, C., *Evidence of three-dimensional asymmetries seeded by high-density carbon-ablator nonuniformity in experiments at the national ignition facility*, Phys. Rev. Lett., vol. 126: 025002 (2021) 16

Chichkov, B. N., Shumsky, S. A. & Uryupin, S. A., *Nonstationary electron distribution functions in a laser field*, Physical Review A, vol. 45, 10: 7475 (1992) 53, 88, 94

Clark, D. S., Weber, C. R., Milovich, J. L., Salmonson, J. D., Kritcher, A. L., Haan, S. W., Hammel, B. A., Hinkel, D. E., Hurricane, O. A., Jones, O. S., Marinak, M. M., Patel, P. K., Robey, H. F., Sepke, S. M. & Edwards, M. J., *Three-dimensional simulations of low foot and high foot implosion experiments on the National Ignition Facility*, Physics of Plasmas, vol. 23, 5: 056302 (2016) 13, 15, 21

Clayton, D. D., *Principles of stellar evolution and nucleosynthesis*, University of Chicago press (1983) 8

Colaïtis, A., Igumenshchev, I., Mathiaud, J. & Goncharov, V., *Inverse ray tracing on icosahedral tetrahedron grids for non-linear laser plasma interaction coupled to 3D radiation hydrodynamics*, Journal of Computational Physics, vol. 443: 110537 (2021) 17, 31, 35

Dahmani, F., *Experimental scaling laws for mass-ablation rate, ablation pressure in planar laser-produced plasmas with laser intensity, laser wavelength, and target atomic number*, Journal of Applied Physics, vol. 74, 1: 622 (1993) 115, 116, 117, 118

Daligault, J. & Dimonte, G., *Correlation effects on the temperature-relaxation rates in dense plasmas*, Physical Review E, vol. 79, 5: 056403 (2009) 63, 64, 67, 71, 79, 83

David, N., Spence, D. J. & Hooker, S. M., *Molecular-dynamic calculation of the inverse-bremsstrahlung heating of non-weakly-coupled plasmas*, Physical Review E, vol. 70, 5: 056411 (2004) 64, 76, 80, 82, 83, 84, 89, 91

Dawson, J. & Oberman, C., *High-Frequency Conductivity and the Emission and Absorption Coefficients of a Fully Ionized Plasma*, Physics of Fluids, vol. 5, 5: 517 (1962) 60, 61, 62, 63, 66, 78, 79, 80, 83, 85, 86

Dawson, J. M., *On the production of plasma by giant pulse lasers*, The Physics of Fluids, vol. 7, 7: 981 (1964) 61, 80, 83

Debayle, A., Ruyer, C., Morice, O., Masson-Laborde, P.-E., Loiseau, P. & Benisti, D., *A unified modeling of wave mixing processes with the ray tracing method*, Physics of Plasmas, vol. 26, 9: 092705 (2019) 17, 31, 35

Decker, C. D., Mori, W. B., Dawson, J. M. & Katsouleas, T., *Nonlinear collisional absorption in laser-driven plasmas*, Physics of Plasmas, vol. 1, 12: 4043 (1994) 84

Delcroix, J.-L. & Bers, A., *Physique des plasmas*, vol. 1, Dunod Paris (1963) 40

Derouillat, J., Beck, A., Pérez, F., Vinci, T., Chiaramello, M., Grassi, A., Flé, M., Bouchard, G., Plotnikov, I., Aunai, N., Dargent, J., Riconda, C. & Grech, M., *Smilei: A collaborative, open-source, multi-purpose particle-in-cell code for plasma simulation*, Comput. Phys. Commun., vol. 222: 351 (2018) 61

Desai, T., Pant, H. C., Khan, M., Sarkar, S. & Chakraborty, B., *Specular reflection as a probe for diagnostics of laser-produced plasmas*, Journal of Plasma Physics, vol. 51, 2: 211 (1994) 114, 115, 116

Devriendt, R. & Poujade, O., *Classical molecular dynamic simulations and modeling of inverse bremsstrahlung heating in low z weakly coupled plasmas*, Physics of Plasmas, vol. 29, 7: 073301 (2022) 59

Dewald, E. L., Milovich, J. L., Michel, P., Landen, O. L., Kline, J. L., Glenn, S., Jones, O., Kalantar, D. H., Pak, A., Robey, H. F., Kyrala, G. A., Divol, L., Benedetti, L. R., Holder, J., Widmann, K., Moore, A., Schneider, M. B., Döppner, T., Tommasini, R., Bradley, D. K., Bell, P., Ehrlich, B., Thomas, C. A., Shaw, M., Widmayer, C., Callahan, D. A., Meezan, N. B., Town, R. P. J., Hamza, A., Dzenitis, B., Nikroo, A., Moreno, K., Van Wonterghem, B., Mackinnon, A. J., Glenzer, S. H., MacGowan, B. J., Kilkenny, J. D., Edwards, M. J., Atherton, L. J. & Moses, E. I., *Early-time symmetry tuning in the presence of cross-beam energy transfer in icf experiments on the national ignition facility*, Phys. Rev. Lett., vol. 111: 235001 (2013) 16

Dewandre, T., *Doppler shift of laser light reflected from expanding plasmas*, Physics of Fluids, vol. 24, 3: 528 (1981) 23

Dimonte, G. & Daligault, J., *Molecular-dynamics simulations of electron-ion temperature relaxation in a classical coulomb plasma*, Phys. Rev. Lett., vol. 101: 135001 (2008) 49, 60, 61, 62, 63, 64, 67, 68, 71, 74, 75, 76, 79, 83, 86, 90

Dittrich, T. R., Hurricane, O. A., Callahan, D. A., Dewald, E. L., Döppner, T., Hinkel, D. E., Berzak Hopkins, L. F., Le Pape, S., Ma, T., Milovich, J. L., Moreno, J. C., Patel, P. K., Park, H.-S., Remington, B. A., Salmonson, J. D. & Kline, J. L., *Design of a High-Foot High-Adiabat ICF Capsule for the National Ignition Facility*, Physical Review Letters, vol. 112, 5: 055002 (2014) 13

Drude, P., *Zur Elektronentheorie der Metalle; II. Teil. Galvanomagnetische und thermomagnetische Effecte*, Annalen der Physik, vol. 308, 11: 369 (1900) 25

Edwards, M. J., Patel, P. K., Lindl, J. D., Atherton, L. J., Glenzer, S. H., Haan, S. W., Kilkenny, J. D., Landen, O. L., Moses, E. I., Nikroo, A., Petrasso, R., Sangster, T. C., Springer, P. T., Batha, S., Benedetti, R., Bernstein, L., Betti, R., Bleuel, D. L., Boehly, T. R., Bradley, D. K., Caggiano, J. A., Callahan, D. A., Celliers, P. M., Cerjan, C. J., Chen, K. C., Clark, D. S.,

Collins, G. W., Dewald, E. L., Divol, L., Dixit, S., Doeppner, T., Edgell, D. H., Fair, J. E., Farrell, M., Fortner, R. J., Frenje, J., Gatu Johnson, M. G., Giraldez, E., Glebov, V. Y., Grim, G., Hammel, B. A., Hamza, A. V., Harding, D. R., Hatchett, S. P., Hein, N., Herrmann, H. W., Hicks, D., Hinkel, D. E., Hoppe, M., Hsing, W. W., Izumi, N., Jacoby, B., Jones, O. S., Kalantar, D., Kauffman, R., Kline, J. L., Knauer, J. P., Koch, J. A., Kozioziemski, B. J., Kyrala, G., LaFortune, K. N., Pape, S. L., Leeper, R. J., Lerche, R., Ma, T., MacGowan, B. J., MacKinnon, A. J., Macphee, A., Mapoles, E. R., Marinak, M. M., Mauldin, M., McKenty, P. W., Meezan, M., Michel, P. A., Milovich, J., Moody, J. D., Moran, M., Munro, D. H., Olson, C. L., Opachich, K., Pak, A. E., Parham, T., Park, H.-S., Ralph, J. E., Regan, S. P., Remington, B., Rinderknecht, H., Robey, H. F., Rosen, M., Ross, S., Salmonson, J. D., Sater, J., Schneider, D. H., Séguin, F. H., Sepke, S. M., Shaughnessy, D. A., Smalyuk, V. A., Spears, B. K., Stoeckl, C., Stoeffl, W., Suter, L., Thomas, C. A., Tommasini, R., Town, R. P., Weber, S. V., Wegner, P. J., Widman, K., Wilke, M., Wilson, D. C., Yeamans, C. B. & Zylstra, A., *Progress towards ignition on the National Ignition Facility*, Physics of Plasmas, vol. 20, 7: 070501 (2013) 12

Eidmann, K., Amiranoff, F., Fedosejevs, R., Maaswinkel, A. G. M., Petsch, R., Sigel, R., Spindler, G., Teng, Y.-l., Tsakiris, G. & Witkowski, S., *Interaction of 1.3-M m laser radiation with thin foil targets*, Physical Review A, vol. 30, 5: 2568 (1984) 115, 117, 128

Eliezer, S., *The interaction of high-power lasers with plasmas*, CRC press (2002) 18, 19, 33, 35, 40, 43, 133

Ersfeld, B. & Bell, A. R., *Self-consistent distributions in collisional absorption of intense laser fields*, Physics of Plasmas, vol. 7, 3: 1001 (2000) 53, 60, 89

Faehl, R. J. & Roderick, N. F., *Intensity dependence of inverse bremsstrahlung absorption in an inhomogeneous standing wave*, The Physics of Fluids, vol. 21, 5: 793 (1978) 79

Ferrante, G., Zarcone, M. & Uryupin, S. A., *Electron distribution functions in laser fields*, Plasma Sources Science and Technology, vol. 10, 2: 318 (2001) 88, 94

Filippov, A. V., Starostin, A. N. & Gryaznov, V. K., *Coulomb Logarithm in Nonideal and Degenerate Plasmas*, Journal of Experimental and Theoretical Physics, vol. 126, 3: 430 (2018) 43

Földes, I. B., Pakula, R., Sakabe, S. & Sigel, R., *Light absorption in laser-heated cavities*, Applied Physics B Photophysics and Laser Chemistry, vol. 43, 2: 117 (1987) 113

Fourkal, E., Bychenkov, V. Y., Rozmus, W., Sydora, R., Kirkby, C., Capjack, C. E., Glenzer, S. H. & Baldis, H. A., *Electron distribution function in laser heated plasmas*, Phys. Plasmas, vol. 8, 2: 8 (2001) 53, 88, 100, 101, 109

Garban-Labaune, C., Fabre, E., Max, C. E., Fabbro, R., Amiranoff, F., Virmont, J., Weinfeld, M. & Michard, A., *Effect of Laser Wavelength and Pulse Duration on Laser-Light Absorption and Back Reflection*, Physical Review Letters, vol. 48, 15: 1018 (1982) 115, 116, 117

Griebel, M., Knapek, S. & Zumbusch, G., *Numerical Simulation in Mlecular Dynamics*, Springer, Berlin (2007) 68

Grinenko, A. & Gericke, D. O., *Nonlinear collisional absorption of laser light in dense strongly coupled plasmas*, Phys. Rev. Lett., vol. 103: 065005 (2009) 60

Haan, S. W., Lindl, J. D., Callahan, D. A., Clark, D. S., Salmonson, J. D., Hammel, B. A., Atherton, L. J., Cook, R. C., Edwards, M. J., Glenzer, S., Hamza, A. V., Hatchett, S. P., Herrmann, M. C., Hinkel, D. E., Ho, D. D., Huang, H., Jones, O. S., Kline, J., Kyrala, G., Landen, O. L., MacGowan, B. J., Marinak, M. M., Meyerhofer, D. D., Milovich, J. L., Moreno, K. A., Moses, E. I., Munro, D. H., Nikroo, A., Olson, R. E., Peterson, K., Pollaine, S. M., Ralph, J. E., Robey, H. F., Spears, B. K., Springer, P. T., Suter, L. J., Thomas, C. A., Town, R. P., Vesey, R., Weber, S. V., Wilkens, H. L. & Wilson, D. C., *Point design targets, specifications, and requirements for the 2010 ignition campaign on the national ignition facility*, Physics of Plasmas, vol. 18, 5: 051001 (2011) 11

Hall, G. N., Jones, O. S., Strozzi, D. J., Moody, J. D., Turnbull, D., Ralph, J., Michel, P. A., Hohenberger, M., Moore, A. S., Landen, O. L., Divol, L., Bradley, D. K., Hinkel, D. E., Mackinnon, A. J., Town, R. P. J., Meezan, N. B., Berzak Hopkins, L. & Izumi, N., *The relationship between gas fill density and hohlraum drive performance at the National Ignition Facility*, Physics of Plasmas, vol. 24, 5: 052706 (2017) 16

Hamza, A. V., Nikroo, A., Alger, E., Antipa, N., Atherton, L. J., Barker, D., Baxamusa, S., Bhandarkar, S., Biesiada, T., Buice, E., Carr, E., Castro, C., Choate, C., Conder, A., Crippen, J., Dylla-Spears, R., Dzenitis, E., Eddinger, S., Emerich, M., Fair, J., Farrell, M., Felker, S., Florio, J., Forsman, A., Giraldez, E., Hein, N., Hoover, D., Horner, J., Huang, H., Kozioziemski, B., Kroll, J., Lawson, B., Letts, S. A., Lord, D., Mapoles, E., Mauldin, M., Miller, P., Montesanti, R., Moreno, K., Parham, T., Nathan, B., Reynolds, J., Sater, J., Segraves, K., Seugling, R., Stadermann, M., Strauser, R., Stephens, R., Suratwala, T. I., Swisher, M., Taylor, J. S., Wallace, R., Wegner, P., Wilkens, H. & Yoxalla, B., *Target development for the national ignition campaign*, Fusion Science and Technology, vol. 69, 1: 395 (2016) 16

Honda, H., Nishimura, H., Miyamoto, S., Ohnuki, D., Fujita, K., Ochi, Y., Miki, H., Takabe, H., Nakai, S. & Mima, K., *Influence of specularly reflected laser light on uniformity of implosion of indirect-drive fusion capsule*, Plasma Physics and Controlled Fusion, vol. 40, 6: 1097 (1998) 17

Igumenshchev, I. V., Goncharov, V. N., Seka, W., Edgell, D. & Boehly, T. R., *The effect of resonance absorption in omega direct-drive designs and experiments*, Physics of Plasmas, vol. 14, 9: 092701 (2007) 18

Igumenshchev, I. V., Marshall, F. J., Marozas, J. A., Smalyuk, V. A., Epstein, R., Goncharov, V. N., Collins, T. J. B., Sangster, T. C. & Skupsky, S., *The effects of target mounts in direct-drive implosions on omega*, Physics of Plasmas, vol. 16, 8: 082701 (2009) 11

Jackson, J. D., *Classical electrodynamics*, American Association of Physics Teachers (1999) 23

Johnston, T. W. & Dawson, J. M., *Correct values for high-frequency power absorption by inverse bremsstrahlung in plasmas*, Phys. Fluids, vol. 16, 5: 722 (1973) 60, 61, 62, 63, 66, 78, 79, 80, 85, 86

Jones, O. S., Cerjan, C. J., Marinak, M. M., Milovich, J. L., Robey, H. F., Springer, P. T., Benedetti, L. R., Bleuel, D. L., Bond, E. J., Bradley, D. K., Callahan, D. A., Caggiano, J. A., Celliers, P. M., Clark, D. S., Dixit, S. M., Doppner, T., Dylla-Spears, R. J., Dzentitis, E. G., Farley, D. R., Glenn, S. M., Glenzer, S. H., Haan, S. W., Haid, B. J., Haynam, C. A., Hicks, D. G., Kozioziemski, B. J., LaFortune, K. N., Landen, O. L., Mapoles, E. R., MacKinnon, A. J., McNaney, J. M., Meezan, N. B., Michel, P. A., Moody, J. D., Moran, M. J., Munro, D. H., Patel, M. V., Parham, T. G., Sater, J. D., Sepke, S. M., Spears, B. K., Town, R. P. J., Weber, S. V., Widmann, K., Widmayer, C. C., Williams, E. A., Atherton, L. J., Edwards, M. J., Lindl, J. D., MacGowan, B. J., Suter, L. J., Olson, R. E., Herrmann, H. W., Kline, J. L., Kyrala, G. A., Wilson, D. C., Frenje, J., Boehly, T. R., Glebov, V., Knauer, J. P., Nikroo, A., Wilkens, H. & Kilkenny, J. D., *A high-resolution integrated model of the National Ignition Campaign cryogenic layered experiments*, Physics of Plasmas, vol. 19, 5: 056315 (2012) 17, 35

Jones, R. D. & Lee, K., *Kinetic theory, transport, and hydrodynamics of a high-z plasma in the presence of an intense laser field*, The Physics of Fluids, vol. 25, 12: 2307 (1982) 53, 60, 61, 62, 63, 66, 78, 79, 80, 85, 86, 88, 100, 108

Kaiser, T. B., *Laser ray tracing and power deposition on an unstructured three-dimensional grid*, Physical Review E, vol. 61, 1: 895 (2000) 31

Kato, Y., Mima, K., Miyanaga, N., Arinaga, S., Kitagawa, Y., Nakatsuka, M. & Yamanaka, C., *Random phasing of high-power lasers for uniform target acceleration and plasma-instability suppression*, Phys. Rev. Lett., vol. 53: 1057 (1984) 119

Kihara, T. & Aono, O., *Unified theory of relaxations in plasmas, i. basic theorem*, Journal of the Physical Society of Japan, vol. 18, 6: 837 (1963) 44, 49

Kilkenny, J. D., Glendinning, S. G., Haan, S. W., Hammel, B. A., Lindl, J. D., Munro, D., Remington, B. A., Weber, S. V., Knauer, J. P. & Verdon, C. P., *A review of the ablative stabilization of the rayleigh–taylor instability in regimes relevant to inertial confinement fusion*, Physics of Plasmas, vol. 1, 5: 1379 (1994) 12

Kline, J., Batha, S., Benedetti, L., Bennett, D., Bhandarkar, S., Hopkins, L. B., Biener, J., Biener, M., Bionta, R., Bond, E., Bradley, D., Braun, T., Callahan, D., Caggiano, J., Cerjan, C., Cagadas, B., Clark, D., Castro, C., Dewald, E., Döppner, T., Divol, L., Dylla-Spears, R., Eckart, M., Edgell, D., Farrell, M., Field, J., Fittinghoff, D., Gatu Johnson, M., Grim, G., Haan, S., Haines, B., Hamza, A., Hartouni, E., Hatarik, R., Henderson, K., Herrmann, H., Hinkel, D., Ho, D., Hohenberger, M., Hoover, D., Huang, H., Hoppe, M., Hurricane, O., Izumi, N., Johnson, S., Jones, O., Khan, S., Kozioziemski, B., Kong, C., Kroll, J., Kyrala, G., LePape, S., Ma, T., Mackinnon, A., MacPhee, A., MacLaren, S., Masse, L., McNaney, J., Meezan, N., Merrill, J., Milovich, J., Moody, J., Nikroo, A., Pak, A., Patel, P., Peterson, L., Piceno, E., Pickworth, L., Ralph, J., Rice, N., Robey, H., Ross, J., Rygg, J., Sacks, M., Salmonson, J., Sayre, D., Sater, J., Schneider, M., Schoff, M., Sepke, S., Seugling, R., Smalyuk, V., Spears, B., Stadermann, M., Stoeffl, W., Strozzi, D., Tipton, R., Thomas, C., RPJ Town, Volegov, P., Walters, C., Wang, M., Wilde, C., Woerner, E., Yeamans, C., Yi, S., Yoxall, B., Zylstra, A., Kilkenny, J., Landen, O., Hsing, W. & Edwards, M., *Progress of indirect drive inertial confinement fusion in the United States*, Nuclear Fusion, vol. 59, 11: 112018 (2019) 16

Kritcher, A. L., Hinkel, D. E., Callahan, D. A., Hurricane, O. A., Clark, D., Casey, D. T., Dewald, E. L., Dittrich, T. R., Döppner, T., Barrios Garcia, M. A., Haan, S., Berzak Hopkins, L. F., Jones, O., Landen, O., Ma, T., Meezan, N., Milovich, J. L., Pak, A. E., Park, H.-S., Patel, P. K., Ralph, J., Robey, H. F., Salmonson, J. D., Sepke, S., Spears, B., Springer, P. T., Thomas, C. A., Town, R., Celliers, P. M. & Edwards, M. J., *Integrated modeling of cryogenic layered highfoot experiments at the NIF*, Physics of Plasmas, vol. 23, 5: 052709 (2016) 13

Krokhin, O., Mikhailov, I. A., Pustovalov, V., Rupasov, A., Silin, V., Sklizkov, G. & Shikanov, A., *Directivity of scattered light and X rays in a laser plasma*, Zhurnal Eksperimentalnoi i Teoreticheskoi Fiziki, vol. 69: 206 (1975) 114, 115, 116

Kruer, W. L., *The physics of laser plasma interaction*, Addison-Wesley, New York (1988) 117

Kull, H. J., *Linear mode conversion in laser plasmas*, The Physics of Fluids, vol. 26, 7: 1881 (1983) 18

Kull, H.-J. & Plagne, L., *Quantum-mechanical dielectric model of the electron–ion collision frequency in strong laser fields*, Physics of Plasmas, vol. 8, 12: 5244 (2001) 60

Kuzmin, S. G. & O'Neil, T. M., *Numerical simulation of ultracold plasmas: How rapid intrinsic heating limits the development of correlation*, Phys. Rev. Lett., vol. 88: 065003 (2002) 64, 68

Landau, L. & Teller, E., *Zur theorie der schalldispersion*, Phys. Z. Sowjetunion, vol. 10, 1: 34 (1936) 60, 61, 62, 66, 78, 79, 80

Langdon, A. B., *Nonlinear Inverse Bremsstrahlung and Heated-Electron Distributions*, Physical Review Letters, vol. 44, 9: 575 (1980) 45, 49, 51, 52, 53, 64, 65, 88, 89, 92, 93, 100, 105, 106, 107, 108, 109

Lawson, J. D., *Some criteria for a power producing thermonuclear reactor*, Proceedings of the Physical Society. Section B, vol. 70, 1: 6 (1957) 10

Le, H. P., Sherlock, M. & Scott, H. A., *Influence of atomic kinetics on inverse bremsstrahlung heating and nonlocal thermal transport*, Phys. Rev. E, vol. 100: 013202 (2019) 60

Lee, Y. T. & More, R. M., *An electron conductivity model for dense plasmas*, The Physics of Fluids, vol. 27, 5: 1273 (1984) 43

Lefebvre, E., Bernard, S., Esnault, C., Gauthier, P., Grisollet, A., Hoch, P., Jacquet, L., Kluth, G., Laffite, S., Liberatore, S., Marmajou, I., Masson-Laborde, P.-E., Morice, O. & Willien, J.-L., *Development and validation of the TROLL radiation-hydrodynamics code for 3d hohlraum calculations*, Nucl. Fusion, vol. 59, 3: 032010 (2018) 17, 35, 61, 88, 136

Lefebvre, E., Cochet, N., Fritzler, S., Malka, V., Aléonard, M.-M., Chemin, J.-F., Darbon, S., Disdier, L., Faure, J., Fedotoff, A., Landoas, O., Malka, G., Méot, V., Morel, P., Gloahec, M. R. L., Rouyer, A., Rubbelynck, C., Tikhonchuk, V., Wrobel, R., Audebert, P. & Rousseaux, C., *Electron and photon production from relativistic laser–plasma interactions*, Nucl. Fusion, vol. 43: 629 (2003) 61

Lennard, A., *On bogoliubov's kinetic equation for a spatially homogeneous plasma*, Annals of Physics, vol. 10, 3: 390 (1960) 44

Li, C.-K. & D., P. R., *Fokker-planck equation for moderately coupled plasmas*, Phys. REv. Lett., vol. 70: 3063 (1993) 53

Liboff, R. L., *Transport coefficients determined using the shielded coulomb potential*, The Physics of Fluids, vol. 2, 1: 40 (1959) 43

Lindl, J., Landen, O., Edwards, J., Moses, E. & NIC Team, *Review of the National Ignition Campaign 2009-2012*, Physics of Plasmas, vol. 21, 2: 020501 (2014) 10, 12, 35

Lindl, J. D., Amendt, P., Berger, R. L., Glendinning, S. G., Glenzer, S. H., Haan, S. W., Kauffman, R. L., Landen, O. L. & Suter, L. J., *The physics basis for ignition using indirect-drive targets on the National Ignition Facility*, Physics of Plasmas, vol. 11, 2: 339 (2004) 17

Lindl, J. D., Haan, S. W., Landen, O. L., Christopherson, A. R. & Betti, R., *Progress toward a self-consistent set of 1d ignition capsule metrics in icf*, Physics of Plasmas, vol. 25, 12: 122704 (2018) 35

Liu, J. M., De Groot, J. S., Matte, J. P., Johnston, T. W. & Drake, R. P., *Measurements of inverse bremsstrahlung absorption and non-Maxwellian electron velocity distributions*, Physical Review Letters, vol. 72, 17: 2717 (1994) 88

LLNL, *Fy 2021 annual report*, https://annual.llnl.gov/fy-2021/threshold-fusion-ignition-2021, accessed: 2022-05-13 (2021) 7, 17

Loomis, E. N., Yi, S. A., Kyrala, G. A., Kline, J., Simakov, A., Ralph, J., Millot, M., Dewald, E., Zylstra, A., Rygg, J. R., Celliers, P., Goyon, C., Lahmann, B., Sio, H., MacLaren, S., Masse, L., Callahan, D., Hurricane, O., Wilson, D. C., Rice, N., Huang, H., Kong, C., Bae, J., Nikroo, A. & Batha, S. H., *Implosion shape control of high-velocity, large case-to-capsule ratio beryllium ablators at the national ignition facility*, Physics of Plasmas, vol. 25, 7: 072708 (2018) 16

Ma, T., Patel, P. K., Izumi, N., Springer, P. T., Key, M. H., Atherton, L. J., Benedetti, L. R., Bradley, D. K., Callahan, D. A., Celliers, P. M., Cerjan, C. J., Clark, D. S., Dewald, E. L., Dixit, S. N., Döppner, T., Edgell, D. H., Epstein, R., Glenn, S., Grim, G., Haan, S. W., Hammel, B. A., Hicks, D., Hsing, W. W., Jones, O. S., Khan, S. F., Kilkenny, J. D., Kline, J. L., Kyrala, G. A., Landen, O. L., Le Pape, S., MacGowan, B. J., Mackinnon, A. J., MacPhee, A. G., Meezan, N. B., Moody, J. D., Pak, A., Parham, T., Park, H.-S., Ralph, J. E., Regan, S. P., Remington, B. A., Robey, H. F., Ross, J. S., Spears, B. K., Smalyuk, V., Suter, L. J., Tommasini, R., Town, R. P., Weber, S. V., Lindl, J. D., Edwards, M. J., Glenzer, S. H. & Moses, E. I., *Onset of Hydrodynamic Mix in High-Velocity, Highly Compressed Inertial Confinement Fusion Implosions*, Physical Review Letters, vol. 111, 8: 085004 (2013) 12

MacKinnon, A. J., Meezan, N. B., Ross, J. S., Le Pape, S., Berzak Hopkins, L., Divol, L., Ho, D., Milovich, J., Pak, A., Ralph, J., Döppner, T., Patel, P. K., Thomas, C., Tommasini, R., Haan, S., MacPhee, A. G., McNaney, J., Caggiano, J., Hatarik, R., Bionta, R., Ma, T., Spears,

B., Rygg, J. R., Benedetti, L. R., Town, R. P. J., Bradley, D. K., Dewald, E. L., Fittinghoff, D., Jones, O. S., Robey, H. R., Moody, J. D., Khan, S., Callahan, D. A., Hamza, A., Biener, J., Celliers, P. M., Braun, D. G., Erskine, D. J., Prisbrey, S. T., Wallace, R. J., Kozioziemski, B., Dylla-Spears, R., Sater, J., Collins, G., Storm, E., Hsing, W., Landen, O., Atherton, J. L., Lindl, J. D., Edwards, M. J., Frenje, J. A., Gatu-Johnson, M., Li, C. K., Petrasso, R., Rinderknecht, H., Rosenberg, M., Séguin, F. H., Zylstra, A., Knauer, J. P., Grim, G., Guler, N., Merrill, F., Olson, R., Kyrala, G. A., Kilkenny, J. D., Nikroo, A., Moreno, K., Hoover, D. E., Wild, C. & Werner, E., *High-density carbon ablator experiments on the National Ignition Facility*, Physics of Plasmas, vol. 21, 5: 056318 (2014) 16

MacPhee, A. G., Smalyuk, V. A., Landen, O. L., Weber, C. R., Robey, H. F., Alfonso, E. L., Baker, K. L., Berzak Hopkins, L. F., Biener, J., Bunn, T., Casey, D. T., Clark, D. S., Crippen, J. W., Divol, L., Farrell, M., Felker, S., Field, J. E., Hsing, W. W., Kong, C., Le Pape, S., Martinez, D. A., Michel, P., Milovich, J., Moore, A., Nikroo, A., Pickworth, L., Rice, N., Stadermann, M., Yeamans, C. & Wild, C., *Hydrodynamic instabilities seeded by the x-ray shadow of icf capsule fill-tubes*, Physics of Plasmas, vol. 25, 8: 082702 (2018) 16

Mahgoub, M., Baehr, J., Grabosch, H., Groß, M., Hakobyan, L., Isaev, I., Ivanisenko, Y., Khojoyan, M., Klemz, G., Krasilnikov, M., Kourkafas, G., Li, J., Malyutin, D., Marchetti, B., Oppelt, A., Otevrel, M., Petrosyan, B., Rosbach, K., Stephan, F. & Vashchenko, G., *Longitudinal phase space studies at the pitz facility*, Proceedings of IPAC2012 125

Manheimer, W. M., *Steady-state planar ablative flow*, Physics of Fluids, vol. 25, 9: 1644 (1982) 118, 133, 135, 138

Marinak, M. M., Haan, S. W., Dittrich, T. R., Tipton, R. E. & Zimmerman, G. B., *A comparison of three-dimensional multimode hydrodynamic instability growth on various national ignition facility capsule designs with hydra simulations*, Physics of Plasmas, vol. 5, 4: 1125 (1998) 17

Marinak, M. M., Kerbel, G. D., Gentile, N. A., Jones, O., Munro, D., Pollaine, S., Dittrich, T. R. & Haan, S. W., *Three-dimensional HYDRA simulations of National Ignition Facility targets*, Physics of Plasmas, vol. 8, 5: 2275 (2001) 35, 61, 88

Masson-Laborde, P. E., Monteil, M. C., Tassin, V., Philippe, F., Gauthier, P., Casner, A., Depierreux, S., Neuville, C., Villette, B., Laffite, S., Seytor, P., Fremerye, P., Seka, W., Teychenné, D., Debayle, A., Marion, D., Loiseau, P. & Casanova, M., *Laser plasma interaction on rugby hohlraum on the omega laser facility: Comparisons between cylinder, rugby, and elliptical hohlraums*, Physics of Plasmas, vol. 23, 2: 022703 (2016) 16

Matte, J. P., Johnston, T. W., Delettrez, J. & McCrory, R. L., *Electron heat flow with inverse bremsstrahlung and ion motion*, Phys. Rev. Lett., vol. 53: 1461 (1984) 60

Matte, J. P., Lamoureux, M., Moller, C., Yin, R. Y., Delettrez, J., Virmont, J. & Johnston, T. W., *Non-Maxwellian electron distributions and continuum X-ray emission in inverse Bremsstrahlung heated plasmas*, Plasma Physics and Controlled Fusion, vol. 30, 12: 1665 (1988) 52, 53, 88, 89, 91, 93, 94, 100, 102, 105, 107, 108

Mead, W. C., Campbell, E. M., Estabrook, K., Turner, R. E., Kruer, W. L., Lee, P. H. Y., Pruett, B., Rupert, V. C., Tirsell, K. G., Stradling, G. L., Ze, F., Max, C. E., Rosen, M. D. & Lasinski, B. F., *Laser irradiation of disk targets at 0.53 μm wavelength*, The Physics of Fluids, vol. 26, 8: 2316 (1983) 115, 117

Meezan, N. B., Edwards, M. J., Hurricane, O. A., Patel, P. K., Callahan, D. A., Hsing, W. W., Town, R. P. J., Albert, F., Amendt, P. A., Berzak Hopkins, L. F., Bradley, D. K., Casey, D. T., Clark, D. S., Dewald, E. L., Dittrich, T. R., Divol, L., Döppner, T., Field, J. E., Haan, S. W., Hall, G. N., Hammel, B. A., Hinkel, D. E., Ho, D. D., Hohenberger, M., Izumi, N., Jones, O. S., Khan, S. F., Kline, J. L., Kritcher, A. L., Landen, O. L., LePape, S., Ma, T., MacKinnon, A. J., MacPhee, A. G., Masse, L., Milovich, J. L., Nikroo, A., Pak, A., Park, H.-S., Peterson, J. L., Robey, H. F., Ross, J. S., Salmonson, J. D., Smalyuk, V. A., Spears, B. K., Stadermann, M., Suter, L. J., Thomas, C. A., Tommasini, R., Turnbull, D. P. & Weber, C. R., *Indirect drive ignition at the National Ignition Facility*, Plasma Physics and Controlled Fusion, vol. 59, 1: 014021 (2017) 12

Meyer, B., Morin, G. & Thiell, G., *Study of preheat effects in ND-laser irradiated finite Al disk targets*, Journal of Applied Physics, vol. 53, 4: 2947 (1982) 115, 117

Milder, A. L., Katz, J., Boni, R., Palastro, J. P., Sherlock, M., Rozmus, W. & Froula, D. H., *Statistical analysis of non-Maxwellian electron distribution functions measured with angularly resolved Thomson scattering*, Physics of Plasmas, vol. 28, 8: 082102 (2021) 49, 88, 89, 100, 101, 107

Milder, A. L., Le, H. P., Sherlock, M., Franke, P., Katz, J., Ivancic, S. T., Shaw, J. L., Palastro, J. P., Hansen, A. M., Begishev, I. A., Rozmus, W. & Froula, D. H., *Evolution of the Electron Distribution Function in the Presence of Inverse Bremsstrahlung Heating and Collisional Ionization*, Physical Review Letters, vol. 124, 2: 025001 (2020) 89

Moll, M., Schlanges, M., Bornath, T. & Krainov, V. P., *Inverse bremsstrahlung heating beyond the first Born approximation for dense plasmas in laser fields*, New Journal of Physics, vol. 14, 6: 065010 (2012) 60

Moody, J. D., Callahan, D. A., Hinkel, D. E., Amendt, P. A., Baker, K. L., Bradley, D., Celliers, P. M., Dewald, E. L., Divol, L., Döppner, T., Eder, D. C., Edwards, M. J., Jones, O., Haan, S. W., Ho, D., Hopkins, L. B., Izumi, N., Kalantar, D., Kauffman, R. L., Kilkenny, J. D., Landen, O., Lasinski, B., LePape, S., Ma, T., MacGowan, B. J., MacLaren, S. A., Mackinnon, A. J., Meeker, D., Meezan, N., Michel, P., Milovich, J. L., Munro, D., Pak, A. E., Rosen, M., Ralph, J., Robey, H. F., Ross, J. S., Schneider, M. B., Strozzi, D., Storm, E., Thomas, C., Town, R. P. J., Widmann, K. L., Kline, J., Kyrala, G., Nikroo, A., Boehly, T., Moore, A. S. & Glenzer, S. H., *Progress in hohlraum physics for the National Ignition Facility*, Physics of Plasmas, vol. 21, 5: 056317 (2014) 17

Mora, P. & Pellat, R., *Self-similar expansion of a plasma into a vacuum*, Physics of Fluids, vol. 22, 12: 2300 (1979) 118, 133, 135, 138

Morozov, I., Reinholz, H., Röpke, G., Wierling, A. & Zwicknagel, G., *Molecular dynamics simulations of optical conductivity of dense plasmas*, Phys. Rev. E, vol. 71: 066408 (2005) 64

Mulser, P., *Hot Matter from High-Power Lasers*, p. 1–71, Springer Berlin Heidelberg (2020) 63, 80, 86

Mulser, P., Cornolti, F., Bésuelle, E. & Schneider, R., *Time-dependent electron-ion collision frequency at arbitrary laser intensity-temperature ratio*, Physical Review E, vol. 63, 1: 016406 (2000) 47, 52, 60, 61, 62, 63, 66, 78, 79, 80, 85, 86, 93, 104

Nagel, S. R., Haan, S. W., Rygg, J. R., Barrios, M., Benedetti, L. R., Bradley, D. K., Field, J. E., Hammel, B. A., Izumi, N., Jones, O. S., Khan, S. F., Ma, T., Pak, A. E., Tommasini, R. & Town, R. P. J., *Effect of the mounting membrane on shape in inertial confinement fusion implosions*, Physics of Plasmas, vol. 22, 2: 022704 (2015) 16

Nishimura, H., Azechi, H., Yamada, K., Tamura, A., Inada, Y., Matsuoka, F., Hamada, M., Suzuki, Y., Nakai, S. & Yamanaka, C., *Experimental study of wavelength dependences of laser-plasma coupling, transport, and ablation processes*, Physical Review A, vol. 23, 4: 2011 (1981) 115, 117

Nishimura, H., Mima, K., Yanase, Y., Banjoya, N., Fujita, H., Iba, K., Matoba, M., Nakai, S. & Yamanaka, C., *Resonance absorption and surface instability at a critical density surface of a plasma irradiated by a CO $_2$ laser*, Plasma Physics, vol. 22, 1: 69 (1980) 115, 116

Offenberger, A. A., Fedosejevs, R., Gupta, P. D., Popil, R. & Tsui, Y. Y., *Experimental results for high intensity KrF laser/plasma interaction*, Laser and Particle Beams, vol. 4, 3-4: 329 (1986) 115, 116, 117

Ordonez, C. A. & Molina, M. I., *Evaluation of the Coulomb logarithm using cutoff and screened Coulomb interaction potentials*, Physics of Plasmas, vol. 1, 8: 2515 (1994) 43

Pandit, R. R., Sentoku, Y., Becker, V. R., Barrington, K., Thurston, J., Cheatham, J., Ramunno, L. & Ackad, E., *Effect of soft-core potentials on inverse bremsstrahlung heating during laser matter interactions*, Physics of Plasmas, vol. 24, 7: 073303 (2017) 69

Park, H.-S., Hurricane, O. A., Callahan, D. A., Casey, D. T., Dewald, E. L., Dittrich, T. R., Döppner, T., Hinkel, D. E., Berzak Hopkins, L. F., Le Pape, S., Ma, T., Patel, P. K., Remington, B. A., Robey, H. F., Salmonson, J. D. & Kline, J. L., *High-Adiabat High-Foot Inertial Confinement Fusion Implosion Experiments on the National Ignition Facility*, Physical Review Letters, vol. 112, 5: 055001 (2014) 13, 15

Peterson, J. L., Casey, D. T., Hurricane, O. A., Raman, K. S., Robey, H. F. & Smalyuk, V. A., *Validating hydrodynamic growth in National Ignition Facility implosionsa)*, Physics of Plasmas, vol. 22, 5: 056309 (2015) 13

Pfalzner, S., *Influence of strong laser fields on the inverse bremsstrahlung collision frequency*, Applied Physics B Photophysics and Laser Chemistry, vol. 55, 4: 368 (1992) 88, 94

Pfalzner, S., *An introduction to inertial confinement fusion*, CRC Press (2006) 10, 17, 39

Pfalzner, S. & Gibbon, P., *Direct calculation of inverse-bremsstrahlung absorption in strongly coupled, nonlinearly driven laser plasmas*, Physical Review E, vol. 57, 4: 4698 (1998) 64, 76, 89, 91

Polishchuk, A. Y. & Meyer-Ter-Vehn, J., *Electron-ion relaxation in a plasma interacting with an intense laser field*, Physical Review E, vol. 49, 1: 663 (1994) 60, 64

Porshnev, P., Ferrante, G. & Zarcone, M., *Electron distribution functions in laser-embedded plasmas*, Physical Review E, vol. 48, 3: 2081 (1993) 53

Porshnev, P. I., Khanevich, E. I., Bivona, S. & Ferrante, G., *Nonlinear inverse bremsstrahlung and highly anisotropic electron distributions*, Physical Review E, vol. 53, 1: 1100 (1996) 53, 88, 95

Poujade, O., Barrios, M. A., Baton, S., Blancard, C., Devriendt, R. & Primout, M., *Rayleigh–taylor mixing may account for the position anomaly in nif microdot spectroscopy experiments*, Physics of Plasmas, vol. 28, 4: 042704 (2021) 36

Poujade, O., Ferri, M. & Geoffray, I., *New radiographic image processing tested on the simple and double-flux platform at omega*, Physics of Plasmas, vol. 24, 10: 102105 (2017) 142

Rand, S., *Inverse bremsstrahlung with high-intensity radiation fields*, Phys. Rev., vol. 136: B231 (1964) 60

Reif, F., *Fundamentals of statistical and thermal physics*, Waveland Press (2009) 40, 44

Ripin, B. H., Decoste, R., Obenschain, S. P., Bodner, S. E., McLean, E. A., Young, F. C., Whitlock, R. R., Armstrong, C. M., Grun, J., Stamper, J. A., Gold, S. H., Nagel, D. J., Lehmberg, R. H. & McMahon, J. M., *Laser-plasma interaction and ablative acceleration of thin foils at 1012–1015 W/cm2*, Physics of Fluids, vol. 23, 5: 1012 (1980) 115, 116

Riz, D., *Calculation and use of multigroup cross sections including electron-photon cascade for a 2d monte carlo neutron-gamma transport code. comparisons with mcnp-4b.*, Proc. of ANS PHYSOR, Pittsburgh, USA (2000) 142

Riz, D. & Chiche, M., *Simulation of energetic ions transport in a plasma by a 3d monte carlo method*, Proc. of the International conference on supercomputing in nuclear applications (SNA-2003), Paris, France (2003) 142

Robey, H. F., Boehly, T. R., Celliers, P. M., Eggert, J. H., Hicks, D., Smith, R. F., Collins, R., Bowers, M. W., Krauter, K. G., Datte, P. S., Munro, D. H., Milovich, J. L., Jones, O. S., Michel, P. A., Thomas, C. A., Olson, R. E., Pollaine, S., Town, R. P. J., Haan, S., Callahan, D., Clark, D., Edwards, J., Kline, J. L., Dixit, S., Schneider, M. B., Dewald, E. L., Widmann, K., Moody, J. D., Döppner, T., Radousky, H. B., Throop, A., Kalantar, D., DiNicola, P., Nikroo, A., Kroll, J. J., Hamza, A. V., Horner, J. B., Bhandarkar, S. D., Dzenitis, E., Alger, E., Giraldez, E., Castro, C., Moreno, K., Haynam, C., LaFortune, K. N., Widmayer, C., Shaw, M., Jancaitis, K., Parham, T., Holunga, D. M., Walters, C. F., Haid, B., Mapoles, E. R., Sater, J., Gibson, C. R., Malsbury, T., Fair, J., Trummer, D., Coffee, K. R., Burr, B., Berzins, L. V., Choate, C., Brereton, S. J., Azevedo, S., Chandrasekaran, H., Eder, D. C., Masters, N. D., Fisher, A. C., Sterne, P. A., Young, B. K., Landen, O. L., Van Wonterghem, B. M., MacGowan, B. J., Atherton, J., Lindl, J. D., Meyerhofer, D. D. & Moses, E., *Shock timing experiments on the national ignition facility: Initial results and comparison with simulation*, Physics of Plasmas, vol. 19, 4: 042706 (2012) 35

Ross, J. S., Ralph, J. E., Zylstra, A. B., Kritcher, A. L., Robey, H. F., Young, C. V., Hurricane, O. A., Callahan, D. A., Baker, K. L., Casey, D. T., Doeppner, T., Divol, L., Hohenberger, M., Pape, S. L., Pak, A., Patel, P. K., Tommasini, R., Ali, S. J., Amendt, P. A., Atherton, L. J., Bachmann, B., Bailey, D., Benedetti, L. R., Hopkins, L. B., Betti, R., Bhandarkar, S. D., Bionta, R. M., Birge, N. W., Bond, E. J., Bradley, D. K., Braun, T., Briggs, T. M., Bruhn, M. W., Celliers, P. M., Chang, B., Chapman, T., Chen, H., Choate, C., Christopherson, A. R., Clark, D. S., Crippen, J. W., Dewald, E. L., Dittrich, T. R., Edwards, M. J., Farmer, W. A., Field, J. E., Fittinghoff, D., Frenje, J., Gaffney, J., Johnson, M. G., Glenzer, S. H., Grim, G. P., Haan, S., Hahn, K. D., Hall, G. N., Hammel, B. A., Harte, J., Hartouni, E., Heebner, J. E., Hernandez, V. J., Herrmann, H., Herrmann, M. C., Hinkel, D. E., Ho, D. D., Holder, J. P., Hsing, W. W., Huang, H., Humbird, K. D., Izumi, N., Jarrott, L. C., Jeet, J., Jones, O., Kerbel, G. D., Kerr, S. M., Khan, S. F., Kilkenny, J., Kim, Y., Kleinrath, H. G., Kleinrath, V. G., Kong, C., Koning, J. M., Kroll, J. J., Landen, O. L., Langer, S., Larson, D., Lemos, N. C., Lindl, J. D., Ma, T., MacDonald, M. J., MacGowan, B. J., Mackinnon, A. J., MacLaren, S. A., MacPhee, A. G., Marinak, M. M., Mariscal, D. A., Marley, E. V., Masse, L., Meaney, K., Meezan, N. B., Michel, P. A., Millot, M., Milovich, J. L., Moody, J. D., Moore, A. S., Morton, J. W., Murphy, T., Newman, K., Di Nicola, J. M. G., Nikroo, A., Nora, R., Patel, M. V., Pelz, L. J., Peterson, J. L., Ping, Y., Pollock, B. B., Ratledge, M., Rice, N. G., Rinderknecht, H., Rosen, M., Rubery, M. S., Salmonson, J. D., Sater, J., Schiaffino, S., Schlossberg, D. J., Schneider, M. B., Schroeder, C. R., Scott, H. A., Sepke, S. M., Sequoia, K., Sherlock, M. W., Shin, S., Smalyuk, V. A., Spears, B. K., Springer, P. T., Stadermann, M., Stoupin, S., Strozzi, D. J., Suter, L. J., Thomas, C. A., Town, R. P. J., Tubman, E. R., Volegov, P. L., Weber, C. R., Widmann, K., Wild, C., Wilde, C. H., Van Wonterghem, B. M., Woods, D. T., Woodworth, B. N., Yamaguchi, M., Yang, S. T. & Zimmerman, G. B., *Experiments conducted in the burning plasma regime with inertial fusion implosions*, Preprint at https://arxiv.org/abs/2111.04640 16

Rupasov, A., Sklizkov, G., Tsapenko, V. & Shikanov, A., *Investigation of the reflection of laser radiation from a dense plasma*, Zh. Eksp. Teor. Fiz, vol. 65: 1898 (1973) 115, 118

Scheiner, B. & Schmitt, M., *The role of incidence angle in the laser ablation of a planar target*, Physics of Plasmas, vol. 26, 2: 024502 (2019) 117

Schlessinger, L. & Wright, J., *Inverse-bremsstrahlung absorption rate in an intense laser field*, Phys. Rev. A, vol. 20: 1934 (1979) 60

Schurtz, G. P., Nicolaï, P. D. & Busquet, M., *A nonlocal electron conduction model for multidimensional radiation hydrodynamics codes*, Physics of Plasmas, vol. 7, 10: 4238 (2000) 21

Seely, J. F. & Harris, E. G., *Heating of a plasma by multiphoton inverse bremsstrahlung*, Phys. Rev. A, vol. 7: 1064 (1973) 60

Seka, W., Baldis, H. A., Fuchs, J., Regan, S. P., Meyerhofer, D. D., Stoeckl, C., Yaakobi, B., Craxton, R. S. & Short, R. W., *Multibeam Stimulated Brillouin Scattering from Hot, Solid-Target Plasmas*, Physical Review Letters, vol. 89, 17: 175002 (2002a) 117

Seka, W., Craxton, R. S., Delettrez, J., Goldman, L., Keck, R., McCRORY, R. L., Shvarts, D., Soures, J. M. & Boni, R., *MEASUREMENTS AND INTERPRETATION OF THE ABSORPTION OF 0.35/am LASER*, OPTICS COMMUNICATIONS, vol. 40, 6: 4 (1982) 115

Seka, W., Craxton, R. S., Keck, R. L., Knauer, J. P., Meyerhofer, D. D., Regan, S. P., Stoeckl, C., Yaakobi, B., Bahr, R. E., Montgomery, D., Baldis, H. & Kirkwood, R., *Laser-Plasma Interaction Diagnostics for ICF Fusion Research*, p. 27–30, Springer US, Boston, MA (2002b) 117

Shaffer, N. R. & Baalrud, S. D., *The Barkas effect in plasma transport*, Physics of Plasmas, vol. 26, 3: 032110 (2019) 60, 61, 62, 65, 68, 71, 75

Shima, Y. & Yatom, H., *Inverse bremsstrahlung energy absorption rate*, Phys. Rev. A, vol. 12: 2106 (1975) 60

Silin, V. P., *Nonlinear high-frequency plasma conductivity*, Soviet Physics JETP, vol. 20: 1510 (1965) 60, 61, 62, 63, 66, 78, 79, 80, 83, 84, 85, 86, 105

Silin, V. P. & Uryupin, S. A., *Absorption of intense electromagnetic radiation in collisions of charged particles*, Sov. Phys. JETP, vol. 54: 485 (1981) 60

Simpson, J. D., Bosch, R. A., Failor, B. H. & Gabl, E. F., *Absorption in high-Z targets illuminated with 527-nm laser light at high intensity using induced spatial incoherence*, Applied Optics, vol. 29, 30: 4447 (1990) 115, 117, 128

Skupsky, S., *"Coulomb logarithm" for inverse-bremsstrahlung laser absorption*, Physical Review A, vol. 36, 12: 5701 (1987) 33, 43, 60, 62, 63, 66, 78, 79, 80, 85, 86

Spitzer, L. & Härm, R., *Transport phenomena in a completely ionized gas*, Phys. Rev., vol. 89: 977 (1953) 21

Suter, L. J., Glenzer, S., Haan, S., Hammel, B., Manes, K., Meezan, N., Moody, J., Spaeth, M., Divol, L., Oades, K. & Stevenson, M., *Prospects for high-gain, high yield national ignition facility targets driven by 2ω (green) light*, Physics of Plasmas, vol. 11, 5: 2738 (2004) 16

Temko, S., *On the derivation of the fokker-planck equation for a plasma*, Soviet Phys. JETP, vol. 4 43

Thompson, A. P., Aktulga, H. M., Berger, R., Bolintineanu, D. S., Brown, W. M., Crozier, P. S., in 't Veld, P. J., Kohlmeyer, A., Moore, S. G., Nguyen, T. D., Shan, R., Stevens, M. J., Tranchida, J., Trott, C. & Plimpton, S. J., *LAMMPS - a flexible simulation tool for particle-based materials modeling at the atomic, meso, and continuum scales*, Comp. Phys. Comm., vol. 271: 108171 (2022) 68, 83, 89

Tommasini, R., Field, J. E., Hammel, B. A., Landen, O. L., Haan, S. W., Aracne-Ruddle, C., Benedetti, L. R., Bradley, D. K., Callahan, D. A., Dewald, E. L., Doeppner, T., Edwards, M. J., Hurricane, O. A., Izumi, N., Jones, O. A., Ma, T., Meezan, N. B., Nagel, S. R., Rygg, J. R., Segraves, K. S., Stadermann, M., Strauser, R. J. & Town, R. P. J., *Tent-induced perturbations on areal density of implosions at the National Ignition Facilitya)*, Physics of Plasmas, vol. 22, 5: 056315 (2015) 12

Tsubakimoto, K., Nakatsuka, M., Nakano, H., Kanabe, T., Jitsuno, T. & Nakai, S., *Suppression of interference speckles produced by a random phase plate, using a polarization control plate*, Optics Communications, vol. 91, 1: 9 (1992) 119

Turnbull, D., Colaïtis, A., Hansen, A. M., Milder, A. L., Palastro, J. P., Katz, J., Dorrer, C., Kruschwitz, B. E., Strozzi, D. J. & Froula, D. H., *Impact of the Langdon effect on crossed-beam energy transfer*, Nature Physics, vol. 16, 2: 181 (2020) 89

Turnbull, D., Michel, P., Chapman, T., Tubman, E., Pollock, B. B., Chen, C. Y., Goyon, C., Ross, J. S., Divol, L., Woolsey, N. & Moody, J. D., *High Power Dynamic Polarization Control Using Plasma Photonics*, Physical Review Letters, vol. 116, 20: 205001 (2016) 35

Turnbull, D., Michel, P., Ralph, J. E., Divol, L., Ross, J. S., Berzak Hopkins, L. F., Kritcher, A. L., Hinkel, D. E. & Moody, J. D., *Multibeam Seeded Brillouin Sidescatter in Inertial Confinement Fusion Experiments*, Physical Review Letters, vol. 114, 12: 125001 (2015) 17, 117

Vandenboomgaerde, M., Bastian, J., Casner, A., Galmiche, D., Jadaud, J.-P., Laffite, S., Liberatore, S., Malinie, G. & Philippe, F., *Prolate-spheroid ("rugby-shaped") hohlraum for inertial confinement fusion*, Phys. Rev. Lett., vol. 99: 065004 (2007) 16

Wang, M., Huang, W., Kondev, F., Audi, G. & Naimi, S., *The AME 2020 atomic mass evaluation (II). tables, graphs and references*, Chinese Physics C, vol. 45, 3: 030003 (2021) 8

Weng, S.-M., Sheng, Z.-M., He, M.-Q., Wu, H.-C., Dong, Q.-L. & Zhang, J., *Inverse bremsstrahlung absorption and the evolution of electron distributions accounting for electron-electron collisions*, Physics of Plasmas, vol. 13, 11: 113302 (2006) 60, 64, 88

Weng, S.-M., Sheng, Z.-M. & Zhang, J., *Inverse bremsstrahlung absorption with nonlinear effects of high laser intensity and non-Maxwellian distribution*, Physical Review E, vol. 80, 5: 056406 (2009) 60, 64, 88

Xu, Y., Zhu, T., Li, S. & Yang, J., *Beneficial effect of ch foam coating on x-ray emission from laser-irradiated high-z material*, Physics of Plasmas, vol. 18, 5: 053301 (2011) 16

Young, P. E. & Estabrook, K. G., *Angularly resolved observations of sidescattered laser light from laser-produced plasmas*, Physical Review E, vol. 49, 6: 5556 (1994) 115

Zimmerman, G. B. & Kruer, W. L., *The lasnex simulation code*, Comm. Plasma Phys. Cont. Fus, vol. 2: 51 (1975) 61

Zylstra, A., Hurricane, O., Callahan, D., Kritcher, A., Ralph, J., Robey, H., Ross, J., Young, C., Baker, K., Casey, D. *et al.*, *Burning plasma achieved in inertial fusion*, Nature, vol. 601, 7894: 542 (2022) 16, 17

Zylstra, A. B., Casey, D. T., Kritcher, A., Pickworth, L., Bachmann, B., Baker, K., Biener, J., Braun, T., Clark, D., Geppert-Kleinrath, V., Hohenberger, M., Kong, C., Le Pape, S., Nikroo, A., Rice, N., Rubery, M., Stadermann, M., Strozzi, D., Thomas, C., Volegov, P., Weber, C., Wild, C., Wilde, C., Callahan, D. A. & Hurricane, O. A., *Hot-spot mix in large-scale hdc implosions at nif*, Physics of Plasmas, vol. 27, 9: 092709 (2020) 16

Zylstra, A. B., Kritcher, A. L., Hurricane, O. A., Callahan, D. A., Baker, K., Braun, T., Casey, D. T., Clark, D., Clark, K., Döppner, T., Divol, L., Hinkel, D. E., Hohenberger, M., Kong, C., Landen, O. L., Nikroo, A., Pak, A., Patel, P., Ralph, J. E., Rice, N., Tommasini, R., Schoff,

M., Stadermann, M., Strozzi, D., Weber, C., Young, C., Wild, C., Town, R. P. J. & Edwards, M. J., *Record energetics for an inertial fusion implosion at nif*, Phys. Rev. Lett., vol. 126: 025001 (2021) 16

ECOLE DOCTORALE

Titre : Étude numérique et expérimentale de l'absorption laser dans un plasma par bremsstrahlung inverse

Mots clés : absorption, réflexion, bremsstrahlung inverse, dynamique moléculaire, laser, plasma

Résumé : La Fusion par Confinement Inertiel (FCI) consiste à comprimer une capsule millimétrique d'un mélange Deutérium-Tritium à l'aide de lasers de puissance jusqu'à atteindre les conditions de fusion thermonucléaire auto-entretenue. Deux méthodes d'irradiation par les lasers de puissance sont possibles. En attaque directe, les lasers sont absorbés par la surface externe de la capsule. En attaque indirecte, la capsule, positionnée au centre d'une cavité en or (hohlraum), est irradiée par un rayonnement X intense issu de l'absorption des lasers par les parois de la cavité. Le retour des expériences de FCI réalisées depuis plus de dix ans aux USA au National Ignition Facility a montré que l'absorption laser par la matière était encore imparfaitement modélisée dans les simulations d'hydrodynamique-radiative utilisées pour les dimensionner et les restituer.
Cette thèse a pour objectif d'améliorer la modélisation d'un des principaux mécanismes de couplage laser/matière en FCI : l'absorption du rayonnement par bremsstrahlung inverse (BI). Nous avons proposé un modèle paramétré à partir d'un grand nombre de modèles de la littérature. Les constantes ajustables ont été évaluées pour ces différents modèles de la littérature (montrant au passage la disparité) et nous avons pu aussi les évaluer par des simulations de dynamique moléculaire classique (DMC) pour des plasmas à deux composantes (électrons-ions) faiblement couplés (d'intérêts pour la FCI) pour les degrés d'ionisation $Z^* = 1$ (faible) et $Z^* = 10$ (modéré). Les résultats de nos simulations de DMC semblent exclure certaines hypothèses qui mènent, dans certains modèles, à une dépendance du logarithme Coulombien (qui est une manifestation des effets collectifs microscopiques dans le processus d'absorption) à la fréquence du laser indépendamment de son intensité. Nous avons aussi implémenté ce modèle paramétré dans le code d'hydrodynamique-radiative TROLL qui a été utilisé pour simuler une série d'expériences de réflexion laser sur plaques (15 matériaux purs testés) réalisées dans le cadre de cette thèse sur l'installation GCLT au CEA DAM. Les résultats préliminaires de la comparaison de ces simulations avec les données expérimentales (réflectivité au cours du temps, imagerie de l'évolution du plasma coronal) permettent une évaluation des paramètres qui pourront être comparés aux valeurs issues de la DMC.

Title : Numerical and experimental study of laser absorption in a plasma by inverse bremsstrahlung

Keywords : absorption, reflection, glint, inverse bremsstrahlung, molecular dynamics, laser, plasma

Abstract : Inertial Confinement Fusion (ICF) consists in compressing a millimeter-sized capsule of a mixture of Deuterium-Tritium using power lasers to reach the conditions of self-sustained thermonuclear fusion. Two methods of irradiation by power lasers are possible. For a direct drive, lasers are absorbed by the outer surface of the capsule. For an indirect drive, the capsule, located at the center of a gold cavity (hohlraum), is irradiated by an intense flux of X-rays resulting from laser absorption by the walls of the cavity. ICF experiments carried out for more than ten years in the USA at the National Ignition Facility have consistently shown that laser absorption by matter was still imperfectly modeled in the hydrodynamic-radiative simulations used for the design and post-shot modelling of these experiments.
This thesis' goal is to improve the modelling of one of the main mechanisms of laser/matter coupling in ICF: radiation absorption by inverse bremsstrahlung (IB). We have proposed a parameterized model out of several models in the literature. The adjustable constants were evaluated for these various models from the literature (showing in passing the disparity) and we also evaluated these constants by classical molecular dynamics (CMD) simulations for two components (electrons-ions) weakly coupled plasmas (of interest to ICF) for ionization $Z^* = 1$ (weak) and $Z^* = 10$ (moderate). CMD simulation results seem to rule out certain hypotheses leading, in certain models, to a dependence of the Coulomb logarithm (which is a manifestation of microscopic collective effects in the absorption process) on the laser frequency regardless of intensity. We also implemented this parameterized model in the hydrodynamic-radiative code TROLL which was used to simulate a series of laser slab experiments (15 pure materials tested) carried out as part of this thesis on the GCLT facility at CEA DAM. The preliminary results of the comparison of these simulations with the experimental data (reflectivity over time, images of the evolution of the coronal plasma) allow an evaluation of the parameters which can be compared with the CMD values.

Institut Polytechnique de Paris
91120 Palaiseau, France